Modelling and Control of Direct Drive Variable Speed Wind Turbine with Interior Permanent Magnet Synchronous Generator

Mujaddid Morshed Chowdhury

B.Sc. Engg., (Electrical and Electronic)

A thesis submitted in fulfillment of the requirements for the degree

Of

Doctor of Philosophy

University of Tasmania

June 2014

Declaration and Statements

Declaration of Originality

"This thesis contains no material which has been accepted for a degree or diploma by the University or any other institution, except by way of background information and duly acknowledged in the thesis, and to the best of my knowledge and belief no material previously published or written by another person except where due acknowledgement is made in the text of the thesis, nor does the thesis contain any material that infringes copyright."

Authority of Access

This thesis may be made available for loan and limited copying and communication in accordance with the Copyright Act 1968.

Statement regarding published work contained in thesis

"The publishers of the papers comprising Chapter 3 and Chapter 5 hold the copyright for that content, and access to the material should be sought from the respective journals. The remaining non published content of the thesis may be made available for loan and limited copying and communication in accordance with the Copyright Act 1968."

……..

M. M. Chowdhury

Acknowledgement

First of all, I would like to thank Almighty Allah to enable me to complete my PhD research.

I would like to express my sincere gratitude and appreciation to my primary supervisor Dr. M. E. Haque for his guidance, support and encouragement throughout my PhD studies. I am also grateful to my co-supervisors for their comments and support on my research works.

I enjoyed the friendly working environment at the School of Engineering & ICT. I would like to thank the laboratory staff for their support. Special thanks to Mr. James Lamont for his support in experimental works in the power lab.

I would like to thank the School of Graduate Research and University of Tasmania for providing me with a scholarship and support during my PhD studies.

I would like to thank my daughter Ashfia, and sons Maheeb and Mihran for their love, patience and the time they spent without me during the research works.

Finally, I would like to thank my father Golam Morshed Chowdhury, my mother Mymun Nesa, my siblings, and my wife Sumaya Noor for their support, cooperation and encouragement.

Abstract

The interest in wind energy system is growing worldwide to reduce dependency on fossil fuel and to minimize the adverse impact of climate change. Currently, doubly fed induction generator (DFIG) based variable speed wind turbine technology with gearbox is dominating the world market share. However, the problems associated with induction generator based wind turbines are reactive power consumption, mechanical stress and poor power quality. Moreover, the gearbox requires regular maintenance as it suffers from faults and malfunctions. Therefore, it is important to adopt technologies that can enhance efficiency, reliability and reduce system cost of wind based power generation system. The performance of a variable speed wind turbine can be enhanced significantly by using a low speed permanent magnet synchronous generator (PMSG) without a gearbox. The main features of PMSG based wind turbines are; gearless operation, higher efficiency, enhanced reliability, smaller size, reduced cost and low losses. The main aim of this thesis is to develop improved control strategies for an efficient and reliable grid interface system for a gearless, direct drive variable speed wind turbine.

This thesis focuses on several aspects of modelling and control of interior permanent magnet (IPM) synchronous generator based grid connected variable speed wind turbine with maximum power extraction (MPE). Both the indirect and direct control strategies are addressed for IPM synchronous generator based variable speed wind turbines. The main contributions of this thesis are; (i) development of parameter measurement methods to determine the parameter of an IPM synchronous generator, (ii) development of an improved indirect vector control scheme for the IPM synchronous generator based direct drive variable speed wind turbine, incorporating maximum torque per ampere trajectory (MTPA) and maximum power extraction (MPE) algorithm (iii) development of direct torque and flux (DTFC) control scheme for the IPM synchronous generator based direct drive variable speed wind turbine, and (iv) development of control and power management strategy for a three level converter based STATCOM with Super-capacitor energy storage to enhance the performance of the proposed wind energy conversion system under various disturbances.

The parameters of IPM synchronous generators have an important influence on the steady state and dynamic performance analysis of the variable speed wind turbine. The knowledge of the machine model and accurate parameters is mandatory to analyze the performance and to design efficient and fast controllers for the variable speed wind turbine. Therefore, accurate measurement of these parameters is essential. This thesis presents simple practical methods of determining parameters such as magnet flux, and, *d*- and *q*-axes inductances of an IPM synchronous generator. An experimental test set-up is developed and the results are presented.

The second contribution of the thesis is to develop an improved indirect vector control scheme for the IPM synchronous generator based direct drive variable speed wind turbine, incorporating maximum torque per ampere trajectory (MTPA) and a maximum power extraction (MPE) algorithm. The main advantage of incorporating MTPA trajectory in the control scheme is that it can generate the required torque with a minimum stator current. Therefore, the stator loss of the IPM synchronous generator is minimized. The proposed control scheme is simulated in *Matlab/SimPowerSystems* environment and experimentally implemented using a DSpace DS1104 digital signal processor (DSP) system. The simulation and experimental results confirm the effectiveness of the developed control scheme to control the direct drive variable speed wind turbine with MPE under varying wind speed.

In an indirect vector control scheme, the IPM synchronous generator torque is controlled by controlling the *d*- and *q*-axes currents. Therefore, the generator torque is controlled indirectly by controlling *d*- and *q*-axes currents in the rotor reference frame. As the calculations are done in the rotor reference frame, a coordinate transformation is necessary in this scheme. This scheme is affected by generator parameter variations and introduces delay in the control system. Therefore, an advanced direct torque and flux control (DTFC) scheme for IPM synchronous generator based variable speed wind turbine with MPE is proposed in this thesis to overcome the drawbacks associated with indirect vector control scheme. The DTFC scheme possesses advantages such as lesser parameter dependence and reduced number of controllers compared with traditional indirect vector control scheme. The direct control scheme is simpler and can eliminate the drawbacks of traditional indirect vector control scheme.

Finally, this research has also developed control and power management strategy for a multilevel converter based STATCOM with Super-capacitor energy storage to ensure the reliable operation and enhance fault ride through capability of the direct drive variable speed wind turbine under various disturbances. Results confirm the effectiveness of the proposed control and power management strategy.

Contents

List of Figures

List of Tables

List of Symbol

μs	micro second
A	cross-sectional area through which the wind passes
C	DC-link Capacitance
C_P	power coefficient
i_a, i_b , i_c	Line output currents of the power inverter
i_d	*d*-axis current
i_q	*q*-axis current
J	inertia
L_A	component of the self-inductance
L_{aa} ,L_{bb} ,L_{cc}	stator self-inductances
$L_{ab,}$ $L_{bc,}$ L_{ca}	stator to stator mutual inductance
L_d	*d*-axis inductance
L_f	line inductance
L_l	armature leakage flux
L_{md} ,L_{mq}	*d*- and *q*- axis magnetizing inductances
L_q	*q*-axis inductance
m	air mass
M	mutual inductance
m_a	modulation index
N_s	stator windings turns number
p	the operator *d/dt*
P_G	real power
P_{G1}	excitation power
P_{G2}	reluctance power
P_T	Turbine power

P_{wind}	power in the wind
Q_G	reactive power
R	the radius of the turbine
R_f	line resistance
R_s	stator resistance
S	per phase complex power
SGs	Synchronous generators
T_g	generator electromagnetic torque
T_m	turbine mechanical torque
TSR	tip-speed to wind speed ratio
v_{ab}, v_{bc} , v_{ca}	Line to line voltages of the power inverter
V_{dc}	DC-link voltage
v_w	wind speed
v_{w1}	upwind velocity of the undisturbed wind
v_{w2}	downwind velocity
v_{wT}	velocity of the wind through the plane of the rotor blades
β	pitch angle
δ	power angle
θ_g	grid voltage angle
θ_r	rotor position
λ	tips speed ratio
λ_d, λ_q	*d*- and *q*- axes stator flux linkages
λ_M	rotor magnet flux
ρ	air density
ϕ_g	grid power factor angle
ω_m	the mechanical speed of the turbine rotor

Abbreviations

AC	Alternative Current
AVR	Autonomic Voltage Regulator
DC	Direct Current
DFIG	Doubly Fed induction generator
DTC	Direct Torque Control
DTFC	Direct Torque and Flux Control
FACTS	Flexible AC Transmission System
HAWT	Horizontal Axis Wind Turbines
IGBT	Insulated Gate Bipolar Transistor
IPM	Interior Permanent Magnet
LVRT	Low Voltage Ride Through
MPE	Maximum Power Extraction
MPP	Maximum Power Point
MTPA	Maximum Torque Per Ampere trajectory
p:u:	per unit value
PCC	Point Common Coupling
PF	Power Factor
PI	Proportional Integral controller
PID	Proportional Integral Derivative controller
PLL	Phase Locked Loop
PMSG	Permanent Magnet Synchronous Generator
PWM	Pulse Width Modulation
SC	Supercapacitor
SCIG	Squirrel Cage Induction Generator
SSSC	Static Synchronous Series Compensator
STATCOM	Static Synchronous Compensator
SVC	Static Var Compensator
SVM	Space Vector Modulation
TCR	Thyristor Controlled Reactor
TSR	Thyristor Switched Reactor

UPFC	Unified power flow controller
VAWT	Vertical Axis Wind Turbines
VSC	Voltage Source Converter
WPP	Wind Power Plant
WRSG	Wound Rotor Synchronous Generator

Chapter 1

Introduction

1.1 Background

Recent trend indicates that wind energy will play a major role to meet the future energy target worldwide to reduce reliance on fossil fuel and to minimize the adverse impact of climate change. Wind energy is the fastest growing generation technology among the renewable energy sources. Over the last decade, the global wind energy capacity has increased rapidly and wind is an important competitor to the traditional sources of energy. In 2013, more than 35 GW of wind power capacity was added to the global wind generation capacity which became 318 GW as shown in Fig.1.1 [1]. Since 2008, annual growth rates of cumulative wind power capacity have averaged 21.4%, and global capacity has increased eightfold over the past decade [1], [2]. Recently, capital costs of wind generation technologies have declined primarily due to the competition and advanced technology development including taller towers, longer blades, and smaller generators in low wind speed areas—have increased capacity factors [1]. The technological development contributed to reduce the costs of wind turbines and made it competitive relative to fossil fuel based generation. Onshore wind-generated power is now more cost competitive on a per kWh basis with new coal/gas fired power plants, in several markets (including Australia, Brazil, Chile, Mexico, New Zealand, South Africa, Turkey, much of the EU, and some locations in India and the United States) [1], [2]. As a result of this trend, high level of wind energy (>30%) will be integrated into the power grid and major challenges and issues will appear, which are needed to be addressed for efficient and reliable operation of the existing power system.

As the wind penetration increases, the structure and dynamics of the power system network will change significantly over the coming decades. Due to the intermittent nature of wind power, the replacement of traditional synchronous generators with power electronic converter-based synchronous generators will introduce special

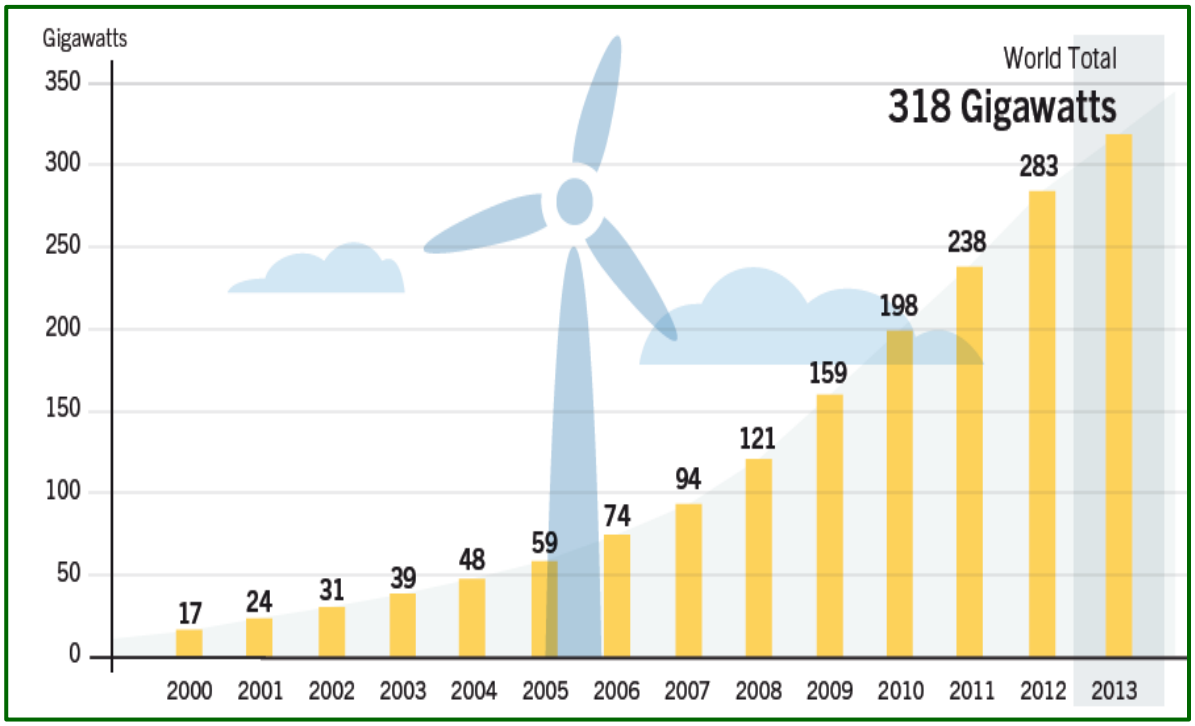

(a) Global wind power capacity (2000-2013)

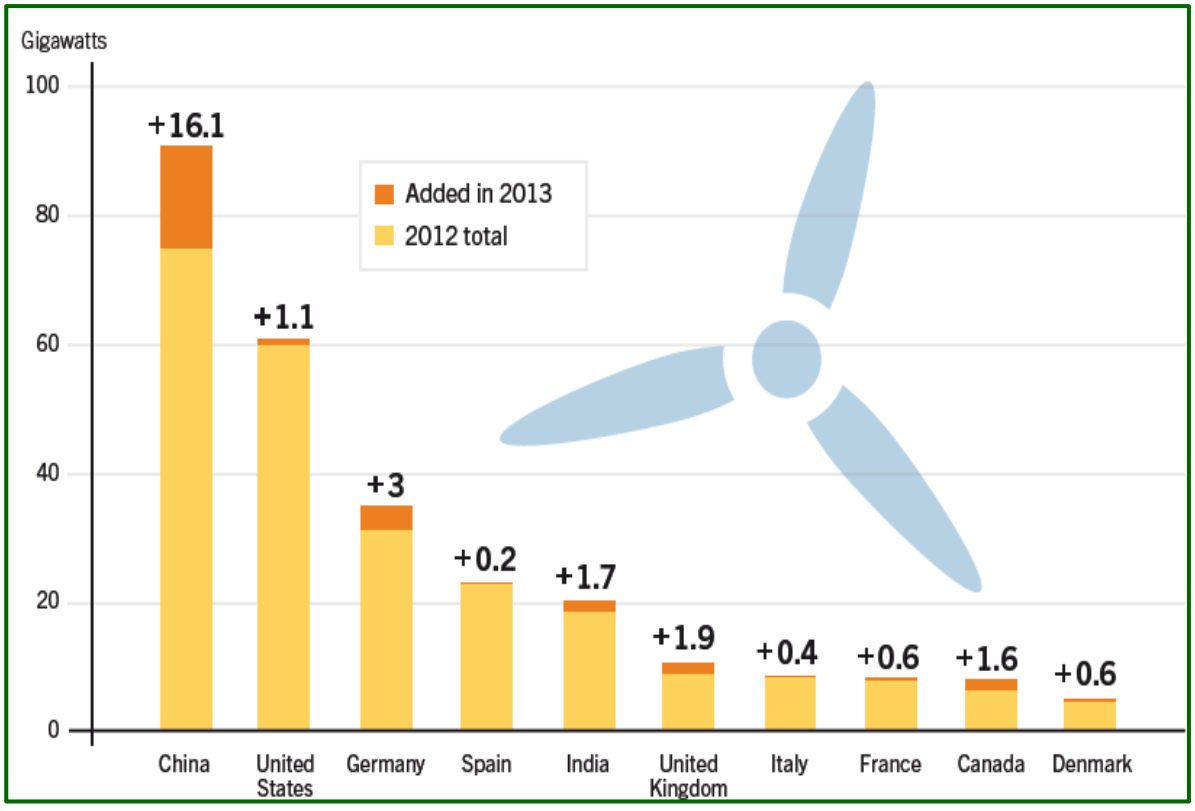

(b) Global wind power capacity and addition, Top 10 countries.

Figure 1.1 Global wind power capacity (2000-2013) [1].

challenges in; grid interconnections and bi-directional power control, tight voltage and frequency regulation, dynamic stability, low voltage fault ride through, satisfy grid code, system security, reliability, and protection [3].

Therefore, a better understanding of the technology involved with the grid integration of the variable speed wind turbines and possible impacts of large scale wind integration to the power grid is mandatory to ensure reliable and secure operation of the power system.

1.2 Recent Trends in Wind Turbine Technologies and Control

Over the last two decades, wind power has become the most promising renewable energy technology due the development in wind turbine aerodynamics, structure, variable speed generator technologies, power electronics and DSP (digital signal processor) based control topologies. The wind turbine industries is continuously moving forward in order to increase efficiency and controllability of the variable speed wind turbines to enhance the large scale grid integration of wind energy conversion system. Recent trend indicates an increase in large scale wind farms, which will contribute to significant share of the energy. They will also introduce new challenges and issues in the power system operation and control. These challenges include integration to the weaker grid, voltage and frequency regulation, dynamic voltage stability under disturbances, power fluctuations and changing dynamics of the conventional power plants [3], [4]. The wind farms will have to fulfil the new grid code requirement for reliable and stable operation of the power system. Currently, the doubly fed induction generator (DFIG) based gear-driven variable speed wind turbine technology dominating the market. However, there is an increasing trend for permanent magnet synchronous generator (PMSG) based gearless direct drive variable speed wind turbine due to superior performance, efficiency, smaller size, less maintenance and enhanced fault ride through capability [3].

1.2.1 Wind Turbine Technologies

1.2.1.1 Fixed Speed Wind Turbine Technology

Fig.1.2 show the fixed speed wind turbine which uses a squirrel cage induction generator (SCIG) directly connected to the grid through a coupling transformer [3]. A capacitor bank is required for the compensation of reactive power requirement of induction generator. The problems associated with induction generator based fixed speed wind turbines are reactive power consumption, mechanical stress and poor power quality [4], [5]. In a fixed speed wind turbine, fluctuations in wind speed are transmitted as fluctuations in the mechanical torque, and that results in fluctuations in the electrical power [4]. The power fluctuations can also lead to large voltage fluctuations in a weak grid system [4]. This configuration does not support any speed control, it requires a stiff grid and its mechanical construction must be able to tolerate high mechanical stress [3].

1.2.1.2 DFIG Based Gear-Driven Variable Speed Wind Turbine Technology

Currently, variable-speed wind turbine technologies are very popular because of their advantages such as increased energy capture, maximum power extraction, higher efficiency and better power quality [4]-[6]. Most of the current installed turbines use doubly fed induction generator (DFIG) based variable speed wind turbines with gearbox as shown in Fig.1.3 (a) [7]-[10]. The advantage of this technology is that it requires power converter with reduced capacity (30% of full capacity) as the converter is connected to the rotor circuit instead of stator circuit [4]. In this configuration, the stator is directly connected to the grid and the rotor is connected to grid through a power converter to control the rotor frequency and the rotor speed [4]. Depending on the size of the frequency converter (usually rated at approximately 30% of nominal generator power) this technology can operates in a wide speed range. Typically, the variable speed range is ±30% around the synchronous speed, which makes this concept attractive and popular from economic point of view [11]. When the generator runs at super-synchronous speed, the electrical power is injected to the grid through both the rotor and the stator. When the generator runs at sub-synchronous speed, the electrical power is delivered into the rotor from the grid [3]. Fig.1.3 (b) and Fig.1.3(c) show self-excited induction generator and wound rotor synchronous generator based gear driven variable speed wind turbines, respectively.

However, the main drawback of this type of wind turbine is the requirement of a gearbox which requires regular maintenance and suffers from faults and malfunctions [4]. Moreover, it increases the overall size of the wind turbine. Another disadvantage of DFIG topology is that it is very sensitive to grid disturbance, especially for the voltage dip, due to the fact that the stator is directly connected to the grid [3]. The voltage dip could cause over voltage and over current in the rotor windings and consequently damaged the rotor side converter [3]. To provide a DFIG with good fault ride through (FRT) the wind turbine and the power converter should have the ability to protect itself, without disconnecting during faults. In order to fulfill this requirement, a crowbar is needed to offer extra protection to bypass the converter by short-circuiting the rotor windings [12].

1.2.1.3 PMSG Based Gearless Direct Drive Variable Speed Wind turbine with Full scale Converter

In this configuration, the generator rotor is directly connected to the turbine rotor without any gearbox and the generator is interfaced with the grid/load using full scale AC-DC-AC power converters as shown in Fig.1.4. This configuration is most suited for full power control as it is connected to the grid through a power converter. The permanent magnet synchronous generators (PMSGs) used in this configuration are low speed generators with suitable number of poles and able to produce higher torque at low speed. The full-scale power converter can perform smooth grid connection over the entire speed range [3]. The power electronic converters used in this configuration have two primary goals: to act as an energy buffer (DC-link) for the power fluctuations caused by the wind turbine and for the transients coming from the grid side and enables the system to control active and reactive power [3]. The main features of PMSG based wind turbines are [13]-[20]:

- gearless operation and enhanced reliability
- simple structure, smaller size and reduced cost
- low mechanical and electrical losses
- higher power factor and efficiency
- no requirement for reactive power support
- higher cost and power losses in the converters.
- No need of external excitation.

This type of wind turbine has a better fault ride through capability compared with the DFIG system with better efficiency and lesser complexity. Therefore, direct drive variable speed wind turbine is becoming more attractive [21]. However, the reactive power requirements can be fulfilled through the power converter control for both DFIG and direct drive wind turbine with full scale converter concepts [3], [22].

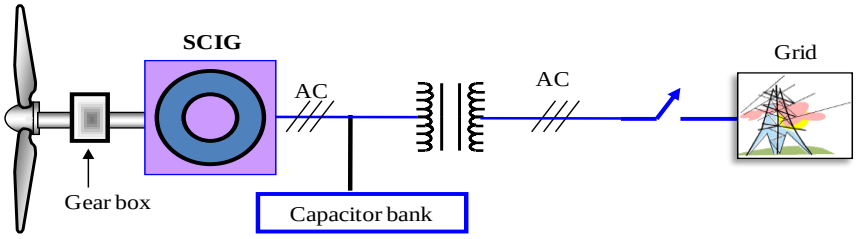

Figure 1.2 Fixed speed wind turbine with induction generator.

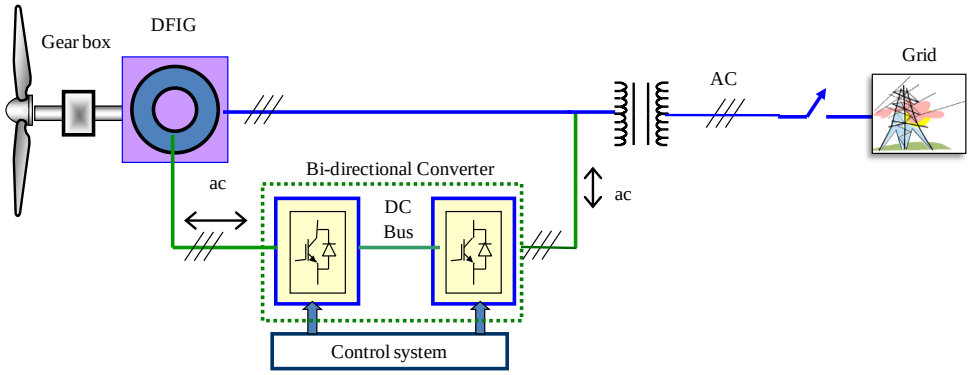

(a) DFIG

(b)

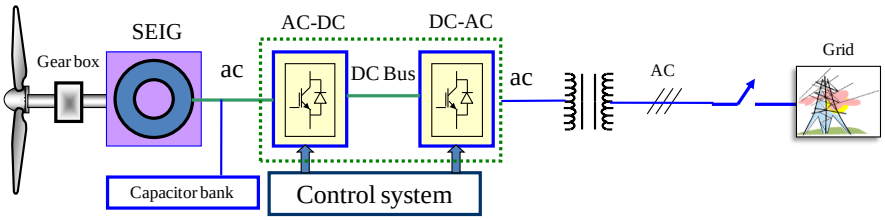

(c) Self excited induction generator (SEIG)

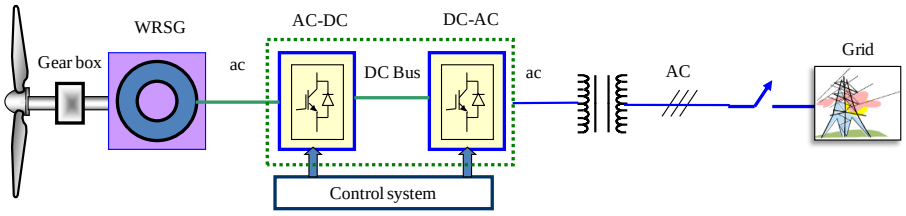

(c) WRSG

Figure 1.3 Gear-driven variable speed wind turbines.

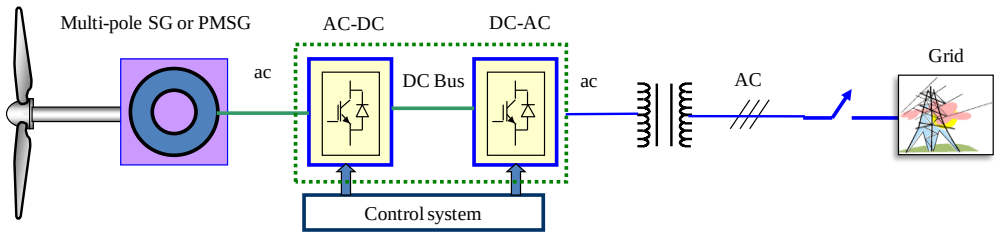

Figure 1.4 Gearless Direct drive variable speed wind turbine PMSG or Multi-pole synchronous generator.

1.3 Problem Statement and Motivation for the Current Research

Recent trends indicates a significant increase in large wind farms with PMSG based gearless direct drive wind turbine technology due to their advantages over induction generator based wind turbine with gearbox. These turbine generators will be connected to the grid through a full scale power electronic converters and expected to have capabilities of voltage/frequency regulation, reactive power support and fault ride through to maintain stable operation and to keep them connected to the grid under various disturbances. Therefore, it is necessary to design and develop reliable and efficient control strategies for PMSG based direct drive variable speed wind turbines to meet the grid code requirement. As the wind penetration into the grid is increasing, an efficient and reliable controller for the wind turbine is very important. This research will investigate the control strategies for a direct drive variable speed wind turbine with interior permanent magnet (IPM) synchronous generator. The main aims of this research include; analysis and modelling, improved controller design and implementation and application of supercapacitor energy storage to ensure dynamic voltage stability and reliable system operation.

Fig.1.4 shows the configuration for a direct drive variable speed wind turbine with PMSG where the generator is interfaced with the grid using back to back voltage source converters. The generator side AC-DC converter is used to control the speed/torque and to extract maximum power under varying wind speeds. The grid side DC-AC converter is used to control the power flow to the grid. The two converters are linked by a dc link capacitor to ensure separate control for each converter. Most of the previous works related to PMSG based wind turbines are based on surface type permanent magnet

synchronous generator [13]-[18]. Several manufacturers including SIEMENS, GE, Suzlon are producing multi MW scale wind turbines, which are based on surface type PMSG for which the *d*-axis and *q*-axis inductances are equal, $L_d=L_q$. However, much attention has not been paid to interior permanent magnet (IPM) synchronous generator based variable speed wind turbines. The IPM synchronous generator (for which $L_d \neq L_q$) can produce more power than that of a surface type PMSG by utilizing their rotor saliency [18]. The IPM generator can be operated over a wide speed range by using flux weakening and allows constant power like operation at speeds higher than the rated speed [18], [19]. This research is focused on the control of IPM synchronous generator based variable speed wind turbine.

Traditionally, PMSG is controlled using switch-mode boost rectifier [13], [23], [24], three switch PWM rectifier [15], vector controlled PWM rectifier [18], [19]. The switch-mode rectifier has simple structure and low cost. However, it introduces high harmonic distortion and unable to control the power factor, which affects the system performance and efficiency [18], [19]. Therefore, vector controlled back to back PWM converter with voltage source converter (VSC) is preferred for IPM synchronous generator based variable speed wind turbines. In a traditional vector control scheme, the *d*-axis current is regulated to zero and the *q*-axis current is controlled to control the torque of the generator in the rotor reference frame. However, in an IPM synchronous generator both *d*- and *q*-axis currents need to be regulated to utilize the rotor saliency and to enhance the system efficiency. In this thesis, an enhanced vector control scheme is presented by incorporating maximum torque per ampere trajectory and maximum power extraction algorithm to enhance system performance with increased energy capture and efficiency, and low losses.

In a vector control scheme, the torque of the generator is controlled indirectly by regulating the *d*-axis current i_d and *q*-axis current i_q according to the generator torque equation. The current control is executed at the rotor *dq*-reference frame, which rotates with the rotor. Therefore, coordinate transformation is involved and a position sensor is, thus, mandatory for the current control loop. All these tasks introduce delays in the system [25],[26]. This control scheme is also affected by the parameter variation. Moreover, the torque response under this type of control is limited by the time constant

of stator windings [25]. Since the last two decades, Direct Torque Control (DTC) scheme has become popular for variable speed ac motor drives. Direct torque control for induction motor was developed by Japanese and German researchers I. Takahashi and T. Noguchi (1984, 1985) [26]; Depenbrock (1985) [27]. Later on, the DTC scheme is implemented for permanent magnet synchronous motor based variable speed drive applications. Recently, the direct control scheme is also applied to induction generator based variable speed wind turbine applications [28]-[30]. However, little attention has been paid to the application of direct control scheme for IPM synchronous generator based direct drive variable speed wind turbine. In this thesis, the direct control scheme is proposed for an IPM synchronous generator based variable speed wind turbine to overcome the problems associated with the traditional indirect vector control scheme. In this scheme, the generator torque and flux linkage are controlled directly and independently by the selection of optimum inverter switching modes. The main features of this control scheme include; simpler control methods, no requirement for coordinate transformation, lesser parameter dependence, and absence of several controllers.

In the past, wind power penetration to the power grid was low and it was not a major concern. With the increased penetration level of wind energy to the power grid, it has become necessary to address problems associated the stability, reliability and security of the power system. Dynamic voltage stability and low voltage ride through (LVRT) or fault ride through (FRT) capability are the basic requirement for the wind firm in many countries. Transmission system operators require the wind farms to be connected to the network during faults or disturbances by proving necessary reactive power support. Wind firms should have the capability to continue uninterrupted power supply under any disturbances and follow the grid code requirements. Dynamic voltage stability and fault ride through are the important issues among the challenges for grid connected wind firms with large penetration level. The application of an energy storage system in a wind farm can minimise some of the major challenges of grid integration of wind farm. Energy storage can play a vital role to smooth the fast wind-induced power variations. This energy storage can also enhance the low voltage ride through capability (LVRT) of wind turbine. In this thesis, issues and impacts associated with the wind integration into the grid are discussed. As a remedial measure, the application of static synchronous compensator (STATCOM) with supercapacitor energy storage is

investigated to enhance the dynamic performance of a grid connected wind firm. The control strategy for the STATCOM with supercapacitor energy storage is developed to enhance the dynamic voltage stability of the wind firm. The STATCOM has the ability to provide voltage support by supplying or absorbing reactive power into the power network under disturbances.

1.4 Contributions of This Research

The main aim of this research is to develop efficient and reliable control strategies for a direct drive IPM synchronous generator based variable speed wind turbine to ensure efficient and reliable grid integration of wind farm. This thesis focuses on several aspects of modelling and control of interior permanent magnet (IPM) synchronous generator based grid connected variable speed wind turbine with maximum power extraction (MPE). Both the indirect and direct control strategies are addressed for IPM synchronous generator based variable speed wind turbine. The main contributions of this thesis are;

(i) Mathematical Analysis and computer modelling of IPM synchronous generator based variable speed wind turbine. The detail analysis of IPM synchronous generator are presented in this thesis, which is required to develop control strategies

(ii) development of parameter measurement methods to determine the parameter of IPM synchronous generator. The accurate machine model and parameters are required to analyse the performance and to design high performance controllers. A simple parameter measurement method is developed in this thesis for the accurate measurement of parameter of IPM synchronous generator.

(iii) development of an improved indirect vector control scheme for the IPM synchronous generator based direct drive variable speed wind turbine, incorporating maximum torque per ampere trajectory (MTPA) and maximum power extraction (MPE) algorithm.

(iv) development of direct torque and flux (DTFC) control scheme for the IPM synchronous generator based direct drive variable speed wind turbine

(v) development of control and power management strategy for a three level converter based STATCOM with Super-capacitor energy storage to enhance

the performance of the proposed wind energy conversion system under various disturbances.

1.5 Thesis Outline

This thesis is structured in seven chapters. The first chapter is started with introduction about the wind turbine technologies and their features, limitations and background. The problem statement and motivation of current research and the contributions of the thesis are presented.

In chapter 2, the mathematical analysis and modelling of wind turbine is presented. The modelling of wind turbine is presented including the stream tube model of air flow for maximum power extraction by a wind turbine. The influence of number of turbine rotor blades is also discussed. Wind turbine power characteristics and different aerodynamic power control strategies are discussed. Finally, different wind turbine configurations are presented.

Chapter 3 presents the detail analysis and *dq*-axis modelling of a permanent synchronous generator (PMSG) used in this research. A simple methods of determining parameters such as magnet flux (λ_M), *d*-axis inductance (L_d) and *q*-axis inductance (L_q) of interior permanent magnet (IPM) synchronous generator, which are used to control the wind turbine generator is presented in chapter 3. The effectiveness of parameter measurement methods are demonstrated by experimental results.

Chapter 4 discusses control strategies for PMSG based direct drive variable speed wind turbine. A review of control strategies for the direct drive wind turbine with PMSG is presented first. Then, the modelling, analysis and control of IPM synchronous generator direct drive variable speed wind turbine using switch-mode rectifier is presented. Finally, an enhanced vector control scheme for interior permanent magnet (IPM) synchronous generator is developed by incorporating maximum torque per ampere trajectory and maximum power extraction algorithm. Finally, simulation and experimental results are presented.

In Chapter 5, the direct control scheme is implemented for an IPM synchronous generator based variable speed wind turbine to overcome the problems associated with the traditional indirect vector control scheme. This scheme has several advantages compared to the traditional vector control scheme as explained in chapter 5. The proposed control scheme is implemented in *Matlab/SimPowerSystems* and results show that the controller can regulate the generator speed extract maximum power under constant and varying wind speed.

Chapter 6 discusses the issues and impacts associated with the wind integration into the power grid. The application of static synchronous compensator (STATCOM) with supercapacitor energy storage is investigated to enhance the dynamic performance of a grid connected wind firm. Simulation model and associated controllers have been implemented in *Matlab/SimpowerSystem* and results are discussed.

Finally, a conclusion and future work recommendations are presented in Chapter 7.

1.6 List of Publications

Refereed Journal Papers

[1] M. M. Chowdhury, M. E. Haque, D. Das, A. Gargoom, and M. Negnevitsky, "Modelling, Parameter Measurement and Sensorless Speed Estimation of IPM Synchronous Generator for Direct Drive Variable Speed Wind Turbine Application", *Intl Transaction on Electrical Energy System,* pp. 1-17, DOI: 10.1002/etep.1933, April,2014.

[2] M. E. Haque, Y. C. Saw and M. M. Chowdhury, "Advanced Control Scheme for an IPM Synchronous Generator Based Gearless Variable Speed Wind Turbine" *IEEE Transaction on Sustainable Energy*, vol.5, no.2, pp. 354-362, April, 2014. [ISSN: 1949-3029].

[3] M. M. Chowdhury, M. E. Haque, and A. Gargoom, "Modeling and DSP Based Control of IPM Synchronous Generator for Direct Drive Variable Speed Wind Energy System", *Renewable Energy*, Under review, 2014.

[4] M. M. Chowdhury, M. E. Haque, and A. Gargoom, "Dynamic Voltage Stability Enhancement of Wind Farm Using Supercapacitor Energy Storage", To be submitted to a Journal.

Refereed Conference Papers

[5] M. M. Chowdhury, M. E. Haque, A. Gargoom and M. Negnevitsky, "Performance Improvement of a Grid Connected Direct Drive Wind Turbine Using Super-capacitor Energy Storage*" IEEE PES Innovative Smart Grid Technologies Conference (ISGT)*, Washington DC, USA, Feb. 24-27, 2013, pp. 1-6. [E-ISBN : 978-1-4673-4895-9].

[6] M. M. Chowdhury, M. E. Haque, A. Gargoom, A. M. O. Haruni, and M. Negnevitsky, "Control of a Grid Connected Direct Drive Variable Speed Wind Turbine*" IEEE PES International Conference on Power System Technology (POWERCON)*, Auckland, New Zealand, Oct.30 to Nov.02, pp. 1-6, 2012.

[7] M. M. Chowdhury, M. E. Haque, A. Gargoom and M. Negnevitsky, ―A Direct Drive Grid Connected Wind Energy System with STATCOM and Super-capacitor Energy Storage‖ *IEEE PES International Conference on Power System Technology (POWERCON)*, Auckland, New Zealand, Oct.30 to Nov.02, pp. 1-6, 2012.

[8] M. M. Chowdhury, M. E. Haque, A. Gargoom and M. Negnevitsky, P. I. Muoka, "Enhanced Control of a Direct Drive Grid Connected Wind Energy System with STATCOM," *Australian Universities International Power Engineering Conference*, Bali, Indonesia, pp. 1-6, Sept. 26 to Sept. 29, 2012.

[9] M. M. Chowdhury, M. E. Haque, M. Aktarujjaman, M. Negnevitsky and A. Gargoom, "Grid integration impacts and energy storage systems for wind energy applications — A review," *IEEE Power and Energy Society General Meeting*, Detroit, MI, USA, pp. 1-8, July 24-29, 2011.

Chapter 2

Modelling of Wind Turbine and Wind Energy System Configurations

2.1 Overview

Wind turbine model is required to design and implement controllers for wind energy conversion system. In this chapter, the mathematical analysis and modelling of wind turbine is presented. This chapter begins with the discussion of the wind source and its characteristics. Then the modelling of wind turbine is presented including the stream tube model of air flow for maximum power extraction by a wind turbine. The influence of number of turbine rotor blades is also discussed. Wind turbine power characteristics and different aerodynamic power control strategies namely passive/active stall control and pitch control are discussed. Finally, wind turbine configurations are presented.

2.2 Wind Source and Characteristics

Wind is a huge source of renewable energy and it is used as an energy source for a long time. Wind is generated by the atmospheric pressure differences which arise from unequal heating of earth's surface by the sun [31]. The sun heats the atmosphere unevenly, so some regions become warmer than others. These warm regions air raise, other air blows in to replace them and wind blows. The irregularities of the earth's surface and rotation of the earth, the heat capacity of the Sun, the cooling effect of the oceans and polar ice caps temperature gradients between land and sea contributes to wind flow [31]-[33].

The sun heats the land more than the seas during the day time. The warmed air rises and creates a low pressure at ground level, which attracts the cool air from the sea. This is called a sea breeze [31]. Since water cools at a lower rate than the land at night, the wind blows in the opposite direction. The land breeze at night generally has lower wind

speeds due to the smaller temperature difference between land and sea at night. Similar breezes are created on mountains as warmer air rises along the heated slopes [31]. During the night, the cooler air goes downhills. The global wind flow in a given area is determined by the temperature variation between the poles and the equator, and the local winds [31].

Wind is a form of solar energy. It is estimated that about 1% of the total incoming solar radiation to the earth is converted into wind energy [31]. The global wind resource is so large and that only small part of it can generate more electrical energy than what is currently being consumed [31]. The equivalent solar energy received by the earth in ten days is enough to fulfil the total energy demand.

Fig. 2.1 shows a typical wind speed and corresponding power variations. The wind is fluctuating in nature, power variations may occur that can affect the wind energy system performance [4].

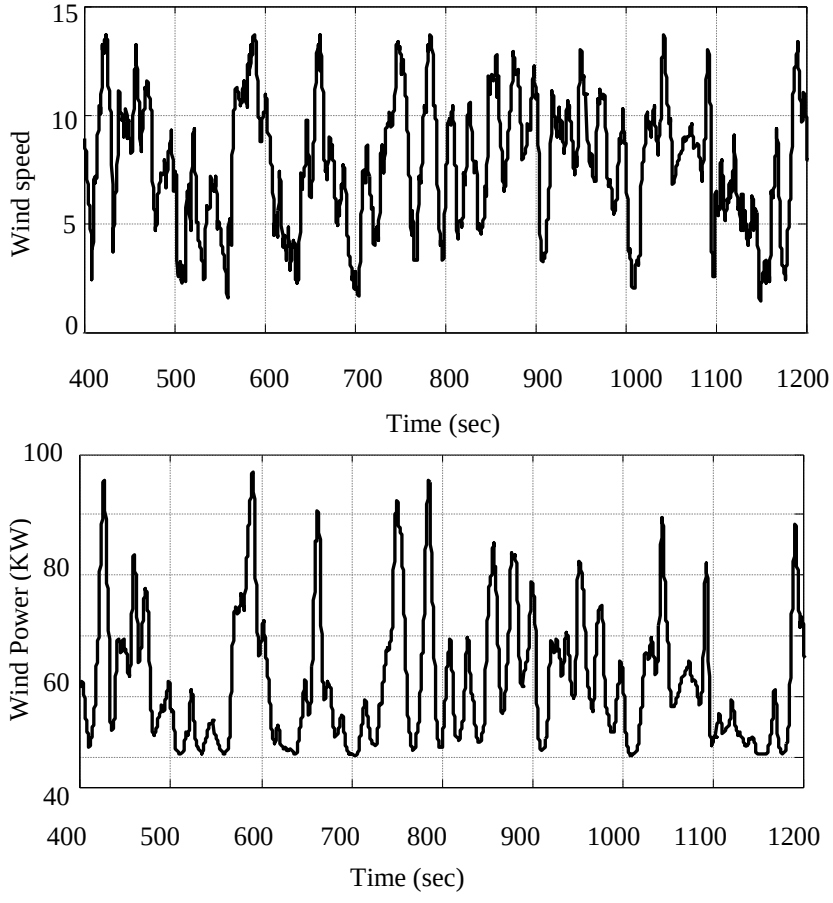

Figure 2.1 Typical wind speed and corresponding power variation.

2.3 Modelling of Wind Turbine

Wind is the movement of air mass and it has kinetic energy. This kinetic energy of the wind can be converted mechanical energy using a wind turbine with rotor blades. This mechanical energy is then converted to electrical energy using a generator.

2.3.1 Power in the Wind

Consider an air mass m flowing through an area *A* with a speed of v_w as shown in Fig. 2.2 [34]. The kinetic energy of wind is given by [34]:

$$K.E = \frac{1}{2} m v_w^2 \tag{2-1}$$

where,

m = air mass (kg)

v_w = wind speed (m/s)

The power is energy per unit time, the power represented by a mass of air moving with a velocity of v_w through an area *A* for a duration of time *T* is given by [34]:

$$P_{wind} = \frac{1}{2} \times \frac{mass}{Time} \times v_w^2 = \frac{1}{2} \times \frac{m}{T} \times v_w^2 \tag{2-2}$$

Since mass flow rate (*m/T*) through area *A* is the product of air density, ρ , air speed v_w and cross-sectional area *A*, then equation (2-2) can be written as

$$P_{wind} = \frac{1}{2} \rho \, A \, v_w^3 \tag{2-3}$$

where,

P_{wind} = power in the wind (W)

ρ = air density (kg/m^3) (at 15^0 C and 1 atm, ρ = 1.225 kg/m^3)

A = cross-sectional area through which the wind passes (m^2)

Figure 2.2 Air mass m flowing through an area A with a velocity v_w

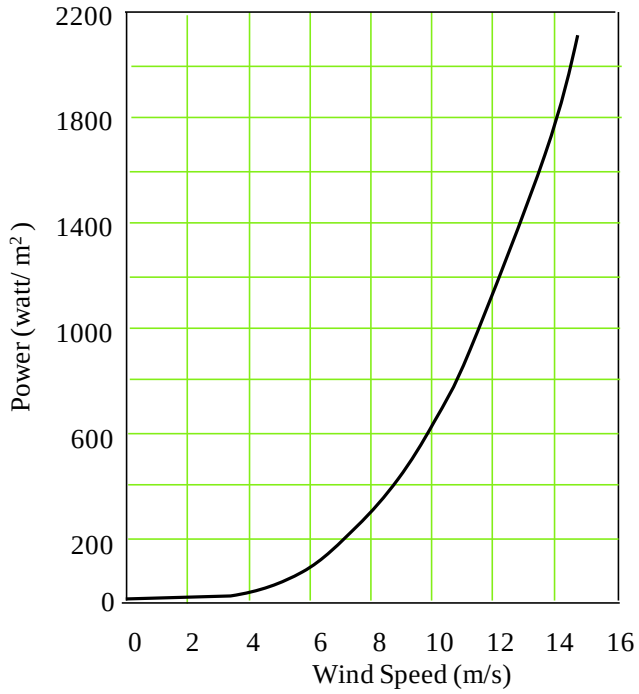

Figure 2.3 Power in the wind (at 15^0C and 1 atm).

A plot of equation (2-3) is shown in Fig.2.3 [34]. The power in the wind increases as the "cube" of the wind speed. This means that the doubling the wind speed increases the power by eight times. Equation (2-3) also suggests that the wind power is proportional to the swept area covered by the wind.

2.3.2 Power Captured by the Wind Turbine

A wind turbine converts the kinetic energy in the wind into mechanical energy using the rotor blades. The amount of energy which the wind transfers to the rotor depends on the density of the air, the rotor swept area, and the wind speed [34]. The rotor blades of the wind turbine capture only part of the available wind power, and the actual power extracted by a wind turbine is given by [34],[35]:

$$P_T = C_p \times P_{wind} = \frac{1}{2}\rho\, A\, v_w^3 \times C_p(\lambda, \beta) \qquad (2\text{-}4)$$

where,

P_T = Turbine power (W)

C_P = Coefficient of performance or power coefficient known as Betz Limit. C_p is the turbine rotor power coefficient, which is a function of tip speed ratio (λ) and pitch angle (β).

Equation (2-4) indicates that there are three options for increasing the power captured by a wind turbine. These are:

- wind speed v_w,
- power coefficient C_P, and
- Swept area $A=\pi l^2$, where l is the blade length

Wind speed cannot be controlled. Therefore, the wind turbine should be located in regions where the wind speed is high to increase the captured power. The captured power is a cubic function of wind speed. Doubling the average wind speed would increase the wind power by eightfold [35].

The German engineer Betz showed that the maximum power extracted from an air stream is 16/27 or 0.59 of the theoretical available power [35].Only 59% of the wind power can be captured by a wind turbine even if the power losses are neglected. The power coefficient of a modern turbine usually varies from 0.2 to 0.5 depending on the turbine speed and number of blades. For a three blade turbine with a rotor diameter of 82 m and power coefficient of C_P=0.36, the captured power is 2 MW at a wind speed of 12 m/s and air density of ρ=1.225 kg/m^3 [35]. Fig. 2.4 shows typical $C_p - \lambda$ characteristics.

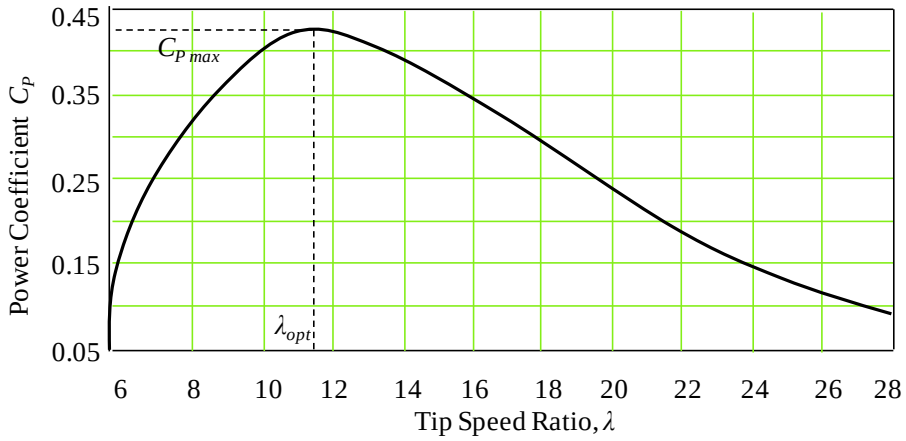

Figure 2.4. Power coefficients versus tip speed ratio.

The coefficient of performance of a wind turbine is influenced by the tip-speed to wind speed ratio (*TSR*), which is given by [35]:

$$TSR = \lambda = \frac{\omega_m R}{v_w} \tag{2-5}$$

$$v_w = \frac{\omega_m R}{\lambda} \tag{2-6}$$

where,

ω_m = the mechanical speed of the turbine rotor (rpm)

R = the radius of the turbine (m).

By substituting v_w from equation (2-6) into equation (2-4), the turbine power can be written as;

$$P_T = \frac{1}{2}\rho\, A\, C_p \left(\frac{\omega_m R}{\lambda}\right)^3 \tag{2-7}$$

2.3.3 Optimum Power Extraction from a Variable Speed Wind Turbine

The wind turbine can produce maximum power when the turbine operates at maximum C_p (i.e. at C_{p_opt}) as indicated in equation (2-4). Therefore, the rotor speed should be kept at an optimum value of the tip speed ratio, λ_{opt} to ensure maximum power extraction from the wind. If there is any change in wind speed the turbine rotor speed should be adjusted accordingly.

The target optimum power can be written from equation (2-7) as;

$$P_{m\_opt} = 0.5\rho\, AC_{p\_opt} \left(\frac{\omega_{m\_opt} \times R}{\lambda_{opt}}\right)^3 = K_{opt}\left(\omega_{m\_opt}\right)^3 \tag{2-8}$$

where, $K_{opt} = 0.5\rho\, AC_{p\_opt} \left(\frac{R}{\lambda_{opt}}\right)^3$ (2-9)

$$\omega_{m\_opt} = \frac{\lambda_{opt}}{R} v_w = K_w v_w \tag{2-10}$$

$$K_w = \frac{\lambda_{opt}}{R}$$

So the target optimum torque can be given by

$$T_{m\_opt} = P_{m\_opt}/\omega_{m\_opt} = K_{opt}\left(\omega_{m\_opt}\right)^2 \tag{2-11}$$

The optimum torque can be calculated from the optimum power as shown in equation (2-11). When the generator speed below the rated speed, the generator follows the equation (2-8). If the generator speed exceeds the rated speed, the wind turbine energy capture must be limited by applying pitch control or driving the machine to the stall point [23].

For a specific wind speed, output power of a wind turbine varies with turbine speed. The mechanical power generated by a wind turbine as a function of the rotor speed for different wind speed is shown in Fig. 2.5 [23]. The optimum power curve which defines maximum energy capture from the fluctuating wind is also shown in Fig 2.5. The controller should regulate the turbine speed to ensure the operation of the turbine keep the turbine on this curve as the wind speed changes. As shown in Fig.2.5, there is a matching turbine rotor speed which produces maximum power for any given wind speed. If the controller can properly designed to follow the variation in wind speed, the wind turbine will capture maximum power at any speed within the operating range [23].

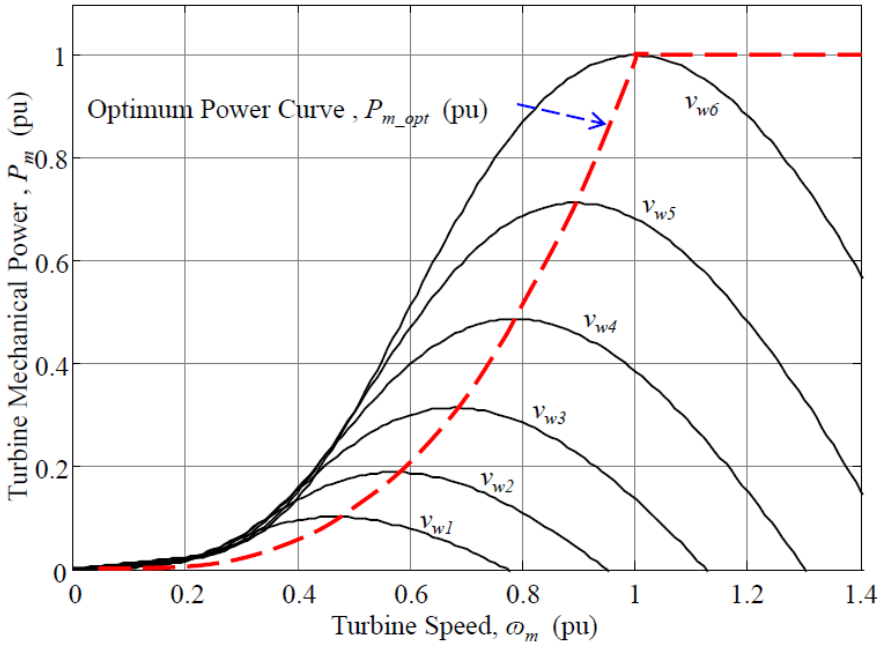

Figure 2.5. Mechanical power generated by turbine as a function of the rotor speed for different wind speed.

2.3.4 Stream Tube Model of Air Flow for Theoretical Maximum Power Extraction

In 1919, the German physicist Albert Betz first formulated the derivation of maximum power that can be extracted from the wind [34]. Betz started the analysis by imagining what happens to the wind as it flows through the blades of wind turbine. As indicated in Fig.2.6, The downwind velocity is lower than upwind velocity due to energy capture by the wind turbine. The wind leaving the turbine blades has a lower velocity and pressure, causing the air to expand downwind of the turbine [34]. An envelope drawn around the air mass that passes through the turbine forms a "***stream tube***" as shown in Fig.2.6 [34]. The downwind velocity is lower than upwind velocity due to energy capture by the wind turbine. What Betz showed was that an ideal wind turbine would slow the wind to one-third of its original speed [34].

The power extracted by the blades P_T is equal to the difference in kinetic energy between the upwind and downwind air flows [34]:

$$P_T = \frac{1}{2} m(v_{w1}^2 - v_{w2}^2) \tag{2-8}$$

where,

v_{w1} = upwind velocity of the undisturbed wind (m/s)

v_{wT} = velocity of the wind through the plane of the rotor blades (m/s)

v_{w2} = downwind velocity (m/s)

$\dot{m}$ = mass flow rate of air within the stream tube

The mass flow rate at the plane of the rotor with a swept area A is

$$\dot{m} = \rho A v_{wT} \tag{2-9}$$

By assuming that the velocity of the wind through the plane of the rotor is the average of the upwind and downwind speeds, we get [34],

$$P_T = \frac{1}{2}\rho A \left(\frac{v_{w1}+v_{w2}}{2}\right)(v_{w1}^2 - v_{w2}^2) \tag{2-10}$$

Let, x be the ratio of downstream to upstream wind speed as given below

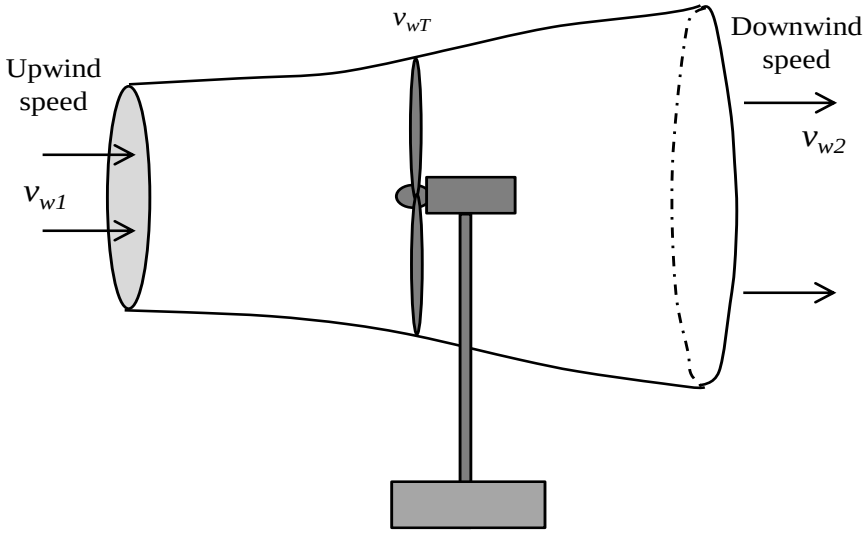

Figure 2.6. Wind leaving the turbine slows and expands as a portion of its kinetic energy is extracted by the wind turbine, forming the stream tube shown [34].

$$x = \frac{v_{w2}}{v_{w1}} \tag{2-11}$$

$$v_{w2} = x v_{w1} \tag{2-12}$$

$$P_T = \frac{1}{2}\rho A \left(\frac{v_{w1}+x v_{w1}}{2}\right)(v_{w1}^2 - x^2 v_{w1}^2) \tag{2-13}$$

$$P_T = \frac{1}{2}\rho A v_{w1}^3 \times \frac{1}{2}[(1+x)(1-x^2)] \tag{2-14}$$

The first part of equation (2-14) shows the power available in the wind and the second part indicate the fraction of the wind power that is extracted by the blades. The second part indicates the efficiency of the wind turbine, usually represented by power coefficient C_p. Thus, the rotor efficiency is given by

$$C_P = \frac{1}{2}(1+x)(1-x^2) \tag{2-15}$$

Therefore, the fundamental relationship for the power captured by the rotor blades is given by

$$P_T = \frac{1}{2}\rho A v_{w1}^3 \times C_P \tag{2-16}$$

For maximum possible rotor efficiency, the derivative of equation (2-15) with respect to x would be equal to zero [34]:

$$\frac{dC_P}{dx} = \frac{1}{2}[(1+x)(-2x) + (1-x^2)] = 0$$

$$\Rightarrow \frac{1}{2}[(1+x)(-2x) + (1+x)(1-x)] = 0$$

$$\Rightarrow \frac{1}{2}[(1+x)(1-3x)] = 0$$

$$\Rightarrow x = -1 \; or \; 1/3$$

$$\therefore x = \frac{v_{w2}}{v_{w1}} = -1 \; or \; 1/3$$

$$v_{w2} = -v_{w1} \quad or \quad v_{w2} = \frac{1}{3} v_{w1}$$

However, in reality upwind speed and downwind speeds are not equal and opposite. The blade efficiency will be maximum if it slows the wind to one-third of its upstream velocity as shown in Fig.2.7 [34].

Substituting x = 1⁄3 in equation (2-15), the theoretical maximum rotor blade efficiency is given by

Rotor efficiency = $C_P = \frac{1}{2}(1+x)(1-x2)$=0.593=59.3% (2-17)

Therefore, the maximum theoretical efficiency of a wind turbine rotor is 59.3%, which is called the ***Betz efficiency*** **or** ***Betz' law*** [34]. For a given wind speed, the wind turbine rotor efficiency is a function of the rate at which the rotor rotates. When the rotor rotates too slowly, the efficiency drops as the turbine blades are bypassing too much wind. When the rotor rotates too fast, the turbine efficiency is dropped as the turbulence caused by one blade increasingly affects the blade that follows [34]. The ***Betz*** factor is a theoretical maximum power coefficient. But there are other effects which can cause decrease in maximum power coefficient. These are [34]:

- rotation of the wake behind the rotor,
- finite number of blades associated tip losses, and
- non-zero aerodynamic drag.

Fig. 2.8 shows actual wake rotation behind the turbine. The overall turbine efficiency is a function of both power coefficient C_p, mechanical and electrical efficiency of wind turbine generator. The overall turbine efficiency $\eta_{overall}$, is given by [36]:

$$\eta_{overall} = C_p \, \eta_{mech+electrical} \tag{2-18}$$

Fig. 2.9 shows tip speed ratio verses maximum power coefficient, which indicates losses due to wake rotation, which is significant at low tip speed ratio [36].

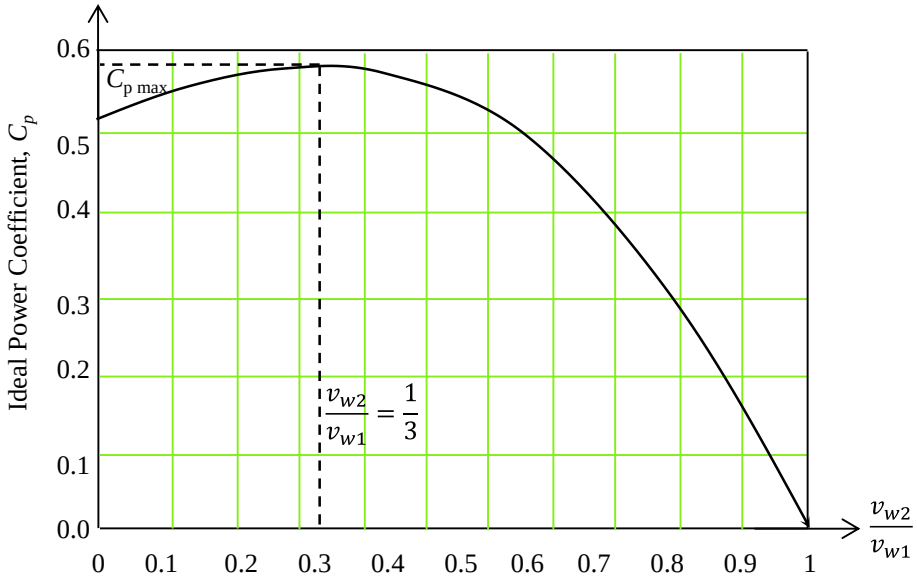

Figure 2.7 Ideal power coefficient verses v_{w2}/v_{w1}.

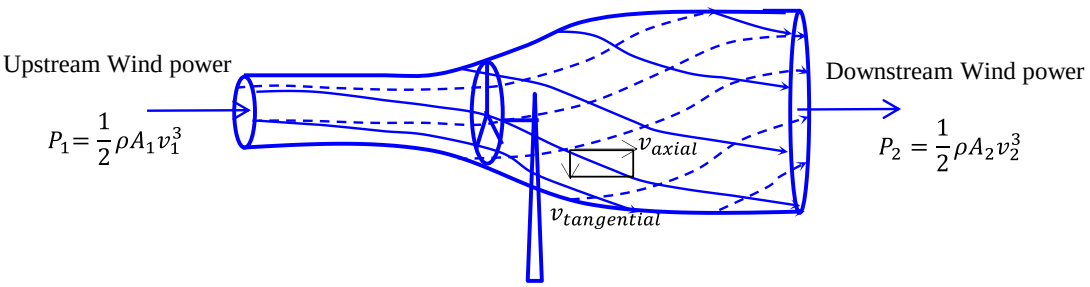

Figure 2.8 Stream tube model including the rotating wake behind a turbine like energy converter.

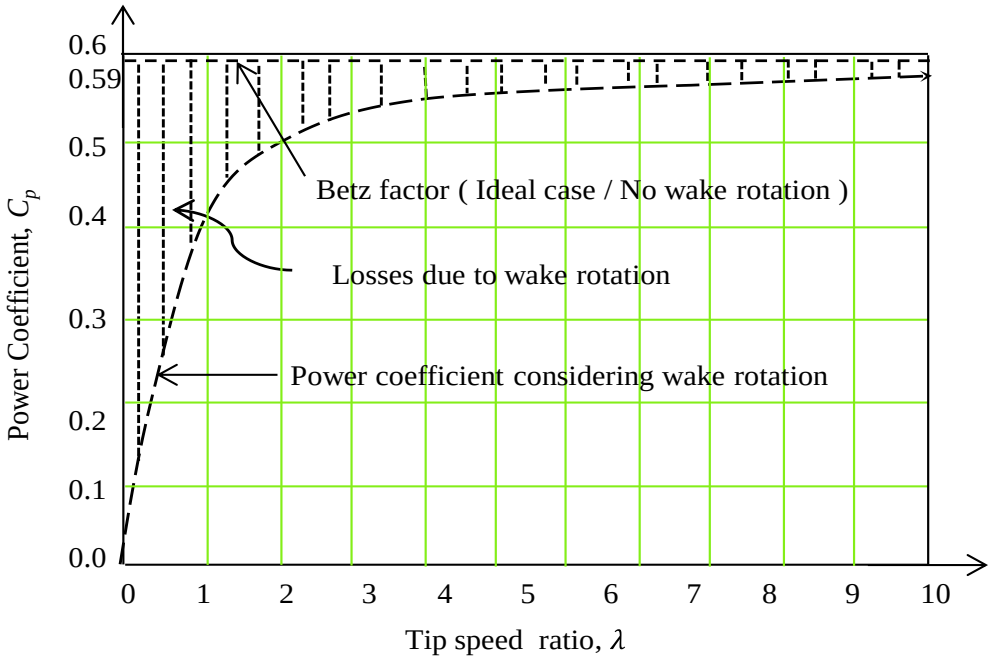

Figure 2.9 Betz factor, rotor real power coefficient considering wake rotation and losses due to wake rotation.

2.4 Influence of the Number of Turbine Blades on the Rotor Power Coefficient

The performance of one, two, three and four blades wind turbine is shown in Fig.2.10. A one blade wind turbine requires higher wind speed to achieve maximum power coefficient. The power co-efficient of a wind turbine increases by about 10% from one blade to two blades, 4% for two blades to three blades and 2% for three blades to four blades rotor [36]. The higher the turbine blade numbers the higher the power coefficient [36]. A trade-off needs to be made in choosing the number of blades in a wind turbine considering size, cost and performances. The three blades rotor presents the best trade-off between mechanical stress, acoustic noise, cost, and rotational speed for large wind turbines [35].

Fig.2.11 (a), (b) and (c) show wind turbine with one, two and three blades, respectively. One blade rotor is aerodynamically unbalanced and moment of inertia changes due to rotation. It shows very high dynamic and mechanical stress [36]. Two blades rotor is dynamically unbalanced and moment of inertia changes due to rotation. It has rotor pulsating profile, similar to a rotating rod. Three blades rotor is aerodynamically balanced and moment of inertia does not change due to rotation [36].

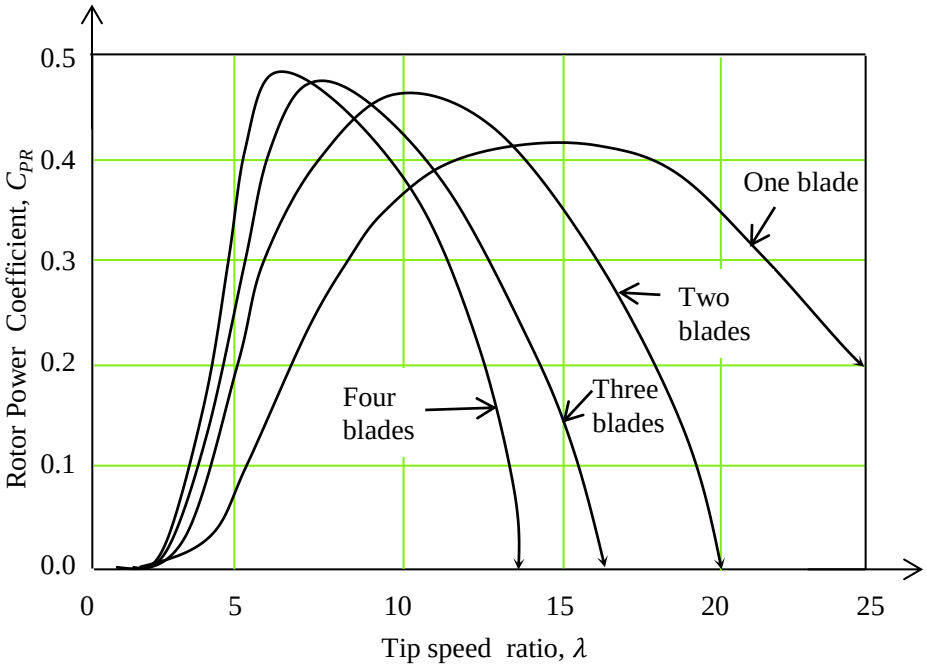

Figure 2.10 Influence of the number of turbine blades on the rotor power coefficient

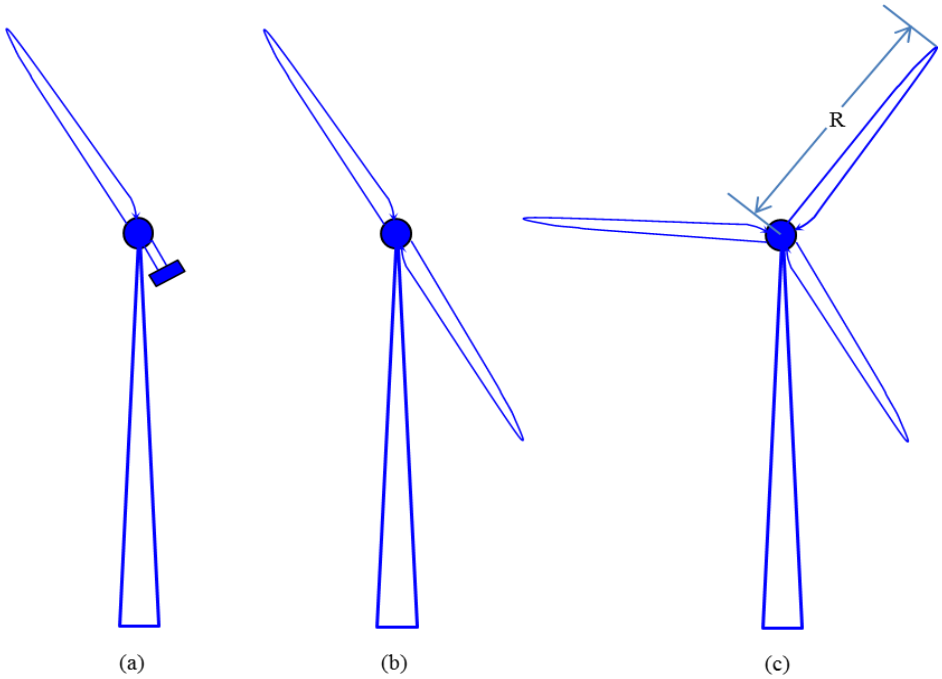

Figure 2.11 (a) One blade wind turbine (b) Two blades wind turbine (c) Three blades wind turbine

2.5 Horizontal Axis and Vertical Axis Wind Turbine

According to the orientation of rotor blades, wind turbine can be classified as

- Horizontal axis wind turbine, and
- Vertical axis wind turbine

2.5.1 Horizontal Axis Wind Turbine (HAWT)

In horizontal axis wind turbines (HAWT), the axis of rotation is horizontal to ground and parallel to the direction of the wind. There may be many designs of the horizontal axis windmills. These turbines can be classified as single-bladed, double-bladed, three-bladed, multi-bladed and bicycle-bladed depending upon the number of blades [4]. Depending upon the orientation of the blades, this turbine can be categorized as up-wind and down-wind turbines. Most of the horizontal axis wind turbines are of the upwind turbine. As the wind changes direction, all horizontal axis wind turbine have some means for keeping the rotor in to wind [37]. The advantages of HAWT s are low cut-in speed, easy furling, high power coefficient [38]. Horizontal axis wind turbines have some disadvantages, which are complex design, higher cost and it requires yaw drive to orient the turbine towards the wind [38]. Fig. 2.12 shows horizontal axis wind turbines [38].

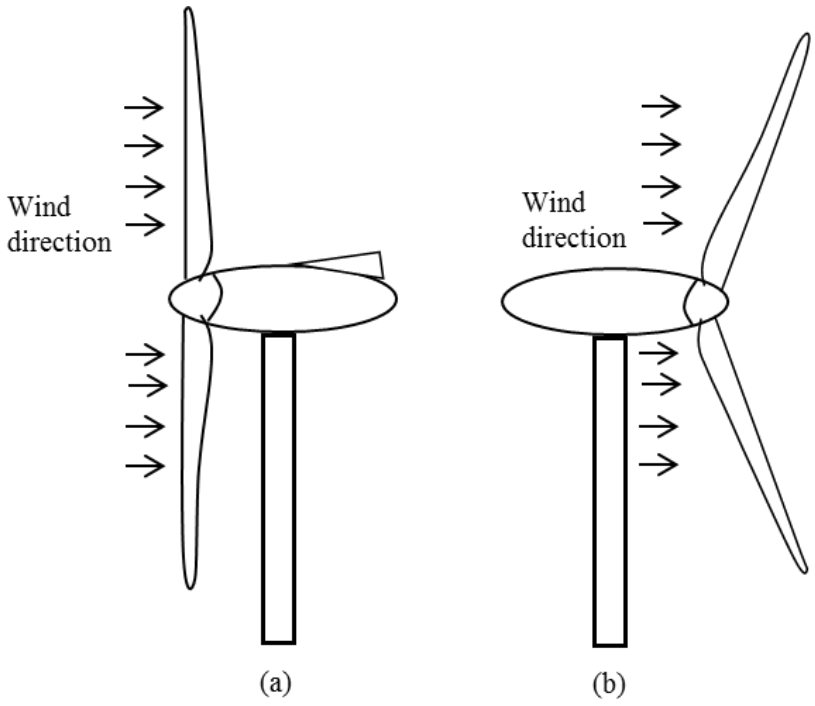

Figure 2.12 Horizontal axis wind turbine (a) upwind turbine (b) downwind turbine.

2.5.2 Vertical Axis Wind Turbine (VAWT)

The axis of rotation of vertical axis wind turbine (VAWT) is vertical to the ground. and almost perpendicular to the direction of wind. The VAWT is also known as cross-wind axis machines. The principal advantages of VAWT over conventional HAWT are that VAWT are Omni directional, i.e. they accept the wind from any direction [38]. This simplifies their design and eliminates the problem imposed by gyroscopic forces on the rotor of conventional machines as the turbines yaw into the wind [38]. VAWTs have a higher air foil pitch angle, giving improved aerodynamics while decreasing drag at low and high pressures [38]. The disadvantages of VAWTs include lower energy capture, low starting torque, inability to self-starting and lower efficiency [34]- [39]. Figure 2.13 shows vertical axis wind turbines [38].

Fig. 2.14 shows a typical C_p-λ curve for three bladed horizontal axis wind turbine and vertical axis Darrieus wind turbine [38]. According to Betz limit power coefficient of lift force operated wind turbine is 59.3%. Normally all HAWTs are lift force operated. On the other hand, maximum power coefficient for drug force operated wind turbine is 29.6%. VAWTs are drag operated. This is why lift machines are preferred over drag machines for wind energy conversion systems [38].

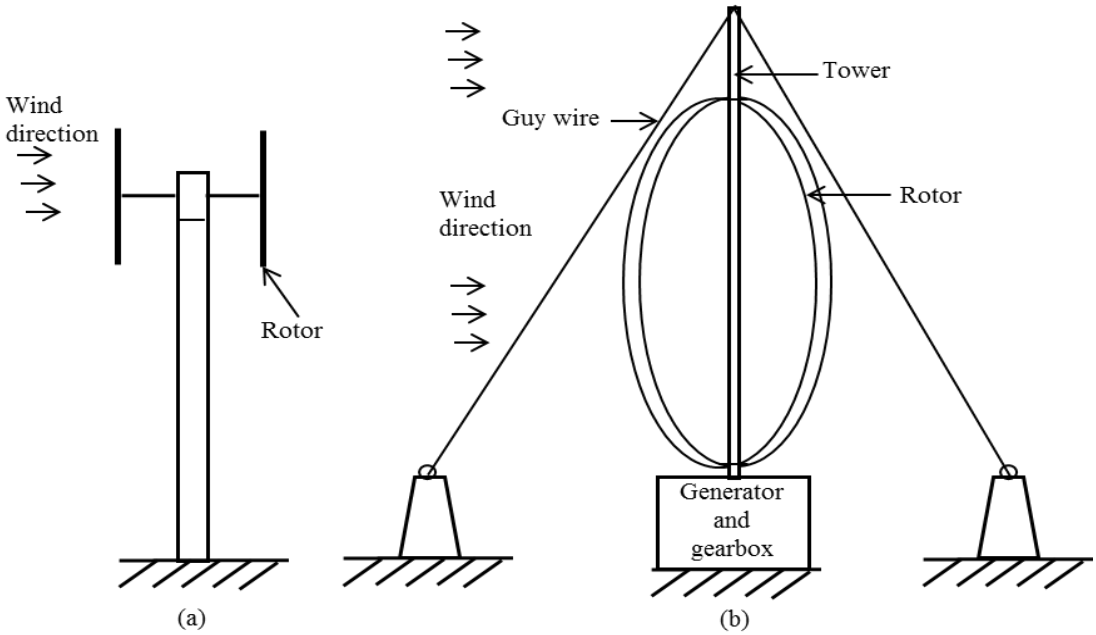

Figure 2.13 Vertical axis wind turbine. (a) Musgrove wind turbine (b) Derries wind turbine

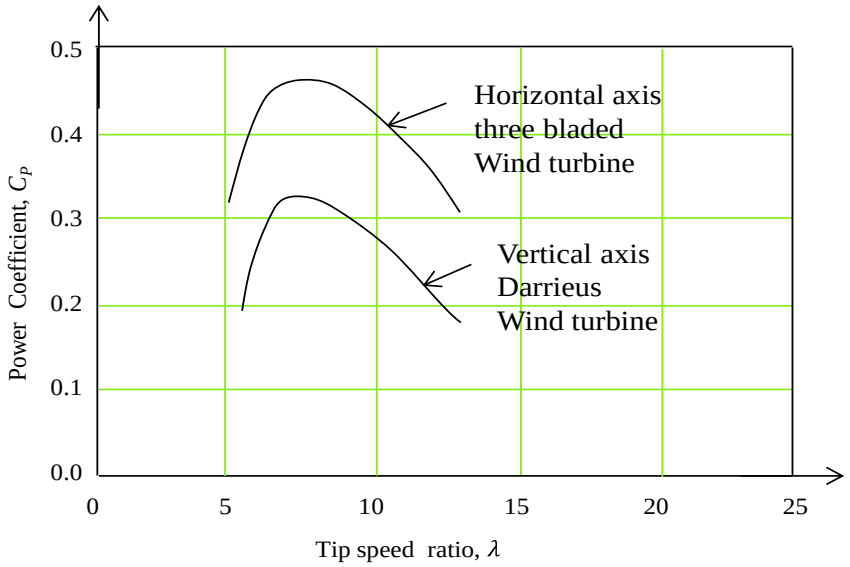

Figure 2.14 Performance characteristics of HAWT and VAWT

2.6 Onshore and Offshore Wind Turbine

Depending on the location there are two types of wind turbines. One is called onshore wind turbine, which is installed in the land. Other one is called offshore wind turbine, which is located at 1 to 75 km away from the shore. So wind turbine can be classified as

- Onshore wind turbine, and
- Offshore wind turbine

2.6.1 Onshore Wind Turbine

In onshore, wind speed significantly reduced due to the obstacles in landscape, mountains, trees and buildings. Onshore wind turbines needs higher tower structure for higher wind speeds. Due to the higher tower structure and large rotor diameter, wind

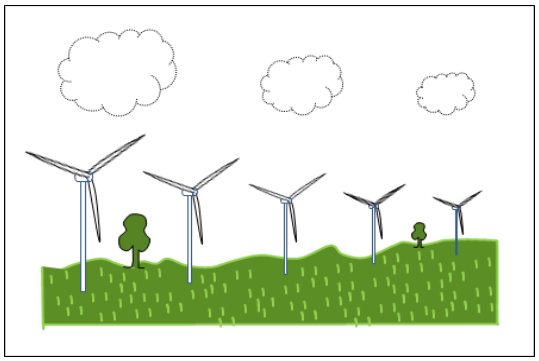

Figure 2.15 Onshore wind farm.

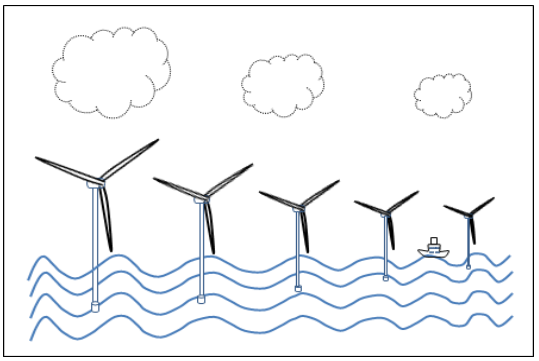

Figure 2.16 Offshore wind farm.

turbine sizes are limited to 1-3 MW [38a]. As it is installed in the solid ground, standard concrete foundations cast on the site and there is unrestricted access to the site. Onshore wind farms installed capacity is normally 10-50 MW [38a].Fig.2.15 shows image of onshore wind farm.

2.6.2 Offshore Wind Turbine

On the other hand due to no obstacle in the offshore, high wind speed is available very close to the water surface. Offshore wind turbines needs lower tower structure for higher wind speeds. Due to the lower tower structure, wind turbine sizes are up to 3-7 MW [38a]. Offshore wind turbine has a greater energy potential but marine conditions like weather, wind, waves, depth of water to the sea bed poses great challenges to the off shore wind farm project delivery and cost. Due to the different offshore sea bed soil condition, it needs different type of complex foundation. Access to the offshore site is restricted due to weather conditions in the sea. Offshore wind farms installed capacity is normally 50-1000 MW [38a]. Fig.2.16 shows image of offshore wind farm.

2.7 Wind Turbine Aerodynamics

The amount of energy captured by a wind turbine is influenced by the aerodynamic design of rotor blades. A well designed wind turbine should be able to limit the power and speed of the rotor for wind speeds above the rated value in order to keep the mechanical stress within the safety limit [35].

2.7.1 Wind Turbine Power Characteristics

The power curve is the most important technical information for a wind turbine. The power characteristics of a wind turbine are defined by the power curve and the power curve relates the mechanical power of the turbine vs wind speed. The power curve is a wind turbine's certificate of performance that is guaranteed by the manufacturer [34],[35]. A typical power curve is shown in Fig.2.17. This curve is characterised by three speeds:

- Cut-in speed
- Rated wind speed
- Cut out wind speed

*The **cut in wind speed*** is the speed at which wind turbine starts to operate and deliver power. Below cut-in wind speed the turbine does not capture enough power to compensate for the power losses in the wind turbine drive train. Therefore, the wind turbine is shut down. The ***rated wind speed*** is the speed at which the wind turbine produce rated power [35]. The ***cut-out*** speed is the highest wind speed at which the turbine is allowed to operate before it shut down [5]. The turbine must be shut down to prevent mechanical damage if the wind speed is above the cut-out speed [35].

As indicated in Fig. 2.17, the wind turbine starts to capture power at the cut-in speed and the captured power is a cubic function of wind speed as given by equation (2-4). The turbine continues to capture power until the wind speed reaches the rated value. The wind turbine generator should be controlled properly with maximum power extraction under varying wind speeds. In this region, blade pitch angle is held constant. By varying generator torque, it is possible to vary rotor speed or tip speed in proportion to wind speed to deliver peak power coefficient C_p and therefore extract maximum power from wind [40]. As the wind speed increases above the rated speed aerodynamic

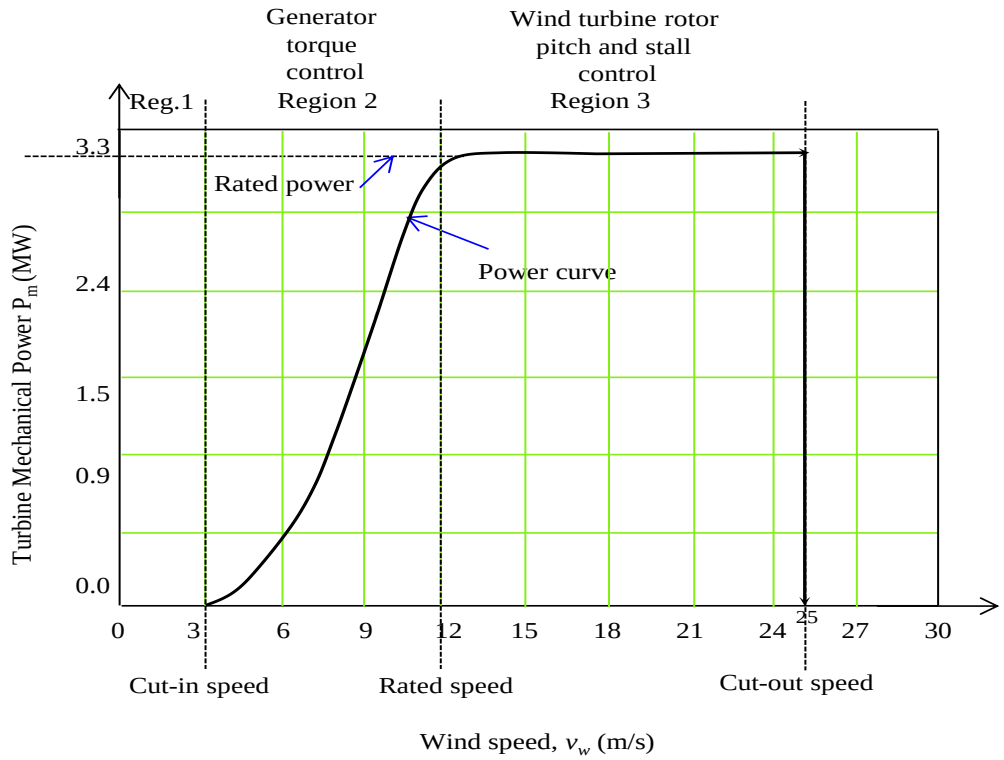

Figure 2.17 Wind turbine power curve in different operating region.

power control is required to keep the power at the rated value. Above the cut-out wind speed, the wind turbine should stop generating power and be shut down [35].

2.7.2 Aerodynamic Power Control of Wind Turbine

The aerodynamics of wind turbines are very similar to that of airplane which can be explained by Bernoulli's principle which states that as the speed of a moving fluid (liquid or gas) increases, the pressure within the fluid decreases [35]. The curved shape of the blade creates a difference between the wind speed above and below the blade as shown in Fig.2.18 [41]. The airflow above the blade is faster than the one below and according to Bernoulli's principle it has the inverse effect on the pressure above and below the rotor blades [5]. The pressure difference between the top and bottom of the blade results in a net lift force on the blade. The produced torque creates the rotational movement of the wind turbine [35].

One of the important parameters for controlling the lift force of the blade is the angle of attack α, (angle between the direction of the wind speed and the cord line of the blade) as shown in Fig.2.19 [35]. For a given blade, its lift force F_w can be adjusted by α. When α is equal to zero, no lift force or torque will be produced, which often occurs when the wind turbine is stopped (parked) for maintenance or repair [35]. Therefore, the angle of attack plays a vital role in determining the amount of force and torque generated by the wind turbine rotor blades. There are different aerodynamic control mechanisms to control the power capture for large wind turbines as shown in Fig.2.18. These are [35]:

- Passive stall control
- Active stall control
- Pitch control, and
- Yaw control

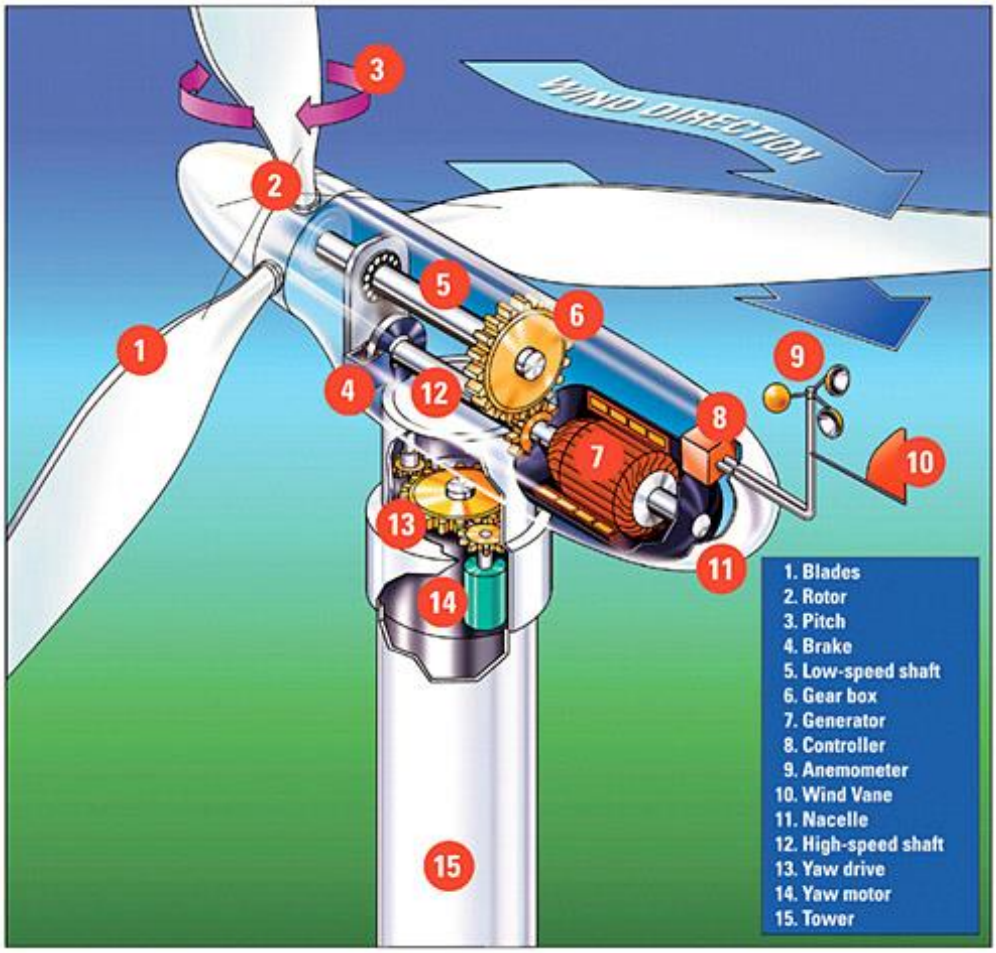

Figure 2.18. Wind Turbine components [41].

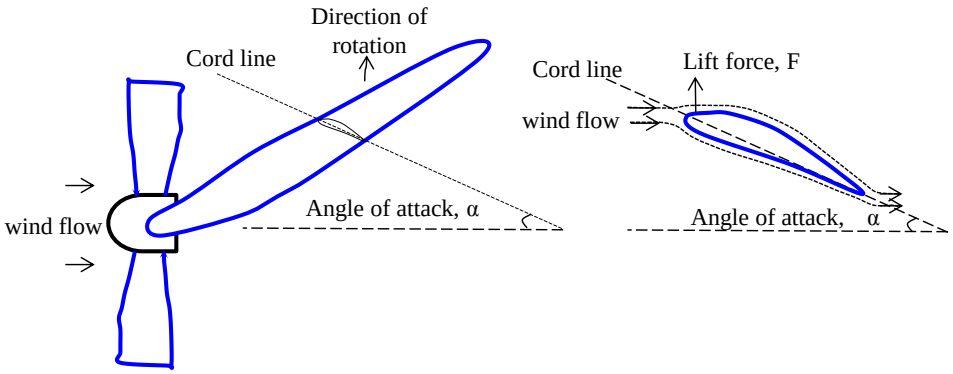

Figure 2.19. Turbine blade aerodynamic and angle of attack.

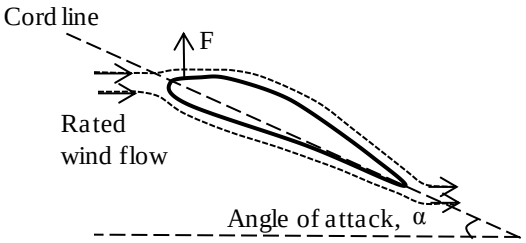

(a) Passive stall at rated wind speed.

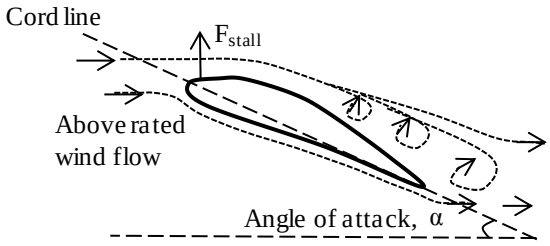

(b) Passive stall at above the rated wind speed.

Figure 2.20. Passive stall control.

2.7.2.1 Passive Stall Control

In this control, the turbine blade is fixed onto the rotor hub at rated angle of attack α. The turbine blades with the rated α can capture maximum power when the wind speed is below or at rated speed. If the wind speed exceeds the rated value, it can cause turbulence on the surface of the blade not facing the wind. This causes the lifting force to be reduced and eventually disappear with the increase in the wind speed, slowing down the rotor speed. This phenomenon is called ***stall*** [35]. The passive-stall control is shown in Fig.2.20 [35], where the lift force produced by higher than rated wind speed, which is the stall lifting force F_{stall} is lower than the rated force F [35].

2.7.2.2 Active Stall Control

The wind turbine with active-stall control has adjustable blades with a pitch controller. The stall phenomenon is induced by the higher wind speed or by increasing the angle of attack of rotor blade. At a wind speed higher than the rated speed, the blades are controlled to turn more into the wind, leading to reduction of captured power by the rotor blades. Therefore, the captured power can be maintained at the rated value by adjusting the angle of attack of the rotor blades [35]. Active stall control is shown in Fig.2.21 [35]. As shown by the dashed blade as shown in Fig.2.21 (b), if the turbine

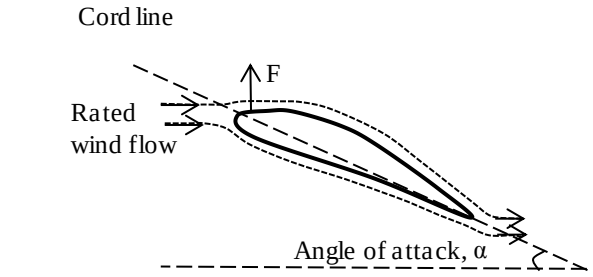

(a) Active stall at rated wind speeds

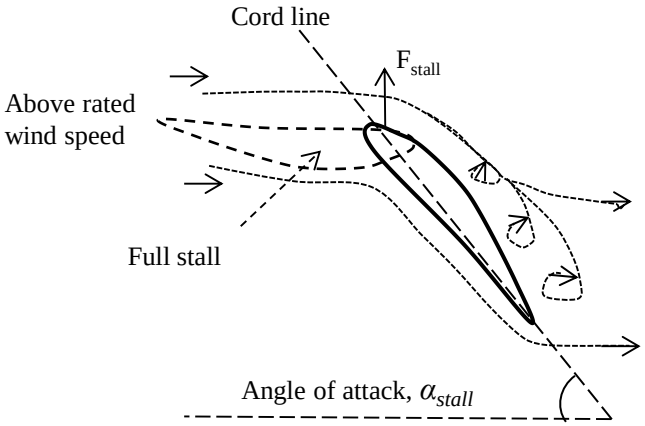

(b) Active stall at above rated wind speeds

Figure 2.21. Active stall control.

blade is turned completely into the wind, the blade loses all interaction with the wind and causes the rotor to stop. This mechanism can be used to stop the turbine and protect it from mechanical damage due to high stress, when the speed is above the cut-out wind speed [35].

2.7.2.3 Pitch Control

The wind turbine with pitch control also has adjustable blades on the rotor hub. At a speed higher than rated speed, the pitch controller reduces reduce the angle of attack, turning the blades (pitching) gradually out of wind. The pressure difference between the front and back of the turbine blade is reduced, leading to a reduction in the lifting force on the blade [35]. The pitch control operation is shown in Fig. 2.22 [35]. At a speed

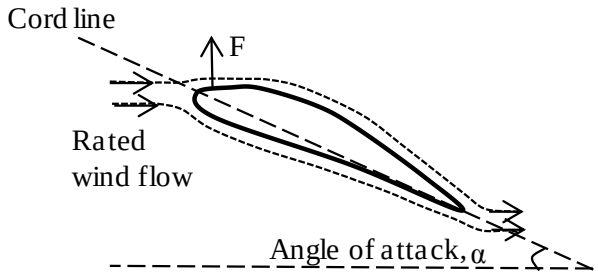

(a) Pitch control at rated wind speed.

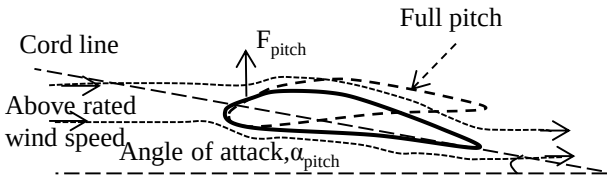

(b) Pitch control at above rated wind speed.

Figure 2.22. Pitch control.

below the rated speed, the blade angle of attack is kept at its rated (optimal) value α. At a speed higher than the rated wind speed, the angle of attack of the blade is reduced, causing a reduction in lift force, F_{pitch}. When the blade is fully pitched, the turbine blade angle of attack is aligned with the wind, as shown by the dashed blade in Fig. 2.22(b), and no lift force will be generated [35]. The performance of the pitch control is given in Fig.2.22(b), where the mechanical power of the turbine operating at above the rated wind speed can be tightly controlled [35]. Traditionally, hydraulics is used in pitch control. But now a day's state of the art technology has introduced faster electro-mechanical system for pitch control applications.

2.7.2.4 Pitch Control vs. Stall Control

The rotating actions on the turbine are used in both the pitch and active stall controls. However, the pitch control turns the turbine blade out of the wind, leading to reduction in lift force, whereas the active-stall control turns the turbine blades into the wind, causing turbulences that reduced the lift force [35]. The passive stall may not be able to keep the captured power P_M at a constant value, as shown in Fig.2.23 and it may exceed the rated power at some wind speeds [35]. The passive stall control was mainly used in early fixed-speed turbines. This control technique was further improved into the active-stall technology [35]. Using the active stall control, it is possible to maintain the rated power above the rated wind speed, as shown in Fig.2.23. Active stall controlled wind turbine with several MW ratings are commercially available. The pitch controls reacts faster than the active-stall control and provide better controllability as shown in Fg.2.23. Pitch control is widely used in modern wind turbine system [35], [42].

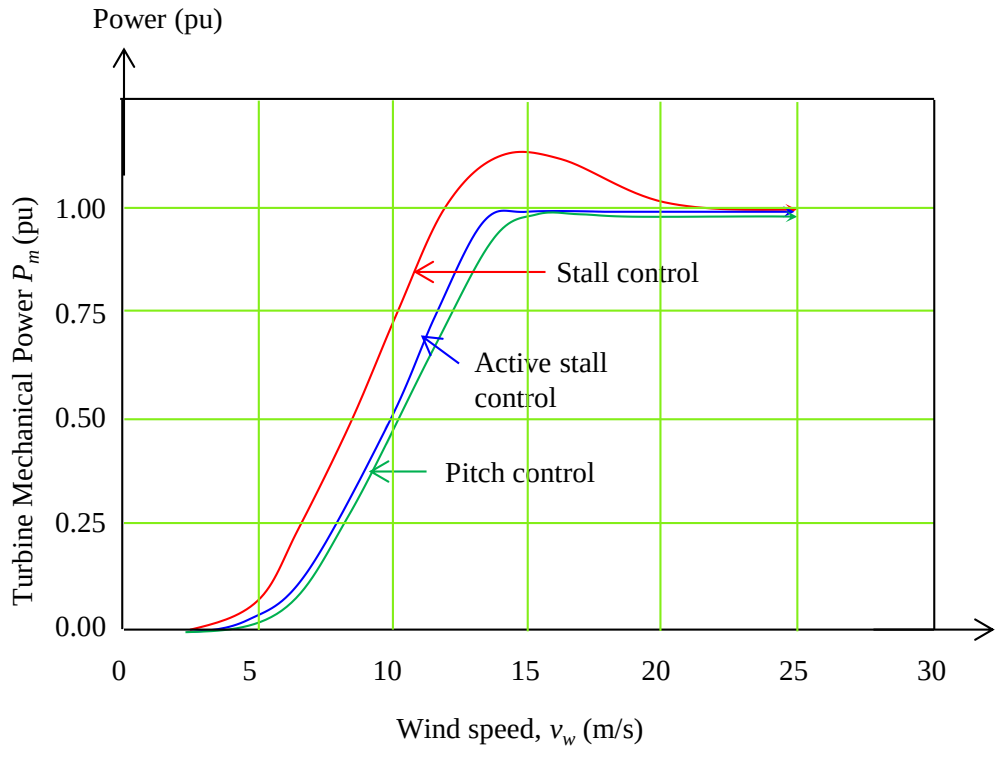

Figure 2.23 Power characteristics of a wind turbine during stall, active and pitch control.

2.8 Wind Energy System Configurations

A number of wind energy conversion system configurations have been developed to reduce cost, increase reliability and efficiency. The wind turbines can be classified as:

- Fixed speed
- Variable speed wind turbine.

Fig. 2.24 shows wind energy system configurations using different type of generators used for fixed speed and variable speed wind turbines.

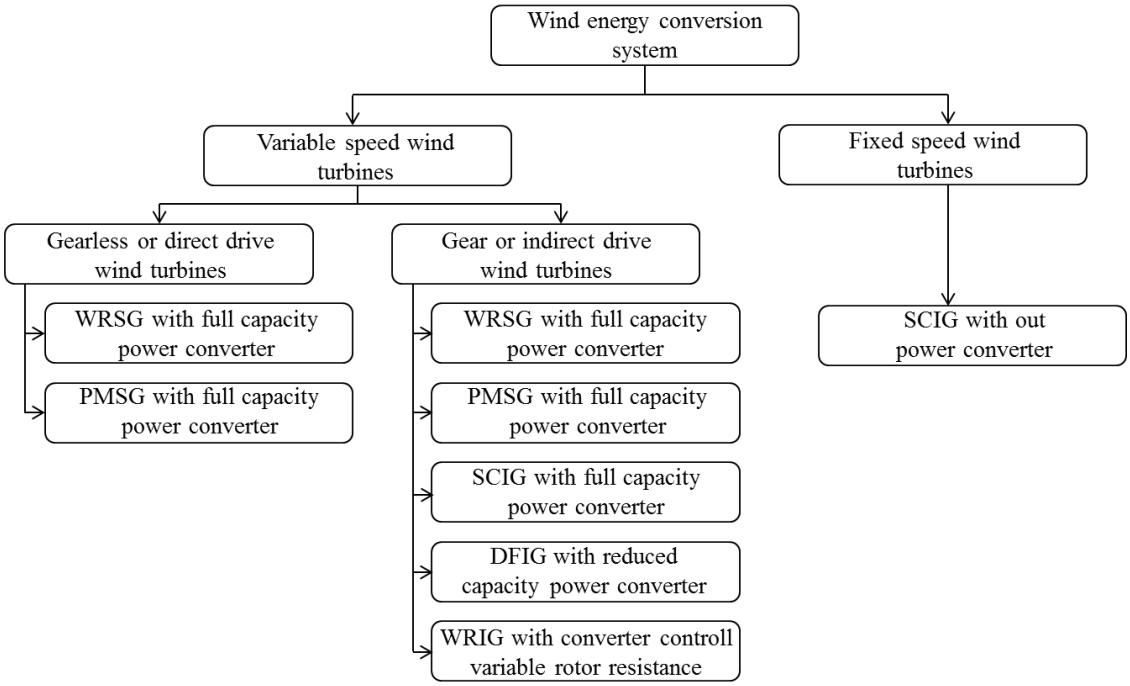

Figure 2.24. Different generators for wind energy conversion system.

2.8.1 Fixed Speed Wind Turbine

A fixed speed wind turbine usually with a squirrel cage induction generator (SCIG) is directly connected to the grid without any power electronic converter [35], [43]. They are designed to achieve maximum efficiency at a particular speed. The fixed speed wind turbine features simple structure, low cost and reliable operation. However, it has a lower energy conversion efficiency compared to a variable speed wind turbine since it can extract maximum power only at one given wind speed [4].

The fixed speed WECS starts to produce power when the wind speed is higher than the cut-in speed (3-4 m/s). At a speed higher than the rated wind speed (13 to 15 m/s), the power captured by the turbine is limited either by active/passive stall or pitch control of the rotor blades [35]. At a speed higher than the cut-out speed (around 25 m/s), the turbine is stopped by either full stall or full pitch of the blades to protect the turbine and generator from possible damage [35]. The rotating speed of large fixed speed turbines is normally in the range of 6 to 15 rpm, whereas the induction generator operates at much higher rpm (750 rom to 1800 rpm). The generator operating speed is determined by the number of poles and grid frequency [35].

As shown in Fig. 2.25, for a given wind speed, there is a corresponding maximum power point (MPP) on the turbine power vs speed curve. However, the fixed speed wind energy system can operate only at one MPP, which is at the rated wind speed as shown in Fig. 2.25. At a speed other than the rated speed, the wind turbine operates at the points which are lower than maximum power [35]. Therefore, a fixed speed wind

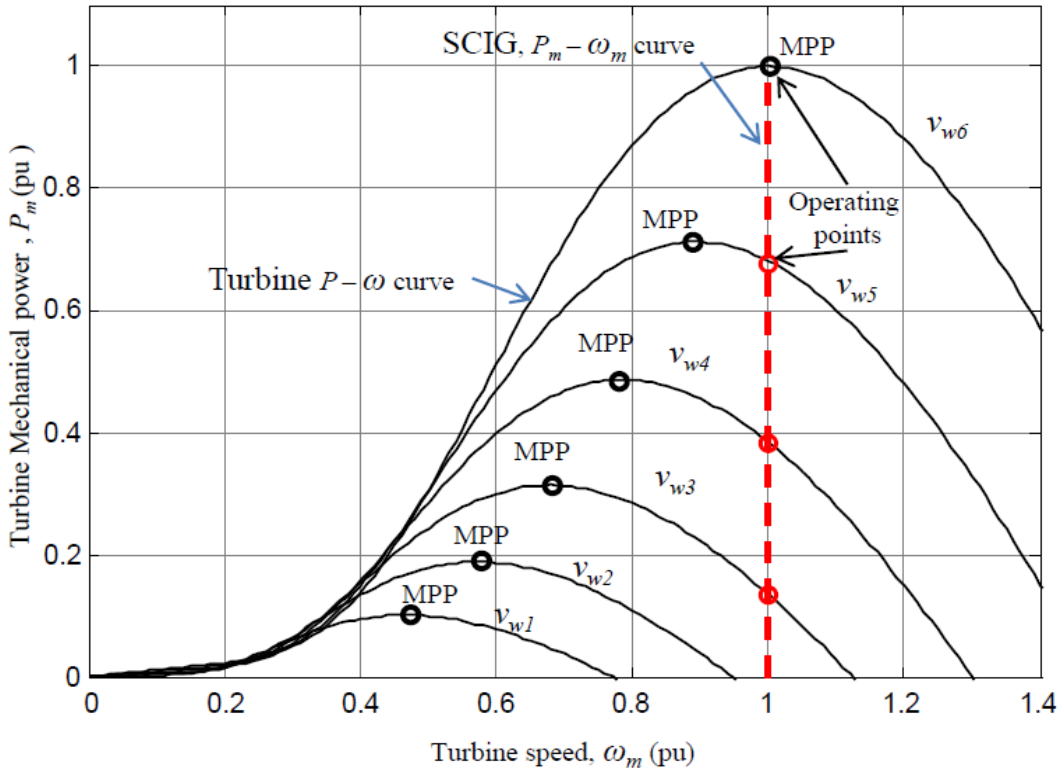

Figure 2.25. System operating point and maximum power points at different wind speeds.

turbine cannot extract maximum power available from the wind, which leads to a lower power conversion efficiency compared to a variable speed wind turbine.

Fig.2.26 shows a grid connected fixed wind energy conversion system using a squirrel cage induction generator. The system includes a wind turbine, gearbox, SCIG, capacitor bank, and a transformer for grid connection. The SCIG is normally used for fixed speed wind turbine applications due to the damping effect [39]. A synchronous condenser or capacitor bank is required for reactive power support in this type of wind turbine. Table 2.1 summarizes the main features of a fixed speed wind turbine [4], [35], [43]-[44].

Table 2.1: Summary of main features of a fixed speed wind turbine

Main Features	Description
Simple and reliable structure	• no power electronic converters • no slip rings or brushes • compact size and light weight
Low costs	• reliable low cost induction generator • no controller for generator
Low conversion efficiency	• fixed speed operation • unable to implement MPPT
Low power quality	• fluctuation in output power • no voltage ride through capability • no reactive power compensation capability
High mechanical stress	• reduction in life span of mechanical component due high stress • the variation in wind speed can cause a fluctuation in the mechanical torque and the electrical power injected to the grid. • the power fluctuations can also lead to large voltage fluctuations in a weak grid.

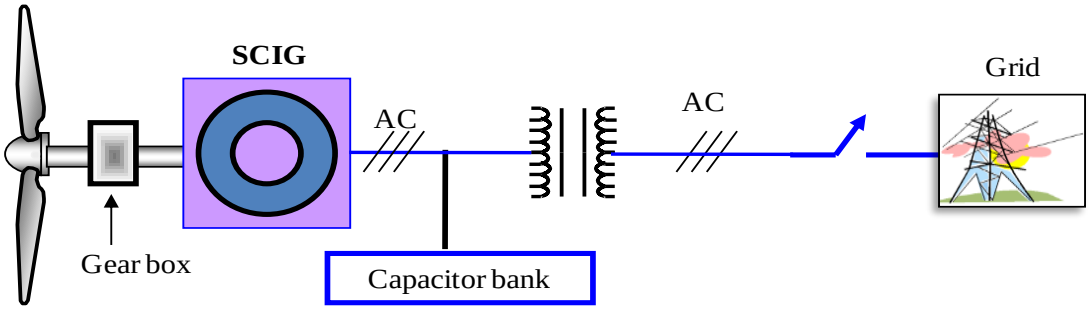

Figure 2.26. Squirrel cage induction generator based fixed speed wind turbine.

2.8.2 Variable Speed Wind Turbine

Variable speed wind turbines are designed to capture maximum energy from the wind over a wide speed range. In a variable speed wind turbine, it is possible to adapt variable rotational speed of the wind turbine to the wind speed to capture maximum power under varying wind speeds. Figure 2.27 shows synchronous generator based variable speed wind turbine. Contrary to a fixed speed system, a variable speed system keeps the generator torque fairly constant and the variations in winds are absorbed by changes in the generator speed [44]. The variable speed wind turbines are equipped with a doubly fed induction generator, wound rotor or permanent magnet synchronous generator and connected to the grid or load through a power converter and coupling transformer.

The variable speed wind turbines can be divided into [35]:

- direct-drive (gearless)
- indirect-drive turbines.

In a gearless direct drive wind turbine, low speed synchronous generators with a higher number of poles are used. The no of poles of synchronous generators is chosen to match the turbine speed without any gearbox. Both wound rotor synchronous generator (WRSG) and permanent magnet synchronous generators (PMSGs) are suitable for the direct drive turbines [35]. However, a full-capacity power converter system is required to supply power to the grid. The direct drive gearless wind turbine system is shown in Fig. 2.27.

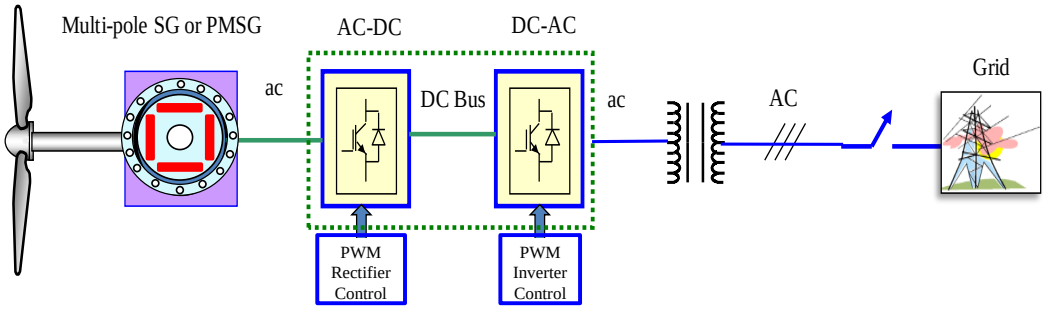

Figure 2.27. PMSG or Multi-pole synchronous generator.

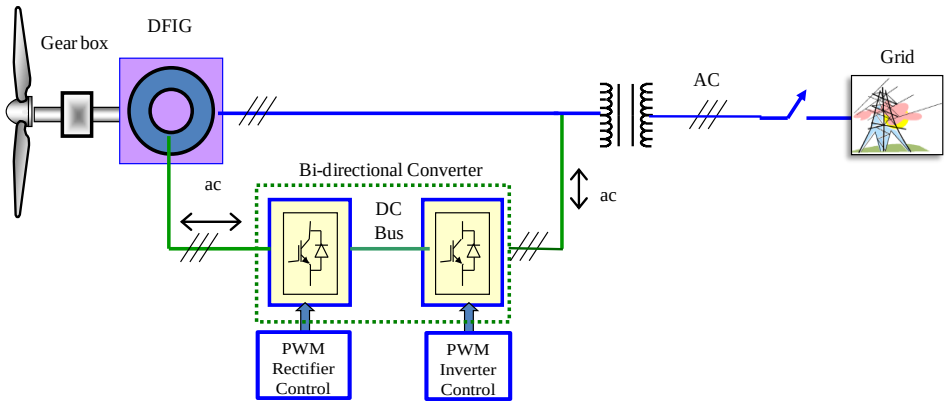

(a) DFIG

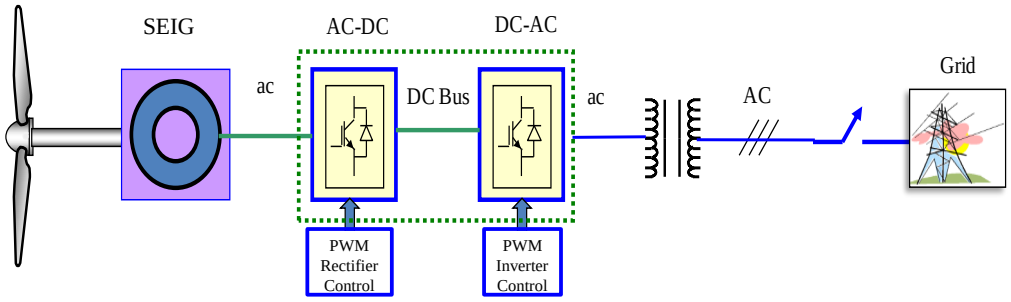

(b) Self-excited induction generator (SEIG)

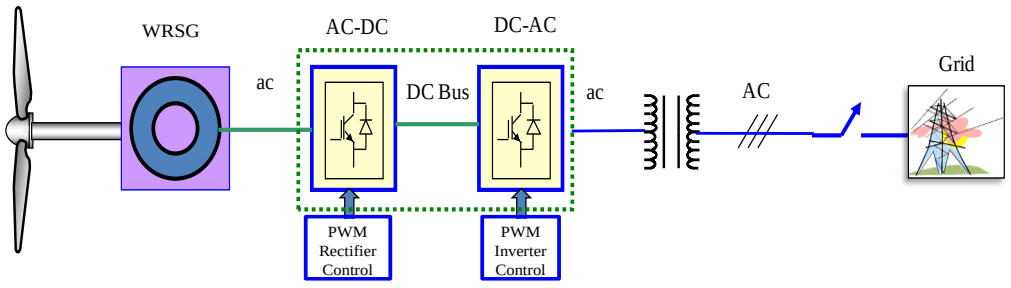

(c) WRSG

Figure 2.28. Indirect drive variable speed wind turbines with gearbox.

Fig. 2.28 shows indirect drive variable speed wind turbines which consists of a wind turbine, mechanical gearbox, generator, power converter and a coupling transformer for grid integration. In Fig. 2.28(a) the rotor circuit of a DFIG can be connected to an external resistor or to an ac system via back to back power converter. It provides variable speed operation with a reduced capacity power converter (30% of full rated power) [35]. As the size of the power converter is smaller, it reduces the system losses. In Fig. 2.28(b) the self-excited induction generator (SEIG) and in Fig. 2.28(c) the wound rotor synchronous generator (WRSG) both are connected to the grid via back to back full rated converter for variable speed wind power generation. Table 2.2 summarizes the main features of a variable speed wind turbine [42]-[46].

Table 2.2: Summary of main features of variable speed wind turbines

Main Features	Description
Increased energy capture and efficiency	• maximum power extraction can be achieved over a wide speed range • variable speed operation allow the turbine to increases the energy capture and efficiency
Low mechanical stress and improved power quality	• wind gusts can be absorbed by storing the as the mechanical inertia of the turbine, creating an "elasticity" that reduces torque pulsations [23]. • increased life span of component due to lower mechanical stress • power converter decouples the grid from the wind turbine and the fluctuation in wind speed is not transmitted to power grid. • improved power quality • ability to low voltage/fault ride through
Complex structure and higher costs and power losses	• requires power converter. • there are losses in power electronic converter • increased cost because of power electronics • converter efficiency plays an important factor in total system efficiency over the entire operating range. • comparatively complex structure and requires controller for the power converter
Low costs	• reliable low cost induction generator • no controller for generator
Simpler pitch control	• pitch angle control is performed at high wind speed to limit maximum output power. At low wind speed the pitch angle control is fixed. The speed control of the generator allows the pitch control time constant to become longer, reducing pitch control complexity and peak power requirement [4].
Reduced acoustic noise	• low-speed operation is possible at low power conditions with reduced acoustic noise.
Isolated operation	• suitable for isolated remote area power supply system where grid is not available.

2.9 Summary

Mathematical analysis and modelling of wind turbine is presented in this chapter. Stream tube model of air flow for maximum power extraction is discussed in detail. Based on Betz analysis, it is shown that the maximum theoretical efficiency of a wind turbine rotor is 59.3%. For a given wind speed, rotor efficiency is a function of the rate at which the rotor rotates. Besides Betz factor, there are other effects which can cause decrease in maximum power coefficient. These are rotation of the wake behind the rotor, finite number of blades associated tip losses and on-zero aerodynamic drag.

The power curve of a wind turbine which relates mechanical power vs wind speed is very important technical information. In this chapter, Wind turbine power characteristics at different wind speeds are discussed which are characterised as cut-in speed, rated speed and cut-out speed. The wind turbine starts to capture power at the cut-in speed and the captured power is cubic function of wind speed. The wind turbine continues to capture power up to until the rated speed and the wind turbine generator is controlled to extract maximum power under varying wind speeds. If the wind speed is too high above the cut-out speed, the turbine must be shutdown to prevent any mechanical damage to the wind turbine.

The aerodynamic power control of wind turbine is discussed. The angle of attack plays a vital role in determining the amount of power captured by a wind turbine rotor blades under fluctuating wind speeds. There are three different aerodynamic control methods (passive stall control, active stall control and pitch control) to control power capture for wind turbines are discussed. Pitch control reacts faster than the active/passive stall control and proved better controllability. Pitch control is widely used in modern wind turbine technologies.

Finally, wind energy system configurations are discussed. Fixed speed wind turbines which are simple, low cost and reliable are designed to achieve maximum power at a particular speed. It has lower energy conversion efficiency compared to a variable speed wind turbine which can extract maximum power at different wind speeds. In a variable speed wind turbine power converter and controllers are required to control and capture maximum power under different wind speeds. A summary of main features of both wind turbines are provided.

Chapter 3

Analysis, Modelling and Parameter Estimation of Permanent Magnet Synchronous Generator

3.1 Overview

The permanent magnet synchronous generator is used in this thesis as wind turbine generator because of their high efficiency, low losses, smaller size, less maintenance, high reliability and the ability to operate without gearbox [16], [47]. The main aspect which distinguishes the Permanent Magnet Synchronous machine from other types of electrical machines is that the rotor magnetic flux is generated by permanent magnets, instead of being supplied by other external power sources as in DC machines and synchronous machines. Therefore, there are no rotor copper losses associated with this type of generator. Another main feature of this type of generator is that it can be designed for higher number of poles which enable it to operate without gearbox. The use of gearbox with the wind turbine adds additional costs and regular maintenance. Therefore, reliability of a variable speed wind turbine can be improved significantly with reduced costs [35], [23]. In this chapter, the detail analysis and *dq*-axis modelling of a permanent synchronous generator (PMSG) used in this research are presented.

The parameters of IPM synchronous generators have an important influence on the steady state and dynamic performance analysis of the variable speed wind turbine. The knowledge of machine model and accurate parameters is mandatory to analyse the performance and to design efficient and fast controllers for the variable speed wind turbine [48]. Therefore, accurate measurement of these parameters is essential for designing control system and predicting performance aspects such as torque response, field-weakening capabilities to maximize energy capture, efficiency and power factor [48]-[51].

In an IPM synchronous generator, the parameters used in the controllers are magnet flux linkage (λ_M), *d*-axis inductance (L_d), and *q*-axis inductance (L_q). The magnet flux can be easily estimated using the open circuit voltage of the generator with reasonable accuracy. However, the measurement of *d*-axis inductance, and *q*-axis inductance require more careful approach as it involves saturation and cross-coupling effects [50],[51]. There are different methods to determine *d*- and *q*-axis inductances such as analytical methods, finite element methods, and experimental measurements. The analytical method to calculate *d*- and *q*-axes inductances has been presented in the literatures [50],[52]. This method suffers when the configuration of the machine is complex and the presence of saturation cannot be neglected. The accuracy of this method depends greatly on the correct determination of form factor and saturation factor, which relies on the machine geometry [50]-[52]. Various techniques for parameter determination using finite element methods are presented in [50], [53]-[59]. In finite-element method, estimated inductance values are fairly accurate and both the saturation and cross-coupling can be studied appropriately. The finite-element estimation is also valuable for performance prediction during the design stage. However, finite element method requires the knowledge of machine geometry and dimensions [51]. These may not be readily available. Moreover, if magnetic saturation is significant, both the self- and mutual inductance, and *d*-axis and *q*-axis inductances are current dependent. The inductances should then be calculated by either the energy perturbation method or the current perturbation method, and the influence of the permanent magnet should be considered [58], [59]. The method described in [59] requires multiple finite-element field solutions, for a range of current perturbations in each winding, and, therefore, demands significant computational effort [50]. There are different methods for determining inductances for salient pole machine [60], [61]. However, all of them are not applicable for IPM synchronous generator particularly those methods require zero rotor field. In an IPM synchronous generator, permanent-magnet poles are buried inside the rotors and the removal of rotor field is not possible [51]. Voltage phasor measurement method for determining *d*- and *q*-axis inductances has been deployed in [62]. However, this method requires a special laboratory arrangement consisting of the test machine, an additional synchronous machine, a prime mover, and brake. There are some simpler methods such as dc bridge test, the instantaneous flux linkage test, standstill torque test, and ac standstill test. These

methods do not require removing the rotor of the machine. The ac standstill test gives fairly accurate values of inductances provided saturation on either axis is marginal. The ac standstill method is used in this work and the advantages of this method over others is that it is easy to perform in laboratory platform and do not require any extra arrangement.

This chapter presents simple methods of determining parameters such as magnet flux (λ_M), *d*-axis inductance (L_d) and *q*-axis inductance (L_q) of interior permanent magnet (IPM) synchronous generator, which are used to control the wind turbine generator. These methods are simple and do not require any complex theory, signal injection or special equipment. The effectiveness of parameter measurement methods are demonstrated by experimental results.

3.2 Generators for Wind Turbine Applications

There are different types of generators used in wind turbine applications. A classification of most common electric generators in wind energy conversion systems is shown in Fig. 3.1 [35]. The generators used for wind turbine applications can be divided into two main groups:

- Synchronous generators (SGs) and
- Asynchronous or Induction generators (IGs).

Synchronous generators can be wound rotor synchronous generator (WRSG) or permanent magnet synchronous generator (PMSG). The PMSG can be designed to have higher number of poles and suitable for direct drive gearless wind turbine applications. Presently, many wind-turbine manufacturers use direct-drive PMSG. A direct drive wind turbine system eliminates gear box, reduces size and costs. However, a direct-drive wind turbine operates at very low speeds 50 to 150 rpm [35].

Asynchronous or induction generators can be squirrel cage type or wound rotor inductance generator (WRIG) types. WRIG also known as doubly fed induction generator (DFIG) as it can supply power from stator or rotor in to grid.

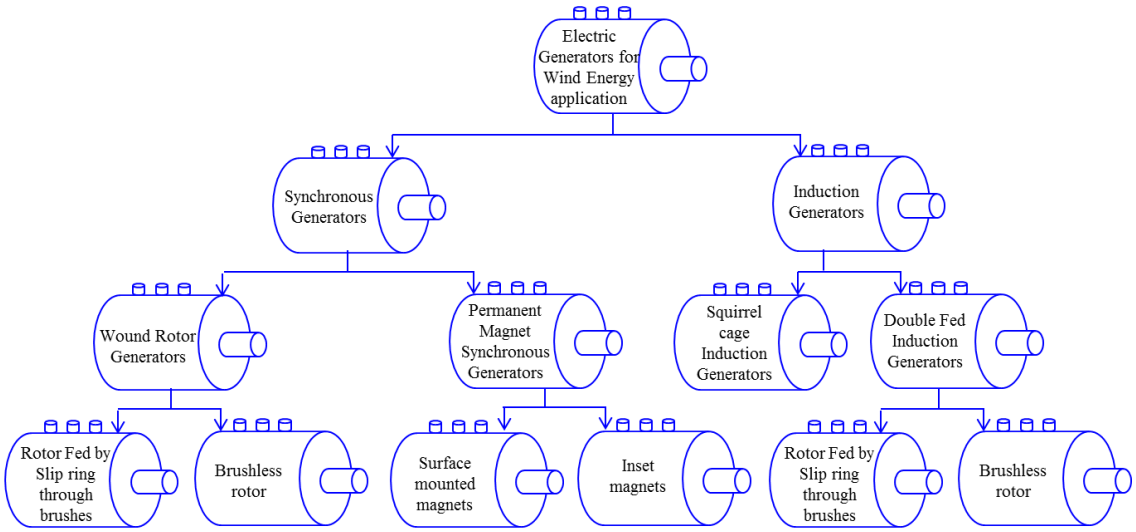

Figure 3.1 Classification of widely used wind turbine Generators

3.3 Permanent Magnet Synchronous Generator for Variable Speed Wind Turbine

PMSGs have become popular for wind turbine applications because of their advantages such as self-excitation, smaller size, low losses, high power factor and efficiency. They offer high power/volume by exploiting their rotor saliency. Many research papers have suggested the application of permanent magnet generator (PMSG) in wind turbines [35], [63]-[68]. Unlike induction generator, the PMSGs do not require magnetizing current as the rotor flux is produced by the permanent magnet and the stator current need only to be torque producing. As there is no copper loss in the rotor due to the use of permanent magnet, the PMSG operates at a higher power factor and it is more efficient than the induction generator [23], [35]. The key reason for the development of the permanent magnet synchronous machines was to remove the foregoing disadvantages of the wound rotor synchronous machine by replacing its field coil, dc power supply, and slip rings with a permanent magnet [23], [35]. PMSG based wind turbine offers following advantages [23],[35],[63]-[68];

- higher efficiency, lower losses and maintenance costs
- suitable for direct drive gearless operation
- higher reliability
- simple structure and no slip rings are required
- no reactive power requirement like an induction generator
- no need for excitation control and no losses in the rotor

- no danger of loss of excitation.

However, High temperatures can demagnetize permanent magnets. Cooling is required for the rotor as the magnetic material is sensitive to temperature [68].

3.3.1 Rotor Configurations of PMSGs

There are various rotor configurations of PMSG with the permanent magnet can be mounted on the surface of the rotor or buried inside the rotor structure. They are known as surface PMSG or interior permanent magnet (IPM) synchronous generator, respectively as shown in Fig. 3.2. The surface PMSGs as shown in Fig. 3.2(a), usually have larger air gap and smaller stator inductances.

According to the flux direction permanent magnet, generators can be classified as [63], [68];

- Axial flux machine (outer or inner rotor)
- Radial flux machine (outer or inner rotor)
- Transversal flux machine

The axial flux slotted machines have a smaller volume for a given power rating, making the power density very high. However, the mechanical dynamic balance must be taken into account as the power rating increases and the outer radius becomes larger. The outer rotor construction is better than inner rotor radial flux construction as the former has advantages such as ease of installation and cooling. Therefore, the outer rotor construction is more suitable to be applied in wind energy systems.

Unlike surface PMSG, the air gap of an interior type PMSG (salient pole) is non-uniform. Fig. 3.3 shows the magnetic flux paths of a four-pole salient pole permanent magnet synchronous machine. The magnetic flux passing through the *d*-axis magnetic circuit has to cross two magnet thicknesses and two air gaps. While the magnet flux passing through *q*-axis magnetic circuit does not have to cross magnet and only crosses two air gaps. Therefore, the *q*-axis inductance is noticeably higher than *d*-axis inductance because reluctance along the *d*-axis is higher than that along the *q*-axis. This

pole saliency distinguishes interior permanent synchronous machine (salient pole) from surface permanent synchronous machine and offers appealing performance in variable speed operations.

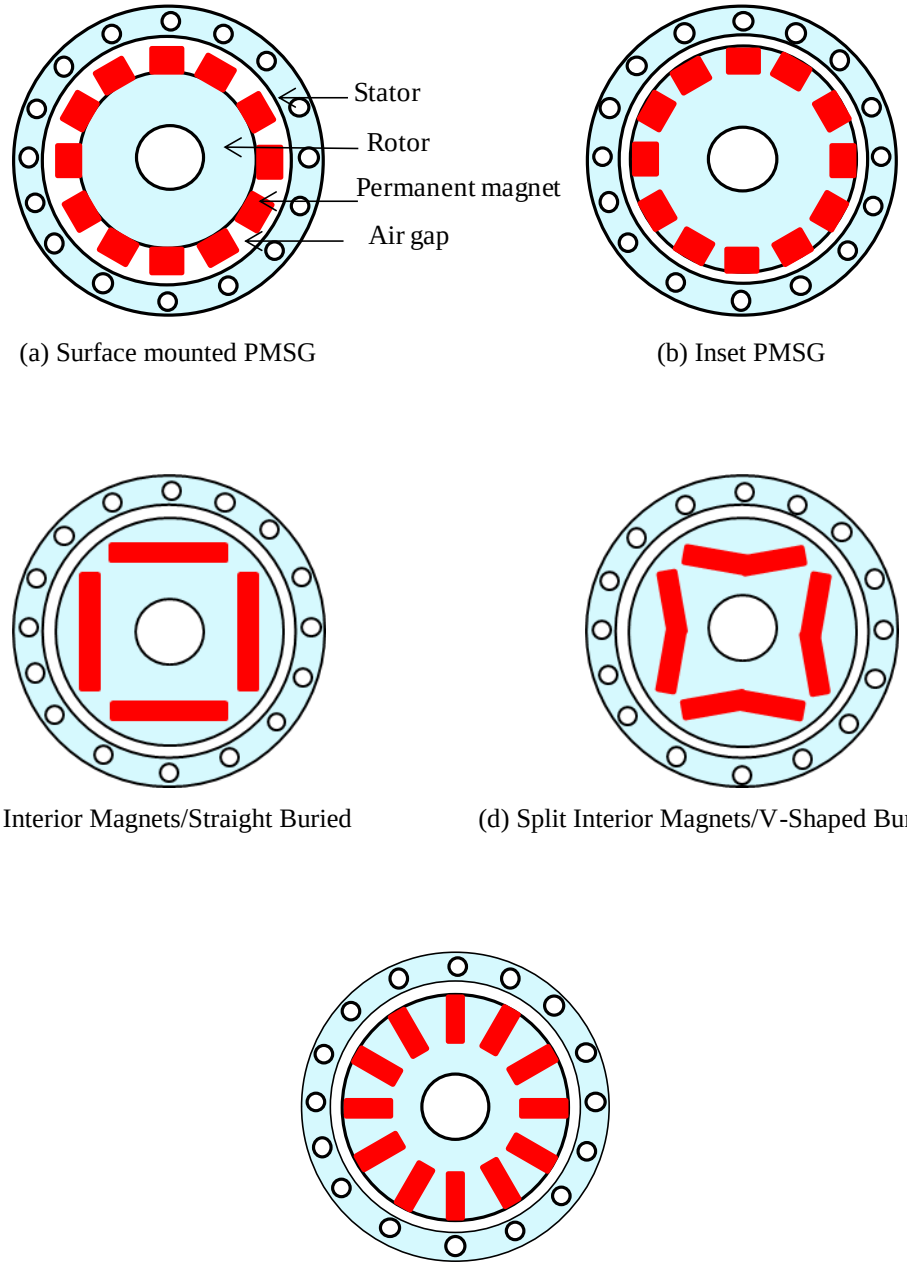

(a) Surface mounted PMSG

(b) Inset PMSG

(c) Interior Magnets/Straight Buried

(d) Split Interior Magnets/V-Shaped Buried

(e) Interior Magnets/Tangential

Figure 3.2 Orientation of permanent magnet materials in PMGs

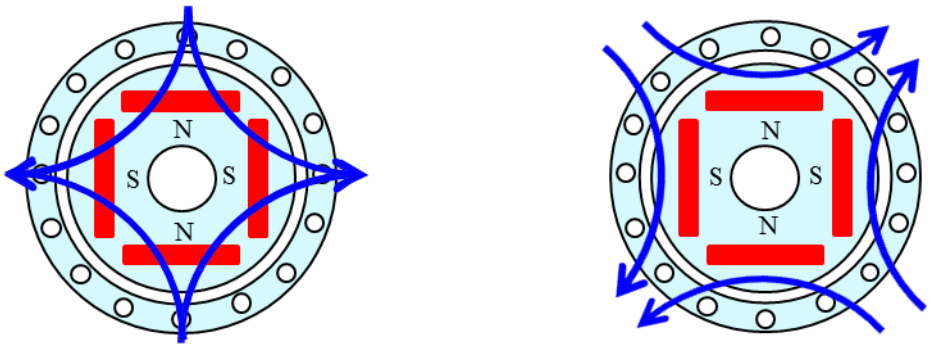

(a) *d*-axis flux magnetic flux path (b) *q*-axis magnetic flux path

Figure 3.3 Magnetic flux paths of a salient pole PM synchronous machine.

3.4 Mathematical Representation of Permanent Magnet Synchronous Generator in Machine Variables

Fig. 3.4(a) and 3.4(b) shows a there phase two poles PMSG and its equivalent circuit respectively. It has 3 phase Y-connected stator windings and a permanent magnet in the rotor. The stator windings are identical windings displaced 120^0, each with a turns number of N_s and resistance R_s. For our analysis we assume that the stator windings are sinusoidal distributed. Damper windings are neglected because the permanent magnet is a poor electrical conductor and the eddy current that flow in the nonmagnetic materials securing the magnets are small. Hence large armature current can be tolerated without significant demagnetization [70].

The stator of a PM synchronous generator is similar to the wound rotor synchronous generator and the back-emf produced by the permanent magnets is the same as that produced by an excited coil. In developing mathematical model for a PMSG we will assume the following [35], [70];

- The stator windings are sinusoidally distributed along the air gap
- Magnetic saturation is negligible
- The back-emf is sinusoidal.
- The variation of phase inductance is sinusoidal

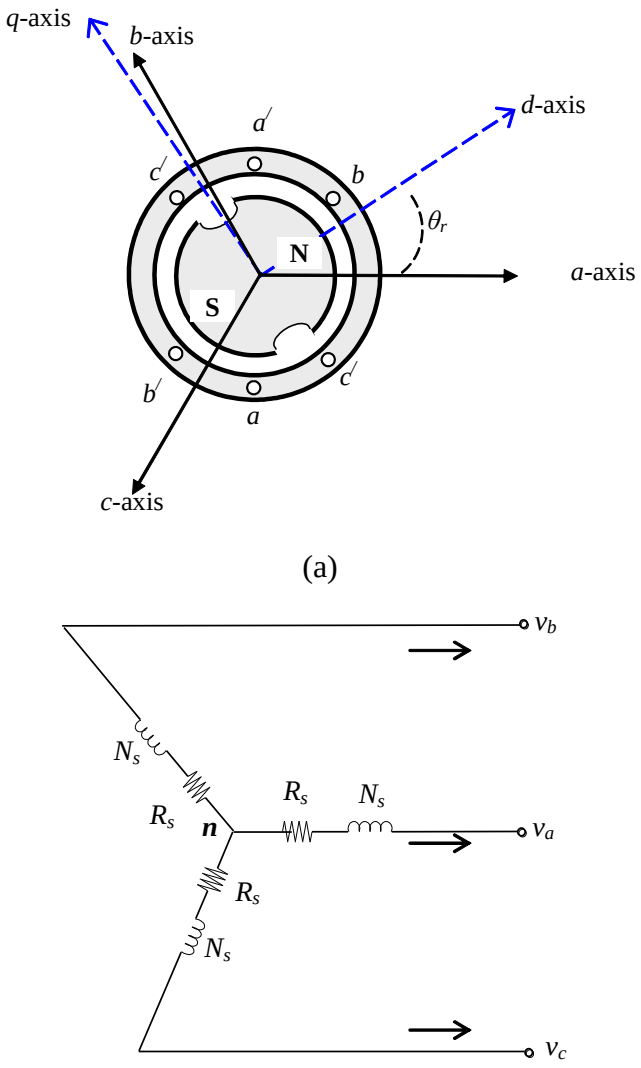

Figure 3.4 (a) Three phase, two pole PMSG (b) Equivalent circuit of PMSG

3.4.1 Inductance and Flux linkage in a PMSG

The variations in inductances in a PMSG are caused by the variations in the permeance of the magnetic flux path due to non-uniform air gap. This is pronounced in the case of a salient pole PMSG in which the permeances in the two axes (*d*-axis and *q*-axis) are significantly different. Even in a non-salient (round rotor) PMSG there are negligible differences in the permeances in the two axes due to the large number of slots associated with the windings. The flux produced by a stator winding follows a path through the stator iron, across the air gap, through the rotor iron, and back across the

air-gap. For a sinusoidal distributed winding the stator self-inductances of a PMSG can be expressed as [70]:

$$L_{aa} = L_l + L_A - L_B \cos 2\theta_r \tag{3-1}$$

$$L_{bb} = L_l + L_A - L_B \cos 2(\theta_r - \frac{2\pi}{3}) \tag{3-2}$$

$$L_{cc} = L_l + L_A - L_B \cos 2(\theta_r + \frac{2\pi}{3}) \tag{3-3}$$

Where L_A is the component of the self-inductance due to space-fundamental air-gap flux, L_l is the armature leakage flux not crossing the air-gap.

The stator to stator mutual inductance can be expressed as;

$$L_{ab} = -\frac{1}{2} L_A - L_B \cos 2(\theta_r - \frac{\pi}{3}) \tag{3-4}$$

$$L_{bb} = -\frac{1}{2} L_A - L_B \cos 2(\theta_r + \frac{\pi}{3}) \tag{3-5}$$

$$L_{cc} = -\frac{1}{2} L_A - L_B \cos 2(\theta_r + \pi) \tag{3-6}$$

For permanent magnet synchronous generator there is no rotor windings. So there will be no rotor inductance or stator to rotor mutual inductance.

The flux linkages can be expressed as:

$$\lambda_a = L_{aa} i_a + L_{ab} i_b + L_{ac} i_c + \lambda_{aM} \tag{3-7}$$

$$\lambda_b = L_{ba} i_a + L_{bb} i_b + L_{bc} i_c + \lambda_{bM} \tag{3-8}$$

$$\lambda_c = L_{ca} i_a + L_{cb} i_b + L_{cc} i_c + \lambda_{cM} \tag{3-9}$$

$$\begin{bmatrix} \lambda_a \\ \lambda_b \\ \lambda_c \end{bmatrix} = L_s \begin{bmatrix} i_a \\ i_b \\ i_c \end{bmatrix} + \begin{bmatrix} \lambda_{aM} \\ \lambda_{bM} \\ \lambda_{cM} \end{bmatrix} \tag{3-10}$$

Where,

$$L_s = \begin{bmatrix} L_{aa} & L_{ab} & L_{ac} \\ L_{ba} & L_{bb} & L_{bc} \\ L_{ca} & L_{cb} & L_{cc} \end{bmatrix} \tag{3-11}$$

and

$$\begin{bmatrix} \lambda_{aM} \\ \lambda_{bM} \\ \lambda_{cM} \end{bmatrix} = \lambda_M \begin{bmatrix} \sin\theta_r \\ \sin(\theta_r - \frac{2\pi}{3}) \\ \sin(\theta_r + \frac{2\pi}{3}) \end{bmatrix} \tag{3-12}$$

and λ_M is the amplitude of the flux linkage established by the permanent magnet as viewed from the stator phase winding. The magnitude of $N_s \frac{d\lambda_m}{dt}$ would be the open circuit voltage induced in each stator phase winding. Damper windings are neglected because the permanent magnet is a poor electrical conductor and the eddy currents that flow in the nonmagnetic materials securing the magnets are small. Hence large armature currents can be tolerated without significant demagnetization [70], [71]. In equation (3-12) it is assumed that the voltage induced in the stator windings by the permanent magnet are constant-amplitude sinusoidal voltages.

For a interior permanent magnet synchronous generator (IPMSG) the self-inductance and mutual inductance vary sinusoidally with the rotor position (θ_r) and ($L_q > L_d$). For a surface permanent magnet generator stator inductances are independent of rotor position and ($L_q = L_d$), because of the uniform air-gap. However, the slots for the stator windings introduce a slight saliency even for the surface PM generator.

3.4.2 Voltage and Torque Equations in Machine variables

The voltage equation of PMSG in machine variables can be expressed using Fig. 3.4(b) as;

$$v_a = -i_a R_s + \frac{d\lambda_a}{dt} \tag{3-13}$$

$$v_b = -i_b R_s + \frac{d\lambda_b}{dt} \tag{3-14}$$

$$v_c = -i_c R_s + \frac{d\lambda_c}{dt} \tag{3-15}$$

The electromagnetic torque in machine variables can be expressed as [70];

$$T_e = \left(\frac{P}{2}\right)\left\{-\frac{(L_{md} - L_{mq})}{3}\left[(i_a^2 - \frac{1}{2}i_b^2 - \frac{1}{2}i_c^2 - i_a i_b - i_a i_c + 2i_b i_c)\sin 2\theta_r + \frac{\sqrt{3}}{2}(i_b^2 i_c^2 - 2i_a i_b + 2i_a i_c)\cos 2\theta_r\right]\right.$$
$$\left. + \lambda_M\left[(i_a - \frac{1}{2}i_b - \frac{1}{2}i_c)\cos\theta_r + \frac{\sqrt{3}}{2}(i_b - i_c)\sin\theta_r\right]\right\} \tag{3-16}$$

where $L_{md} = \frac{3}{2}(L_A + L_B)$ and $L_{mq} = \frac{3}{2}(L_A - L_B)$ are the magnetizing inductances.

The above expression for torque is positive for generator action with positive direction of current assumed out of the stator terminals. The torque and rotor speed are related by [70]:

$$T_e = -J\left(\frac{2}{P}\right)\frac{d\omega_r}{dt} + T_I \tag{3-17}$$

where J is the inertia expressed in kilogram-meter^2 ($kg.m^2$) or joules-seconds^2 ($J.s^2$). The input torque T_I is positive for a torque input to the shaft of the synchronous machine.

3.4.3 d-q Modelling of Permanent Magnet Synchronous Generator

The well-known machine model in *dq*-reference frame which is synchronously rotating with the rotor, where *d*-axis is aligned with the magnet axis and *q*-axis is orthogonal to *d*-axis, is usually used for analysing the PM synchronous machine [35] . R.H Park incorporates a change of variables in the analysis of synchronous machines [70]. He transformed the stator variables to the rotor reference frame that eliminates the time-varying inductances in the voltage equations [70]. Fig. 3.5 shows the *d-q* axes transformation of a PMSG.

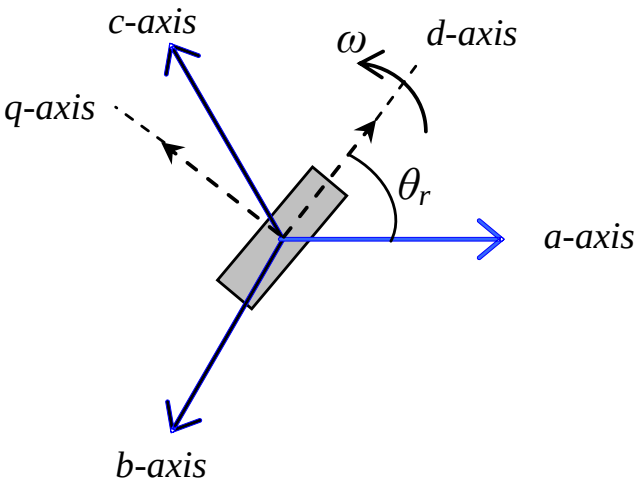

Figure 3.5 Three phase to *d-q* transformation.

The park transformation is used to derive the *d-q* model [70];

$$\begin{bmatrix} f_{ds} \\ f_{qs} \\ f_{os} \end{bmatrix} = \frac{2}{3} \begin{bmatrix} \cos\theta_r & \cos(\theta_r - \frac{2\pi}{3}) & \cos(\theta_r + \frac{2\pi}{3}) \\ \sin\theta_r & \sin(\theta_r - \frac{2\pi}{3}) & \sin(\theta_r + \frac{2\pi}{3}) \\ \frac{1}{2} & \frac{1}{2} & \frac{1}{2} \end{bmatrix} \begin{bmatrix} f_{as} \\ f_{bs} \\ f_{cs} \end{bmatrix} \tag{3-18}$$

For the inverse transformation we have

$$\begin{bmatrix} f_{as} \\ f_{bs} \\ f_{cs} \end{bmatrix} = \begin{bmatrix} \cos\theta_r & \sin\theta_r & 1 \\ \cos(\theta_r - \frac{2\pi}{3}) & \sin(\theta_r - \frac{2\pi}{3}) & 1 \\ \cos(\theta_r + \frac{2\pi}{3}) & \sin(\theta_r + \frac{2\pi}{3}) & 1 \end{bmatrix} \begin{bmatrix} f_{ds} \\ f_{qs} \\ f_{os} \end{bmatrix} \tag{3-19}$$

The angular velocity, ω_r, and the angular displacement, θ_r, of the arbitrary reference frame are related by

$$\theta_r = \int \omega_r \, dt \qquad \text{or} \qquad \theta_r = \int_0^t \omega_r(t) \, dt + \theta_r(0) \tag{3-20}$$

In the above equations,

- f can be either voltage, current, flux linkage, or electric charge
- the frame of reference may rotate at any constant or varying angular velocity or it may remain stationary.
- Note that $f_{as,}\, f_{bs,}\, f_{cs}$ are not phasors. They are instantaneous quantities that may be any function of time.

The *d*-*q* model of PMSG in synchronous reference frame is shown in Fig. 3.6. The *d*- and *q*- axes voltages of PMSG can be given by

$$v_d = -i_d R_s - \omega_r \lambda_q + p\lambda_d \tag{3-21}$$

$$v_q = -i_q R_s + \omega_r \lambda_d + p\lambda_q \tag{3-22}$$

where λ_d and λ_q are the *d*- and *q*- axes stator flux linkages. If λ_M is the rotor magnetic flux produced by the permanent magnets in the rotor, then stator flux linkage can be written as

$$\lambda_d = -L_d i_d + \lambda_M \tag{3-23}$$

$$\lambda_q = -L_q i_q \tag{3-24}$$

with

$$L_d = L_{ls} + L_{md} \tag{3-25}$$

$$L_q = L_{ls} + L_{mq} \tag{3-26}$$

$$\vec{\lambda}_s = \lambda_d + j\lambda_q \tag{3-27}$$

$$\vec{V}_s = V_d + jV_q \tag{3-28}$$

$$\vec{i}_s = i_d + ji_q \tag{3-29}$$

The torque equation of the permanent magnet synchronous generator is given by [70]:

$$T_g = -\frac{3}{2}P\left(\lambda_d i_q - \lambda_q i_d\right) = -\frac{3}{2}P[\lambda_M i_q + \left(L_d - L_q\right) i_d i_q] \tag{3-30}$$

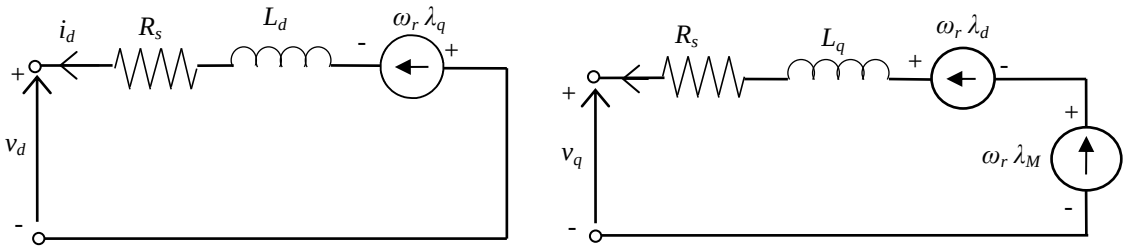

(a) *d*-axis equivalent circuit (b) *q*-axis equivalent circuit

Figure 3.6 *d-q* model of PMSG in synchronous reference frame

In equations (3-21) to (3-30), v_d, v_q, i_d, i_q, L_d and L_q are the *d* and *q* axes stator voltages, currents and inductances respectively. L_{ls} is the leakage inductance, L_{md} and L_{mq} are the *d*- and *q*- axis magnetizing inductance, *R* is the stator resistance, ω_r ($=\omega$) is the electrical rotor speed in rad/sec, *P* is the number of pole pairs and *p* is the operator *d/dt*. The torque equation (3-30) consists of two terms namely excitation torque and reluctance torque. For the surface PMSG, the reluctance torque is zero, since $L_d = L_q$, while for the IPM synchronous machine, higher torque can be induced for the same i_d and i_q if ($L_d - L_q$) is larger [35].

3.4.4 Phasor Diagram and Power Angle Characteristics of Permanent Magnet Synchronous Generator

3.4.4.1 Power Angle Characteristics of a Non-salient Pole PMSG

The per phase equivalent circuit and phasor diagram for the relationship between voltages and current of surface permanent magnet synchronous generator is shown in Fig. 3.7 and Fig. 3.8 (a),(b) respectively. The terminal voltage $V_t \angle 0^0$ is considered as the reference phasor in drawing the phasor diagram. Using the equivalent per phase circuit diagram of a PMSG shown in Fig. 3.7, we get

$$E_f = V_t + I_a R_a + I_a jX_s = \left|E_f\right| \angle \delta \tag{3-31}$$

It is important to note that the angle δ between V_t and E_f is positive for the generating action and negative for motoring action. The angle δ is known as the ***power angle*** and it plays an important role in power transfer and in the stability of PMSG operation. The

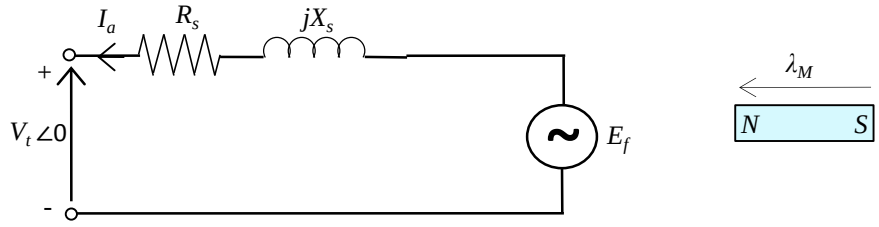

Figure 3.7 per phase equivalent circuit of PMSG.

PMSG is considered to deliver a lagging current to the load or infinite bus represented by V_t.

The per phase complex power *S* at the terminal is

$$S = P_G + jQ_G \tag{3-32}$$

The real power P_G and reactive power Q_G per phase are

$$P_G = 3V_t I_a \cos\theta \tag{3-33}$$

and

$$Q_G = 3V_t I_a \sin\theta \tag{3-34}$$

If R_a is neglected (since $X_s >> R_a$), Then $|Z_s| = \sqrt{R_a{}^2 + X_s^2} = |X_s|$ and the phasor diagram becomes as shown in Fig. 3.8(b).

From Fig. 3.8 (b)

$$E_f \sin\delta = X_s I_a \cos\theta \qquad \Rightarrow I_a \cos\theta = \frac{|E_f|}{|X_s|}\sin\delta \tag{3-35}$$

From equation (3-33),

$$P_G = 3\frac{|V_t||E_f|}{|X_s|}\sin\delta = P_{G\_\max}\sin\delta \qquad \text{watts} \tag{3-36}$$

where,

$$P_{G\_\max} = \frac{|V_t||E_f|}{|X_s|} \tag{3-37}$$

From Fig. 3.8 (b), $E_f \cos\delta = V_t + X_s I_a \sin\theta$, and from equation (3-34), we get

$$Q_G = 3V_t\left(\frac{E_f \cos\delta - V_t}{X_s}\right) = \frac{3|V_t||E_f|}{X_s}\cos\delta - \frac{|V_t|^2}{|X_s|} \qquad \text{VAR} \qquad (3\text{-}38)$$

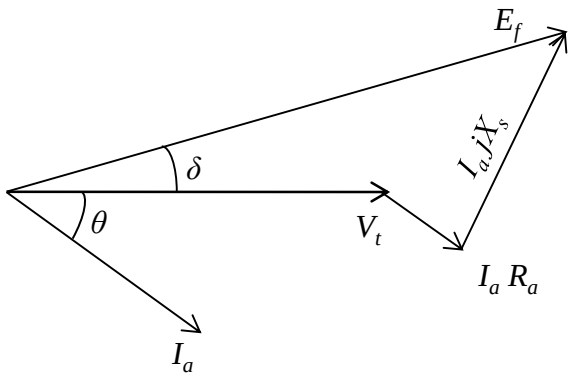

(a) Phasor diagram of surface PMSG (non-salient)

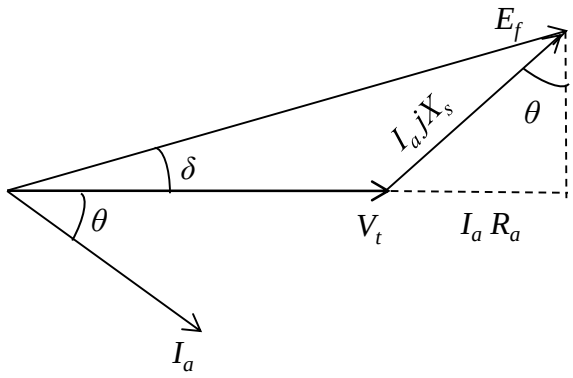

(b) Phasor diagram of surface PMSG (neglecting R_a)

Figure 3.8 Phasor diagram of surface PMSG

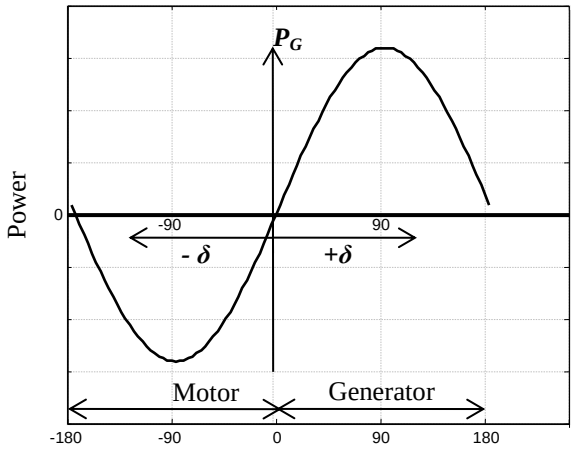

Figure 3.9 Power angle characteristics of a non-salient pole permanent magnet synchronous machine.

This power P_G is positive when the angle δ is negative, i.e., when rotor poles (field) lag the stator poles (field) by δ. Thus when the machine motors, δ < 0, and when it generates δ > 0. This is depicted in Fig.3.9.

If ω_s is the synchronous speed, which is the same as the rotor speed, the developed torque becomes

$$T_{G\_develop} = \frac{P_G}{\omega_s} = \frac{3}{\omega_s}\frac{|V_t||E_f|}{|X_s|}\sin\delta = T_{G\_\max}\sin\delta \qquad \text{Nm} \qquad (3\text{-}39)$$

For motoring δ is negative and torque becomes positive. In case of generating, δ is positive and the power and torque become negative. The angle δ is called torque angle. For a fixed voltage and frequency, the torque depends on δ, and is proportional to the excitation voltage E_f.

If $\delta = 90^0$, the torque in equation (3-39) becomes maximum and the maximum developed torque, which is called pull-out torque, can be written as

$$T_{G\_pullout} = \frac{3VE_f}{\omega_m X_s} \qquad (3\text{-}40)$$

3.4.4.2 Power Angle Characteristics of a Salient Pole PMSG

In the equivalent circuit for a salient pole synchronous generator, these *d*-axis and *q*-axis synchronous reactance must be considered as shown in Fig. 3.10(b).The component currents (I_d, I_q) produces component voltage drops (jI_dX_d) and (jI_qX_q). The phasor relations are

$$E_f = V_t + I_aR_a + I_d(jX_d) + I_q(jX_q) \tag{3-41}$$

$$I_a = I_d + I_q \tag{3-42}$$

Neglecting stator resistance, the phasor diagram of a salient pole PMSG is shown in Fig. 3.11. The complex power per phase is given by

$$S = V_tI_a^* = |V_t|\angle -\delta\ (|I_q| - j|I_d|)^* = |V_t|\angle -\delta\ (|I_q| + j|I_d|) \tag{3-43}$$

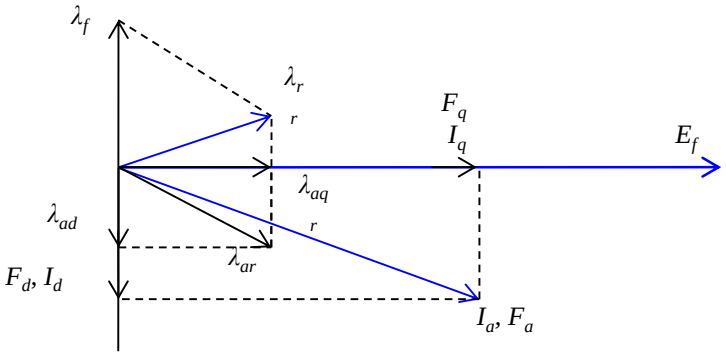

(a) MMF and flux

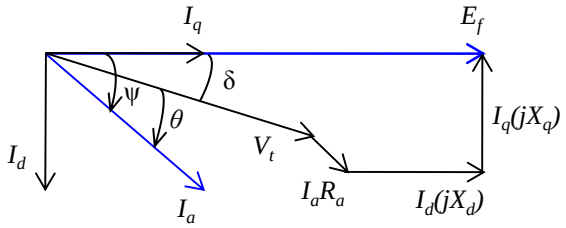

(b) Phasor diagram showing voltage and currents

Fig. 3.10 Phasor diagrams of a salient pole permanent magnet synchronous generator.

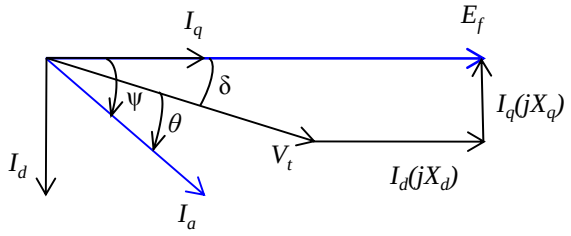

Figure 3.11 Phasor diagrams of a salient pole PMSG neglecting armature resistance

From the phasor diagram of Fig. 3.11, we get

$$|I_d| = \frac{|E_f| - |V_t|\cos\delta}{X_d} \tag{3-44}$$

$$|I_q| = \frac{|V_t|\sin\delta}{X_q} \tag{3-45}$$

Substituting equation (3-44) and equation (3-45) in equation (3-43), we get

$$S = \frac{|V_t^2|}{X_q}\sin\delta \times \angle(-\delta) + \frac{|V_t||E_f|}{X_d}\angle(90^0 - \delta) - \frac{|V_t^2|}{X_d}\cos\delta \times \angle(90^0 - \delta) = P_G + jQ_G \tag{3-46}$$

$$S = V_t I_a^* = |V_t| \angle -\delta\ (|I_q| + j|I_d|)$$

$$S = |V_t| \angle -\delta\ (\frac{|V_t|\sin\delta}{X_q} + j\frac{|E_f| - |V_t|\cos\delta}{X_d})$$

$$S = |V_t| \angle -\delta\ (\frac{|V_t|\sin\delta}{X_q} + j\frac{|E_f| - |V_t|\cos\delta}{X_d})$$

From equation (3-46), the real power is given by

$$P_G = \frac{|V_t||E_f|}{X_d}\sin\delta + \frac{|V_t^2|(X_d - X_q)}{2X_d X_q}\sin 2\delta \tag{3-47}$$

$$= P_{G1} + P_{G2} = \text{excitation power} + \text{reluctance power}$$

The maximum resultant power is higher than that of a non-salient pole generator for the same excitation voltage the reactive power is given by

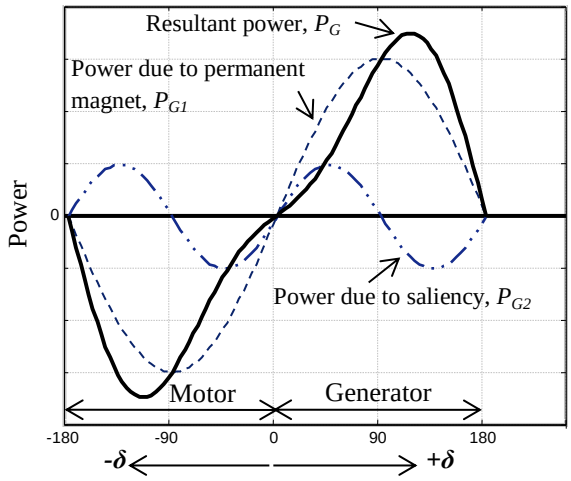

Figure 3.12 Power angle characteristics of a salient pole PMSG $(L_q > L_d)$.

$$Q_G = \frac{|V_t||E_f|}{X_d}\cos\delta - |V_t^2|\left|\frac{\sin^2\delta}{X_q} + \frac{\cos^2\delta}{X_d}\right| \tag{3-48}$$

Figure 3.12 shows the power angle characteristics of IPM synchronous generator which indicates the excitation power, reluctance power and the resultant power.

3.5 Parameter Measurement of IPM Synchronous Generator [48]

The most common parameters of IPM synchronous generator used in the implementation of control algorithms for variable speed wind turbine are,

- R_a– Armature resistance,
- L_d - the direct axis inductance,
- L_q - the quadrature axis inductance, and
- λ_M - the permanent magnet Flux linkage

These parameters are used to calculate control rules in the vector or direct control scheme of IPM synchronous generator based variable speed wind turbine. These parameters can also be used for sensor less speed estimation of the IPM synchronous generator. For proper implementation of control algorithm the accurate values of these parameter should be known.

3.5.1 Armature Resistance (R_a) Measurement

The stator resistance of the generator can be easily measured from the standard DC measurement. Winding resistance value is highly temperature dependent. When winding resistance R_0 is measured, temperature T_0 (^{0}C) of the winding must be recorded and the resistance R_t at another temperature T should be calculated using the following formula,

$$R_t = R_0 (K+T) / (K+T_0) \quad (3\text{-}49)$$

where, K is the constant determined by the material (K=234.5 for copper). Resistance value at 25°C is often used for published data.

3.5.2 Determination of Magnet Flux Linkage (λ_M)

The magnet flux linkage of IPM synchronous generator is determined by measuring the open circuit voltage of the generator at different speeds as shown in Table 3.1. The IPM synchronous generator is driven by an Induction motor. Fig.3.13 shows the IPM synchronous generator open circuit line to line voltage at 1200 rpm. The open circuit voltage of the IPM synchronous generator is almost sinusoidal. This waveform can be approximated as,

$$v_{ab} = 481.5 \sin(\omega t) \quad (3\text{-}50)$$

where, v_{ab} = instantaneous line to line voltage of IPM synchronous generator

$\omega = \frac{2\pi}{60} \times N_r \times \frac{P}{2}$ (rad/sec)

P = number of poles

N_r = generator speed (rpm)

If the generator open circuit voltage is assumed to be sinusoidal, it is related to generator speed and phase voltage as,

$$V_p = \omega \times \lambda_M \quad (3\text{-}51)$$

and the calculated magnet flux is 0.5217 Wb. Fig. 3.14 shows the IPM generator open circuit line to line voltage vs generator speed. It is observed that the generator open circuit voltage is almost linear up to the rated voltage of the generator.

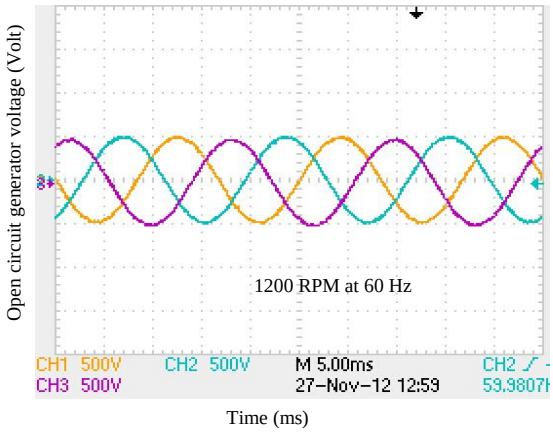

Figure 3.13 Back emf of the IPM synchronous generator at 734 rpm.

Table 3.1: IPM Synchronous Generator Open Circuit Voltage at Different speeds

Generator Speed (N_r) (rpm)	Generator Speed () (rad/sec)	Generator Frequency (Hz)	Open circuit Line Voltage (Volts)	Open circuit Phase Voltage (Volts)	Magnet flux linkage (λ_M)
200	62.80	10	56.42	32.5751	0.5187
400	125.60	20	112.68	65.0577	0.5180
600	188.40	30	169.73	97.9965	0.5202
800	251.20	40	226.22	130.6120	0.5200
1000	314.00	50	283.60	163.7413	0.5215
1200	376.80	60	340.48	196.5820	0.5217
1400	439.60	70	396.31	228.8164	0.5205
1600	502.40	80	450.60	260.1617	0.5178
1700	533.80	85	480.50	277.4249	0.5197

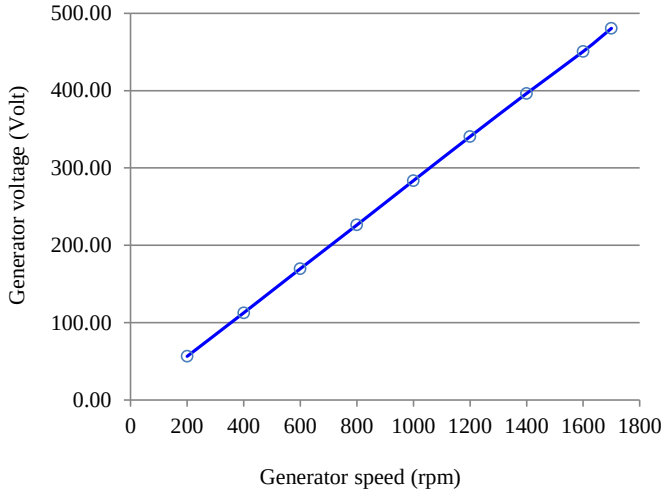

Figure 3.14 IPM synchronous generator open circuit line to line voltage vs generator speed.

3.5.3 Measurement of d-axis Inductance (L_d) and q-axis Inductance (L_q)

The IPM synchronous generator can be characterized by its *d*-axis inductance L_d and *q*-axis inductance L_q. As is seen from the torque equation (3-30), the reluctance torque per ampere is proportional to (L_q - L_d) while the saliency ration (L_q/L_d) determines many of the machine operation characteristics such as field weakening range and power factor. These synchronous inductances are independent of the permanent magnets and can be measured before or after the magnets are put into the rotor. AC standstill method is used to measure the *d*- and *q*-axis inductances in this paper. The *d*- and *q*-axis inductances can be calculated from self and mutual inductances of the stator winding. For sinusoidally distributed windings, the phase self- and mutual-inductances, *L* and *M*, can be expressed as functions of the rotor angle, θ_r.

$$L = L_0 \pm \cos 2\theta_r + L_{ls} \tag{3-52}$$

$$M = M_0 \pm M_2 \cos\left(2\theta_r \pm 2\pi/3\right) \tag{3-53}$$

Where,

L= self-inductance (H)

L_{ls}= leakage inductance

M= mutual inductance (H) and

θ_r = rotor position

Each inductance has a constant term (L_0 and M_0) and a second harmonic term (L_2 and M_2). It has been shown in [71] that for sinusoidally distributed windings

$$M_0 = -L_0/2 \tag{3-54}$$

$$L_2 = M_2 \tag{3-55}$$

Assuming negligible space harmonics due to distributed windings, the *d- and q*-axis inductances are therefore obtained from the following equations,

$$L_d = \frac{3}{2}(L_0 + L_2) + L_l \tag{3-56}$$

$$L_q = \frac{3}{2}(L_0 - L_2) + L_l \tag{3-57}$$

However, for a machine with significant space harmonics, the relationship in equations (3-57) and (3-58) is no longer valid. The more general definition is as follows [72].

$$L_d = (L_0 - M_0) - \left(\frac{L_2}{2} + M_2\right) + L_{ls} \tag{3-58}$$

$$L_{dq} = (L_0 - M_0) + \left(\frac{L_2}{2} + M_2\right) + L_{ls} \tag{3-59}$$

3.5.4 Measurement of d-axis Inductance (L_d) and q-axis Inductance (L_q) for Machine with Accessible Neutral Point [48]

The connection diagram of the test for a Y-connected IPM generator with access to neutral point of the stator windings is shown in Fig. 3.15. The phase "*a*" is excited by a single phase supply and the line current and induced voltage in phase "*b*" or phase "*c*" are measured for different rotor position. The self-inductance and mutual inductances of the stator winding at each rotor position can be estimated by the following equations:

$$L_a(\theta) = \frac{\sqrt{\left(\frac{V_a}{I_a}\right)^2 - (R_a)^2}}{2\pi f} \tag{3-60}$$

$$M_{ab}(\theta) = \frac{V_b}{2\pi f} \tag{3-61}$$

where,

V_a - supplied phase voltage (V), f - frequency (Hz), V_b-measured phase voltage in phase "*b*" (V), I_a - measured phase current (A), and R_a- stator resistance (Ω). The

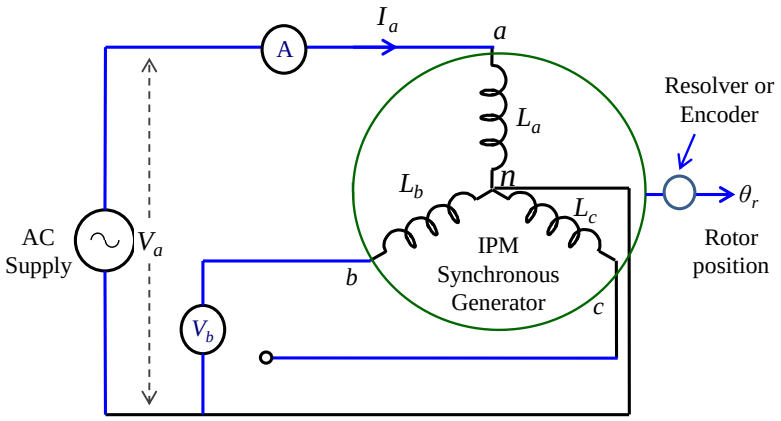

Figure 3.15 Circuit connection diagram for *d*- and *q*-axis inductance measurement (with neutral connection available).

calculated L_a and M_{ac} can be plotted against the rotor positions. From these plots, the measured self and mutual inductances can be expressed as a function of rotor position in the form of equations (3-57) and (3-58) by using curve fitting technique. The constant terms (L_0 and M_0) and a second harmonic terms (L_2 and M_2) are then determined from these equations. Finally *d*- and *q*-axis inductances can be determined from equation (3-56) and equation (3-57). This procedure can be repeated for a series of rotor positions between 0 to 360^0.

3.5.5 Measurement of d-axis Inductance (L_d) and q-axis Inductance (L_q) for Machine with Inaccessible Neutral Point

The IPM synchronous generator under test does not have access to neutral point of stator windings. Therefore, a connection diagram for the test is developed as shown in Fig. 3.16. The generator is excited by ac voltage as shown in the connection diagram. The line current and induced phase voltages are measured at different rotor positions. The self-inductance of the winding at each rotor position is estimated by

$$L_a(\theta) = \frac{2}{3}\frac{\sqrt{\left(\frac{V_T}{I_a}\right)^2 - \left(\frac{3}{2}R_a\right)^2}}{2\pi f} \tag{3-62}$$

The calculated L_a is then plotted against rotor positions. The voltage and current for various rotor positions were recorded. The test is performed for a value of current starting from 1 A to 7 A. Fig. 3.17 shows voltage and current waveforms supplied to the generator stator armature and they are almost sinusoidal. Fig. 3.18 shows the plot of L_{aa}

for the current values of 1A to 7A. Using Fig. 3.17(a), the self-inductance can be approximated as,

$$L_{aa}(\theta) = 0.036105 + 0.01861 \sin(2\theta) \quad (3\text{-}63)$$

From the maximum and minimum values of the self-inductance (L_{aa}) in Fig. 9(a), the measured *d*-axis and *q*- axis inductances are,

$$L_d = 0.01749 \text{ H} \quad (3\text{-}64)$$

$$L_q = 0.05472 \text{ H} \quad (3\text{-}65)$$

Table 3.2 shows the *d*-axis and *q*-axis inductance values measured at different generator current values. Fig.3.19 shows the variation of inductances with generator currents. It is seen that the *d*-axis inductance is almost constant and the *q*-axis inductance varies with stator current due to magnetic saturation. The effective air-gap in the permanent magnet machine is small and therefore the effects of magnetic saturation due to the armature reaction are dominant. Especially, the *q*-axis inductance L_q varies depending on the *q*-axis current and as a result, the control performances of the generator will be affected by the magnetic saturation. The parameters of the IPM synchronous generator under test are shown in Table 3.3.

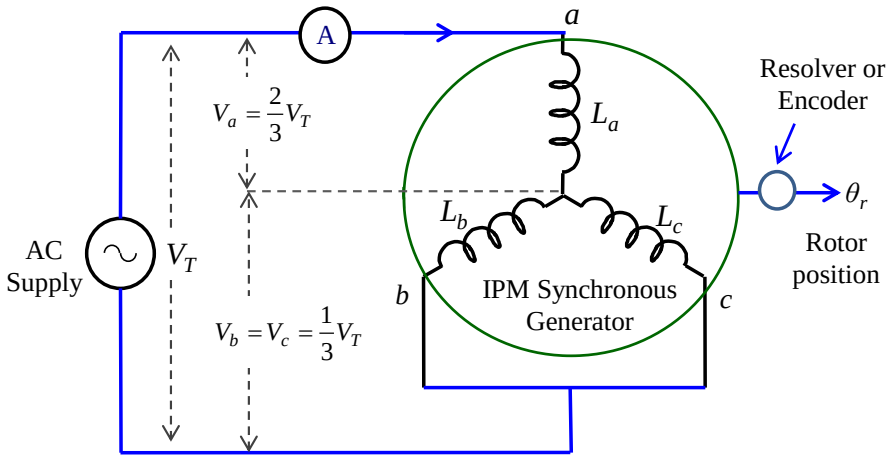

Figure 3.16 Circuit connection diagram for *d*- and *q*-axis inductance measurement (without access to neutral point).

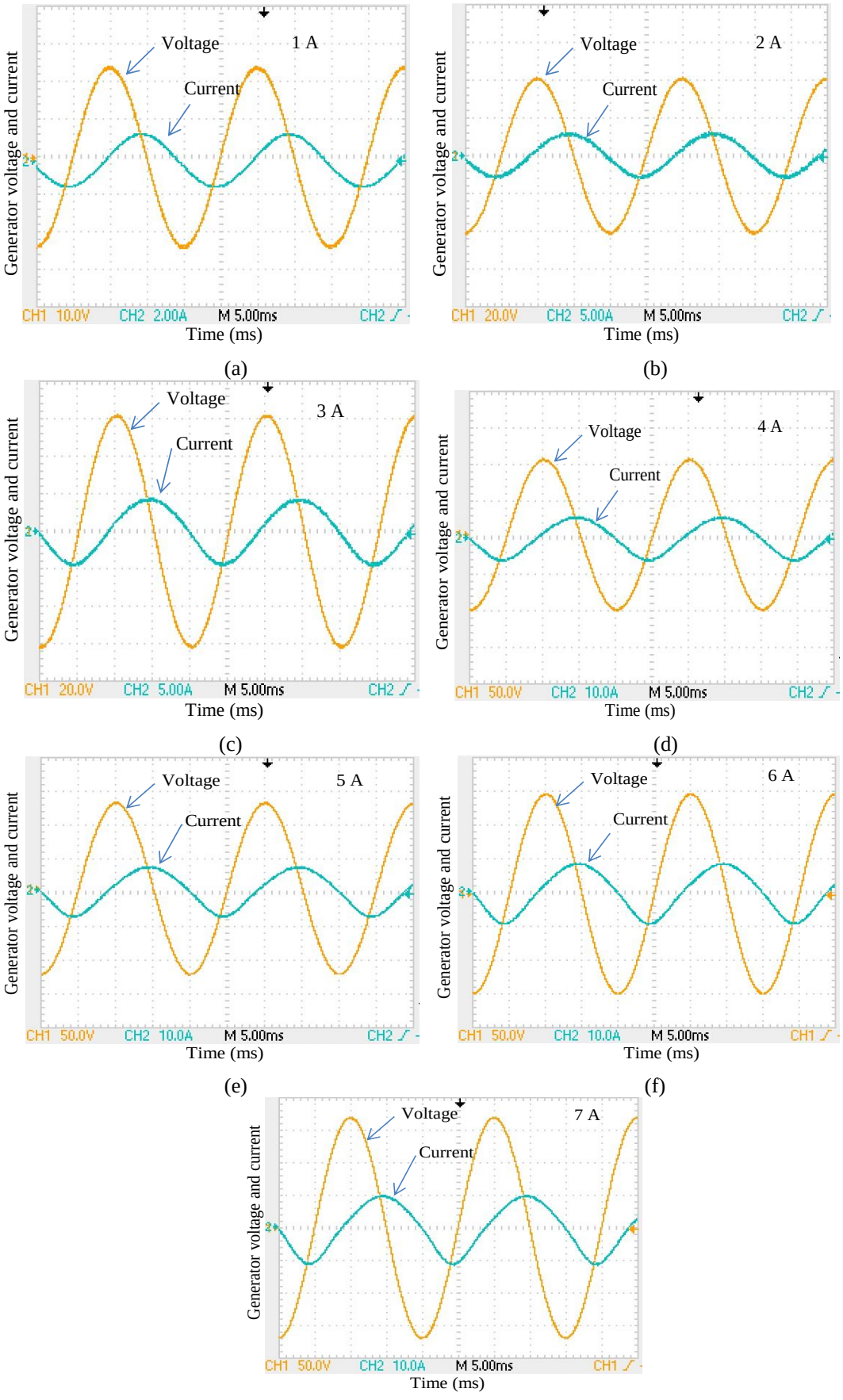

Figure 3.17 Generator voltage and current waveforms at different generator currents.

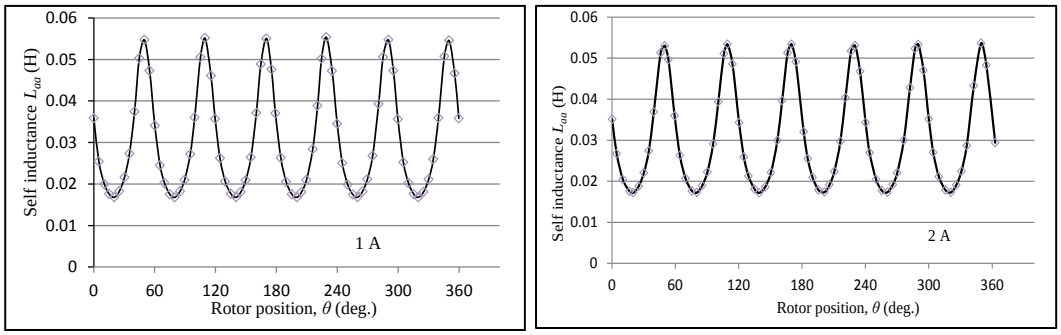

(a) (b)

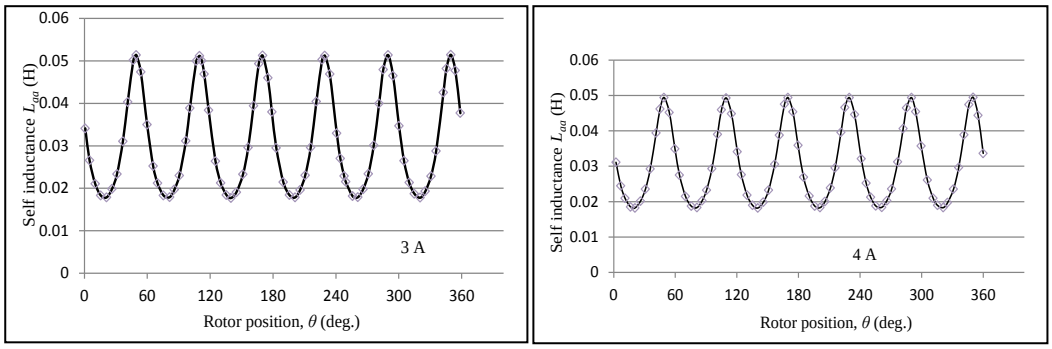

(c) (d)

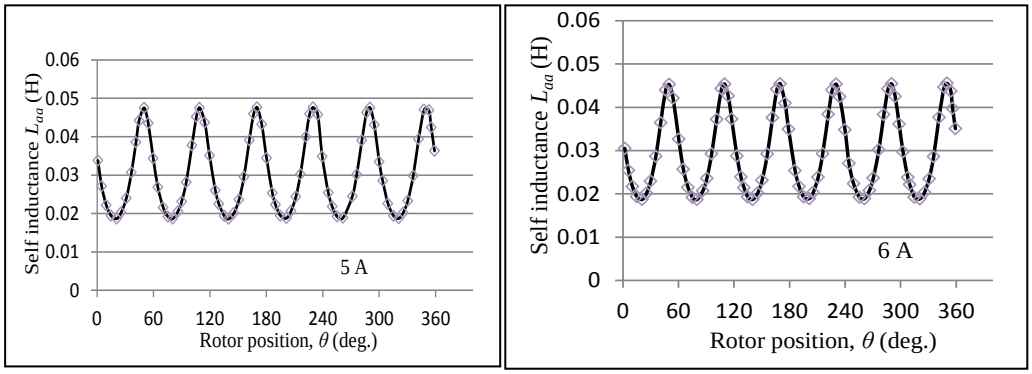

(e) (f)

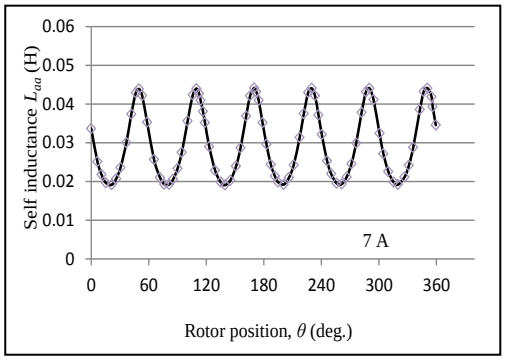

(g)

Figure 3.18 Measured self-inductance of IPM synchronous generator.

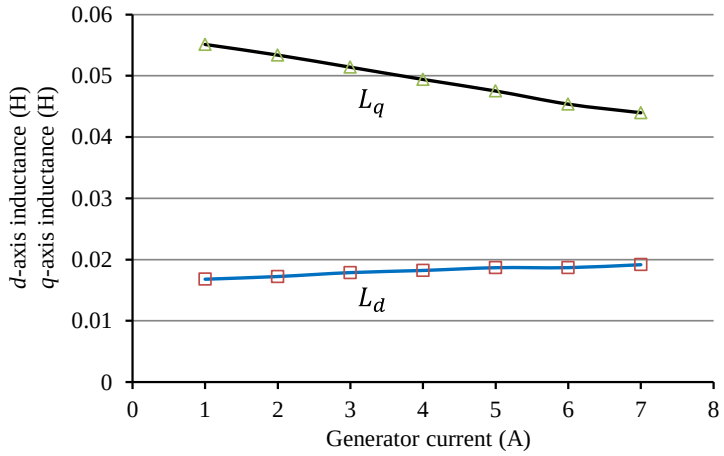

Figure 3.19 Measured *d*- and *q*-axis inductances vs. generator current.

3.5.6 Experimental Setup

The parameters of the IPM synchronous generator are measured using the methods explained in Section 3. Table 3.3 shows the parameters of the machine. The tests were performed using a set up as shown in Fig. 3.20. To measure the magnet flux linkage, the IPM synchronous generator was driven by an induction motor controlled by a variable speed drive as shown in Fig. 3.20. The voltage and current were recorded for various rotor positions to measure the *d*- and *q*-axis inductances. An electronic brake is used to block the rotor and to minimize vibration. A resolver interfaced with NI Lab VIEW is used to measure the rotor positions.

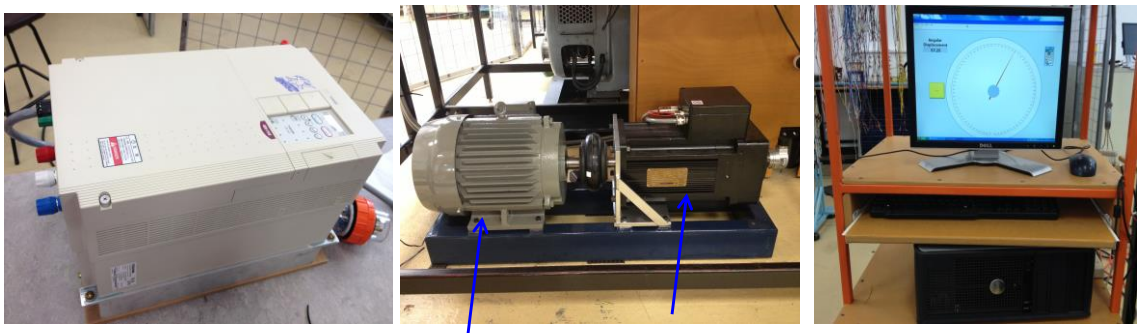

Figure 3.20 Experimental test set up for the parameter measurement.

Table 3.2: *d*-axis and *q*-axis inductances at different generator currents

Generator current (A)	L_d (mH)	L_q (mH)
1	17.49	54.72
2	17.22	53.38
3	17.87	51.40
4	18.22	49.41
5	18.67	47.52
6	18.68	45.37
7	19.16	43.97

Table 3.3: Parameters of the IPM Synchronous Generator

Parameters	Values
Machine Model	Kollmorgen BH 822C-43
Rated power	4.7 kW
Rated speed	1280 rpm
Maximum speed	1600 rpm
Maximum rated voltage	400 V AC rms (480 V max)
Magnet flux linkage λ_M	0.52 Wb
d-axis inductance L_d	17.49 mH
q-axis inductance L_q	54.72 mH
Number of poles	6
Armature resistance	1.35 (dc)/ 1.56 (ac) Ω
Rotor Inertia kg-m² (lb-in.-s²):	0.0049 (0.0036)
Static Friction (less shaft seal) N-m (lb-in.):	0.637 (5.64)

3.6 Summary

The detail analysis and *dq*-axis modelling of a permanent synchronous generator are presented in this chapter. The accurate parameter of PMSG is necessary to design controllers for wind energy conversion system. Simple methods of determining the parameters of IPM synchronous generator such as magnet flux, *d*-axis and *q*-axis inductances have been developed. These parameters can be used in the controller of wind turbine generator. Experimental tests were performed in the laboratory condition using the developed methods and test results are discussed. The generator model and measured parameters of IPM synchronous generator are used in the work presented in Chapter 4 to 6.

Chapter 4

Control of Permanent Magnet Synchronous Generator Based Direct Drive Variable Speed Wind turbine

4.1 Overview

In this chapter, control strategies for PMSG based direct drive variable speed wind turbine are discussed. A review of control strategies for the direct drive wind turbine with PMSG is presented first. Then, the modelling, analysis and control of a PMSG based direct drive variable speed wind turbine using switch-mode rectifier is presented. Finally, an enhanced control scheme for interior permanent magnet (IPM) synchronous generator is developed by incorporating maximum torque per ampere trajectory (MTPA) and maximum power extraction (MPE) algorithm. The main advantage of incorporating MTPA trajectory in the control scheme is that it can generate the required torque with a minimum stator current. Therefore, MTPA control scheme minimizes the stator loss of the IPM synchronous generator and ensures maximum utilization of stator current. The detail analysis of the control scheme and pulse width modulation (PWM)) rectifier is presented. The proposed control scheme is simulated in *Matlab/SimPowerSystems* and experimentally implemented using DSpace DS1104 digital signal processor (DSP) system. Simulation and experimental results are presented and discussed. Results confirm the effectiveness of the control scheme to control the direct drive variable speed wind turbine with maximum power extraction under varying wind speeds.

4.2 Review of Control Strategies for Direct Drive Variable Speed Wind Turbine with PMSG

The interest in variable speed wind turbines is increasing due to their advantages over the fixed speed wind turbines. The problems associated with induction generator based fixed speed wind turbines are reactive power consumption, mechanical stress and poor power quality [73], [74]. In a fixed speed wind turbine, fluctuations in wind speed are transmitted as fluctuations in the mechanical torque, and that results in fluctuations in the electrical power [4]. The power fluctuations can also lead to large voltage fluctuations in a week grid system [4]. Unlike a fixed speed wind turbine, variable speed wind turbines can operate at maximum power point with reduced fluctuations by regulating the generator speed, which increases energy capture, efficiency and improve power quality [4]. Currently, doubly fed induction generator based variable speed wind turbine technology is dominating the world market [4]-[10]. The advantage of this technology is that it requires power converter with reduced capacity (30% of full capacity) as the converter connected to the rotor circuit instead of stator circuit [4]. However, the main drawback of this type of wind turbine is the requirement of a gearbox which requires regular maintenance and suffers from faults and malfunctions [4]. Moreover, it increases the overall size of the wind turbine.

Recently, the popularity of direct drive, gearless, permanent magnet synchronous generator based variable speed wind turbines is increasing due to their advantages over induction generator based wind turbine with gearbox. The main features of PMSG based wind turbines are [8]-[17]:

- gearless operation and enhanced reliability
- simple structure, smaller size and reduced cost
- low mechanical and electrical losses
- higher power factor and efficiency
- no requirement for reactive power support

Most of the previous works related to PMSG based wind turbines are based on surface type permanent magnet synchronous generator [7-17], [20-21]. Several manufacturers including SIEMENS, GE, Suzlon are producing multi MW scale wind turbines, which are based on surface type PMSG for which the *d*-axis and *q*-axis inductances are equal,

L_d=L_q. Much attention has not been paid to interior permanent magnet (IPM) synchronous generator based variable speed wind turbines. The IPM synchronous generator (for which $L_d \neq L_q$) can produce more power than that of a surface type PMSG by utilizing their rotor saliency [18]. The IPM generator can be operated over a wide speed range by using flux weakening and allows constant power like operation at speeds higher than the rated speed [18], [19]. This work concentrated on the control of IPM synchronous generator based variable speed wind turbine.

PMSG based variable speed wind turbine is controlled using switch-mode boost rectifier [13], [23], [77], three switches PWM rectifier [15], vector controlled PWM rectifier [18], [78]. Each method has its own advantages and drawbacks.

The switch-mode rectifier using a diode rectifier and boost dc to dc converter is suitable for low power applications. This type of converters has advantages such as [18], [19], [78]:

- simple structure
- low cost
- high reliability
- simple control algorithm
- allow maximum power point tracking

However, it introduces high harmonic distortion and unable to control the power factor, which affects the system performance and efficiency [18], [19]. In this topology, power semiconductor device has to endure high instantaneous voltage and current stress. Moreover, it introduces torque oscillations which result in decreasing efficiency and lifetime. There are several topologies which are investigated to reduce system cost by lowering the number of power electronic switches [15],[77]–[80]. A three-switch buck-type rectifier based generator side converter is used in [15]. This topology is robust but requires an extra stage to boost dc voltage.

Vector controlled back to back PWM converter with voltage source converter (VSC) is preferred for IPM synchronous generator based variable speed wind turbines. In a traditional vector control scheme of PMSG, the *d*-axis current is regulated to zero and the *q*-axis current is controlled to control the torque of the generator in the rotor

reference frame. However, in an IPM synchronous generator both *d*- and *q*-axis currents need to be regulated to utilize the rotor saliency and to enhance the system efficiency. In the proposed control scheme, the IPM synchronous generator is controlled using MTPA trajectory and MPE algorithm to enhance system performance with increased energy capture and efficiency. The MTPA control produces a given torque with a minimum stator current which maximizes the utilization of the stator current and minimizes the stator losses of the IPM generator [35].

4.3 Indirect Control Strategies for Generator Side Converter of PMSG Based Direct Drive Variable Speed Wind Turbine

There are many control strategies available for PMSG based direct drive variable speed wind turbines. These control strategies can be classified as:

- *Indirect control strategies*- where torque/speed of the wind turbine generator is controlled by controlling *d*-and *q*-axes stator current i_d and i_q in the rotating reference frame.
- *Direct control strategies*- where torque/speed of the wind turbine generator is controlled by direct control of stator flux linkage and torque in the stator reference frame.

The indirect control strategies of PMSG based variable speed wind turbines using a single switch switch-mode rectifier and six switch PWM voltage source converters are presented in the following sections.

4.4 Modelling, Analysis and Control of PMSG Based Variable Speed Wind Turbine with Switch-mode Rectifier

4.4.1 System Structure

Fig. 4.1 shows the system structure of a PMSG based variable speed wind turbine using switch mode rectifier. The system consists of

- Diode bridge rectifier
- Boost dc- dc converter with associated controllers
- DC link capacitor
- Inverter with controllers for grid interface or to supply power to a local load

- Filter
- Coupling transformer
- Grid or local load

As the wind speed changes, the output of the generator varies in amplitude and frequency. The function of the power electronic interface and associated controllers is to produce an output with regulated voltage and frequency to supply power to the grid or local load. The diode rectifier converts the variable output AC voltage to DC voltage and the boost DC to DC converter the rectifier output DC voltage to a higher regulated DC voltage level suitable for the inverter operation. The output of the switch-mode rectifier can be controlled by controlling the duty cycle of the IGBT (insulated gate bipolar transistor) switch at any wind speed to extract maximum power from the wind turbine [80]. The boost DC-DC converter should be designed properly so that the DC link voltage at the inverter input is maintained to a fixed level over the entire operating range of the generator for wind speeds between cut-in speed and rated speed. This will ensure the delivery of maximum captured power to the grid or local load [35]. The vector controlled IGBT inverter is used to interface the wind energy system with the grid. For a standalone system, the inverter is controlled to regulate output voltage and frequency. An energy storage and dump load is used to regulate voltage and frequency in a stand-alone system.

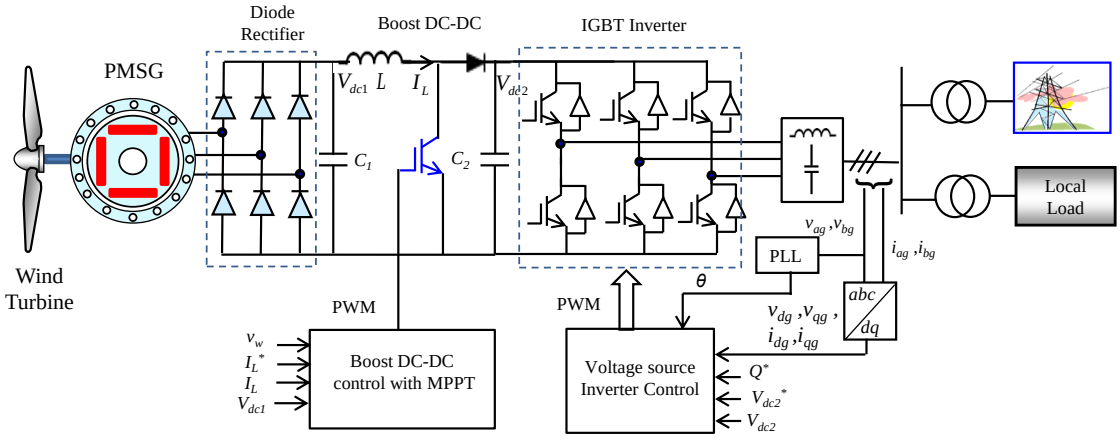

Figure 4.1 PMSG based variable speed wind Turbine with diode rectifier and boost DC-DC converter.

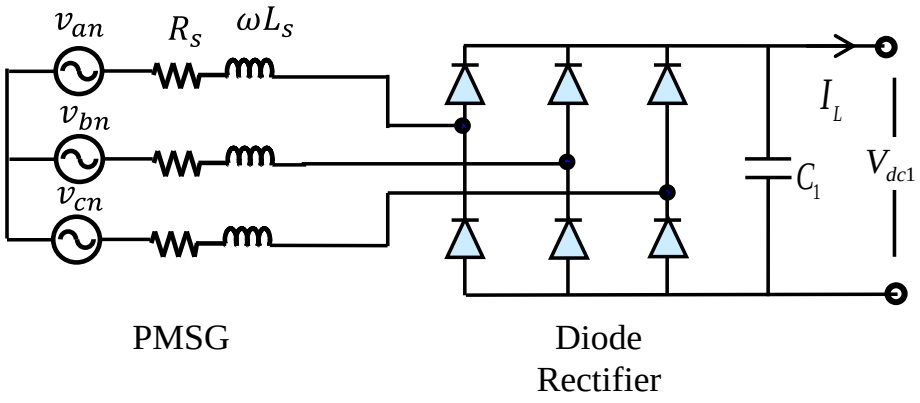

Figure 4.2 PMSG with three phase diode rectifier

4.4.2 Three Phase Diode Rectifier

Figure 4.2 shows the PMSG with a three phase diode rectifier. In Fig.4.2, R_s is the stator resistance L_s is the stator inductance of PMSG. The instantaneous phase voltages of PMSG are given by:

$$v_{an} = V_m \sin(\omega t) \quad (4\text{-}4)$$

$$v_{bn} = V_m \sin(\omega t - 120°) \quad (4\text{-}5)$$

$$v_{cn} = V_m \sin(\omega t - 240°) \quad (4\text{-}6)$$

Where, V_m is the peak value of phase voltage.

As line to line voltage leads the phase voltage by 30^0, the instantaneous line to line generator output voltages are given by:

$$v_{ab} = \sqrt{3}\, V_m \sin(\omega t + 30°) \quad (4\text{-}7)$$

$$v_{bc} = \sqrt{3}\, V_m \sin(\omega t - 90°) \quad (4\text{-}8)$$

$$v_{ca} = \sqrt{3}\, V_m \sin(\omega t - 210°) \quad (4\text{-}9)$$

The rectifier average output voltage V_{dc1} is (neglecting R_s and X_s) [25]:

$$V_{dc1} = \frac{1}{\pi/3} \int_{\pi/3}^{2\pi/3} \sqrt{3}\, V_m sin\omega t\, d\omega t = \frac{3\sqrt{3}V_m}{\pi} = \frac{3V_{m(L-L)}}{\pi} = 1.654\, V_m \quad (4\text{-}10)$$

Where, $V_{m(L-L)} = \sqrt{2}V_{(L-L),rms}$ is the peak line to line voltage of the PMSG output.

The amplitude of ac voltage terms are [81]:

$$V_n = \frac{6V_{m(L-L)}}{\pi(n^2-1)} \qquad where, n = 6,12,18 \ldots\ldots\ldots$$

As the output voltage ripple is periodic with period1/6 of the rectifier input, the harmonics in the output are of order $6 \times k\omega, k = 1,2,3 \ldots\ldots\ldots$.

The Fourier series of the currents in phase a of the ac line is [25]:

$$i_a(t) = \frac{2\sqrt{3}}{\pi} I_0 \left(cos\omega_0 t - \frac{1}{5}cos5\omega_0 t + \frac{1}{7}cos7\omega_0 t - \frac{1}{11}cos11\omega_0 t + \frac{1}{13}cos13\omega_0 t - \cdots\right) \quad (4\text{-}11)$$

where $i_a(t)$ consists of the terms at the fundamental frequency of the ac system and harmonics of order $6k \pm 1$, $k = 1,2,3,\ldots\ldots\ldots$

If the generator inductance L_s is considered as shown in Fig.4.3, the current transfer from one diode to the other occurs gradually over a commutation interval μ. The commutation process causes a voltage drop and reduces the dc output voltage. Considering the generator leakage inductance the rectifier output dc voltage can be given as [81],

$$V_{dc1} = \frac{3V_{m(L-L)}}{\pi}\left(1 - \frac{X_s I_L}{V_{m(L-L)}}\right) \quad (4\text{-}12)$$

The generator leakage inductance L_s lowers the average output voltage of the three phase rectifiers.

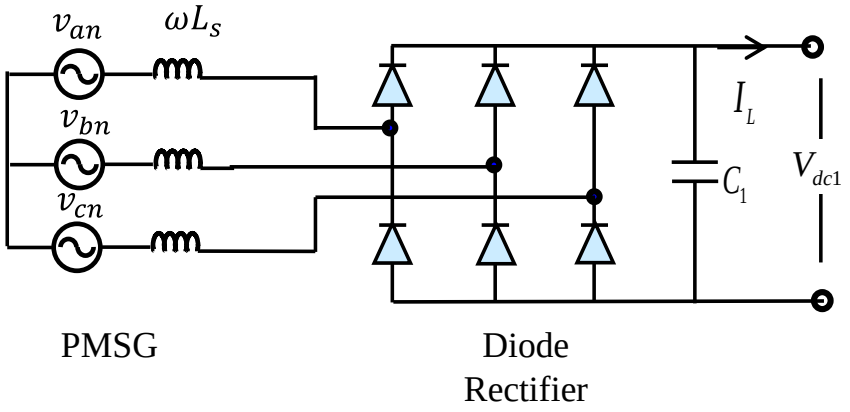

Figure 4.3 PMSG with three phase diode rectifier with generator inductance L_s.

4.4.3 Design of Boost DC-DC Converter

The output of the three phase rectifier is fed to the input of the boost DC-DC converter to step up the DC link voltage (V_{dc2}) to a suitable level for the proper operation of the inverter.Fig.4.4 show the boost dc to dc converter. The boost DC-DC converter is designed in such a way that the DC link voltage which is the input to the inverter is regulated under different wind speeds. The boost dc-dc converter is controlled to extract maximum power under varying wind speed as shown in Fig.4.5.

The output of the boost DC-DC converter is given by [81]:

$$V_{dc2} = \frac{V_{dc1}}{1-D} \tag{4-13}$$

where,

$V_{dc1} = input\ \ voltage\ to\ the\ boost\ DC-DC\ converter$ (V)

$V_{dc2} = output\ \ voltage\ of\ the\ boost\ DC-DC\ converter$ (V)

$D = \frac{T_s}{T_{on}} = duty\ ratio\ of\ the\ switch$

The minimum inductance for continuous conduction of the boost DC-DC converter can be calculated from,

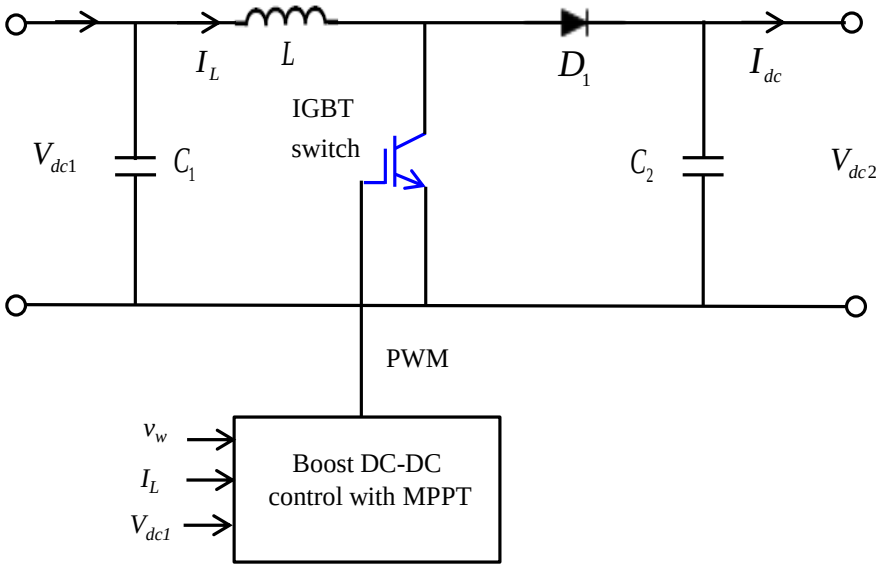

Figure 4.4 Boost Dc-DC converter.

$$L_{min} = \frac{D(1-D)^2}{2f_s} \tag{4-14}$$

where,

$$f_s = \frac{1}{T_s} = switching\ frequency\ (Hz)$$

The inductance value for the boost converter should be higher than this value to ensure continuous conduction.

The output ripple voltage of the boost converter can be written as,

$$\frac{\Delta V_{dc2}}{V_{dc2}} = \frac{DT_s}{RC_2} = \frac{D}{RC_2 f_s} \tag{4-15}$$

and the capacitor C_2 can be calculated as

$$C = \frac{D}{RCf_s \times \frac{\Delta V_o}{V_0}} \tag{4-16}$$

where,

$R = \frac{V_{dc2}}{I_{dc}}$ = output resistance (Ω)

4.4.4 Control of Boost DC-DC Converter with Maximum Power Extraction

To extract optimum power under fluctuating wind speeds, the speed of the generator needs to be regulated by controlling the IGBT switch of the boost DC-DC converter. By regulating the wind turbine rotor speed (or generator speed) optimally, the tip speed ratio (λ) of the turbine can be controlled at the optimum value to obtain maximum C_P under variable wind speed. The optimal wind turbine rotor speed (or generator speed) is proportional to the wind speed. Therefore, the maximum mechanical power is captured by the wind turbine by regulating the generator speed under different wind speeds. Fig.4.5 shows the proposed algorithm for maximum power extraction (MPE) from the variable speed wind turbine. This algorithm requires following steps and inputs:

- Measure wind speed v_w
- Calculate reference speed for maximum power extraction from

  $$\omega_m^* = \frac{\lambda_{opt}}{R} v_\omega = K_\omega v_\omega \tag{4-17}$$

- The speed controller output will give the reference current I_L^*

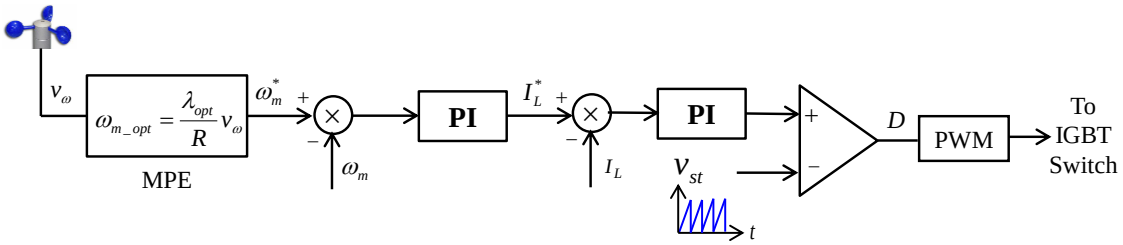

Figure 4.5 Proposed maximum power extraction algorithm under varying wind speed.

- Measure the input inductor current to the boost converter I_L
- The error between reference and measured line currents is passed through proportional-integral (PI) to produce duty cycle, *D*.
- Finally the duty cycle, *D* is used to produce the required PWM pulses for the IGBT switch of the boost DC-DC converter.

4.4.5 Simulation Model

The wind energy conversion system of Fig.4.1 is implemented using dynamic system simulation software *MatlabSimpowerSystem*. The simulation model is developed based on Kollmorgan BH822 IPM synchronous machine. The parameters of the IPM synchronous generator are measured experimentally and are given in Chapter 3 Table 3.3. The power converter and the controllers with maximum power extraction algorithm are also implemented and included in the model. The sampling time used for simulation is 20 μs.

4.4.6 Simulation Results and Discussions

Fig.4.6 shows the performance of generator side switch-mode converter controller with maximum power extraction for variable wind speeds. Fig.4.6 (a) and (b) show the generator speed response and inductor current response, respectively. It is observed that the generator speed and inductor current follow their references quite well and allow the generator to extract maximum power under fluctuating wind speeds. Fig.4.6 (d) to (f) show the turbine torque response, generator electromagnetic torque response and generated power, respectively. Fig. 4.7 shows the expanded view of Fig.4.6 to show the controller performances clearly. Fig.4.8 shows the generated power vs turbine speed

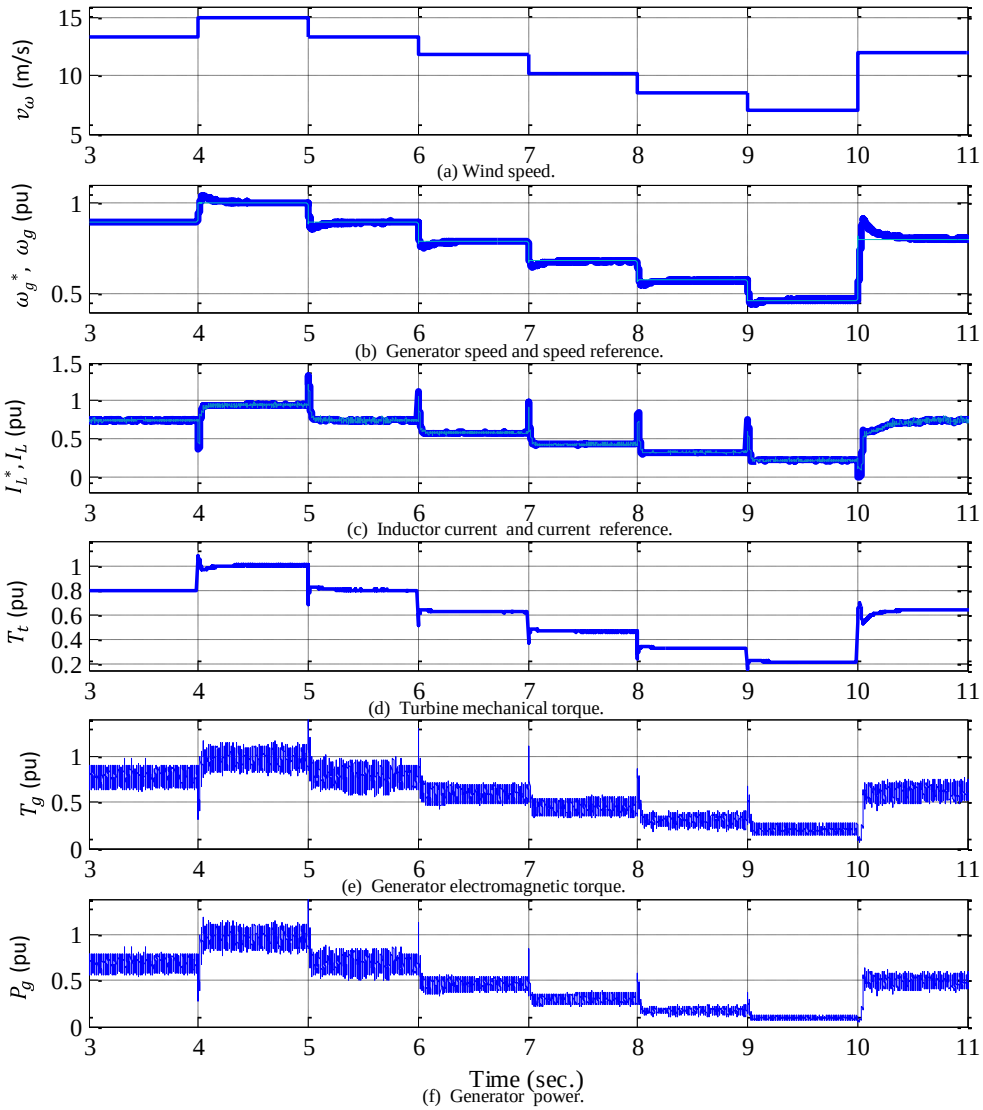

Figure 4.6 Performance of generator side switch-mode converter controller with maximum power extraction.

response. It is seen that the turbine mechanical power follow the optimum powr curve quite well and the generator can extract maximum power under variable wind speeds.

Fig.4.9 show the generator torque, voltage and current responses under steady state at the rated operating conditions. As shown in Fig.4.9 (b) and (c), the generator voltage and current waveforms are distorted due to the nonlinear characteristics of the switch mode rectifier. The generator current waveform contains harmonic which causes torque ripples as shown in Fig.4.9 (a).This is a drawback of diode rectifier based wind energy

conversion system. However, it can operate with a power factor close to unity. Fig.4.9 (d) shows the generator line to line voltage and line current. As expected, the line current is lagging the line voltage by around 30^0.

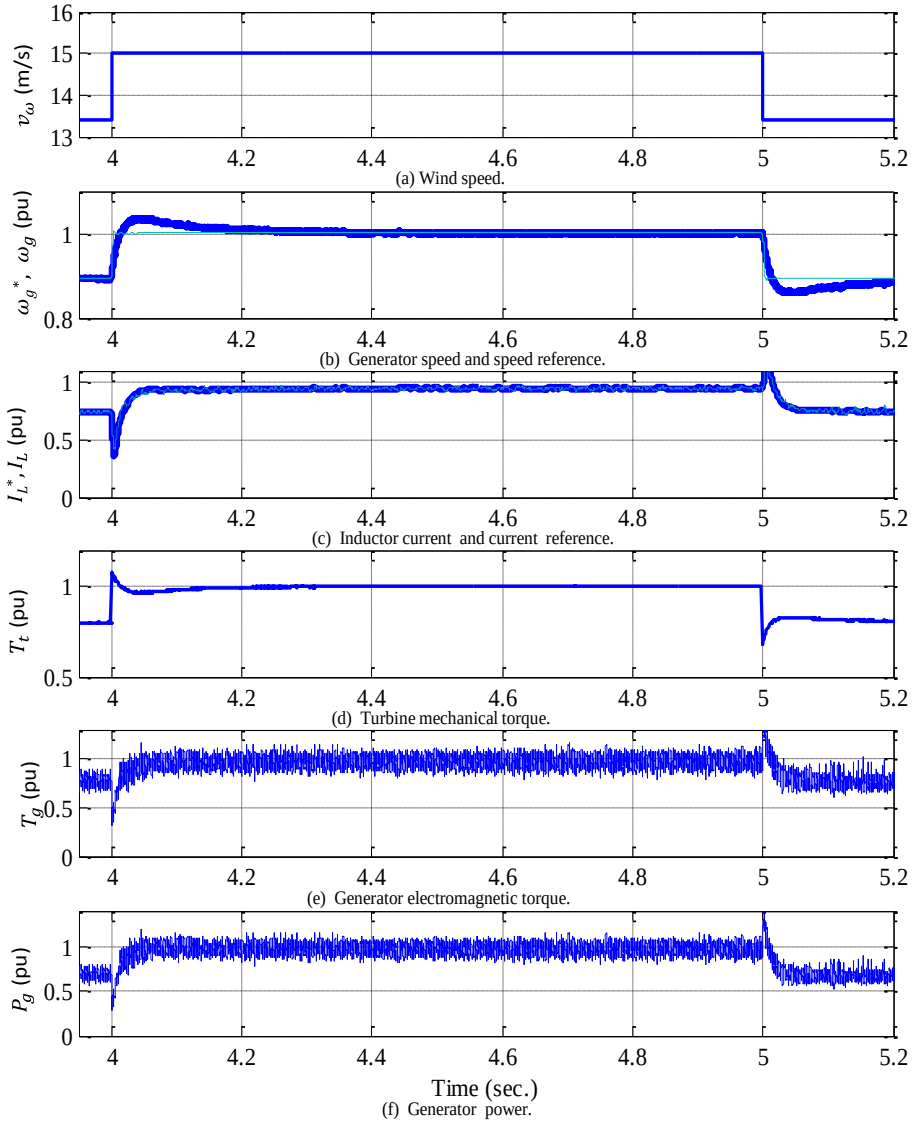

Figure 4.7 Performance of generator side switch-mode converter controller with maximum power extraction (Expanded view).

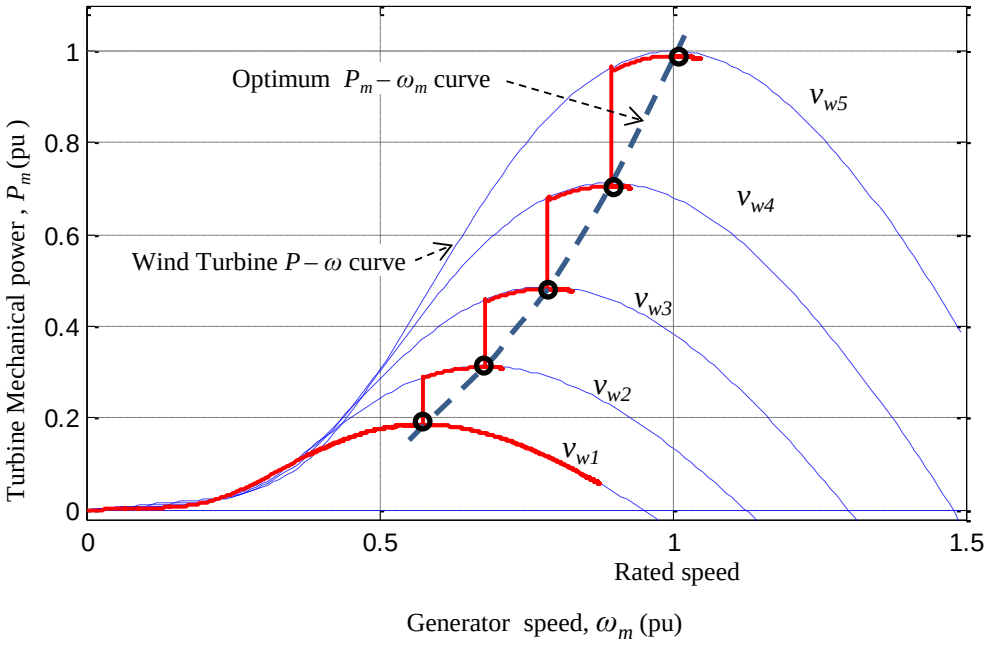

Figure 4.8 Generator power vs turbine speed.

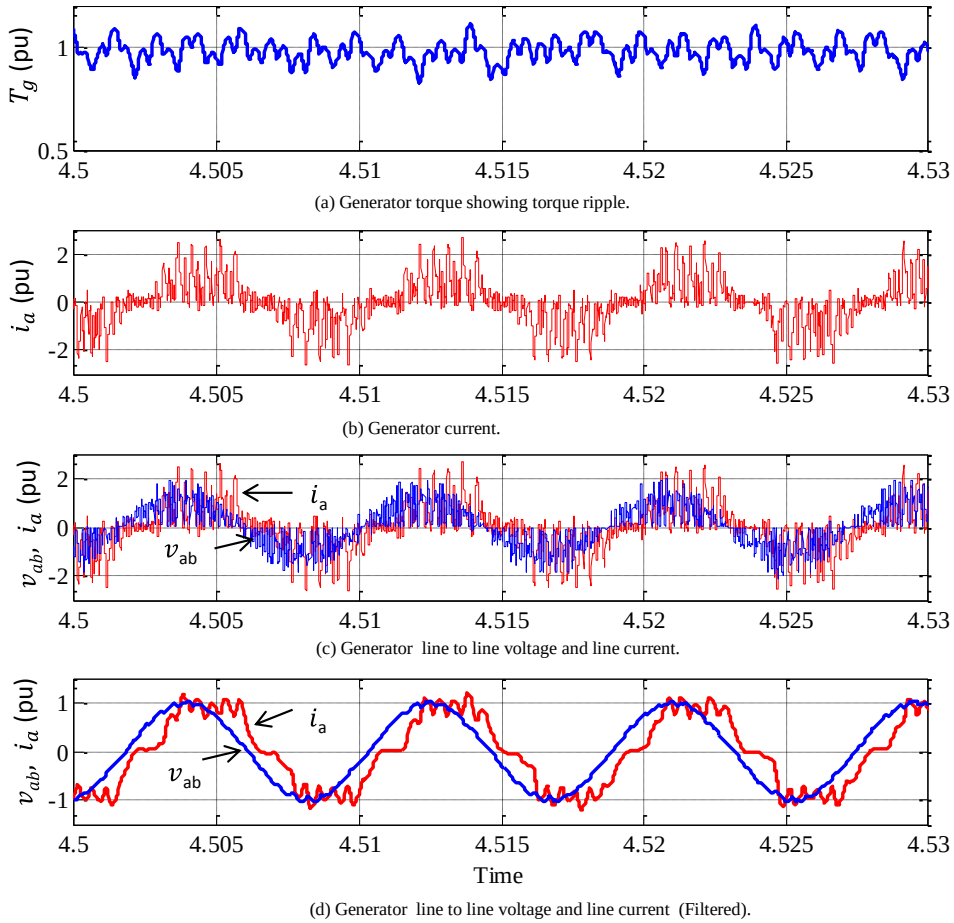

(a) Generator torque showing torque ripple.

(b) Generator current.

(c) Generator line to line voltage and line current.

(d) Generator line to line voltage and line current (Filtered).

Figure 4.9 Generator torque, voltage and current responses at the rated operating conditions.

4.5 Control of PMSG Based Direct Drive Variable Speed Wind Turbine with Back to Back PWM Converter

The control of PMSG based variable speed wind energy conversion system using three phase diode rectifier and boost DC-DC converter as discussed in section 4.5 has advantages of simple structure, low cost, simple controller and close to unity power factor operation. However, it possesses some drawbacks such as harmonics in generator current which introduce torque ripples and affect generator efficiency [15], [16]. Moreover, this type of converter is not suitable for large scale wind turbine applications. In this section, the control of PMSG based wind energy conversion system using back-back PWM converters is presented which has better performance. This topology can solve the problems associated with three phase diode rectifier and boost DC-DC converter based wind energy conversion system. It can provide unity power factor operation (UPF) and low current harmonic content. The PWM converter also provides dc bus voltage boost and regulation and compensates harmonics and reactive power at the point of common coupling of the wind turbines [82].

4.5.1 System Structure

Fig. 4.10 shows the system structure of a PMSG based variable speed wind turbine using back to back PWM converter. The system consists of

- Generator side PWM rectifier with controller
- DC link capacitor
- Grid/load side PWM inverter to supply power to a local load
- Filter
- Coupling transformer to provide isolation between grid and wind turbines
- Grid or local load

The control of this type of wind energy conversion system includes:

- Generator side PWM rectifier control to extract maximum active power available from the wind turbine using maximum power extraction algorithm
- Grid side PWM inverter control with reactive power and dc link voltage controllers.

This type of wind energy conversion system requires full rated converters and processes full power from the generator to the grid/load. The control of grid side

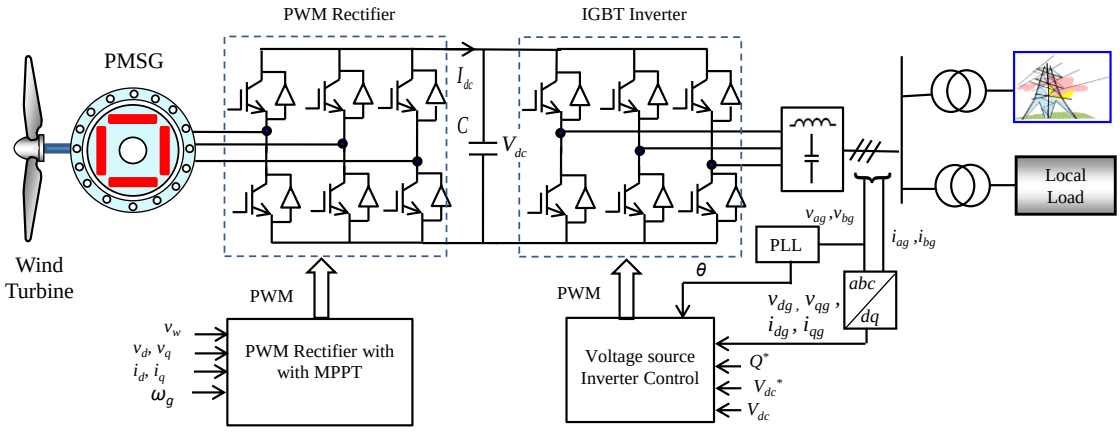

Figure 4.10 PMSG based variable speed wind Turbine with back to back PWM converters.

converter is decoupled from generator side control which facilitates the system design and increases the operating range of the generator [82].

4.5.2 Analysis of PWM Rectifier

Fig.4.11 show the PWM rectifier circuit connected to the PMSG. R_s and L_s represent generator resistance and inductance, respectively. The generator inductor L_s introduces current source characteristics of the input circuit and provide boost feature of the converter [82]. The inductance voltage v_L equals the difference between the generator voltage v_{an} and the converter input voltage v_{con}. The PWM rectifier circuit consists of three legs with IGBT (or GTO thyristor). The analysis of PWM rectifier is presented on a per phase basis as shown in Fig.4.12 [83]. The PWM voltage source converter operates in rectifier mode if the converter voltage $V_{con,A}$ is made to lag the generator voltage V_{an} by an angle δ. This causes the power to flow from generator ac side to the DC link as shown in Fig.4.13.

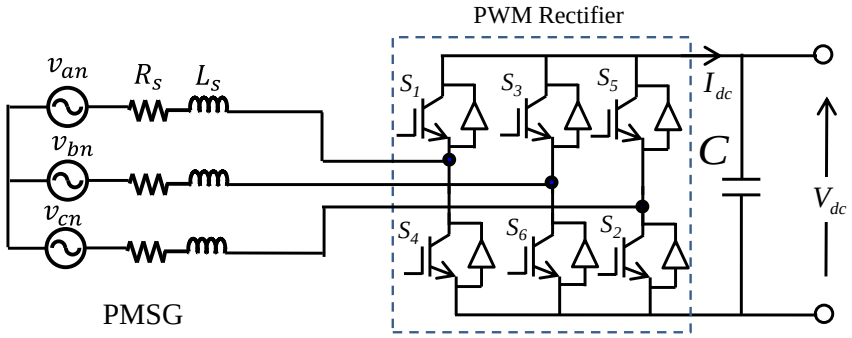

Figure 4.11 PWM rectifier circuit connected to the PMSG.

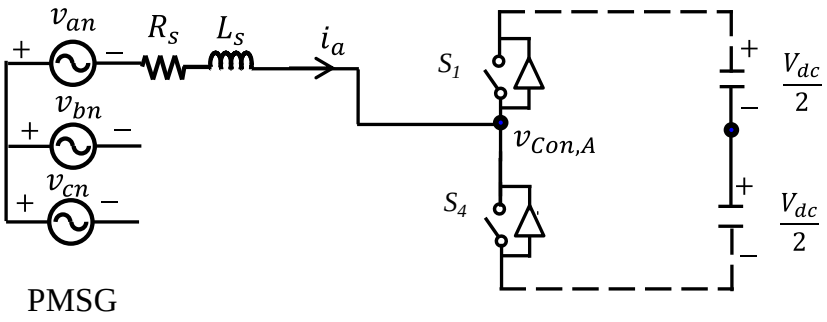

Figure 4.12 Per phase representation of PWM rectifier connected to the PMSG.

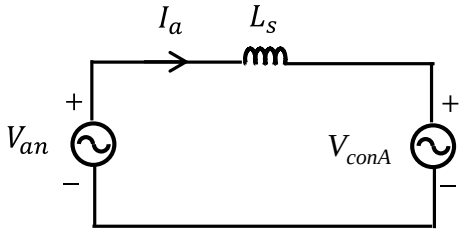

Figure 4.13 Steady state per phase equivalent circuit.

The power transfer from AC side to DC link is given by [27]:

$$P = \frac{V_{an} \times V_{conA}}{X_s} sin\delta \tag{4-18}$$

where,

$V_{an} = rms\ fundamental\ generator\ phase\ \ voltage\ (V)$

$V_{conA} = rms\ fundamental\ converter\ voltage\ (V)$

$\delta = power\ angle\ (deg.)$

The power angle δ can be controlled by controlling the phase displacement of the command sinusoidal waveforms [83]. If the reference voltage is set to lag the fundamental generator voltage V_{an} by the fundamental component of $V_{con,A}$, then it will lag the generator fundamental voltage by the same angle. The condition for power transfer from the generator AC side to DC link is stated by equation (4-18). The amplitude modulation index m_a determines the magnitude of converter voltage V_{conA} [83].

Neglecting stator resistance and using Fig.4.13, we get

$$V_{an} = V_{conA} + I_a R_s + I_a jX_s = V_{conA} + I_a jX_s = |V_{an}| \angle \delta \tag{4-19}$$

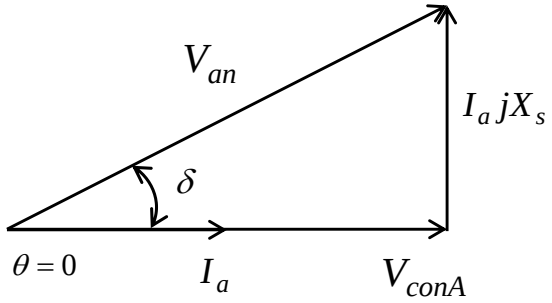

Figure 4.14 Phasor diagram of the PWM rectifier at unity power factor.

Fig.4.14 shows the phase diagram which explains the rectifier mode of operation of the PWM voltage source converter. The input power factor angle θ of the PWM rectifier can also be controlled by controlling the power angle, δ. The converter voltage is given by

$$V_{conA} = V_{an} - I_a jX_s \tag{4-20}$$

The rms fundamental component of the converter voltage at the AC input terminal is $V_{conA,1}$ depends on the values of generator voltage (V_{an}), current (I_a) and reactance (X_s). The value of fundamental converter voltage $V_{conA,1}$ can be determined for a given generator voltage, generator current, power factor and reactance. The amplitude of dc link voltage is determined by the modulation index m_a and $V_{conA,1}$ [83]. The amplitude of V_{dc} is given by [83]:

$$V_{dc} = 2\sqrt{2}\frac{V_{conA}}{m_a} \tag{4-20}$$

$$\text{Or} \quad V_{dc} = \frac{2\sqrt{2}}{\sqrt{3}}\frac{V_{conAB}}{m_a} \tag{4-21}$$

Where,

V_{conA} = *rms fundamental converter voltage (V)*

V_{conAB} = *rms line to line fundamental converter voltage (V)*

The switches of the PWM rectifier should be rated at least at the DC link voltage. The frequency modulation ratio m_f is defined as the ratio of the frequency of the carrier signal and reference (control) signal is given by

$$m_f = \frac{f_{carrier}}{f_{reference}} = \frac{f_{tri}}{f_{sine}} = \frac{f_s}{f_1} = \frac{\text{frequency of triangular waveform}}{\text{frequency of control signal}} \quad (4\text{-}22)$$

Increasing the carrier frequency (increasing m_f) increases the frequencies at which the harmonic occur. The harmonic content of the current and voltage is less with higher switching frequency. However, the high switching frequencies causes higher losses in the switches used to implement the converter [81]. Therefore, a trade-off needs to be made between the switching frequency and harmonic content for the converter.

4.5.3 Control of Generator Side PWM Rectifier with Maximum Power Extraction

The main purpose of the IPM synchronous generator side converter controllers is to extract maximum power under variable wind speeds and to limit the peak absorbed power for the safe operation of the wind turbine under varying wind speeds. Fig.4.15 shows the control structure of the generator side PWM rectifier with maximum power extraction under varying wind speeds.

4.5.3.1 The Proposed Maximum Power Extraction Algorithm

The mechanical turbine power vs turbine speed is shown in Fig.4.16. The optimum power curve is also shown in Fig.4.16. There is a matching turbine speed that produces maximum power under variable wind speeds. The purpose of the controller is to operate the turbine on this curve by regulating the generator speed at different wind speeds to extract maximum power. If the wind turbine generator speed is controlled using the reference generator speed which properly follow the change in wind speed, the wind turbine will extract maximum power at any wind speed in the operating region.

The proposed control algorithm for the generator side PWM rectifier with maximum power extraction involves following steps and inputs:

- Measure wind speed v_w
- Determine the generator speed reference

  The expression for optimum power is given by equation (2-7) which is re-written below for convenience as

$$P_{m\_opt} = 0.5\rho\, AC_{p\_opt}\left(\frac{\omega_{m\_opt}\times R}{\lambda_{opt}}\right)^3 = K_{opt}\left(\omega_{m\_opt}\right)^3 \tag{4-23}$$

where, $K_{opt} = 0.5\rho\, AC_{p\_opt}\left(\frac{R}{\lambda_{opt}}\right)^3$ and $\omega_{m\_opt} = \frac{\lambda_{opt}}{R} v_w = K_w v_w$

Therefore, the generator speed reference is

$$\omega_m^* = \frac{\lambda_{opt}}{R} v_\omega = K_\omega v_\omega \tag{4-24}$$

- Measure the generator speed using speed sensor.
- The error between reference generator speed and measured speed is: $e_\omega = \omega_m^* - \omega_m$.

This error is the input to the PI controller and the PI controller output will give the torque reference T_g^*. The generator is controlled by controlling *d*- and *q-axes* current using maximum torque per ampere control (MTPA), which is discussed in sub-section 4.6.3.2.

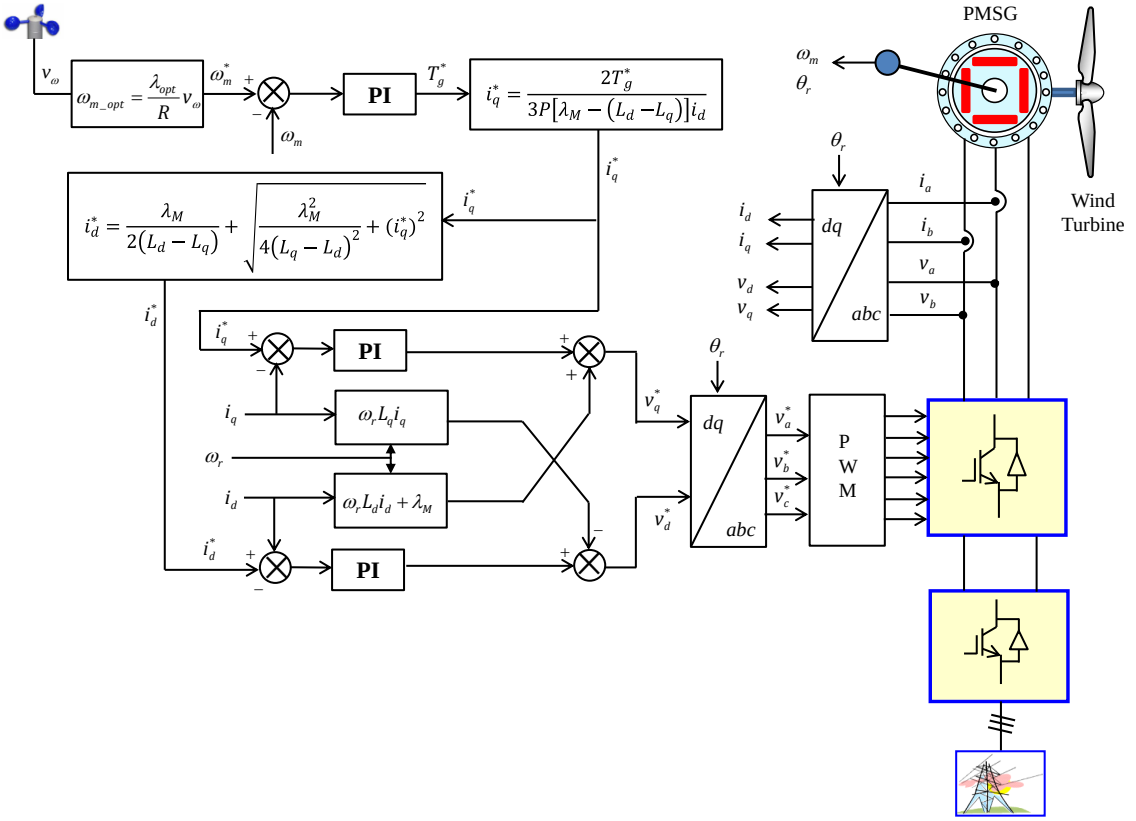

Figure 4.15 Control of Generator side converter with MTPA and maximum power extraction.

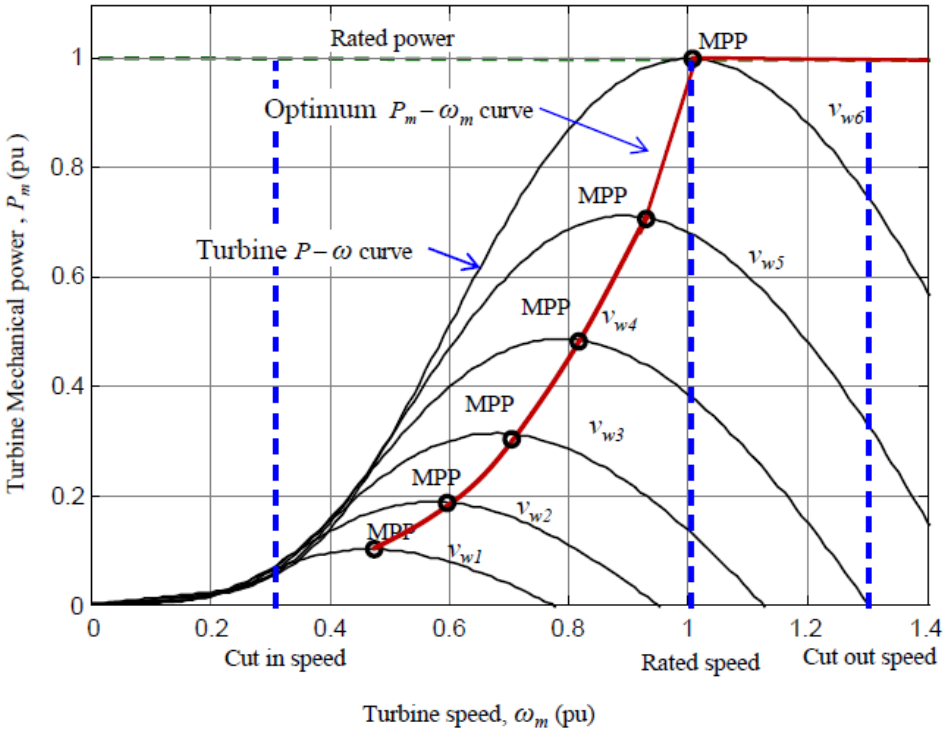

Figure 4.16. Mechanical turbine power vs wind speeds.

4.5.3.2 Control of PMSG with Maximum Torque Per Ampere (MTPA) Control

The *d*- and *q*- axes voltages of PMSG are given by equations (3-22) and (2-23), which are re-written below for convenience,

$$v_d = -i_d R_s - \omega_r \lambda_q + p\lambda_d \tag{4-25}$$

$$v_q = -i_q R_s + \omega_r \lambda_d + p\lambda_q \tag{4-26}$$

The *d*- and *q*-axes stator flux linkages can be written as

$$\lambda_d = -L_d i_d + \lambda_M \tag{4-27}$$

$$\lambda_q = -L_q i_q \tag{4-28}$$

The maximum torque per ampere control produces a given torque with a minimum stator current [26]. The IPM synchronous generator torque is given by [35]:

$$T_g = \frac{3}{2} P\left(\lambda_d i_q - \lambda_q i_d\right) = -\frac{3}{2} P[\lambda_M i_q + \left(L_d - L_q\right) i_d i_q] \tag{4-29}$$

where, λ_d ,λ_q - *d*- and *q*- axes stator flux linkages.

i_d, i_q, L_d and L_q are the *d*- and *q*- axes, currents and inductances respectively.

λ_M - permanent magnet flux linkage.

ω_r - the electrical rotor speed in rad/sec,

p - the operator d/dt

P- *number of* pole pairs

The torque equation in (4-29) consists of two terms. The first term is the excitation torque and the second term is the reluctance torque. The excitation torque is produced by the interaction of the magnet flux linkage and q- axis current. It does not depend on i_d. The reluctance torque is proportional to the product of i_d and i_q and to the difference of *d*-axis and *q*-axis inductances.. For an IPM synchronous generator, higher torque can be generated if the difference in inductance (L_d - L_q) is larger. This is an important feature of an IPM synchronous generator.

The IPM synchronous generator current is given by

$$\bar{i}_s = i_d + ji_q \tag{4-30}$$

and

$$i_s = \sqrt{i_d^2 + i_q^2} \tag{4-31}$$

from which, we get

$$i_d = \sqrt{i_s^2 - i_q^2} \tag{4-32}$$

Substituting equation (4-32) in equation (4-29), we get

$$T_g = \frac{3}{2} P[\lambda_M i_q + (L_d - L_q)(\sqrt{i_s^2 - i_q^2}) i_q] \tag{4-33}$$

To find the maximum torque per ampere, we can differentiate equation (4-33) and set the derivative equal to zero. We get

$$\frac{i_q^2}{i_d}(L_d - L_q) = -\lambda_M + (L_d - L_q) i_d \tag{4-34}$$

From which, we get

$$i_d = \frac{\lambda_M}{2(L_d - L_q)} \pm \sqrt{\frac{\lambda_M^2}{4(L_q - L_d)^2} + i_q^2} \qquad \text{where, } L_d \neq L_q \tag{4-35}$$

For a given generator torque and magnet flux linkage, the *d*- and *q*-axes stator currents for the MTPA scheme can be obtained by solving equation (4-29) and (4-35). Therefore, for an IPM synchronous generator, the *d*- and *q*-axis current references are given by

$$i_q^* = \frac{2T_g^*}{3P[\lambda_M - (L_d - L_q)]i_d} \tag{4-36}$$

$$i_d^* = \frac{\lambda_M}{2(L_d - L_q)} + \sqrt{\frac{\lambda_M^2}{4(L_q - L_d)^2} + (i_q^*)^2} \tag{4-37}$$

Where i_d is the measured *d*-axis stator current, T_g^* is generated by the speed controller output.

The space vector diagram of the generator with MTPA control is given in Fig.4.17 [35], where δ is the angle of the stator current vector with respect to the *q*-axis, given by [35]:

$$\delta = \tan^{-1}\frac{i_d}{i_q} = \frac{\pi}{2} - \theta_i \qquad \text{for } 0 \le \theta_i \le \pi/2 \tag{4-38}$$

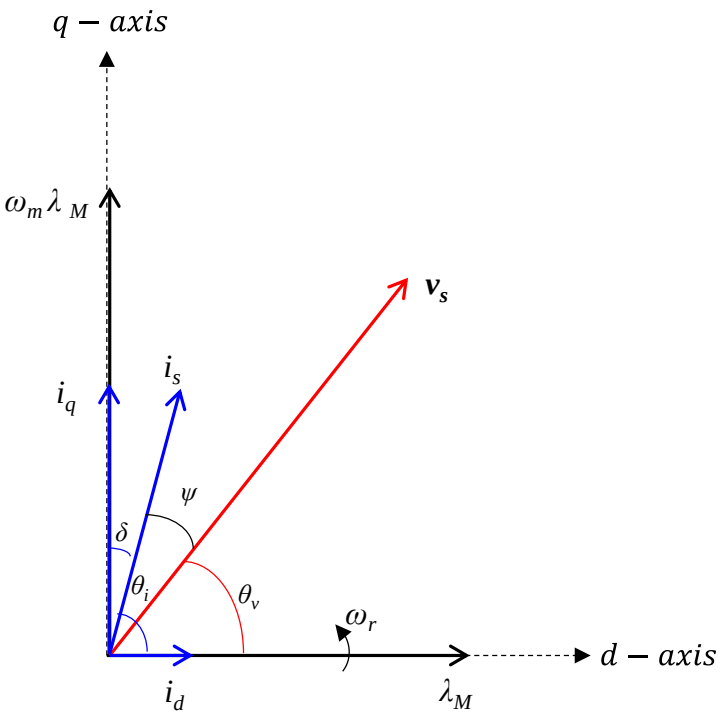

(a) Space vector diagram.

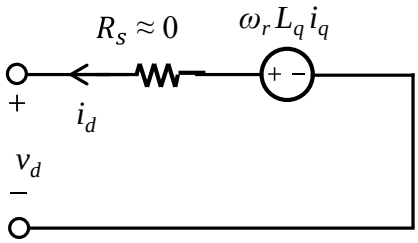

(b) *d*-axis current .

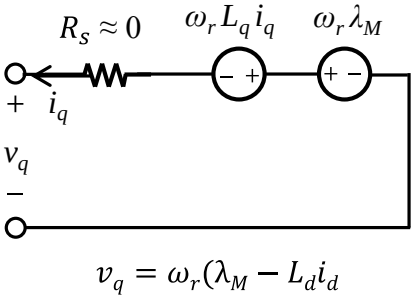

(c) *q*-axis current.

Figure 4.17 Space vector diagram of IPM synchronous generator with maximum torque per ampere control.

Fig.4.18 shows trajectory of generator torque (0.8 pu) with different values of stator *dq*-axes rms currents [35]. As shown in Fig.4.18, the stator rms current I_s reaches its lowest value (0.85 pu) at I_d of 0.44 pu. The MTPA operation is achieved at the point *Q*.

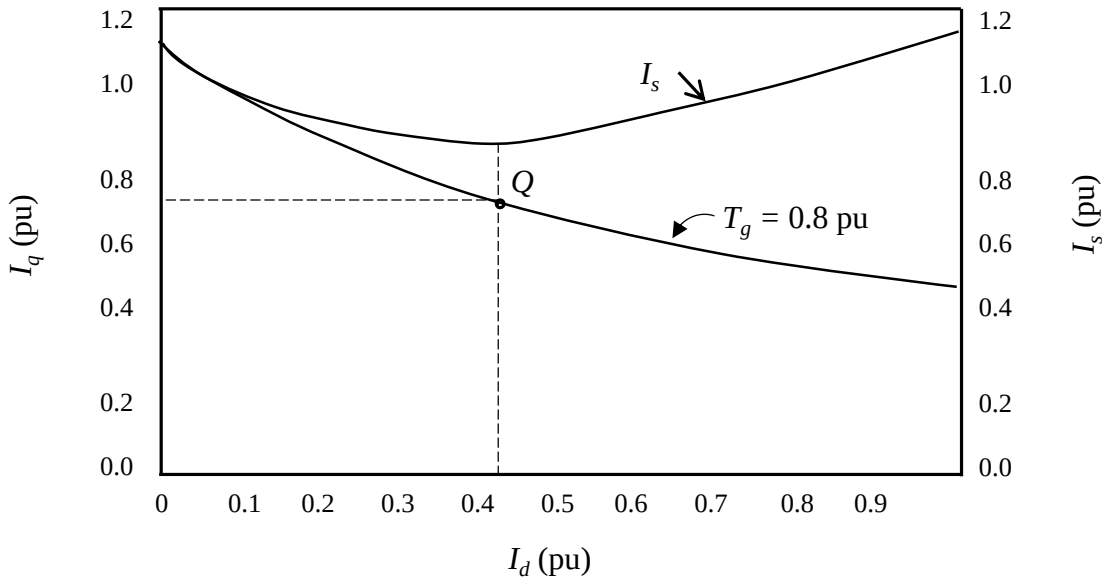

Figure 4.18 Trajectory of stator current at T_g = 0.8 pu.

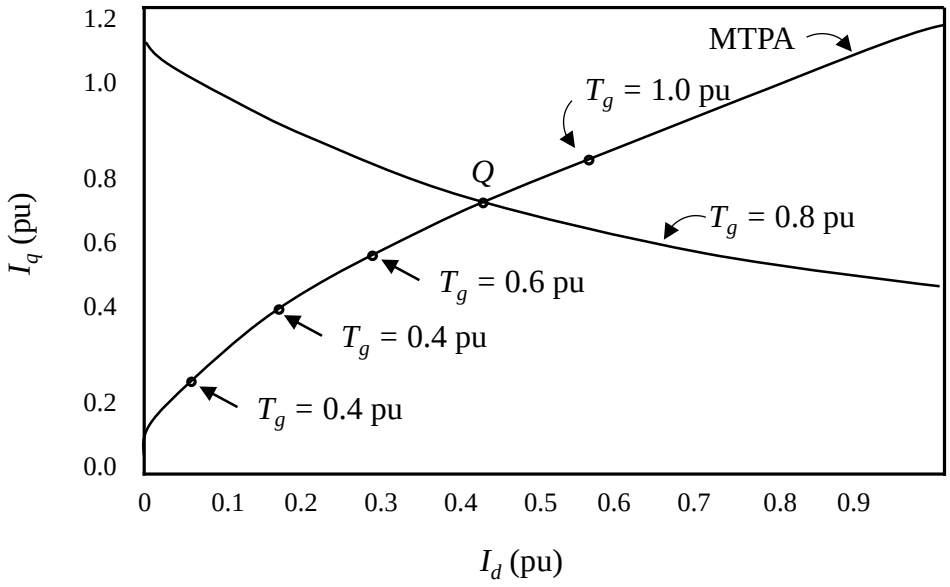

Figure 4.19 Trajectory of maximum torque per ampere control.

Fig.4.19 shows the trajectory of the generator torque produced by the MTPA control scheme [35]. The MTPA trajectory intersects with the 0.8 pu torque at point *Q*, where the torque is produced with a minimum stator current. The main feature of the MTPA control method is that it can produce a given torque with a minimum generator current [35]. It ensures maximum utilization of the stator current and minimizes the stator losses [35].

4.5.3.3 Simulation Model

The wind energy conversion system of Fig.4.10 is implemented using *Matlab/SimPowerSystems.* The generator side converter with MTPA control with maximum power extraction as shown in Fig.4.15, is implemented. The IPM synchronous generator data used for the simulation is given in Chapter 3 Table 3.3. The sampling times for the torque and speed control loops are 20 µs and 100 µs, respectively. The *Matlab/SimPowerSystems* wind turbine model is used in this work. The input to the wind turbine model is wind speed and the output is torque.

4.5.3.4 Simulation Results and Discussions

Fig.4.20 shows the performance of MTPA controller for generator side PWM rectifier with maximum power extraction under varying wind speed. The reference speed and actual speed are shown in Fig.4.20 (b). It is seen that the generator speed follows its reference quite well and allow the generator to extract maximum power under fluctuating wind speeds. The d- and q-axes currents together with their references are shown in Fig.4.20(c) and Fig.4.20 (d), respectively for the wind speed shown in Fig.4.20 (a). It is observed that *d-axis* and *q*-axis currents follow their respective references well and regulate the generator current under different wind speeds. The modulation index of the PWM rectifier is shown in Fig.4.20 (e). Fig. 4.21 shows the expanded view of Fig. 4.20 to show the controller performances clearly. Fig. 4.22(a) to (c) show the generator electromagnetic torques, turbine mechanical torque and generator power responses, respectively.

Fig.4.23 (a) to (c) shows response at rated operating condition for generator torque, current, line voltage, respectively. It is noted that vector control with MTPA improves the performance of the system compared to switch-mode rectifier (diode rectifier + boost dc to dc converter) as shown in Fig.4.9. The ripples in torque, current and voltage are reduced significantly and improved the total harmonic distortion. Fig.4.24 shows the locus of generator stator current vector under MTPA control. It is observed that the stator current vector moves along the MTPA trajectory to extract maximum power at variable wind speeds.

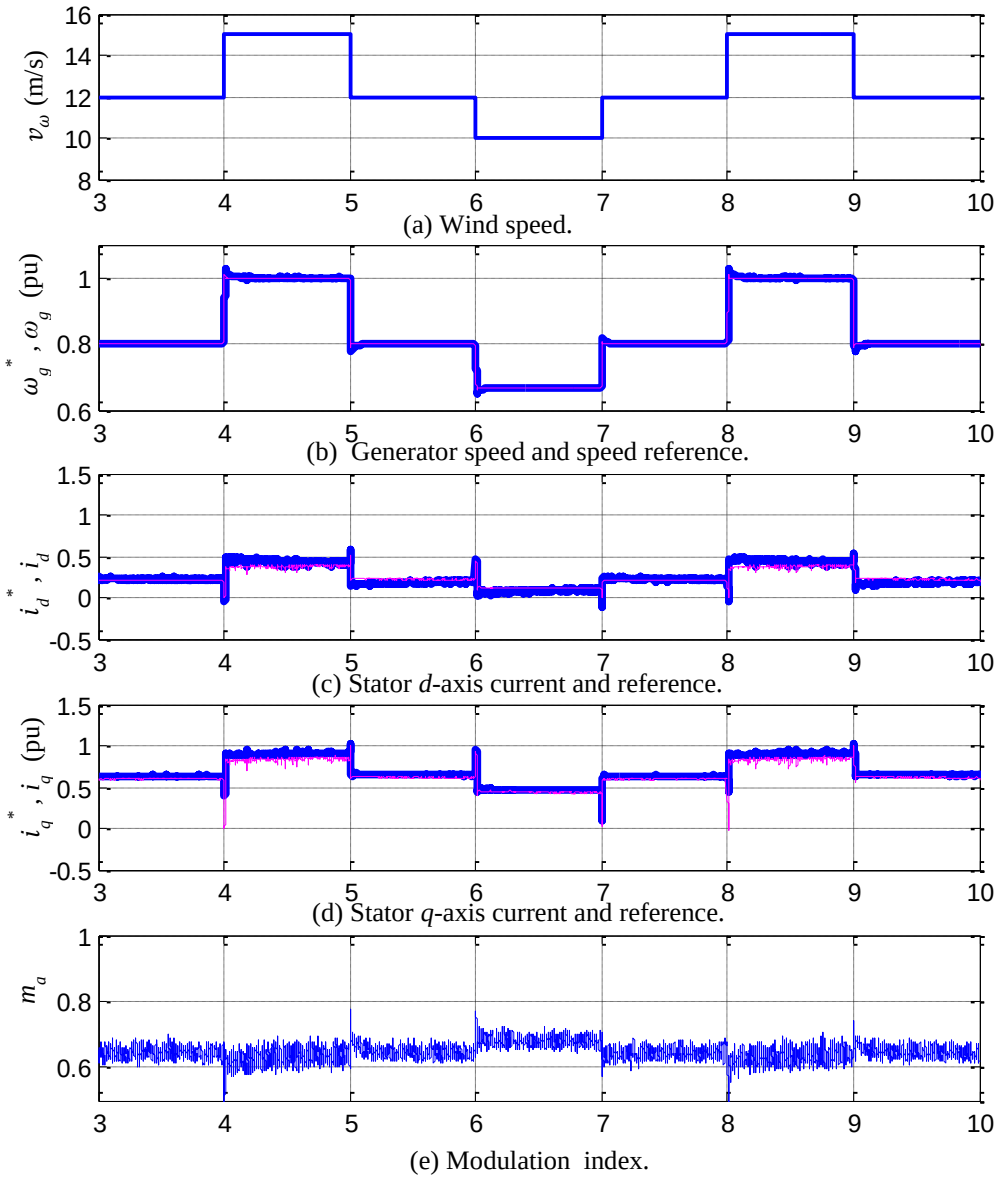

Figure 4.20 Performance of MTPA controller for generator side PWM rectifier with maximum power extraction under varying wind speed.

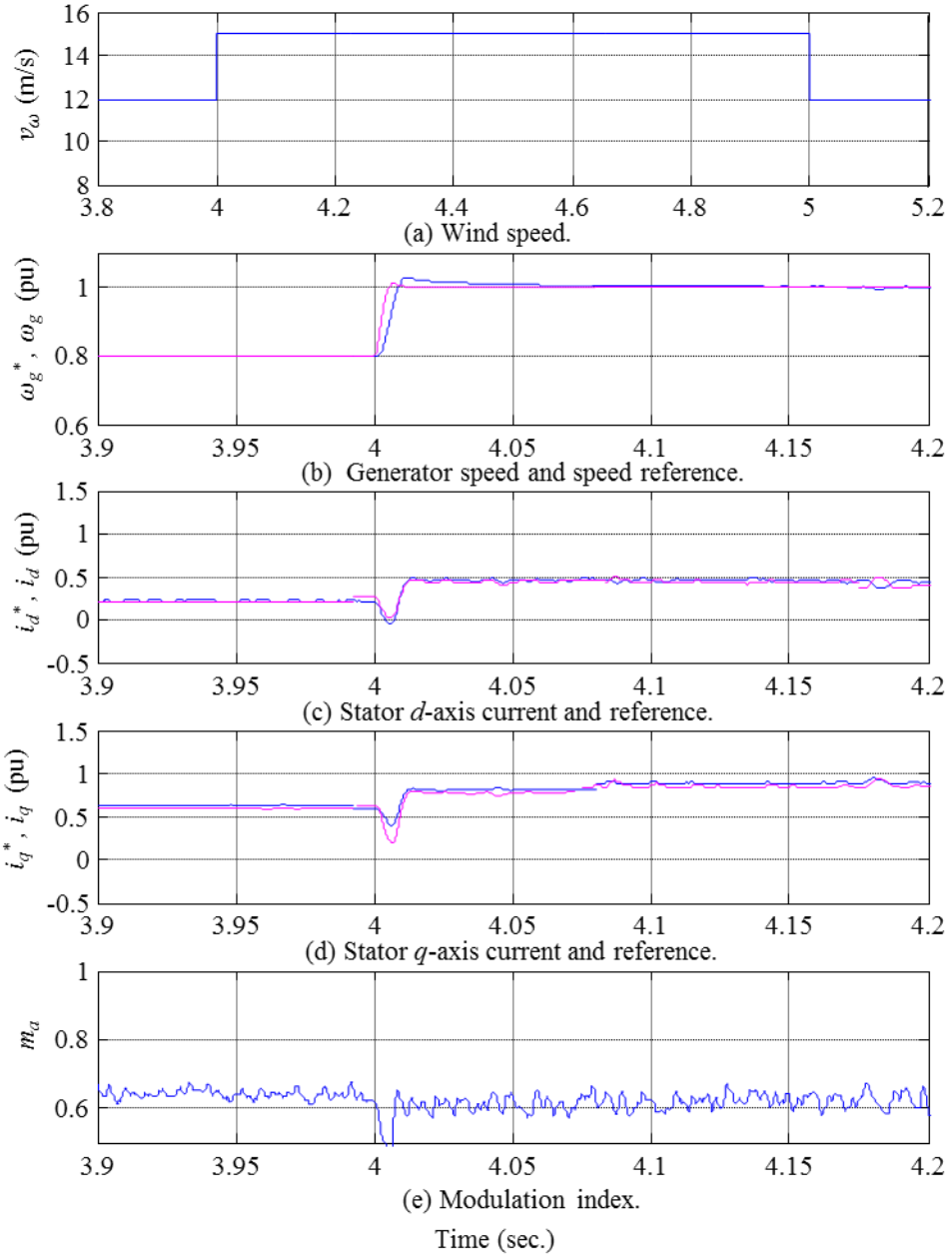

Figure 4.21 Performance of MTPA controller for generator side PWM rectifier with maximum power extraction under varying wind speed. (Expanded view).

.

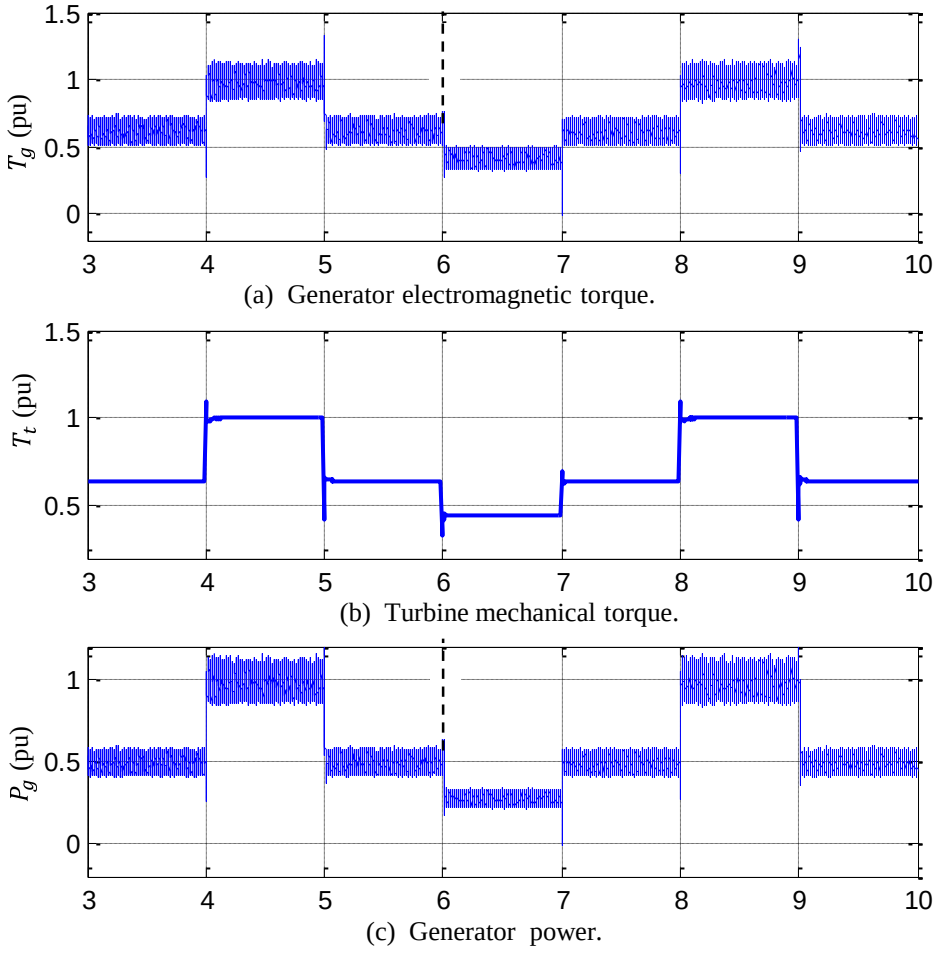

Figure 4.22 Generator electromagnetic torque, turbine mechanical torque and generator power responses under varying wind speed.

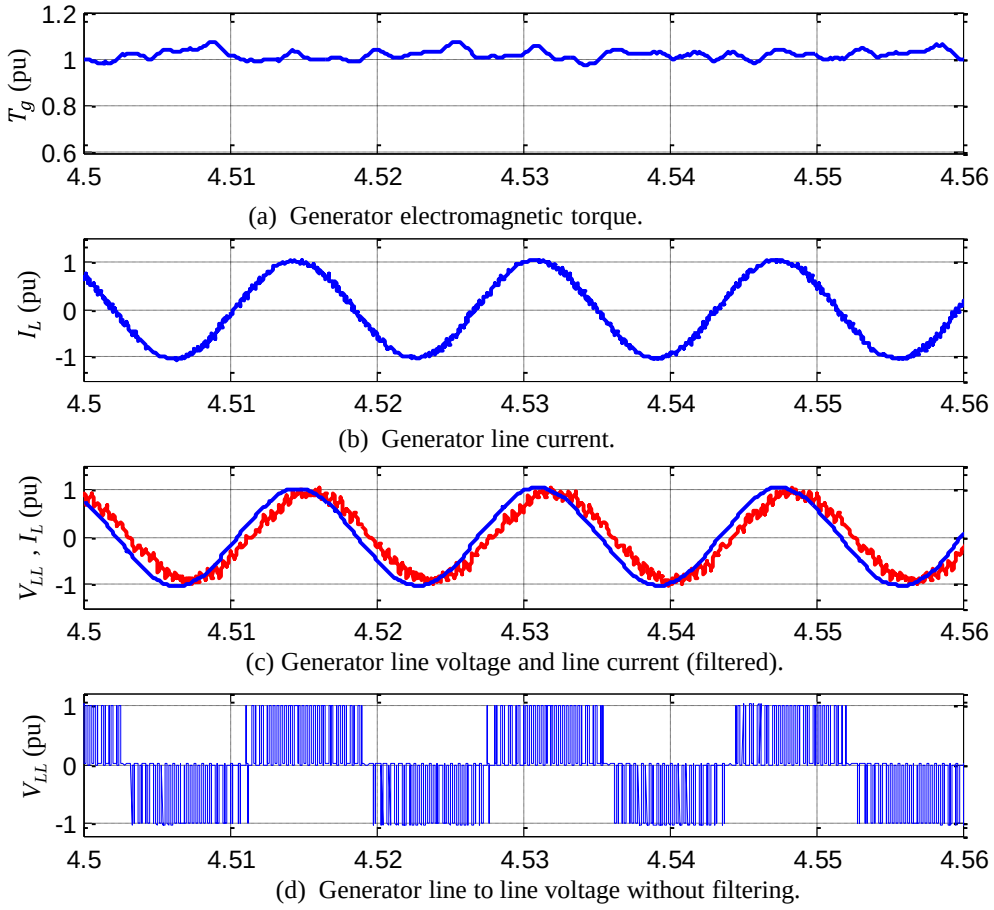

Figure 4.23 Generator voltages, current and torque responses at rated operating condition.

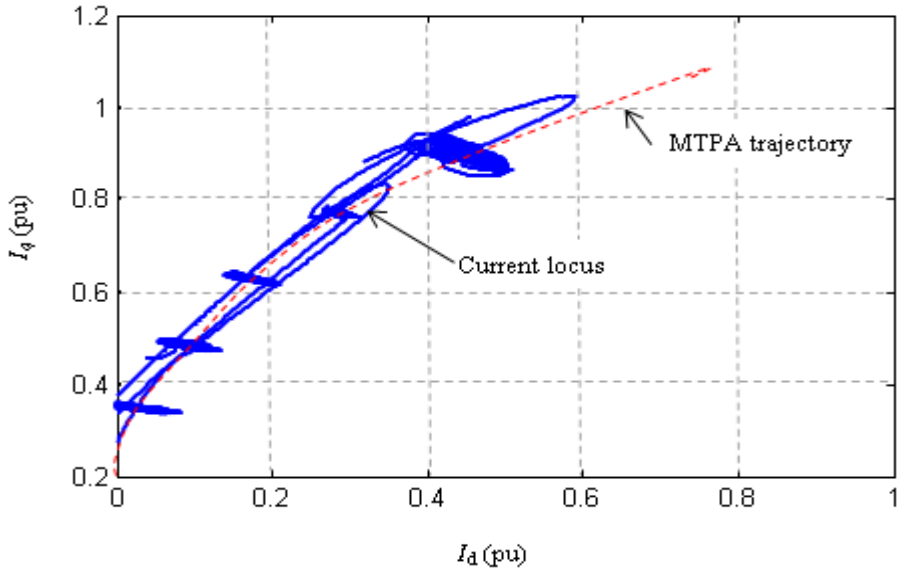

Figure 4.24 Locus of generator stator current vector under MTPA control.

Fig.4.25(a) shows the transient responses of generator speed and power and Fig.4.25(b) shows the generator electromagnetic torque and turbine mechanical torque, respectively. During 3.99 < t < 4.0 sec, the wind turbine generator operates in steady state. At t = 4 sec, the wind speed is increased to the rated value. The turbine mechanical torque increased to rated value instantly, however, the generator speed increases to rated value gradually due to rotor inertia. The difference between the turbine mechanical torque (T_m) and the generator electromagnetic torque (T_g) causes the generator to accelerate and the rotor speed increases accordingly. Finally, the wind turbine generator reaches its steady state rated value.

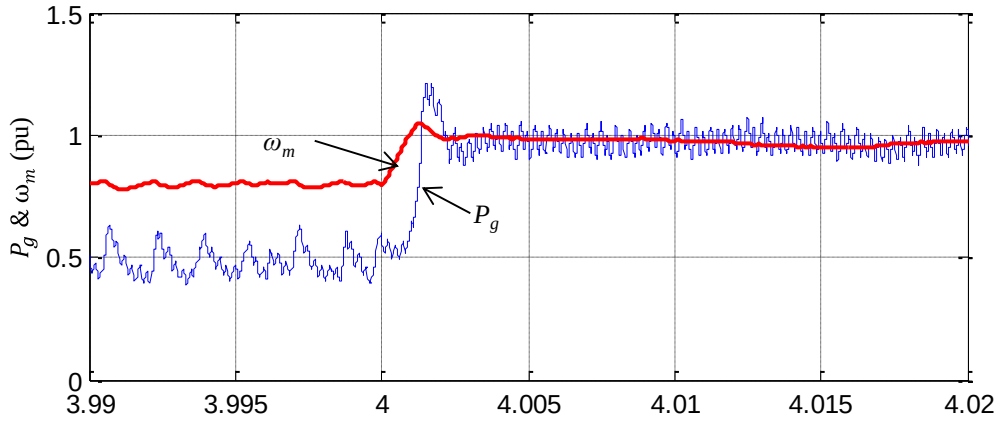

(a) Transient response of generator speed and power.

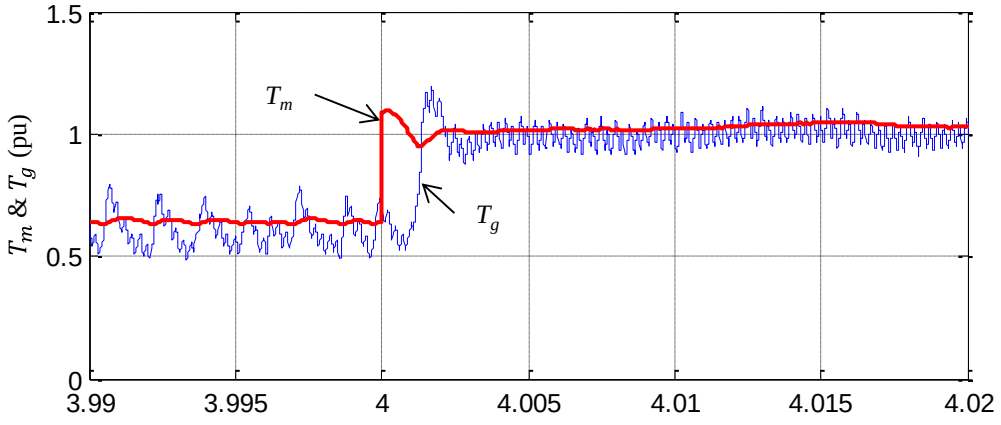

(b) Transient response of turbine mechanical torque and generator electromagnetic torque.

Time (sec.)

Figure 4.25 Transient responses of generate speed, generate power, turbine torque and generator torque when wind speed increased to rated value at t = 4 sec.

Fig. 4.26 shows a comparison of torque responses between vector control with MTPA trajectory using PWM rectifier and switch-mode rectifier. The switch mode rectifier consists of diode rectifiers and a boost dc to dc converter. Fig. 4.26(a) clearly shows that torque ripple is less with vector control with MTPA trajectory than that with the switch-mode rectifier as shown in Fig. 4.26(b).

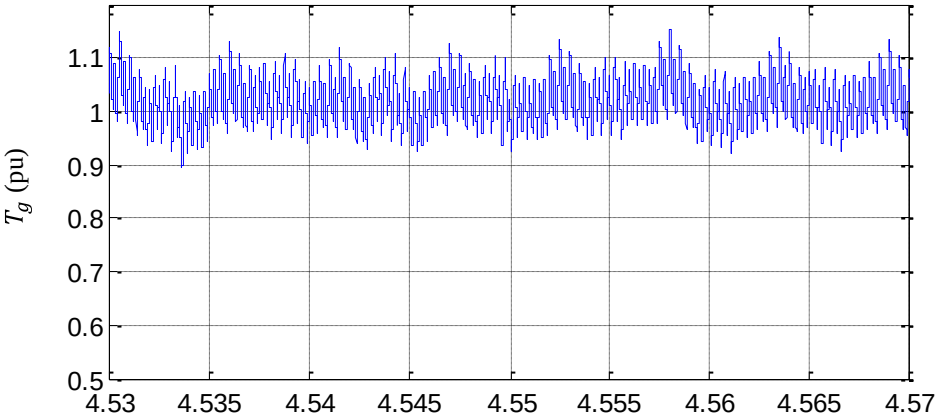

(a) Torque response under Vector control with MTPA using PWM rectifier.

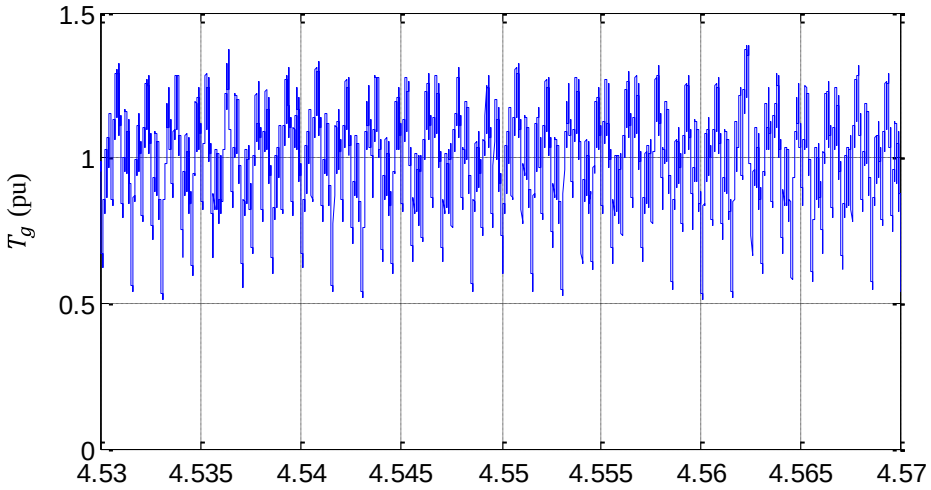

(b) Torque response with switch-mode rectifier (with diode rectifier and boost dc to dc converter).

Time (sec.)

Figure 4.26 Comparison of torque responses under vector control with PWM rectifier and switch-mode rectifier.

Fig.4.27 shows the maximum power extraction under varying wind speed. The difference between the turbine torque T_m and generator torque T_g determines the acceleration and deceleration of the wind turbine generator. The accelerating torque is the difference between the turbine mechanical torque and the torque given by the optimum curve. Consider Fig.4.27, the wind turbine generator is operating at point 'a' and the wind speed is increased from v_{w3} to v_{w4} (point b). The difference in torque between T_m and T_g causes the wind turbine generator to accelerate. Finally, the generator reaches the operating point 'c' where the accelerating torque is zero. A similar situation occurs when the wind speed is reduced to a lower value. Therefore the wind turbine generator will extract maximum power by regulating the generator speed at varying wind speeds.

Fig.4.28 shows the comparison of maximum power extraction using switch-mode rectifier (blue) and PWM rectifier with MTPA control (red). The performance of MTPA control is slightly better than switch-mode rectifier based converter.

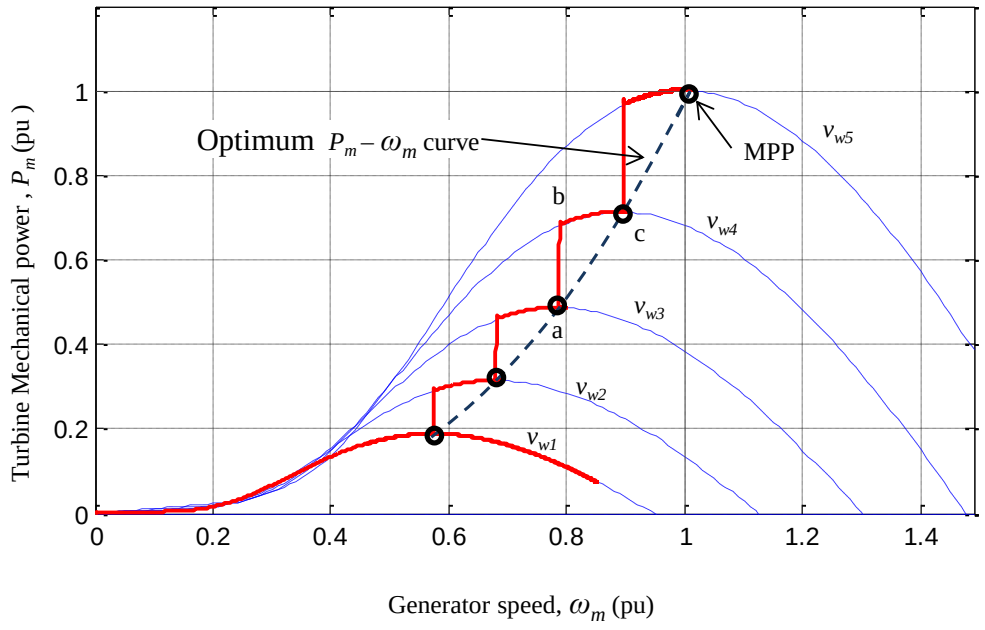

Figure 4.27 Maximum power extraction under varying wind speed (mechanical power vs generator speed).

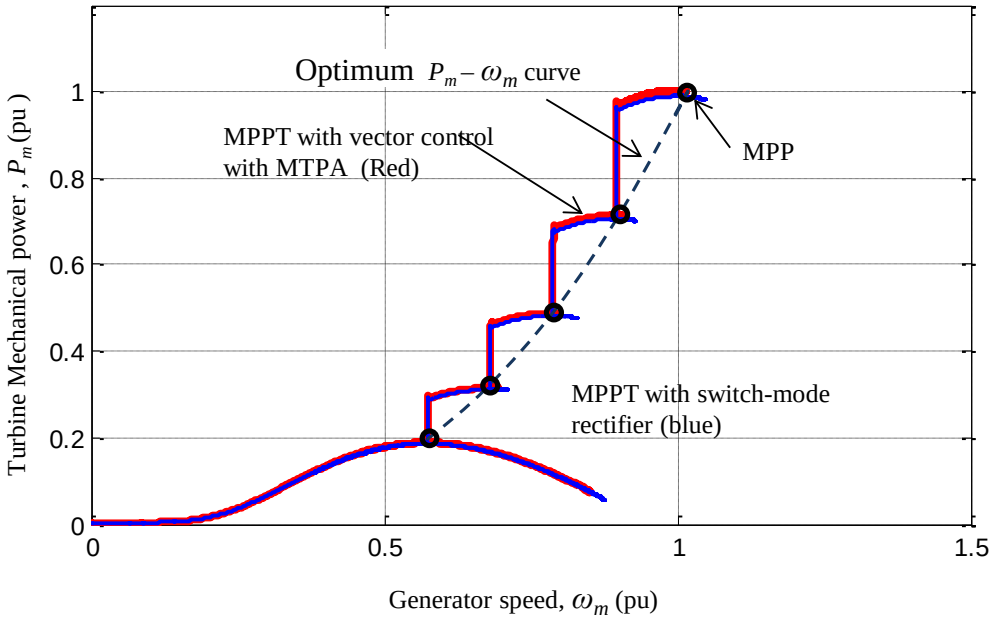

Figure 4.28 Comparison of Maximum power extractions under two control methods.

4.6 Control of Inverter in Grid Connected Mode

The function of the grid side inverter is to interface the wind turbine generator with the grid and control the active/reactive power flow to the grid. Fig.4.29 shows a grid connected wind energy conversion system with a voltage source inverter with the controllers. There are different control strategies which are used to control the grid side converter. They all are focused on the same objectives, which are; control of the DC-link voltage, control of active/reactive power supplied to the grid, grid synchronization to ensure reliable operation of the system [35],[84]. Fig.28 (b) shows the vector control scheme of the grid side PWM inverter. The control strategy consists of two control loops. The inner loop controls the grid current and the outer loop controls the dc link voltage and the reactive power The outer loops regulate the power flow of the system by controlling the active and reactive power injected to the grid [35],[84].

4.6.1 Vector Control of Grid Side Inverter with Decoupled Current Controller

The grid side inverter can be modulated using the PWM scheme and inverter output voltage is given by [35], the average dc input voltage to the inverter is given by,

$$V_{LL,rms} = V_{AB,rms} = \frac{\sqrt{3}}{2\sqrt{2}} m_a \times V_{dc} = 0.612 m_a V_{dc} \text{ for } 0 < m_a \leq 1 \qquad (4\text{-}39)$$

and the dc link voltage is given by

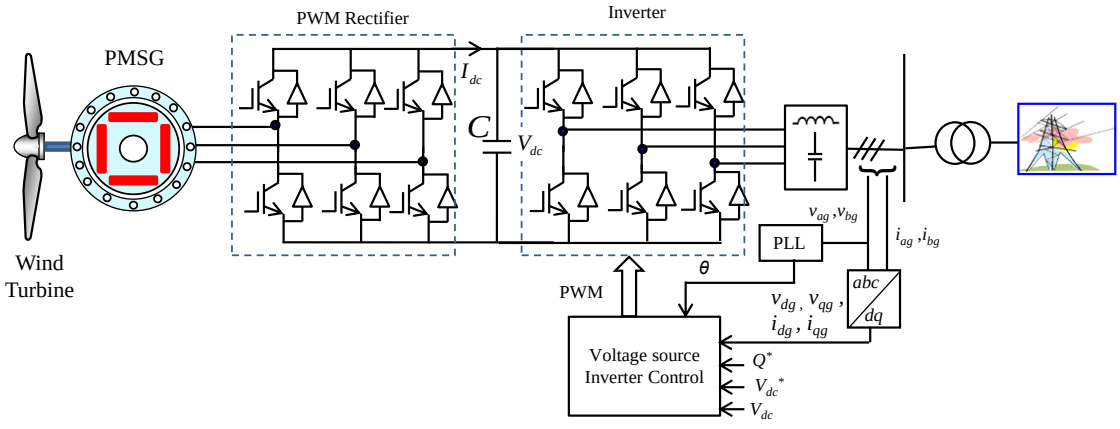

Figure 4.29 PMSG based variable speed wind Turbine with back to back PWM converters.

$$V_{dc} = \frac{2\sqrt{2}}{\sqrt{3}} \frac{V_{LL}}{m_a} = 2\sqrt{2} \frac{V_{ai1}}{m_a} \quad (4\text{-}40)$$

Where,

$V_{LL,rms} = Line\ to\ line\ rms\ voltage\ (V)$

$V_{dc} = dc\ link\ voltage\ (V)$

$V_{ai} = rms\ value\ of\ fundamental\ component\ of\ \ inverter\ phase\ voltage\ (V)$

$m_a = modulation\ index\ of\ the\ inverter$

Assuming that V_{ai1} is equal to the rms value of grid phase voltage V_g, which can be considered constant for grid connected system, the DC voltage can be boosted to a high value by a small m_a [84].

The active and reactive power from wind energy system supplied to the grid can be given by

$$P_g = 3V_g I_g \cos\varphi_g \quad (4\text{-}41)$$

$$Q_g = 3V_g I_g \sin\varphi_g \quad (4\text{-}42)$$

where,

$V_g = rms\ grid\ phase\ voltage\ (V)$

$I_g = rms\ grid\ current\ (A)$

$\varphi_g = grid\ power\ factor\ angle\ (deg.)$

The active power $P_g < 0$ indicates that power is flowing from wind energy system to the grid. The grid operator may require the wind farm to provide a controllable reactive power to the grid for voltage stability in addition to the active power. Therefore, the inverter can operate with the power factor angle in the range of $90^0 \leq \varphi_g \leq 270^0$ [84].

4.6.1.2 Detection of Grid Voltage Angle

The vector control scheme is implemented in the synchronous reference frame, where all the variables are of DC components in steady state. This simplifies the design of controller for the grid side inverter. Assuming that the grid voltages v_{ag}, v_{bg}, v_{cg}, are here phase balanced sinusoidal waveforms, the grid voltage angle can be calculated as [84],

$$\theta_g = tan\left(\frac{v_\beta}{v_\alpha}\right) \quad (4\text{-}43)$$

where v_β and v_α can be obtained from three phase *abc* to two phase $\alpha\beta$ transformation as [28],

$$v_\alpha = \frac{2}{3}\left(v_{ag} - \frac{1}{2}v_{bg} - \frac{1}{2}v_{cg}\right) = v_{ag} \tag{4-44}$$

$$v_\beta = \frac{2}{3}\left(\frac{\sqrt{3}}{2}v_{bg} - \frac{\sqrt{3}}{2}v_{cg}\right) = \frac{\sqrt{3}}{2}\left(v_{ag} + v_{bg}\right) \tag{4-45}$$

for $v_{ag} + v_{bg} + v_{cg} = 0$

The grid voltage angle is used for the transformation of variables (voltage/current) from stationery *abc* to rotating *dq* synchronous frame or from *dq* synchronous frame to *abc* stationery frame through *dq*-transformation equation. There are various methods are available to detect grid voltage angle θ_g. The grid voltage may contain harmonics. Therefore, digital filters or phase locked loop (PLL) may be used for the detection of grid voltage angle θ_g.

4.6.1.3 Vector Control in dq- synchronous Reference Frame

Fig.4.30 shows the block diagram for the vector control scheme for the grid side inverter with decoupled current controller. There are three control loops in this control scheme. These are

- Two inner current control loops for the *dq* axis current i_{dg} and i_{qg}.
- One dc link voltage control loop to regulate the dc link voltage

The voltage balance across the line inductance L_f is given by

$$\begin{bmatrix} v_{ag} \\ v_{bg} \\ v_{cg} \end{bmatrix} = R_f \begin{bmatrix} i_{ag} \\ i_{bg} \\ i_{cg} \end{bmatrix} + L_f \frac{d}{dt}\begin{bmatrix} i_{ag} \\ i_{bg} \\ i_{cg} \end{bmatrix} + \begin{bmatrix} v_{ai} \\ v_{bi} \\ v_{ci} \end{bmatrix} \tag{4-46}$$

The instantaneous power in a three phase system is given by:

$$P(t) = v_{ag}i_{ag} + v_{bg}i_{bg} + v_{cg}i_{cg} = \begin{bmatrix} v_{ag} & v_{bg} & v_{cg} \end{bmatrix}\begin{bmatrix} i_{ag} & i_{bg} & i_{cg} \end{bmatrix}' \tag{4-47}$$

Where, L_f and R_f are the line inductance and resistance respectively. v_{ai}, v_{bi}, v_{ci} represent voltages at the inverter output. i_{ag}, i_{bg}, i_{cg} are the line currents. The line resistance R_f is negligibly small and it is normally neglected in the analysis.

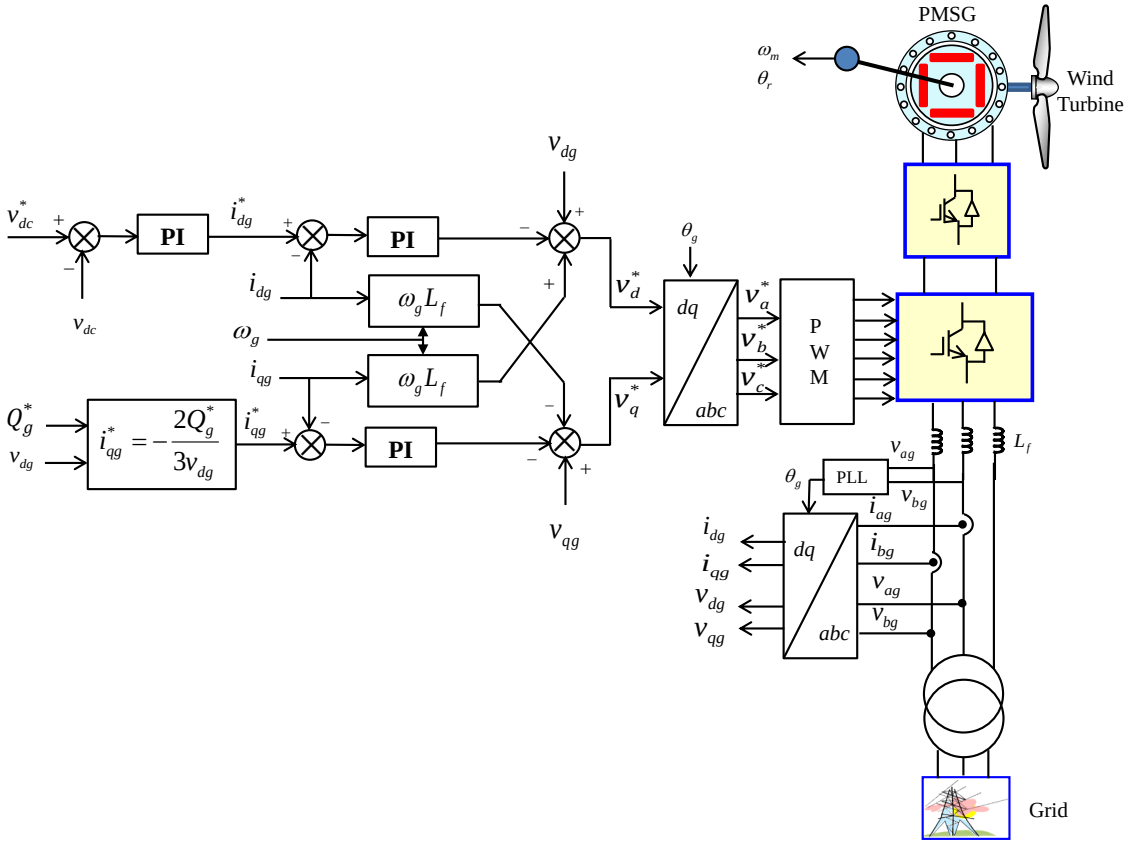

Figure 4.30 Vector control of grid side inverter with decoupled current controllers.

Fig.4.31 shows the vector representation of variables in *abc* and *dq*-reference frames. Transforming the voltage equations using *dq* transformation in the rotating reference frame [35]:

$$v_{dg} = v_{d1} - R_f i_{dg} - L_f \frac{di_{dg}}{dt} + \omega L_f i_{qg} \tag{4-48}$$

$$v_{qg} = v_{q1} - R_f i_{qg} - L_f \frac{di_{qg}}{dt} - \omega L_f i_{dg} \tag{4-49}$$

$$\left|V_g\right| = \sqrt{\left(v_{dg}\right)^2 + \left(v_{qg}\right)^2}$$

Using *dq* transformation, the active and reactive powers are given by

$$P_g = \frac{3}{2}\left(v_{dg} i_{dg} + v_{qg} i_{qg}\right) \tag{4-50}$$

$$Q_g = \frac{3}{2}\left(v_{dg} i_{qg} + v_{qg} i_{dg}\right) \tag{4-51}$$

If the reference frame is as $v_{qg} = 0$ and $v_{dg} = \left|V_g\right|$, the equations for active and reactive power can be written as,

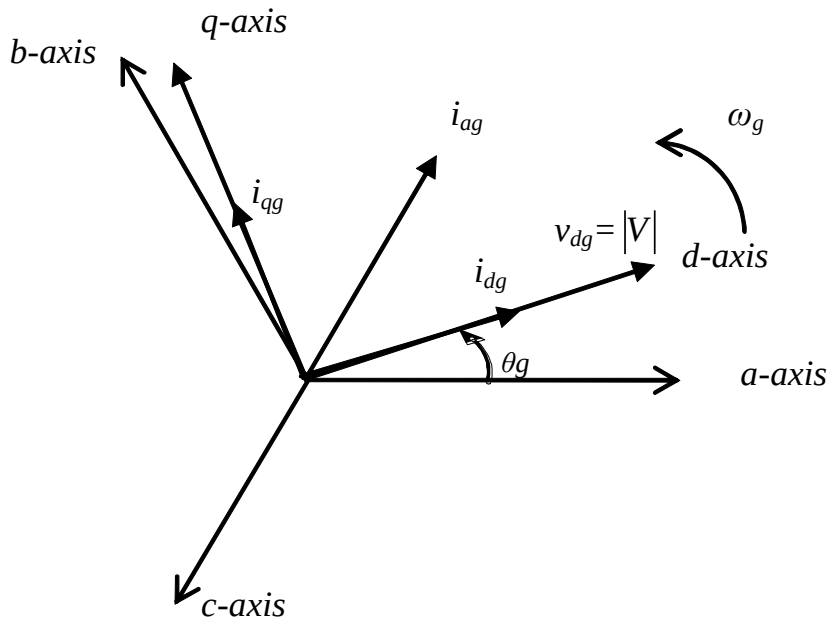

Figure 4.31 Stationary *abc* frame to rotating synchronous reference frame transformation

$$P_g = \frac{3}{2}\left(v_{dg} i_{dg}\right) = \frac{3}{2}\left|V_g\right| i_{dg} \tag{4-52}$$

$$Q_g = \frac{3}{2}\left(v_{dg} i_{qg}\right) = \frac{3}{2}\left|V_g\right| i_{qg} \tag{4-53}$$

The above equations show that the active and reactive power can be controlled by controlling *d*-axis and *q*-axis currents, respectively.

The *q*-axis current reference i_{qg}^* can be obtained from

$$i_{qg}^* = \frac{Q_g^*}{-1.5 v_{dg}} \tag{4-54}$$

Where, Q_g^* reactive power reference. For unity power factor, $Q_g^* = 0$, for leading power factor $Q_g^* = -ve$ and for lagging power factor $Q_g^* = +ve$.

The PI controller for the dc link voltage generates the reference for d-axis current, i_{dg}^* according to the operating condition of the inverter. The dc link voltage v_{dc} at the input of the inverter is regulated to a fixed value set by its reference v_{dc}^*. If the losses in the inverter are neglected, the active power at the inverter output ac side is equal to the dc input power to the inverter. Thus,

$$P_g = \frac{3}{2}\left(v_{dg} i_{dg}\right) = v_{dc} i_{dc} \tag{4-55}$$

The dc link voltage reference can calculated as,

$$V_{dc} == 2\sqrt{2}\,\frac{V_{ai1}}{m_a} = 3.53 \text{ pu} \qquad \text{(for } m_a\text{=0.8 and } V_{ai1} \text{ = 1 pu)} \tag{4-56}$$

Neglecting R_f, the *d*- and *q*-axes voltages across the grid side line inductance are given by

$$v_{dg} - v_{di} = -\omega_g L_g i_{qg} + L_f \frac{di_{dg}}{dt} \tag{4-57}$$

$$v_{qg} - v_{qi} = \omega_g L_f i_{dg} + L_f \frac{di_{qg}}{dt} \tag{4-58}$$

$$\frac{di_{dg}}{dt} = (v_{dg} - v_{di} + \omega_g L_f i_{qg}) / L_f \tag{4-59}$$

$$\frac{di_{qg}}{dt} = (v_{qg} - v_{qi} - \omega_g L_f i_{dg}) / L_f \tag{4-60}$$

where,

ω_g = the speed of the synchronous reference or the angular frequency of the grid (rad/sec.)

$\omega_g L_f i_{qg}$ and $\omega_g L_f i_{dg}$ = induced speed voltages [V]

The equations (4-59) and (4-60) show that the derivative of *d*-axis and *q*-axis currents are related to both *d*-axis and *q*-axis variables, which means that the system is cross-coupled. If there is any change in *q*-axis variables, that will affect the *d*-axis current. Similarly a change in *d*-axis variable will also affect the *q*-axis current. A decoupled current controller is necessary to solve this problem which is shown in Fig.4.30. The output of the de-coupled current controllers can be given by

$$v_{di} = -(k_P + K_I / S)(i^*_{dg} - i_{dg}) + \omega_g L_f i_{qg} + v_{dg} \tag{4-61}$$

$$v_{qi} = -(k_P + K_I / S)(i^*_{qg} - i_{qg}) + \omega_g L_f i_{dg} + v_{qg} \tag{4-62}$$

From equation (4-59) and (4-60), we get

$$\frac{di_{dg}}{dt} = (k_P + K_I / S)(i^*_{dg} - i_{dg}) / L_f \tag{4-63}$$

$$\frac{di_{qg}}{dt} = (k_P + K_I / S)(i^*_{qg} - i_{qg}) / L_f \tag{4-64}$$

Equations (4-63) and (4-64) indicates that the d axis and q-axis currents are decoupled. The decoupled control simplify the design of PI controllers enhance the system performance.

4.6.1.4 Simulation Results and Discussions

The grid-side inverter and its controller are implemented in *Matlab/SimpowerSystems*. The vector control of grid side inverter with decoupled current controllers of Fig.4.30 is implemented. There inner current control loop is to control the *d*-axis and *q*-axis current and outer loop is to control the dc link voltage. The sampling time used for inner and outer control loops are 20 μs and 100 μs, respectively.

Fig.4.32 shows the performance of the grid-side inverter controllers in grid connected mode. Fig.4.30 (a) to (d) show DC link voltage, reactive power, *d*-axis current, *q*-axis current responses at different wind speeds as shown in Fig.4.20(a). It is seen that the DC link voltage, reactive power, *d*-axis and *q*-axis currents follow their references quite well under variable wind speeds. The controller is able to regulate the dc link voltage quite well. Fig.4.33 shows the DC link voltage, current and power responses in grid connected mode at different wind speeds.

Fig.4.34 shows the grid voltage, current, frequency and active power and reactive power injected to the grid. As the wind speed changes, the active power supplied to the grid also changes. There is no reactive power supplied to the grid as the reactive power reference is selected as zero. The grid voltage and frequency are regulated at rated values at different wind speeds. Fig. 4.35 shows the instantaneous grid voltage and current at rated condition.

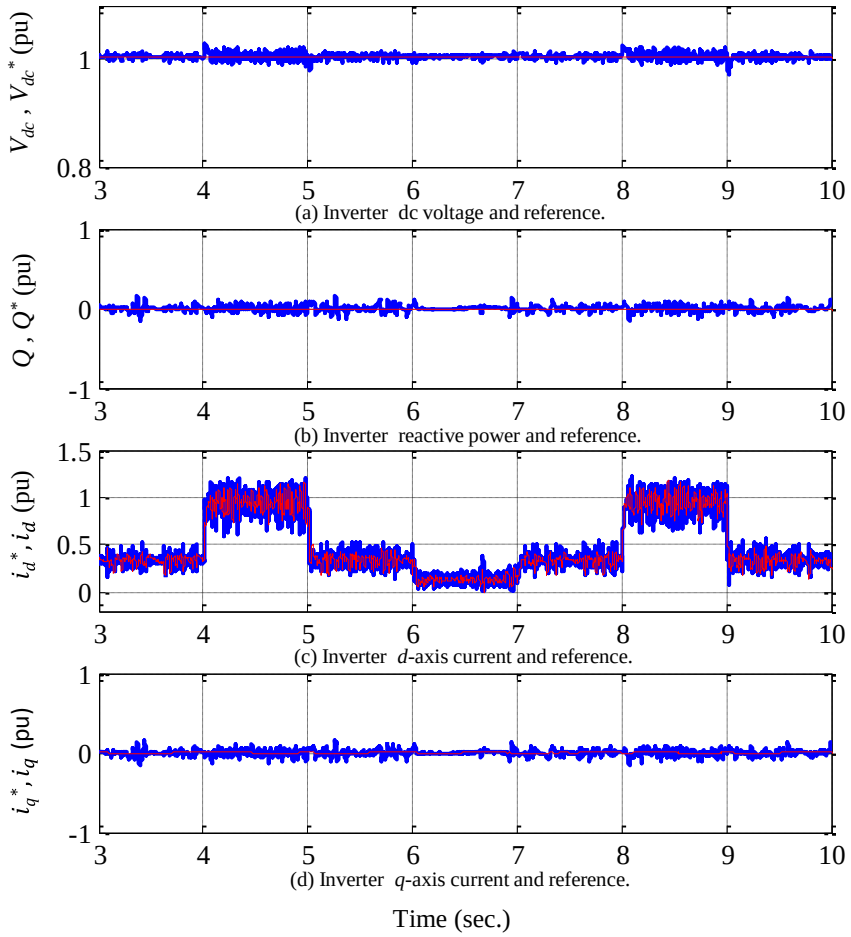

Figure 4.32. Performance of the grid side inverter controllers in grid connected mode.

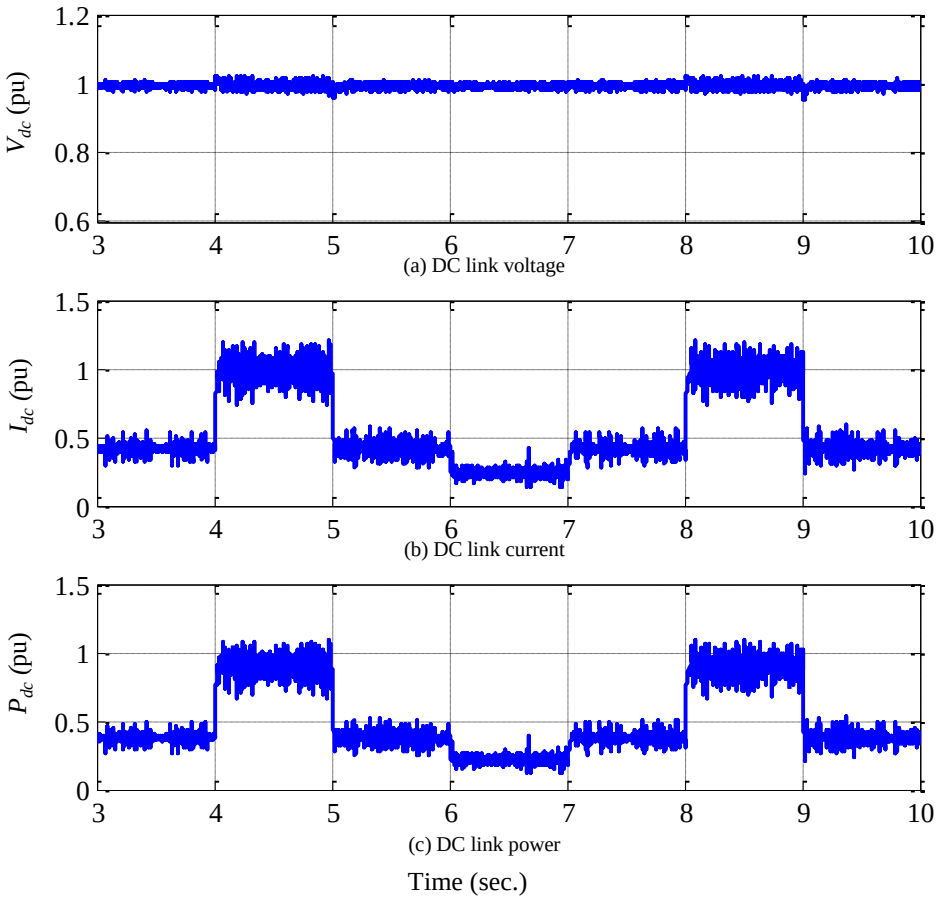

Figure 4.33. DC link voltage, current and power responses in grid connected mode.

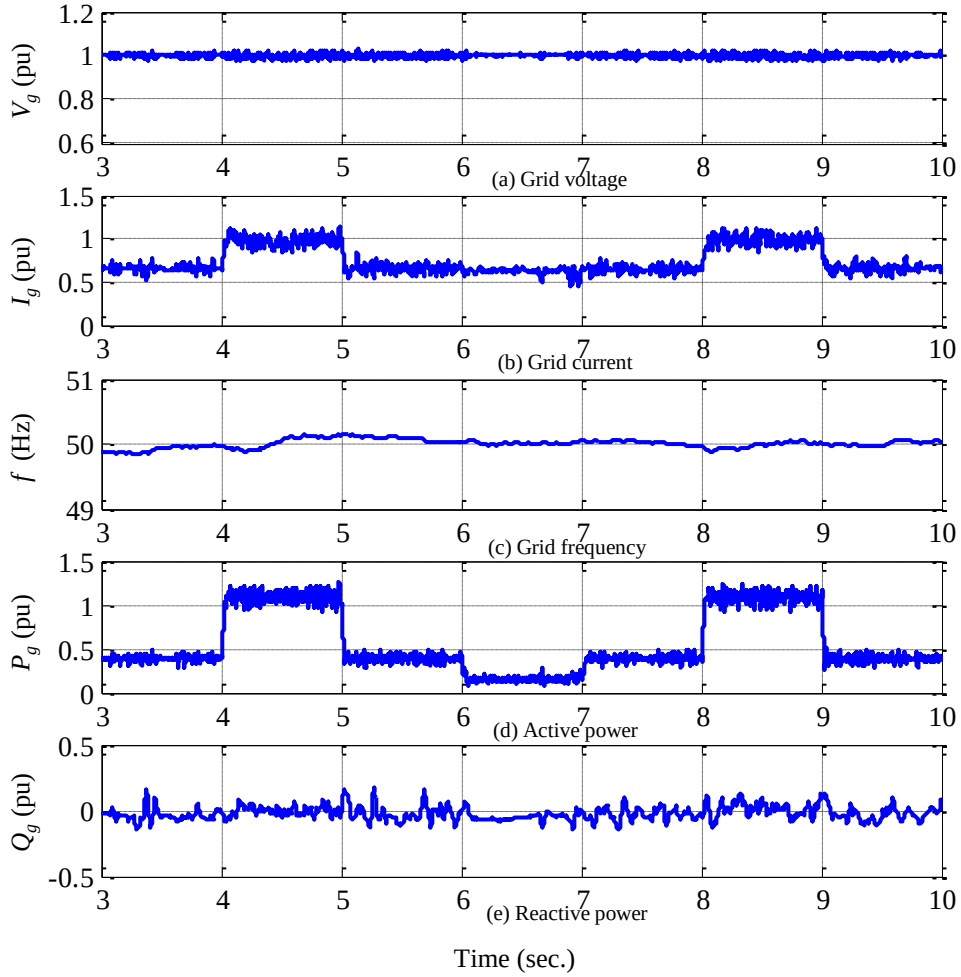

Figure 4.34. Grid voltage, current, frequency, active power and reactive power responses in grid connected mode.

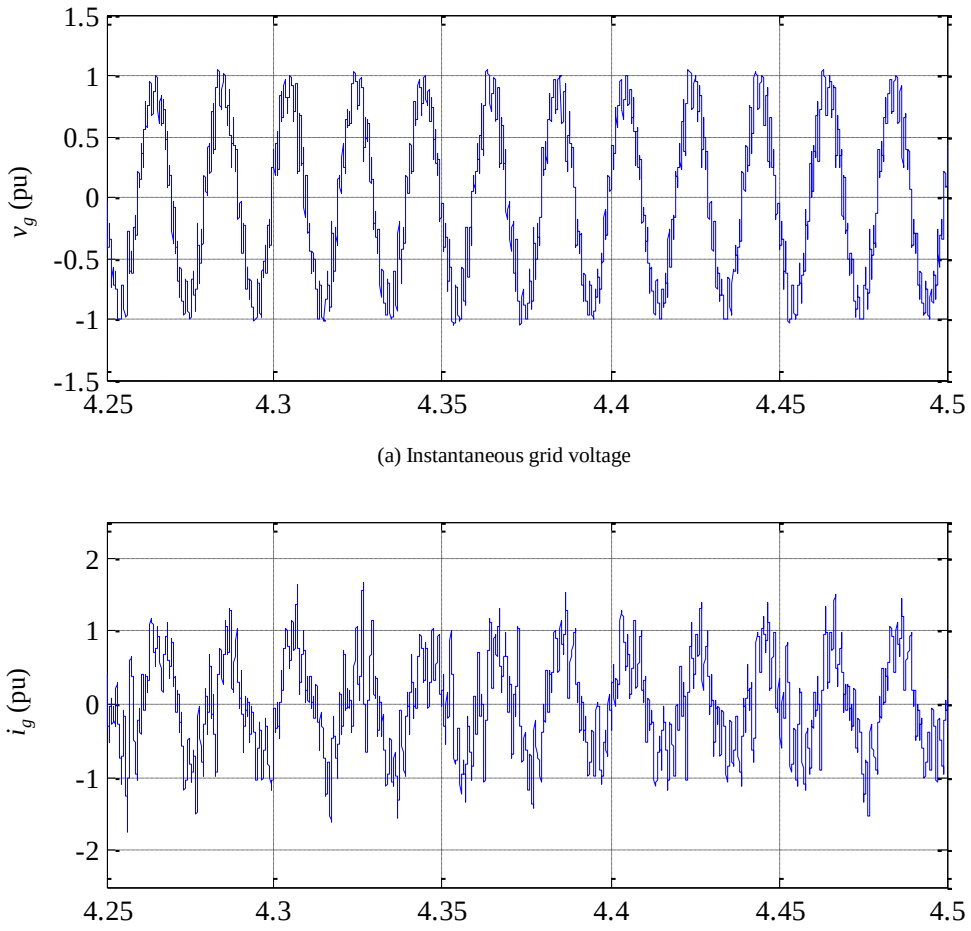

Figure 4.35. Instantaneous grid voltage and current at rated condition.

4.7 Control of Inverter in Stand-Alone Mode

In stand-alone mode, the function of the load side inverter is to regulate the inverter output voltage and frequency as there is no grid existence. Fig.4.36 shows the control structure of the load side inverter in stand-alone mode which are implemented in the rotating reference frame. The vector control scheme with decoupled current controllers is used in the rotating reference frame. The angular speed of the rotating reference frame is set at $\omega = 2\pi f$ in the controller, which is the electrical frequency of the inverter out voltage (load voltage) and current. The outer loop is the voltage controller and the inner loop is the current controller. The PI controller regulates the output voltage by controlling the d-axis voltage to the rated value at different wind speeds and load transient. The PI controllers in the inner control loop control the *d*- and *q*-axis current. The decoupled current controllers are implemented by adding the compensation terms to compensate for the cross coupling due to the output filter inductance. Battery energy storage and dump loads are used to maintain the dc link voltage.

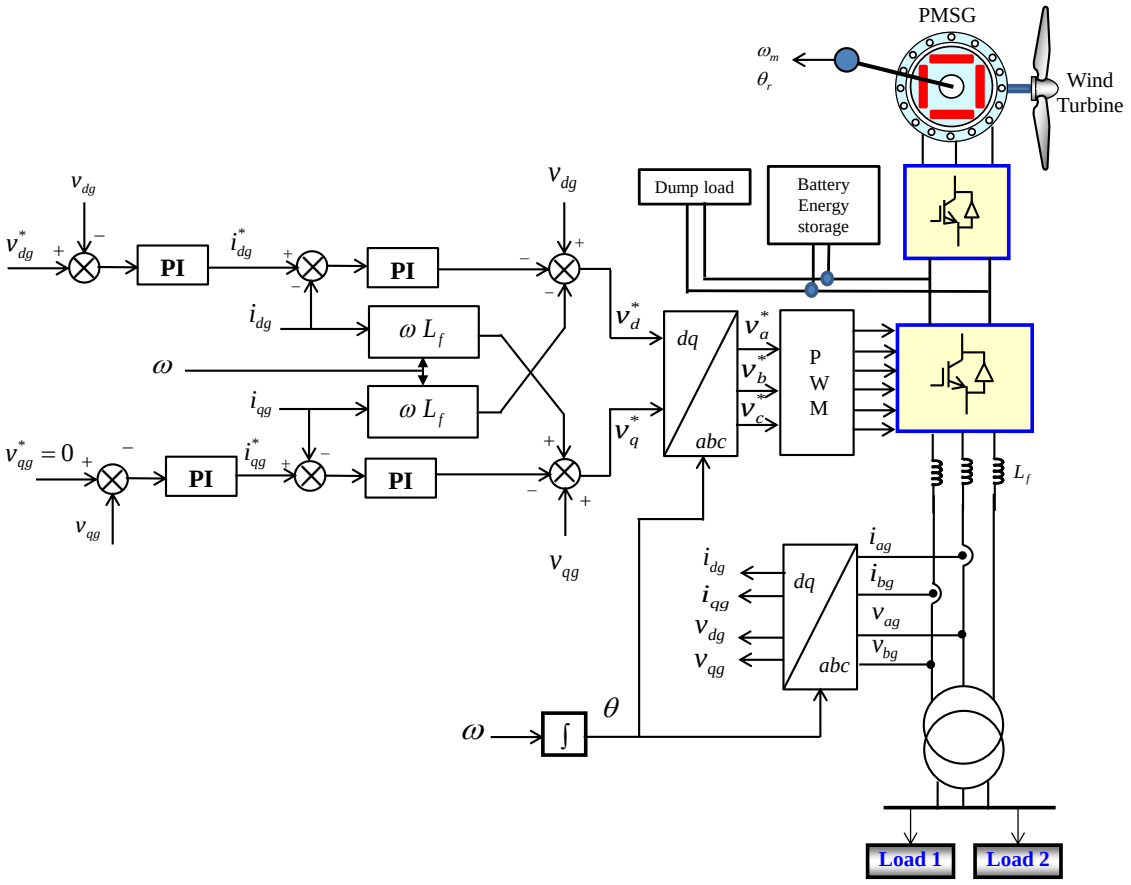

Figure 4.36. Control of load side inverter in stand-alone mode.

4.7.1 Simulation Results and Discussions

The load side inverter and it's controllers of Fig.4.36 are implemented in *Matlab/SimPowerSystems.* The sampling time for inner current and outer voltage control loops are 20 µs and 100 µs, respectively.

Figure 4.37 shows the performance of the load side inverter controller in stand-alone mode. Fig.4.37(a) show the d-axis voltage and it's reference. It is observed that the d-axis voltage follows the reference properly and regulate the voltage at different wind speeds (as shown in Fig.4.20). The *d*- and *q*-axis currents are shown in Fig 4.37 (b) and (c) together with their references, respectively. The *d*- and *q*-axis current follow their references and regulate the power flow to the load. As the q-axis voltage reference is set to zero the q-axis current is zero.Fig.4.37 (d) shows the modulation index of the inverter which changes with change in wind speed and power supplied to the load.

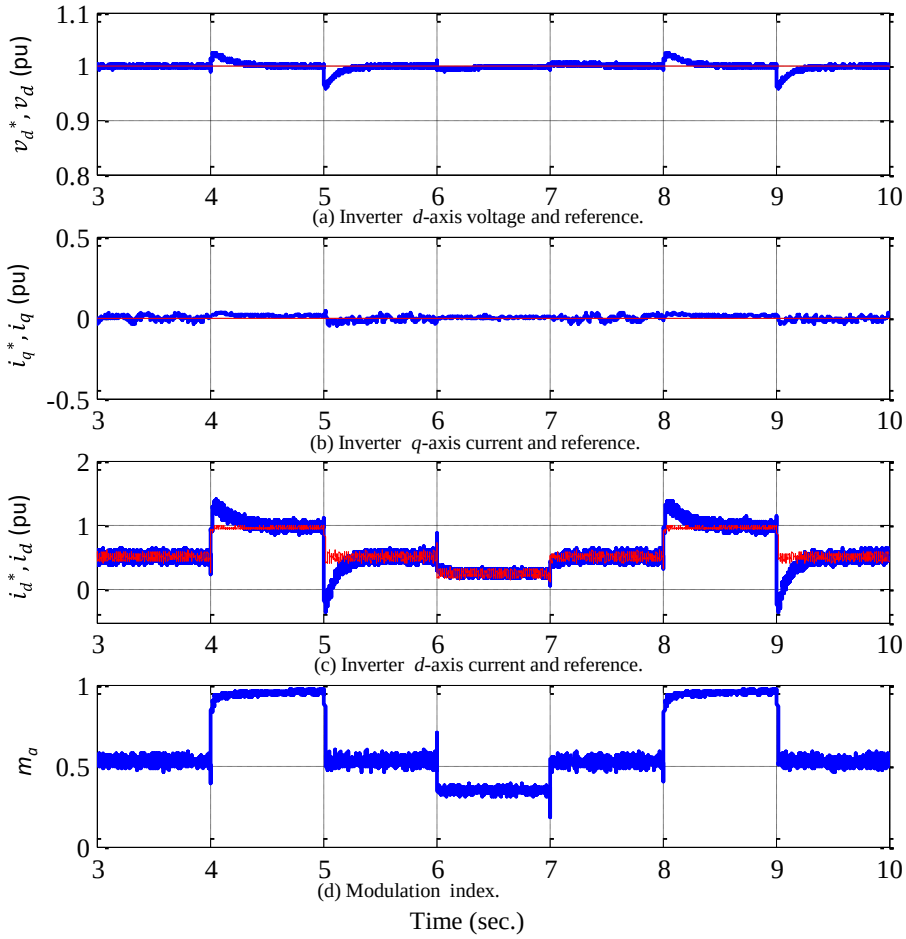

Figure 4.37. Performance of the load side inverter controller in stand-alone mode.

Fig.4.38(a) to (d) show the load voltage, load current, active power and reactive power responses in stand-alone mode. As shown in this figure, the load side voltage (line-line) is regulated at rated value and the load current changes to control the power flow to the load. Fig.4.39(a) and (b) show the instantaneous load voltage (phase) and current in stand-alone mode.Fig.4.39(c) shows that the phase voltage is in phase with phase current and the inverter is supplying active power at unity power factor. Fig.4.40 shows the rms inverter output voltage, frequency and modulation index. It is seen that the inverter output voltage frequency is regulated quite well.

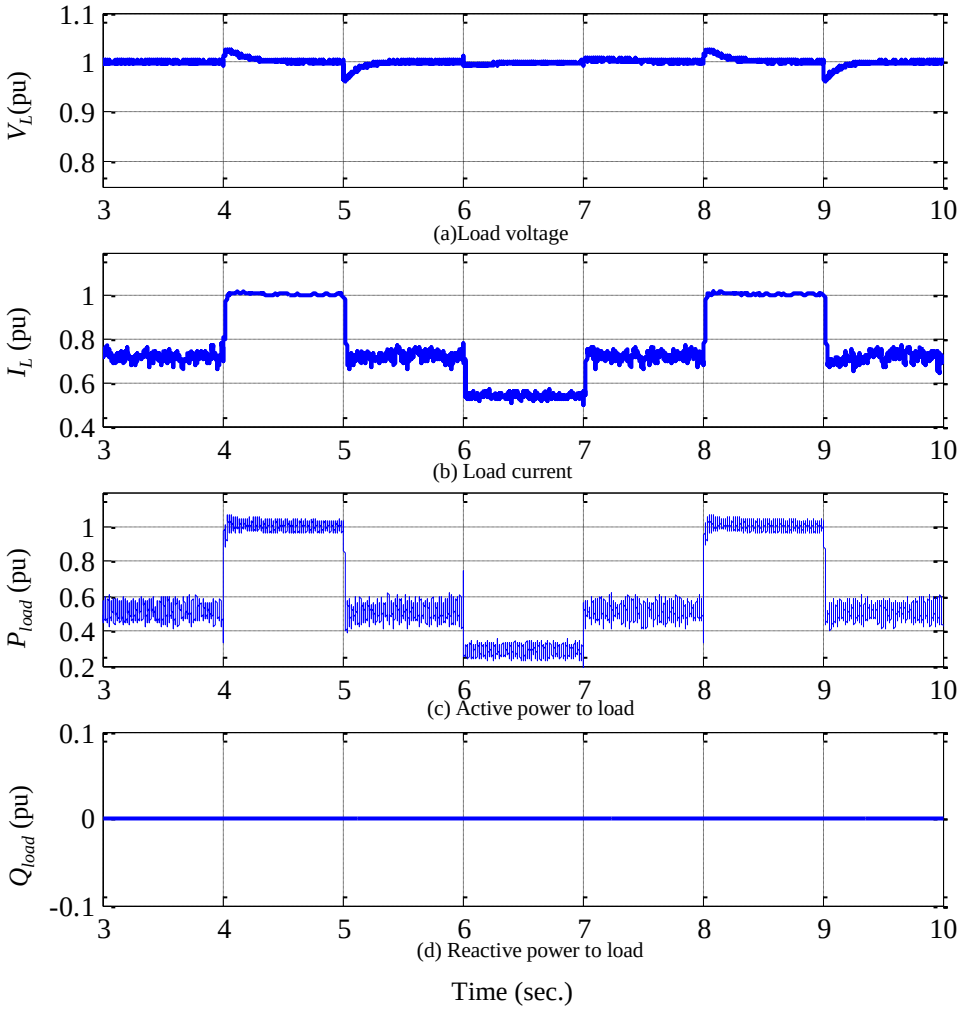

Figure 4.38. Load voltage, current, active power, reactive power responses in stand-alone mode

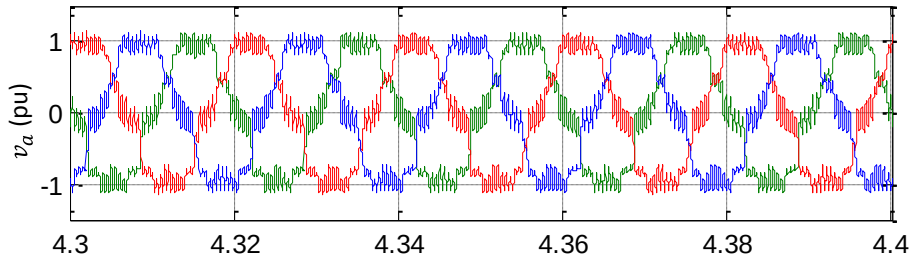

(a) Invert output voltage.

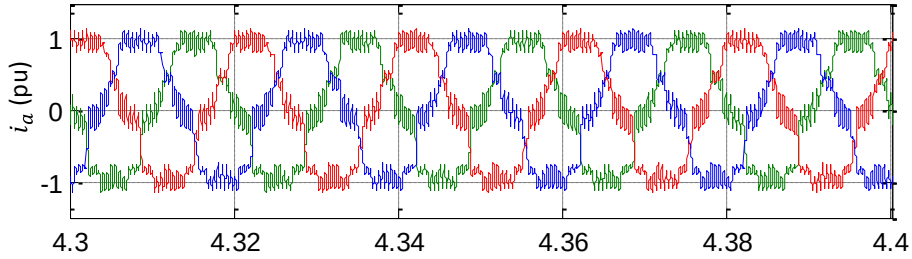

(b) Invert output current.

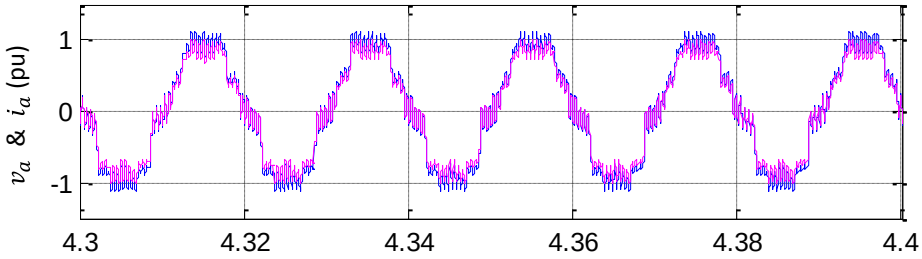

(c) Invert output phase voltage and current at rated condition.

Time (sec.)

Figure 4.39. Instantaneous load voltage and current in stand-alone mode.

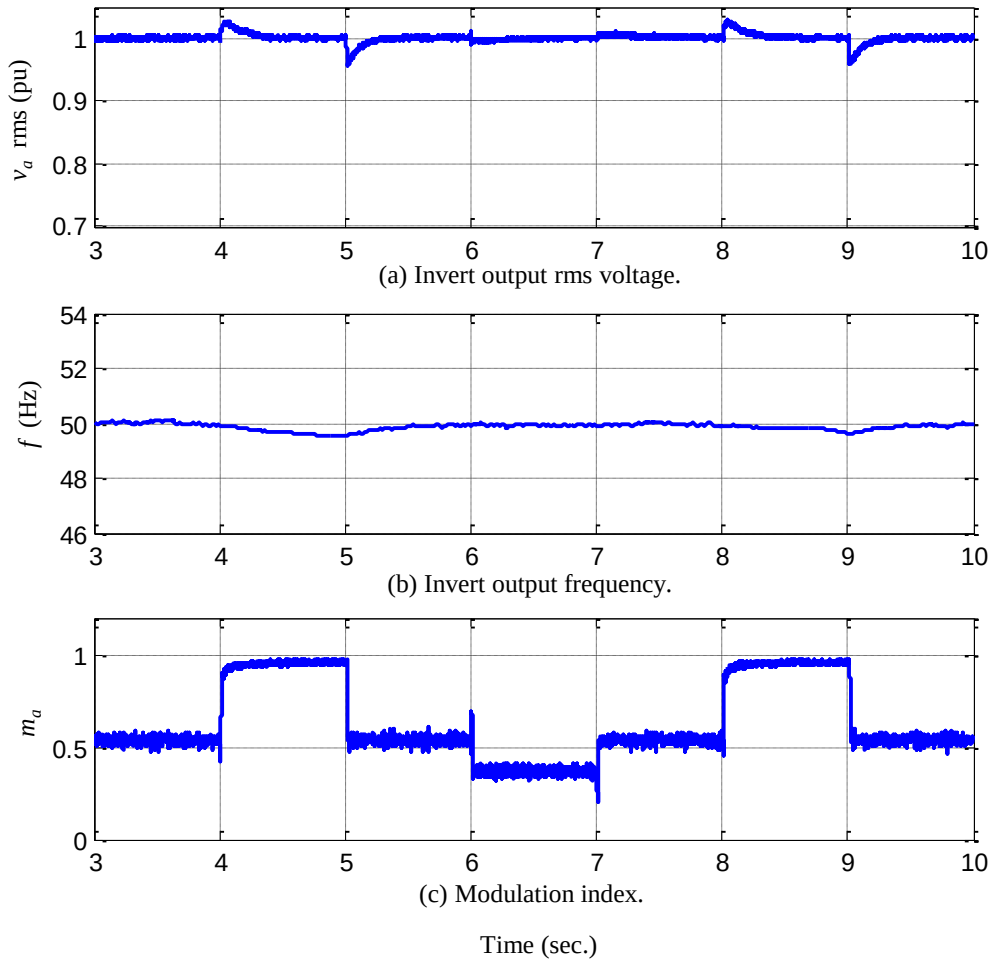

Figure 4.40. Inverter output rms voltage, frequency and modulation index.

4.8 Experimental Results

The generator side controller with MTPA control and maximum power extraction is experimentally implemented. The IPM synchronous generator parameters are shown in Chapter 3 Table 3.3. The vector control with MTPA trajectory is implemented using DSpace DSP1104 board with digital signal processor. The sampling time used for the inner current control loop is 100 μs and that of the outer speed control loop is 500 μs. A current sensor board is built using current sensors (LA-55P) to measure currents and a voltage sensor board is designed to measure voltage which is required in the controller implementation. The generator speed is measured using incremental encoder Heidenhahn ROD 426 with 5000 pulses. This encoder utilises photoelectric scanning to precisely measure position and angular velocity of the generator rotor. Fig. 4.41 shows the photo for the experimental setup. The experimental set up include the following:

- Computer
- DSpace DS1104 DSP boards
- DS1104 connection panel with connections for position encoder, ADC, DAC, PWM signals.
- Voltage sensor board
- Current sensor board
- Variable speed motor drive with an induction motor
- IPM synchronous generator
- Load bank

To simulate the wind turbine, a variable speed motor drive is connected to the induction motor which is controlled by a variable speed motor drive. The variable speed drive is controlled using wind input signal to vary the torque/speed command to the induction motor. The induction motor and the IPM synchronous are coupled together through a shaft as shown in Fig.4.41.

Figure 4.42 shows the performance of the DSP based vector controller with MTPA trajectory for a wind speed variations of 7 m/s-8m/s-9 m/s-10 m/s-9 m/s- 8 m/s. Fig.4.42(a) shows the IPM synchronous generator speed response which is following its reference quite well. As the wind speed changes, the speed controller regulates the

speed of the generator to extract maximum power under varying wind speeds. Fig.4.42(b) and (c) show the *q*-axis and *d*-axis currents which are following their respective reference currents quite well under varying wind speed. Fig.4.42(d) shows the torque response. It is seen that torque follows its reference. Fig.4.42(e) shows the generator power, which changes with wind speed. Fig. 4.43 shows the maximum power extraction by the wind turbine under varying wind speed. Fig. 4.44 shows the inverter output voltage and current at rated load. It is seen that the voltage and current are in phase as the generator supplying active power only.

The experimental results confirm the effectiveness of the MTPA control scheme and show very good dynamic and steady state performance. The control scheme is able to to extract maximum power from the wind turbine under varying wind speeds.

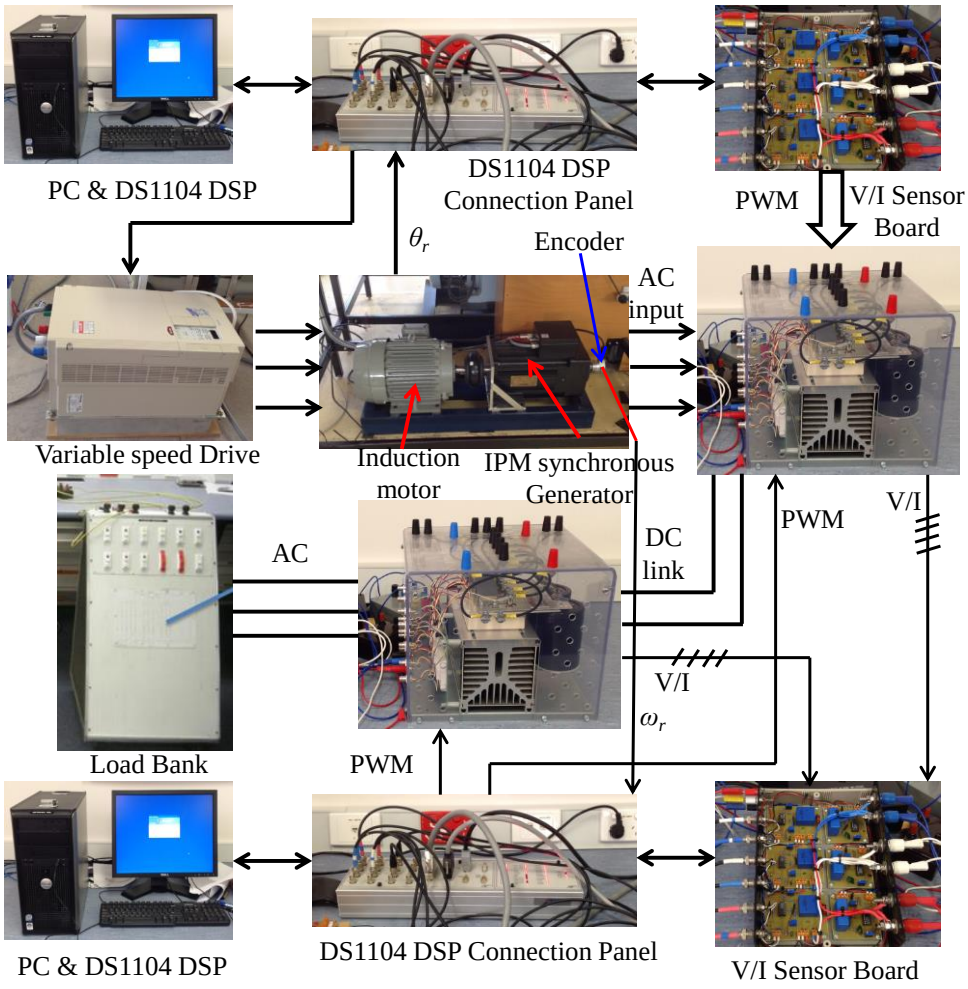

Figure 4.41 Experimental Set up.

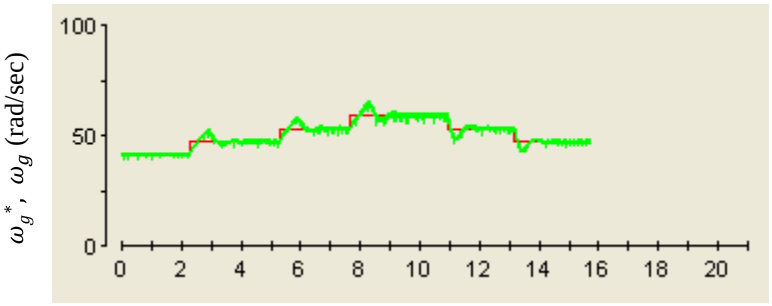

(a) Generator speed and reference.

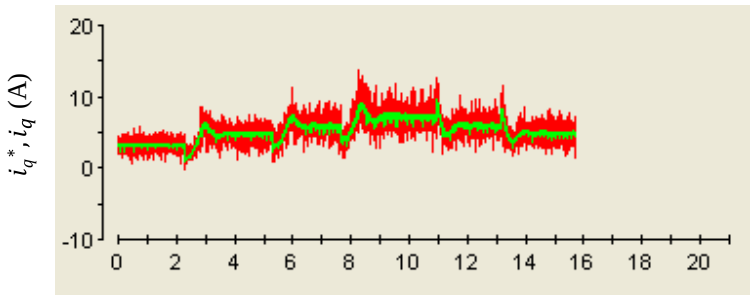

(c) Generator *q*-axis current and reference.

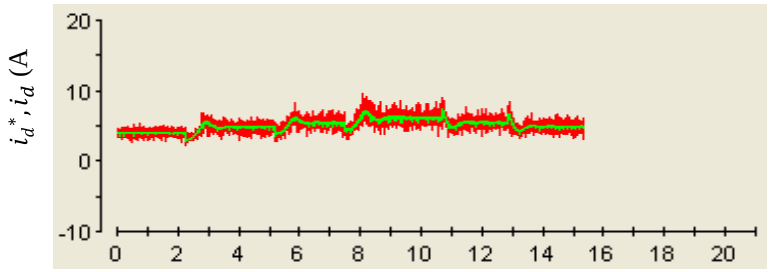

(d) Generator *d*-axis current and reference.

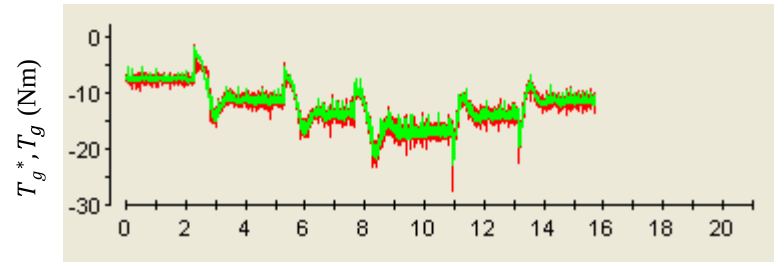

(e) Generator torque and torque reference.

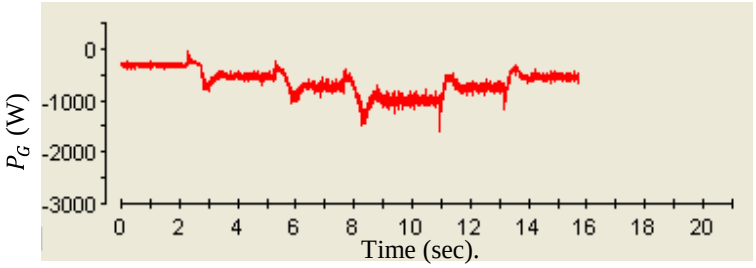

(e) Generator power.

Figure 4.42. Performance of the DSP based vector controller for a wind speed variation of 7 m/s-8m/s-9 m/s-10 m/s- 9 m/s- 8 m/s.

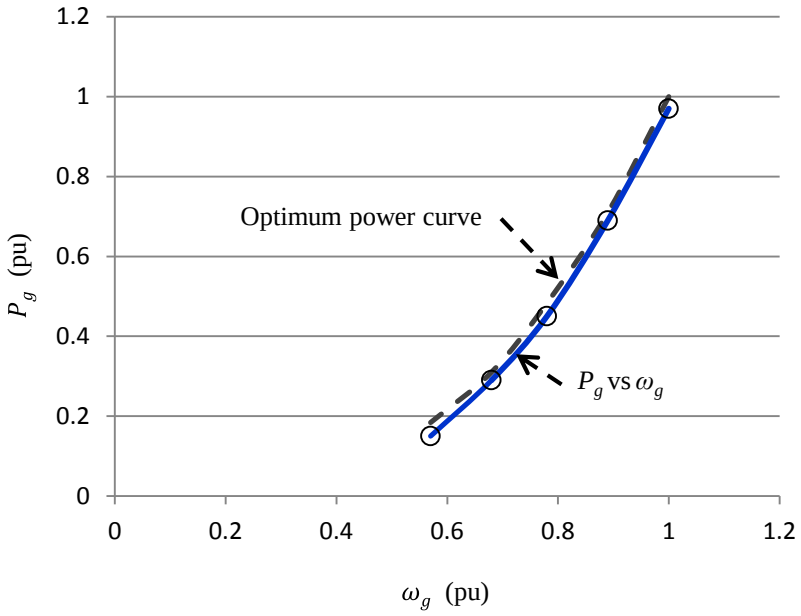

Figure 4.43. Maximum power extraction under varying wind speed (Experimental Results).

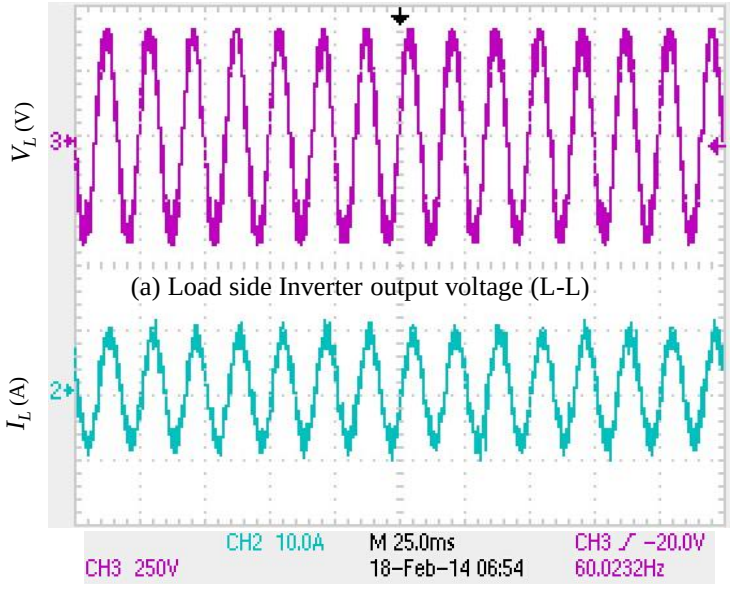

(a) Load side Inverter output voltage (L-L)

Time (ms)

(b) Load current

Figure 4.44. Inverter output voltage and current at rated load.

4.9 Summary

The indirect control strategies for permanent magnet synchronous generator (PMSG) based direct drive variable speed wind turbine are presented in this chapter. Control strategies for the direct drive wind turbine with PMSG are reviewed. The control of PMSG based direct drive variable speed wind turbine using switch-mode rectifier is presented. Control algorithm with maximum power extraction is presented and simulation results are discussed. Finally, an enhanced control scheme for interior permanent magnet (IPM) synchronous generator is developed by incorporating maximum torque per ampere trajectory (MTPA) and maximum power extraction (MPE) algorithm with the control scheme of generator side PWM rectifier to enhance the system performance and efficiency. The main advantage of incorporating MTPA trajectory in the control scheme is that it can generate the required torque with a minimum stator current. Therefore, the stator loss of the IPM synchronous generator is minimized. The MTPA control scheme ensures maximum utilization of the stator current. The detail analysis of the converter and the control scheme is presented. The proposed control scheme is simulated in *Matlab/SimpowerSystems* environment and experimentally implemented using DSpace DS1104 digital signal processor (DSP) system. The simulations and experimental results confirm the effectiveness of the proposed control scheme and shows very good dynamic and steady state performance. The control scheme can perform well and is able to extract maximum/optimum power under varying wind speeds. However, this control scheme has some drawbacks/limitations which are discussed in Chapter 5, and a more advanced control scheme for a direct drive IPM synchronous generator based variable speed wind turbine is presented.

Chapter 5

Direct Control Scheme of IPM Synchronous Generator Based Direct Drive Variable Speed Wind Turbine

5.1 Overview

The indirect control strategies using switch-mode rectifier and six switch voltage source converter based vector control scheme for permanent magnet synchronous generator are discussed in Chapter 4. Among the indirect control schemes of PMSGs, the vector control scheme is the most popular one. Traditional vector control scheme which is widely used in modern permanent magnet synchronous generator based variable speed wind energy conversion system in the range of kW to MW. In these wind turbines, the surface types PMSGs without rotor saliency are used, where the *d*-axis current reference is set to zero ($i_d^* = 0$) and *q*-axis current i_q is controlled to control generator torque/speed. In chapter 4, an improved control scheme for IPM synchronous generator based variable speed wind turbine is developed using MTPA control and results are presented. In this scheme, the generator torque is controlled indirectly via current control. The output of the speed controller generates the *d*- and *q*-axes current references, which are in the rotor reference frame. The generator developed torque is controlled by regulating the *d*-axis current i_d and *q*-axis current i_q according to the generator torque equation. The current control is executed at the rotor *dq*-reference frame, which rotates with the rotor. Therefore, coordinate transformation is involved and a position sensor is, thus, mandatory for the current control loop. All these tasks introduce delays in the system [25],[26]. This control scheme is also affected by the parameter variation. Moreover, the torque response under this type of control is limited by the time constant of stator windings [25].

Since the last two decades, Direct Torque Control (DTC) scheme has become popular for variable speed ac motor drives [85]. Direct torque control for induction motor was developed by Japanese and German researchers I. Takahashi and T. Noguchi (1984, 1985) [86]-[88]; Depenbrock (1985) [27],[89]. Later on, the DTC scheme is implemented for permanent magnet synchronous motor based variable speed drive applications [85], [91]-[93]. Recently, the direct control scheme is also applied to induction generator based variable speed wind turbine applications [28]-[30], 94. However, much attention has not been paid to the application of direct control scheme for permanent synchronous generator based variable speed wind turbine.

In this Chapter, the direct control scheme is implemented for an IPM synchronous generator based variable speed wind turbine to overcome the problems associated with the traditional indirect vector control scheme. In this scheme, the generator torque and flux linkage are controlled directly and independently by the selection of optimum inverter switching modes. Since all the calculations in direct control scheme are done in the stator reference frame, there no need for coordinate transformations and the requirement of continuous rotor position is eliminated. The direct control scheme has several advantages compared to the traditional vector control scheme. These are:

- simpler control method
- no requirement for coordinate transformation
- lesser parameter dependence
- absence of several controllers

The proposed control scheme is implemented in *Matlab/SimPowerSystems* and results show that the controller can regulate the generator speed extract maximum power under constant and varying wind speed.

5.2 The Proposed Direct Control Scheme for IPM Synchronous Generator Based Variable Speed Wind Turbine

5.2.1 The Concept of Direct Torque and Flux Control of IPM Synchronous Generator

In an indirect vector control scheme, the IPM synchronous generator torque is controlled by controlling the *d*- and *q*-axis current. Therefore, the generator torque is controlled indirectly by controlling *d*- and *q*-axes current in the rotor reference frame. As the calculations are done in the rotor reference frame, a coordinate transformation is necessary in this scheme. This scheme is affected by generator parameter variations and introduces delay in the control system.

In a direct torque and flux control scheme (DTFC) of IPM synchronous generator torque and flux are controlled directly and independently without using *d*- and *q*- axes current controllers. The torque and flux are controlled using two hysteresis controllers and by selecting optimum converter switching modes as shown in Fig.5.1. The selection rule is made to restrict the torque and flux linkage errors within the respective torque and flux hysteresis bands to achieve the desired torque response and flux linkage [76],[92], [93], [95]. The required switching voltage vectors can be selected by using a switching-voltage vector look-up table as shown in Table 5.1 [92]. The selection of the voltage space vectors can be determined by the position of the stator flux linkage vector and the outputs of the two hysteresis comparators. The hysteresis control blocks compare the torque and flux references with estimated torque and flux, respectively. When estimated torque/flux drops below its differential hysteresis limit, the torque/flux status output goes high. When estimated torque/flux rises above differential hysteresis limit, the torque/flux output goes low. The differential limits, switching points for both torque and flux are determined by the hysteresis bandwidth [92],[95]. The appropriate stator voltage vector can be selected using the switching logic to satisfy both the torque and flux status outputs. There are six voltage vectors and two zero-voltage vectors that a voltage source converter can produce. The combination of the hysteresis control block (torque and flux comparators) and the switching logic block replaces the need for a traditional PWM modulator.

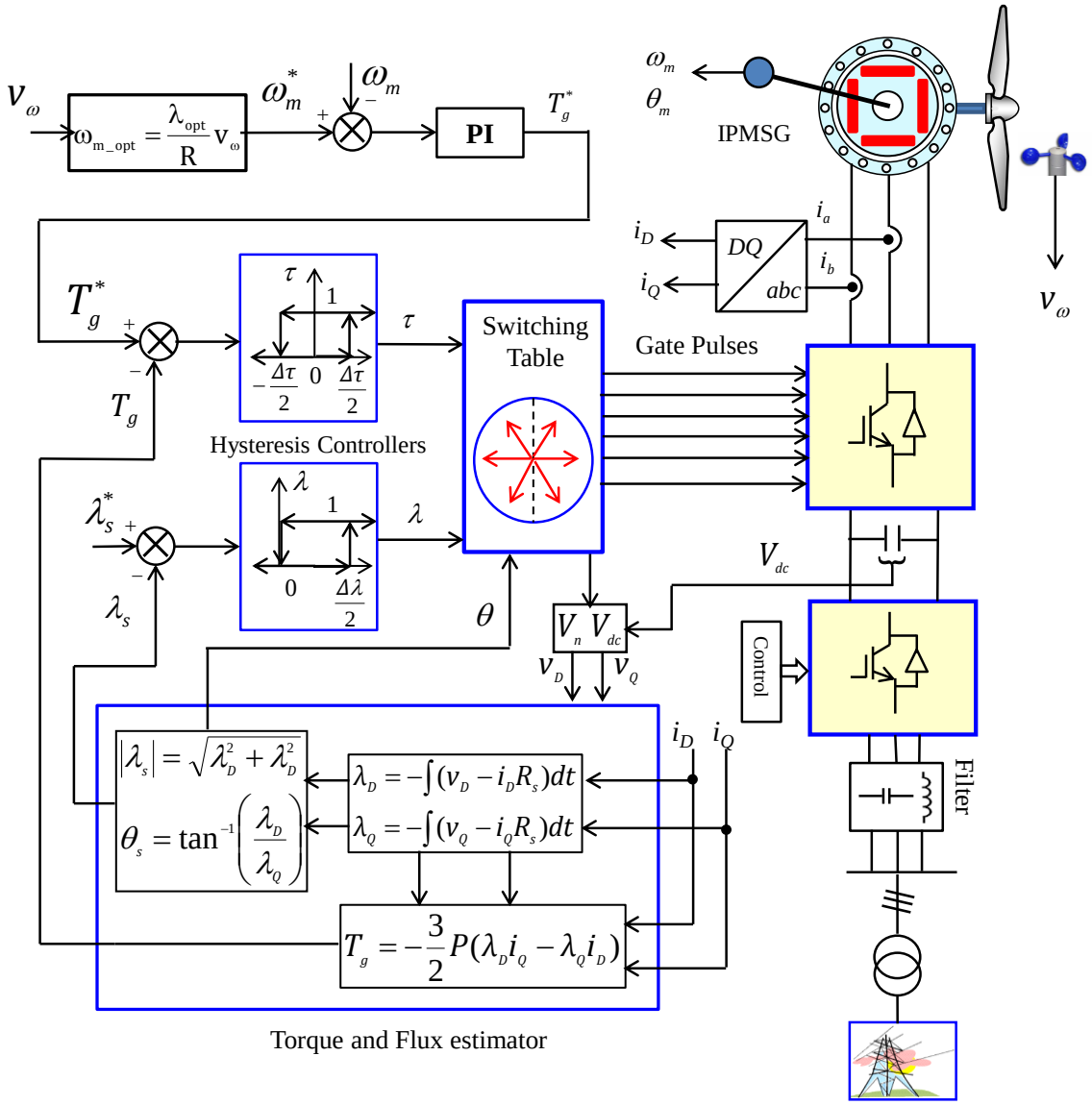

Figure 5.1 Proposed DTFC scheme of IPM synchronous generator.

5.2.2 *Analysis of Direct Torque and Flux Control Scheme of IPM Synchronous Generator[76]*

The relationship among stator flux (*xy*) reference, rotor flux (*dq*) reference, and stationary (*DQ*) reference frames are shown in Fig.5.2. The optimal switching logic of DTFC scheme is based on the spatial relationship of start flux, current, voltage and rotor flux linkage. If the stator resistance is neglected, the angle between the stator and rotor flux linkages δ becomes the power angle. In the steady state, δ is constant corresponding to a load torque and both stator and rotor fluxes rotate at the synchronous speed. In transient operation, δ varies and the stator and rotor fluxes rotate at different

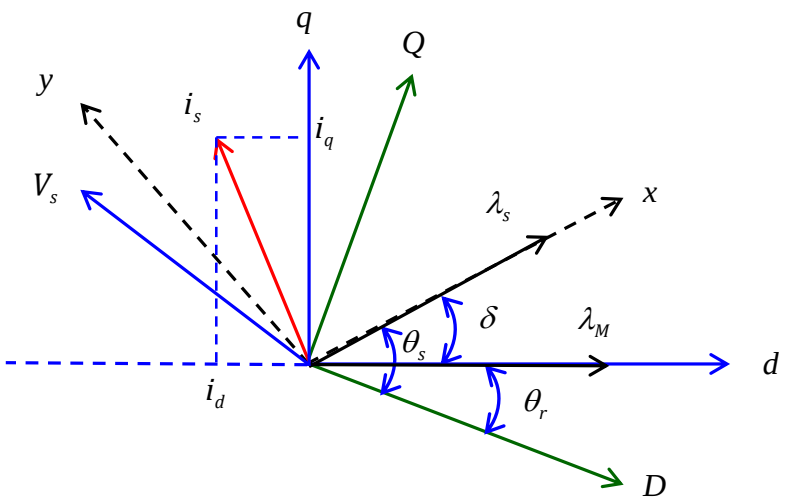

Figure 5.2 The stator and rotor flux linkages in different reference frames.

speeds. The magnitude of stator flux is normally kept as constant as possible, and torque is controlled by varying the angle δ, between the stator flux vector and the rotor flux vector [92].

In DTFC scheme, the stator flux linkage is estimated by integrating the difference between the input voltage and the voltage drop across the stator resistance as given by,

$$\lambda_D = -\int (v_D - i_D R_s) dt \tag{5-1}$$

$$\lambda_Q = -\int (v_Q - i_Q R_s) dt \tag{5-2}$$

In the stationary reference frame, the stator flux linkage phasor is given by

$$|\boldsymbol{\lambda_s}| = \sqrt{\lambda_D^2 + \lambda_Q^2} \tag{5-3}$$

and

$$\angle\theta_s = \tan^{-1}\left(\lambda_Q / \lambda_D\right) \tag{5-4}$$

The electromagnetic torque is given by,

$$T_g = -\frac{3}{2} P(\lambda_D i_Q - \lambda_Q i_D) \tag{5-5}$$

The torque equation in terms of δ and generator parameters is given by [92],

$$T_g = -\frac{3P|\boldsymbol{\lambda_s}|}{4L_d L_q}\left(2\lambda_M L_q \sin\delta - |\boldsymbol{\lambda_s}|(L_q - L_d)\sin 2\delta\right) \tag{5-6}$$

Table 5.1. Switching Table for DTFC

θ		θ_1	θ_2	θ_3	θ_4	θ_5	θ_6
λ	τ						
λ=1	τ =1	$\boldsymbol{V_2}$(110)	$\boldsymbol{V_3}$(010)	$\boldsymbol{V_4}$(011)	$\boldsymbol{V_5}$(001)	$\boldsymbol{V_6}$(101)	$\boldsymbol{V_1}$(100)
	τ =0	$\boldsymbol{V_6}$(101)	$\boldsymbol{V_1}$(100)	$\boldsymbol{V_2}$(110)	$\boldsymbol{V_3}$(010)	$\boldsymbol{V_4}$(011)	$\boldsymbol{V_5}$(001)
λ =0	τ =1	$\boldsymbol{V_3}$(010)	$\boldsymbol{V_4}$(011)	$\boldsymbol{V_5}$(001)	$\boldsymbol{V_6}$(101)	$\boldsymbol{V_1}$(100)	$\boldsymbol{V}$2(110)
	τ =0	$\boldsymbol{V_5}$(001)	$\boldsymbol{V_6}$(101)	$\boldsymbol{V_1}$(100)	$\boldsymbol{V_2}$(110)	$\boldsymbol{V_3}$(010)	$\boldsymbol{V_4}$(011)

5.2.2.1 Control of Stator Flux Linkage by Selecting Proper Stator Voltage Vector

The stator voltage vector $\boldsymbol{v_s}$ for a three phase machine with balanced sinusoidally distributed stator windings is defined by the following equation,

$$\boldsymbol{v_s} = \frac{2}{3}\left(v_a + v_b e^{j2\pi/3} + v_c e^{j4\pi/3}\right) \tag{5-7}$$

where, the phase "*a*" axis is taken as the reference position, v_a, v_b, v_c are the instantaneous values of line to neutral voltages. In Fig.5.3, the ideal bidirectional switches represent the power switches with their antiparallel diodes. The primary voltages, v_a, v_b, v_c are determined by the status of these three switches (S_a, S_b, S_c). Therefore, there are six non-zero voltage vectors, $\boldsymbol{V_1}$(100), $\boldsymbol{V_2}$(110),……, and $\boldsymbol{V_6}$(101), and two zero voltage vectors, $\boldsymbol{V_7}$(000) and $\boldsymbol{V_8}$(111). The six non-zero voltage vectors are 60^0 apart from each other as in Fig.5.4. These eight voltage vectors can be expressed as,

$$\boldsymbol{v_s}(S_a, S_b, S_c) = V_D\left(S_a + S_b e^{j2\pi/3} + S_c e^{j4\pi/3}\right) \tag{5-8}$$

where, V_D =2/3 V_{DC} and V_{DC} = DC link voltage.

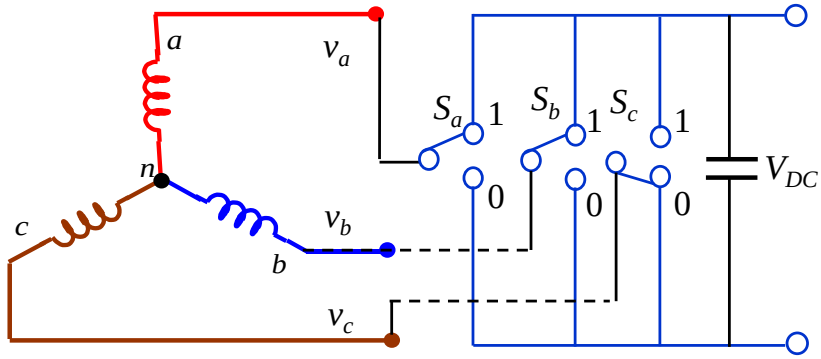

(a) A rectifier connected to IPM synchronous generator.

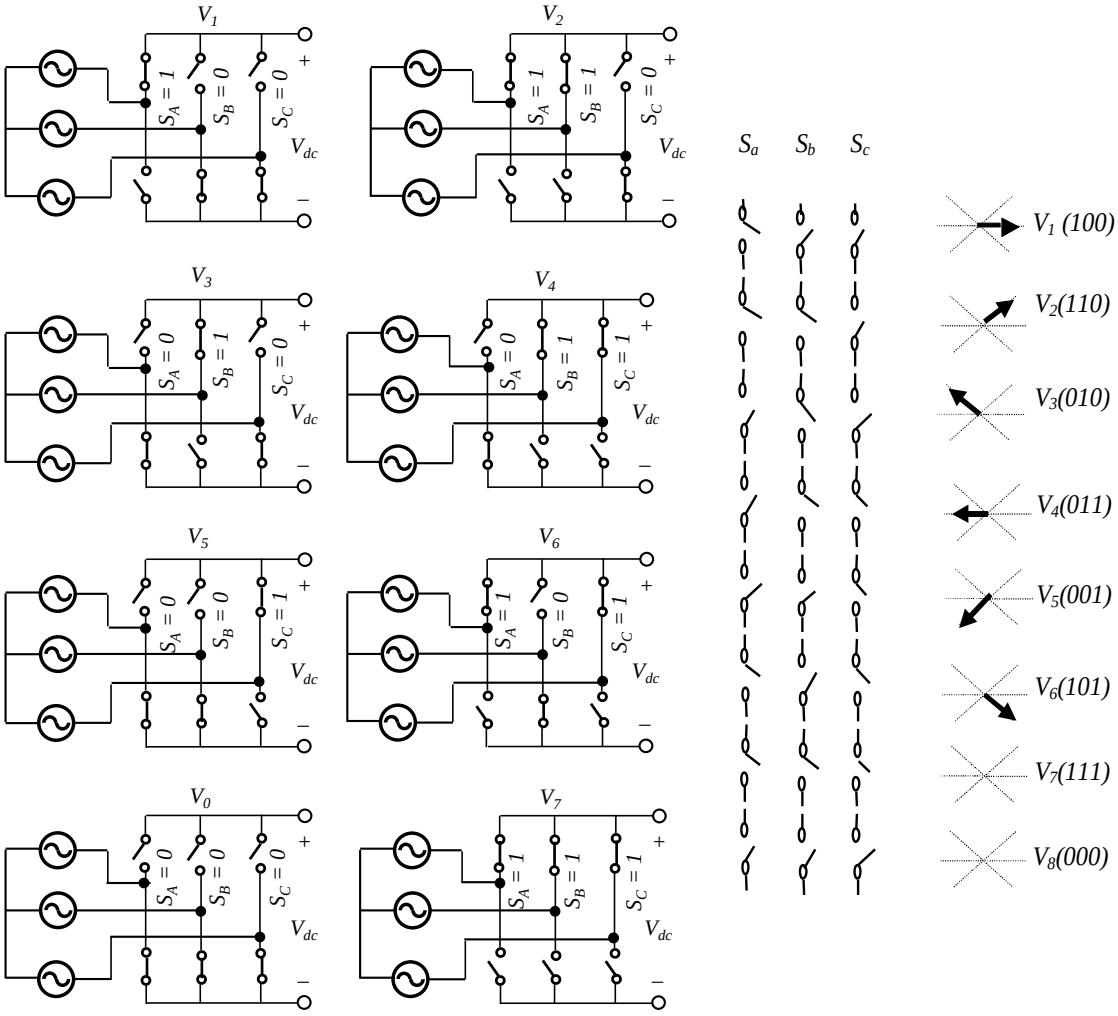

(b) Switching modes

Figure 5.3. A rectifier connected to IPM synchronous generator and switching modes.

5.2.2.2 Control of Amplitude of Stator Flux Linkage

The stator flux linkage in the stationary reference frame can be given as,

$$\boldsymbol{\lambda}_s = \int (\boldsymbol{v}_s - \boldsymbol{i}_s R_s)\, dt \tag{5-9}$$

Equation (5-9) can be written as,

$$\boldsymbol{\lambda}_s = \boldsymbol{v}_s t - R_s \int \boldsymbol{i}_s\, dt \tag{5-10}$$

Equation (5-10) implies that the tip of the stator flux linkage vector, $\boldsymbol{\lambda}_s$, will move in the direction of the applied voltage vector if the stator resistance is neglected as shown in Fig.5.4. By how far the tip of the stator flux linkage will move is determined by the duration of time for which the stator vector is applied. In Fig.5.5, the voltage vector plane is divided into six regions, θ_1 *to* θ_6 to select the voltage vectors for controlling the amplitude of the stator flux linkage. In each region, two adjacent voltage vectors are selected to keep the switching frequency minimum. Two voltages may be selected to increase or decrease the amplitude of $\boldsymbol{\lambda}_s$. For instance, voltage vectors $\boldsymbol{V}_2$ and $\boldsymbol{V}_3$ are selected to increase or decrease the amplitude of $\boldsymbol{\lambda}_s$ respectively, when $\boldsymbol{\lambda}_s$ is in region θ_1 and the stator flux vector is rotating in counter clockwise direction.

In this way, the amplitude of $\boldsymbol{\lambda}_s$ can be controlled at the required value by selecting the proper voltage vectors. How the voltage vectors are selected for keeping $\boldsymbol{\lambda}_s$ within a hysteresis band is shown in Fig.5.5 for a counter clockwise direction of $\boldsymbol{\lambda}_s$. The hysteresis band here is the difference in radii of the two circles in Fig.8. To reverse the rotational direction of $\boldsymbol{\lambda}_s$, voltage vectors in the opposite direction should be selected. For example, when $\boldsymbol{\lambda}_s$ is in region θ_1 and is rotating in the clockwise direction, the voltage vectors pair, $\boldsymbol{V}_5$ and $\boldsymbol{V}_6$, are selected to reverse the rotation of $\boldsymbol{\lambda}_s$ [92],[95], [76].

5.2.2.3 Control of Rotation of $\boldsymbol{\lambda}_s$

The effect of two non-zero voltage vectors, $\boldsymbol{V}_7$ and $\boldsymbol{V}_8$, is more complicated. It is seen from equation (5-10) that $\boldsymbol{\lambda}_s$ will stay at its original position when zero voltage vectors are applied. This is true for induction machine since the stator flux linkage is uniquely determined by the stator voltage, where the rotor voltages are always zero. In the case of an IPM synchronous generator, $\boldsymbol{\lambda}_s$ will change even when the zero voltage vectors are applied since magnet flux $\boldsymbol{\lambda}_M$ continues to be supplied by the rotor and it will rotate with

the rotor. In other words, λ_s should always be in motion with respect to the rotor flux linkage. Therefore, zero voltage vectors are not used for controlling λ_s in IPM synchronous machine [92], [95].

The electromagnetic torque is controlled by controlling the direction of rotation of λ_s according to the torque equation (5-6). For counter clockwise operation, if the actual torque is smaller than the reference value, the voltage vectors which keep λ_s rotating in the same direction are selected. The angle δ increases as fast as it can and the actual torque increases as well. Once the actual torque is greater than the reference value, the voltage vectors which keep λ_s rotating in the reverse direction are selected instead of the zero voltage vectors. The angle δ decreases and torque decreases too. By selecting the voltage vectors in this way, λ_s is rotated all the time and its rotational direction is determined by the output of the hysteresis controller for the torque [92], [95]. The six-vector switching table for controlling both the amplitude and rotating direction of λ_s is as shown in Table 5.1 [92], and is used for both directions of operations. In Table 5.1, λ and τ are the outputs of the hysteresis controllers for flux linkage and torque, respectively. If λ = 1, then the actual flux linkage is smaller than the reference value. The same is true for the torque. θ_1 to θ_6 are the region numbers for the stator flux linkage positions.

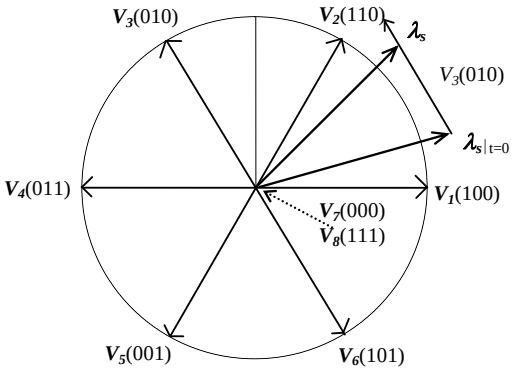

Figure 5.4. Available stator voltage vectors.

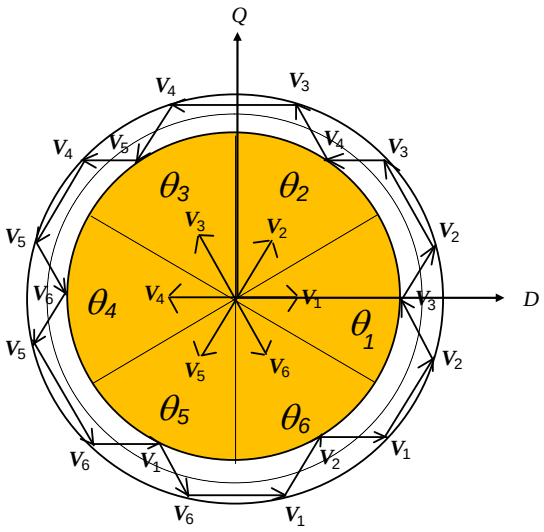

Figure 5.5. The control of the amplitude of stator flux linkage.

5.3 Implementation of DTFC Scheme for IPM Synchronous Generator Based Variable Speed Wind Turbine

The direct control scheme for IPM synchronous generator is shown in Fig.5.1, where the switching scheme used is as in Table 5.1. The three-phase variables are transformed into stationary *DQ*-axes variables. As shown in Fig.5.1 torque error and flux error are the inputs to the flux hysteresis comparator and torque hysteresis comparator, respectively. The outputs of the hysteresis comparators (τ,λ) are inputs to the voltage-switching selection look-up table. As shown in Fig.5.1, this scheme is not dependent on generator parameters except the stator resistance. Moreover, all calculations are in the stator *DQ*-reference frame and without any co-ordinate transformation [76].

The *DQ*-axes flux linkage components $\lambda_{D(k)}$ and $\lambda_{Q(k)}$, at the *k-th* sampling instant can be calculated as,

$$\lambda_{D(k)} = T_s\left[-v_{D(k-1)} + R_s i_{D(k)}\right] + \lambda_{D(k-1)} \tag{5-11}$$

$$\lambda_{Q(k)} = T_s\left[-v_{Q(k-1)} + R_s i_{Q(k)}\right] + \lambda_{Q(k-1)} \tag{5-12}$$

where, T_s is the sampling time and the variables with subscript *k* are their values at the *k-th* sampling instant and variables with *k-1* are the previous samples. The *DQ*-axes

currents can be obtained from the measured three-phase currents and the *DQ*-axes voltages are calculated from the measured DC-link voltage. Table 5.2 shows v_D and v_Q axes voltages for the applied voltage vectors [92].

The amplitude of the stator flux linkage is calculated from

$$\left|\lambda_{s(k)}\right| = \sqrt{\lambda_{D(k)}^2 + \lambda_{Q(k)}^2} \qquad \text{and} \qquad \theta_s = \angle\tan^{-1}\left(\lambda_{Q(k)} / \lambda_{D(k)}\right) \tag{5-13}$$

The developed torque is calculated from

$$T_{g(k)} = -\frac{3}{2} P\left(\lambda_{D(k)}\, i_{Q(k)} - \lambda_{Q(k)}\, i_{D(k)}\right) \tag{5-14}$$

The generator developed torque, in terms of the stator and rotor flux linkage amplitudes is also given by

$$T_{g(k)} = -\frac{3P\left|\lambda_{s(k)}\right|}{4L_d L_q}\left[2\lambda_M L_q \sin\left\{\delta_{(k)}\right\} - \left|\lambda_{s(k)}\right|(L_q - L_d)\sin 2(\delta_{(k)})\right] \tag{5-15}$$

Table 5.2: *DQ*-axes voltages (V_D = 2/3 V_{DC}) [76]

	V_1	V_2	V_3	V_4	V_5	V_6
v_D	V_D	0.5 V_D	-0.5 V_D	-V_D	-0.5V_D	0.5 V_D
v_Q	0	0.886 V_D	0.886 V_D	0	-0.886 V_D	-0.886 V_D

5.4 Control of Grid Side Voltage Source Inverter with Decoupled Vector Control Scheme

Fig.5.6 shows the vector control scheme for the grid side voltage source inverter to control the active and reactive power flow to the grid. The analysis of the control scheme is discussed in Section 6.4 of Chapter 4. The control scheme includes:

- Two inner current control loops which control the *d*- and *q*-axes current in the rotating reference frame.
- The outer control loops control the DC link voltage and reactive power. The outer loops regulate the active/reactive power flow to the grid by control *d*- and *q*-axes currents.

5.5 Results and Discussions

The direct torque and flux control scheme as shown in Fig.5.1 for a grid connected direct drive variable speed wind turbine with IPM synchronous generator is implemented in *Matlab/SimPowerSystems*. The IPM synchronous generator parameters are shown in Table 3.3 in Chapter 3. The switching table for the DTFC scheme is shown in Table 5.1. The bandwidths of torque and flux hysteresis controllers are 10% of their rated values. A smaller hysteresis bandwidth is used to reduce ripples in torque of the generator. The sampling times for the torque and speed control loops are 20μs and 100 μs, respectively. The decoupled vector control scheme for the grid side voltage control scheme as shown in Fig.5.6 is also implemented in *Matlab/SimPowerSystems*. The sampling times for the inner current control loops and outer control loops are 20 μs and 100 μs, respectively.

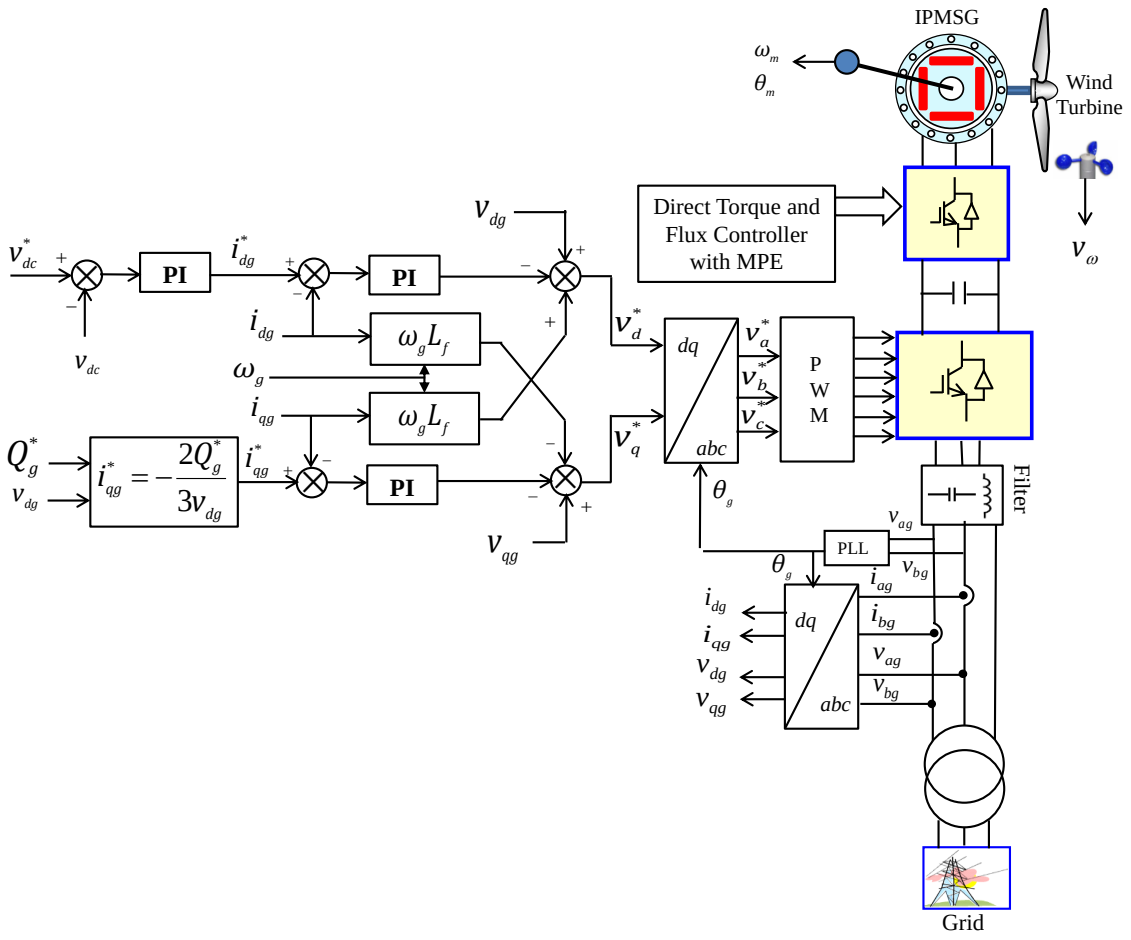

Figure 5.6. Control of grid side voltage source inverter with decoupled vector control scheme.

5.5.1 Performance of the Generator Side Direct Torque and Flux Controller

Fig.5.7 shows the performance of DTFC scheme with an IPM synchronous generator based variable speed wind turbine. Fig.5.7(a) to Fig 5.71(e) show the wind speed, generator speed response, torque response, flux linkage response and generator power, respectively. Fig.5.7(b) shows the IPM synchronous generator speed response an dits reference. The measured speed follows the reference speed quite well and the speed controller regulates the generator speed under variable wind speeds. It is seen in Fig.5.7(c) and 5.7(d) that the torque and flux linkages follow following their respective references and regulate the torque and flux of the generator at varying wind speeds. Fig.5.8 shows the locus of stator flux linkage which is a circle as expected.

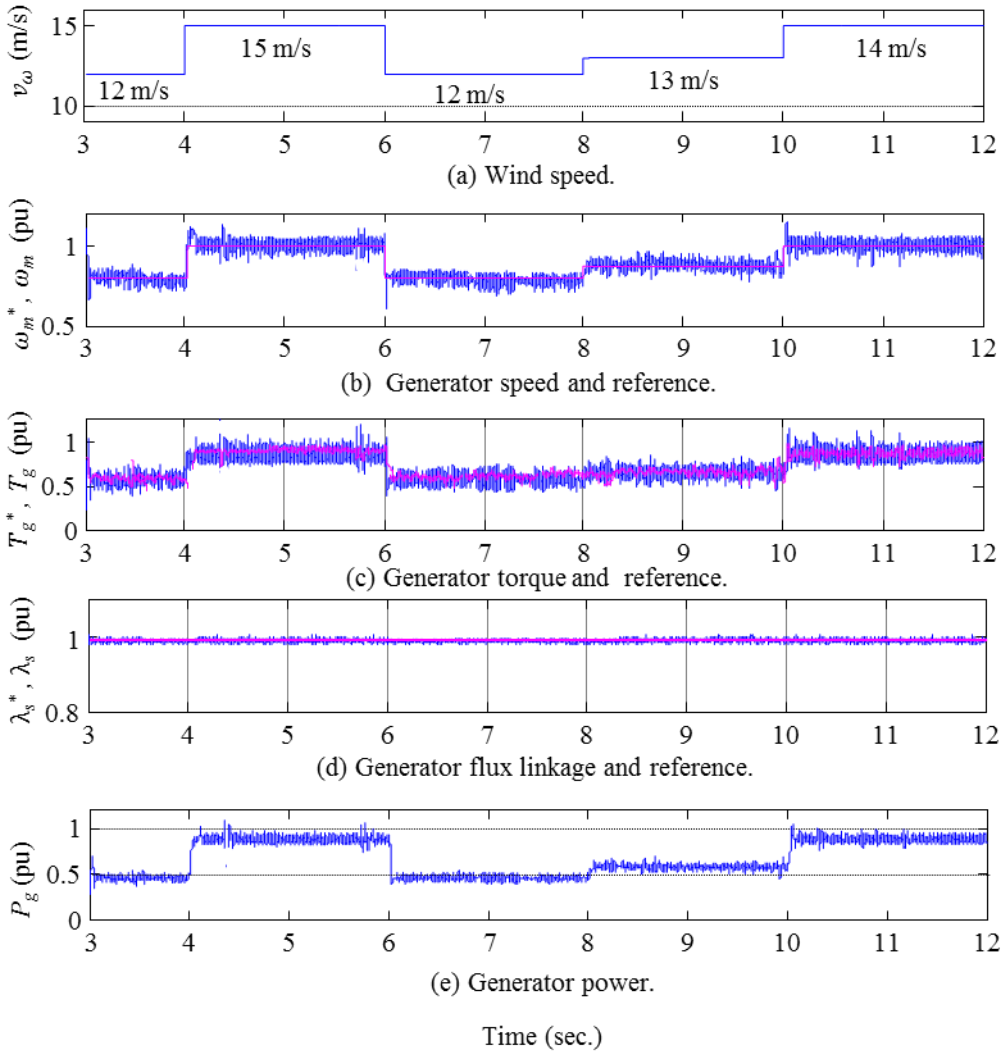

Figure 5.7. The performance of DTFC scheme of IPM synchronous generator based variable speed wind turbine under varying wind speed.

Fig. 5.9 show the maximum power extraction at different wind speeds direct torque and flux control scheme. It is observed that the measured power can track the optimum power curve quite well and extract maximum power at different wind speeds.

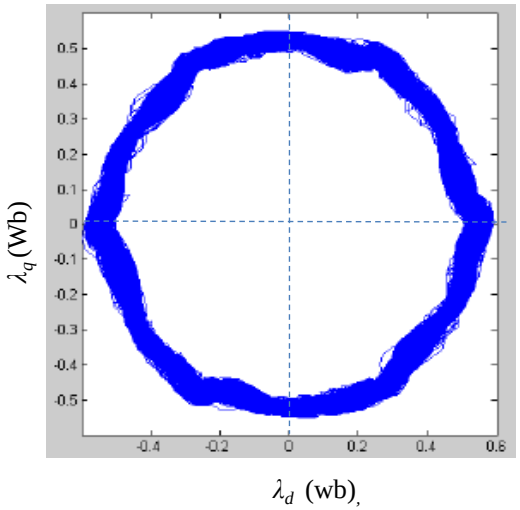

Figure 5.8. Locus of the stator flux linkage of IPM synchronous generator.

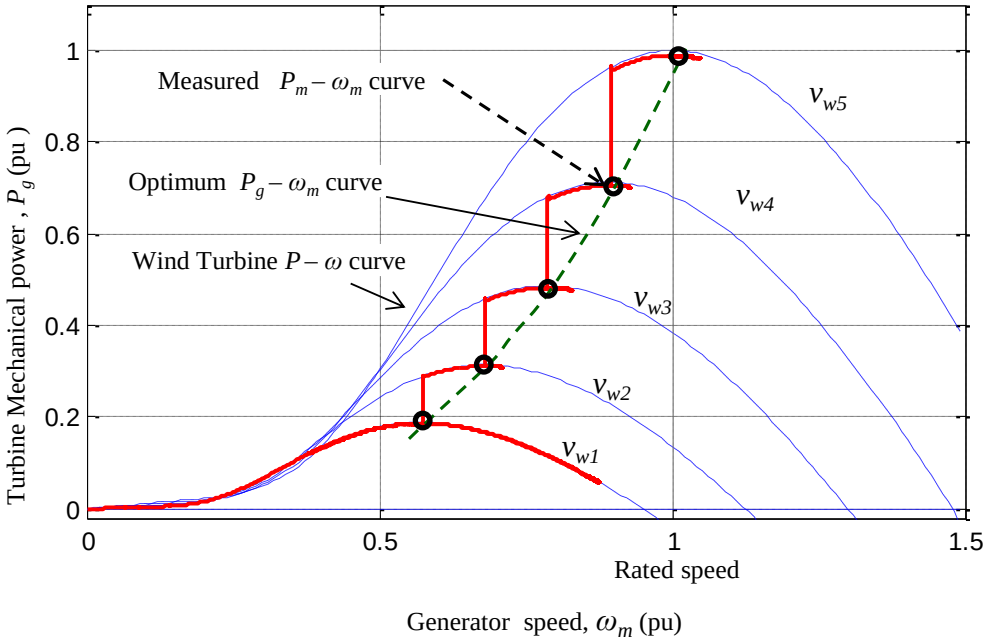

Figure 5.9. Maximum power extraction from an IPM synchronous generator based variable speed wind turbine

It is observed that the direct torque and flux control scheme shows similar performance to that of indirect vector control scheme as shown in Chapter 4. However, the control structure is simple and there is no rotor position is required with DTFC scheme as all the calculations are done in stator reference frame. In indirect vector control, the rotor position is required as all the calculations are done in the rotor reference frame. The direct control scheme possesses several advantages compared to indirect vector control scheme such as lesser parameter dependence, torque and flux control without rotor position and PI controller which reduce the associated delay in the controllers. However, the torque ripple in DTFC scheme is higher than the indirect vector control scheme. Some methods to minimize the torque/speed ripples in IPM machines have been proposed in literature, which need to be considered in future research.

5.5.2 Performance of the Decoupled Vector Control Scheme of the Grid Side Inverter

Fig.5.10 shows the performance of the decoupled vector control scheme for the grid side inverter under varying wind speed as shown in Fig.5.7(a). Fig.5.10 (a) to (d) show the dc link voltage, *d*-axis current, *q*-axis current and reactive power responses together with their respective references. It is observed that dc link voltage, *d*-axis current, *q*-axis current and reactive power follow their references quite well under varying wind speed. Fig.5.11 shows the grid voltage, grid current, active power, reactive power and frequency responses. The grid side converter controllers show very good dynamic and steady state performance under varying wind speeds.

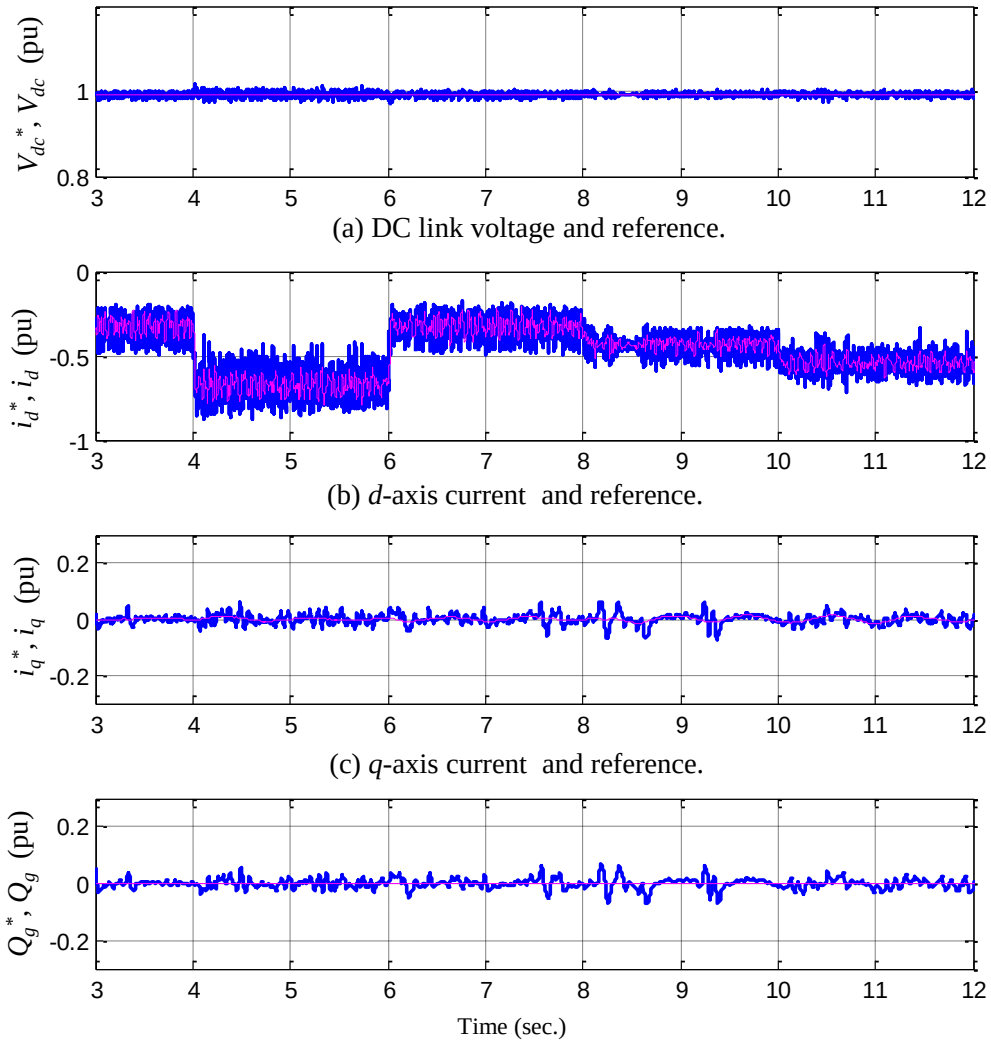

(a) DC link voltage and reference.

(b) *d*-axis current and reference.

(c) *q*-axis current and reference.

(d) Reactive power and reference.

Figure 5.10 Performance of the grid side decoupled vector controller for the voltage source inverter under varying wind speeds.

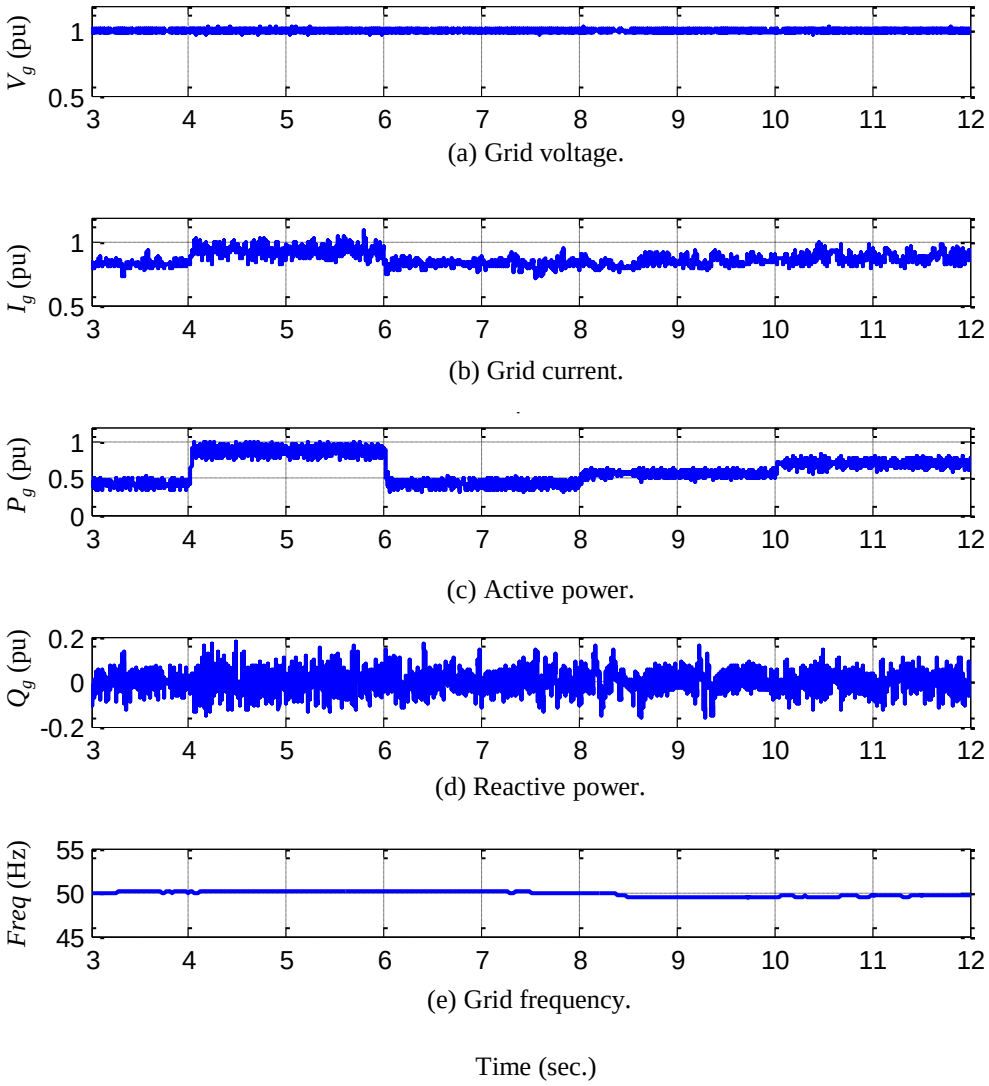

Figure 5.11. Grid voltage, current, active power, reactive power and frequency responses under varying wind speed.

5.6 Summary

Direct torque and flux control scheme for IPM synchronous generator based variable speed wind turbine is presented in this chapter. The proposed control scheme is implemented in *Matlab/SimpowerSystems*. In this control scheme, no rotor position is required as all the calculations are done in stator reference frame. The proposed DTFC scheme possesses several advantages compared with indirect vector control scheme such as; (i) lesser parameter dependence; (ii) torque and flux control without rotor position and PI controller which reduce the associated delay in the controllers, and (iii) sensorless operation without mechanical sensor. Results show that the DTFC scheme can operate under varying wind speeds can extract maximum power. The decoupled vector control scheme for the control of grid side voltage source inverter is also implemented in *Matlab/SimpowerSystems*. The grid side converter controllers can control the dc-link voltage, *d*-axis, current, *q*-axis current and reactive power quite well and show very good dynamic and steady state performance under varying wind speeds.

Chapter 6

Dynamic Performance Enhancement of a Grid Connected Wind Farm with STATCOM and Supercapacitor Energy Storage

6.1 Overview

Recent development in variable speed wind turbine generator technologies, associated power electronics and digital signal processors (DSPs) enables the rapid increase in global wind energy capacity and wind energy penetration to power grid is increasing dramatically. Due to the intermittent nature of wind power, the replacement of traditional synchronous generators (which provide the ancillary services) with power electronic converter-based wind energy systems will introduce several challenges [43], [96], [97]. Therefore, a better understanding of the technology involved with the grid integration of the variable speed wind turbines and possible impacts of large scale wind integration to the power grid is mandatory to ensure sustainability, reliability and security of the future power system [96]. In the past, wind power penetration to the power grid was low and it was not a major concern. With the increased penetration level of wind energy to the power grid, it has become necessary to address problems associated the stability, reliability and security of the power system. Dynamic voltage stability and low voltage ride through (LVRT) or fault ride through (FRT) capability are the basic requirement for the wind firm in many countries. The transmission system operators (TSOs) requires that wind farms remain connected in case of faults at major transmission levels leading to a voltage depression. These faults can lead to loss of wind generation if wind farms do not have the low voltage ride through capability [43]. Wind farms should have the capability to continue uninterrupted power supply under any disturbances and follow the grid code requirements.

Dynamic voltage stability and fault ride through are the important issues among the challenges for grid connected wind firms with large penetration level. The challenges

and issue associated with the wind energy integration can be eliminated or minimized by integrating energy storage (such as supercapacitor, batteries) in a wind farm [43]. This storage system can be used to enhance LVRT capability of wind firm and to improve dynamic voltage stability.

There are different techniques available to enhance LVRT capability of PMSG wind firm during voltage dips. Among them, control of blade pitch angle, control of converter, use of active crow bar, use of DC energy storage and use of FACTS devices such as static var compensator (SVC) and static synchronous compensator (STATCOM).

In this chapter, issues and impacts associated with the wind integration into the grid are discussed. The application of static synchronous compensator (STATCOM) with supercapacitor energy storage is investigated to enhance the dynamic performance of a grid connected wind firm. The vector control scheme discussed in Chapter 3 is used for generator side converter and grid side converter. The control strategy for the STATCOM with supercapacitor energy storage is developed to enhance the dynamic voltage stability of the wind firm. The main motivation for using choosing STATCOM is its ability to provide voltage support either by supplying and/or absorbing reactive power into the power grid. Simulation model and associated controllers have been implemented in *Matlab/SimpowerSystem* and results are discussed.

6.2 Issues and Impacts of Wind Energy Integration into the Grid

The integration of wind generation into the grid wind power can introduce many technical challenges and issues though it has many advantages over other renewable based source. These problems become more pronounced as the penetration level of wind increases [98], [99]. The challenges and issues associated with the wind generation and integration to the grid are [43], [98]-[113]:

- intermittency of wind
- system inertia and frequency regulation
- ramping due to wind speed fluctuations
- power quality requirement for grid integration

- dynamic voltage stability
- bi-directional power control,
- tight voltage and frequency regulation,
- stabilization of power flow,
- low voltage fault ride through capability
- changing power system dynamics,
- satisfy new grid code requirement,
- system security, reliability and stability
- new safety and protection requirements

6.3 Grid Code and Interconnection Requirements

6.3.1 Low Voltage Ride Through or Fault Ride Through Capability of Wind Turbines[43]

Low voltage ride through capability is the ability of wind turbine to remain connected to the grid under fault without loss of generation. The factors which can effect LVRT are; fault type and location, fault clearance time, level of the voltage sag, grid size, active reactive power demand after fault clearance, system load etc. [113]. In a traditional power system, the factors influence LVRT are generator inertia, reactance, active and reactive power balance, excitation system and AVR [113]. As the penetration level of wind is increasing, utility companies are required to make sure that the power system operate properly and maintain system stability under any external disturbances. Utility operators of many countries have introduced new grid-code requirement for wind farm connection. Examples include are Spain, Denmark, Germany and Brazil [44], [113].

Fig.6.1 shows the fault ride through requirement of several countries [44]. The grid-codes define the wind farm operation boundary. These grid-codes are important for wind turbine manufacturers, developers and utility companies. The fault ride through capability is regarded as the main challenge to the wind turbine manufacturer among the grid-code requirement [44],[113].

In Australia, a wind plant must have low voltage ride through capability down to 0% of the rated line voltage for 220 ms for 220 kV connection and 120 ms for 250 kV

connection. It means a wind plant must be able to operate continuously for 120ms for 220kV line and 220 ms for 250 kV line at 0% of the rated line voltage, measured at the high voltage side of the wind plant sub-station transformer [114].

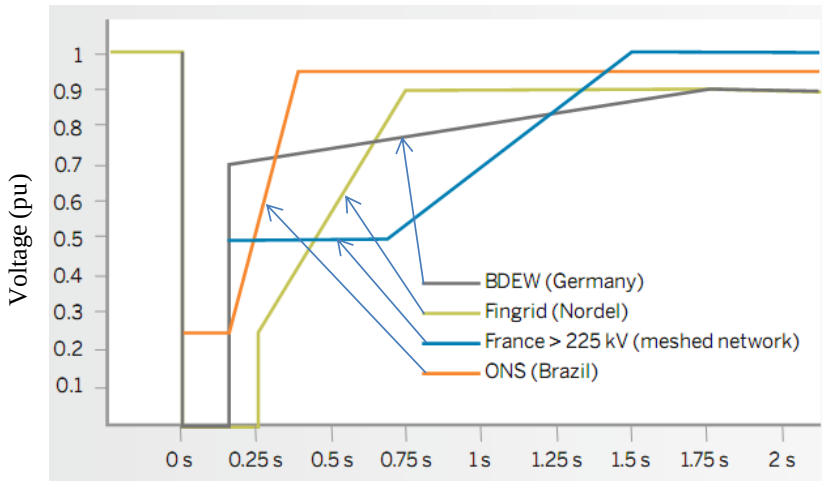

(a)

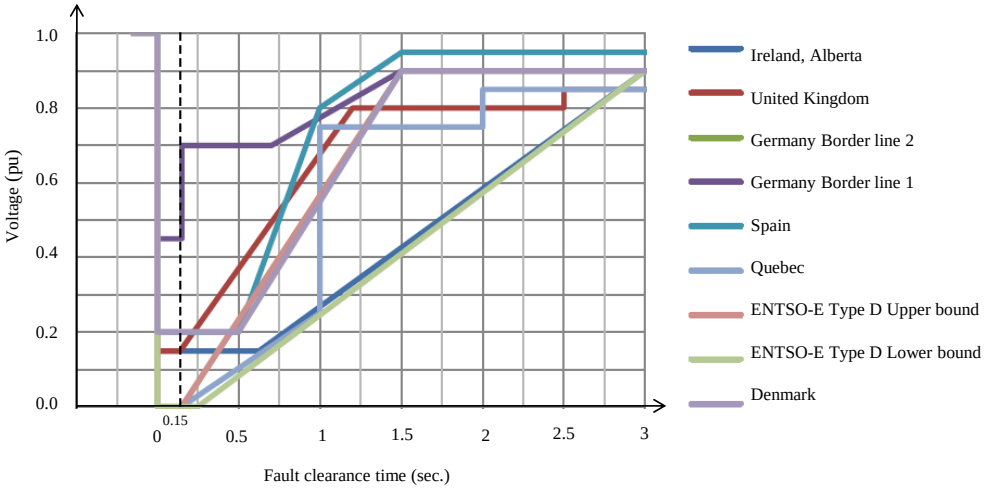

(b)

Figure 6.1. Fault ride through requirement for some countries.

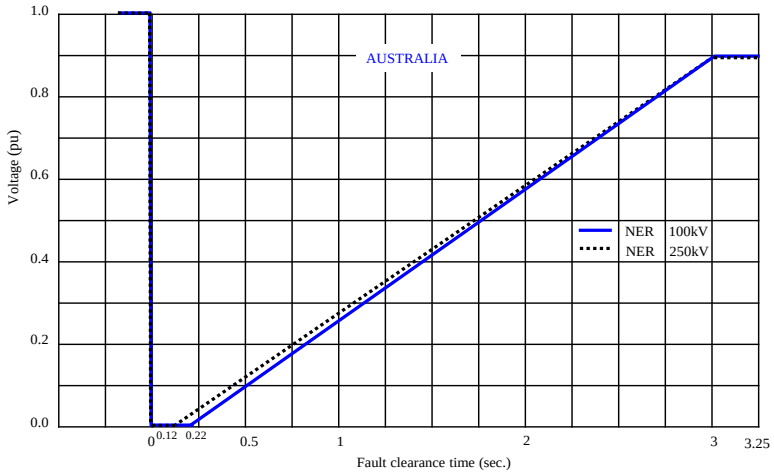

Figure 6.2. Fault ride through requirement for Australia.

Fig.6.2 shows the fault ride through requirement of Australia for 100kV and 250kV wind power plants [43], [114].

6.3.2 Active Power Control

The active power control of a generator in the electricity network is of fundamental demand to the Transmission System Operators (TSOs) to maintain the supply-demand balance as well as maintain system frequency within acceptable limits in order to control network flows and manage congestion [114]. As large capacity wind power plants are connected to the grid in many regions, the active power control is necessary for the wind farms according to TSO demands [114].

6.3.3 Reactive Power Control

In the past most of the wind turbine generators were induction generators, which absorbs reactive power from the grid even during normal operation. So an effective reactive power management is essential to maintain the low voltage issues. Nowadays the wind farms are installed with the variable speed type fitted with Dual Feed Induction Generators (DFIGs), Permanent Magnet Synchronous Generators (PMSGs). DFIGs operate at close to unity power factor (PF) and may supply some reactive power during grid disturbances. PMSGs operate at unity PF and supply some reactive power during grid disturbances. Due to the increasing penetration level of wind power into the grid wind farm must provide the reactive power exchange with the grid according to TSO demands [114].

Fig.6.3 shows wind farms 10 sec averaged the reactive power exchange with the Danish grid [115]. When the wind turbine delivers the rated active power (1 pu) to the grid, it should be able to produce a maximum reactive power of +0.1 pu to support the grid voltage. When the wind turbine delivers no active power (0 pu) to the grid, it should be able to consume no more than -0.1 pu of reactive power [115].

Fig.6.4 shows one of the three possible variants of German TSO's reactive power demand from wind power plant as a function of the voltage at nominal active power [115]. Depending on location and strength of the grid, three variants were introduced by the German TSO's. When the 110kV wind turbine delivers the nominal active power to the grid, if grid voltage drops to 96kV, it should be able to produce a maximum reactive power of +0.33 pu to +0.48 pu to support the grid voltage. If grid voltage increases to127kV, WPP will be able to consume no more than -0.228 pu of reactive power.

Fig.6.5 shows one of the three possible variants of German TSO's reactive power demand from wind power plant as function of the active power for the cases when the WPP is working at de-rated power for different ranges of voltages inside the normal operation range [115]. The *x*-axis represents the reactive power which should be supported in relation to the operational installed active power in percentage. The y-axis represents the instantaneous active power in relation to the available installed active power in percentage.

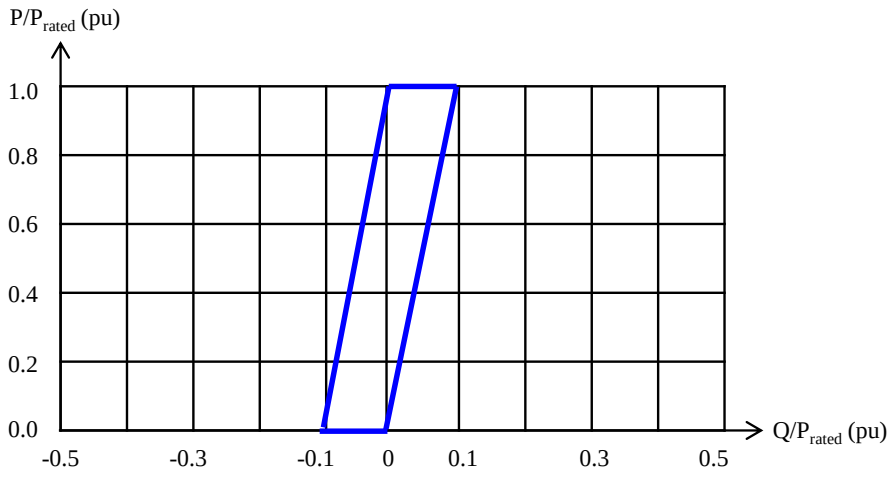

Figure 6.3 Danish TSO's reactive power demand for wind power plants during normal operation [115].

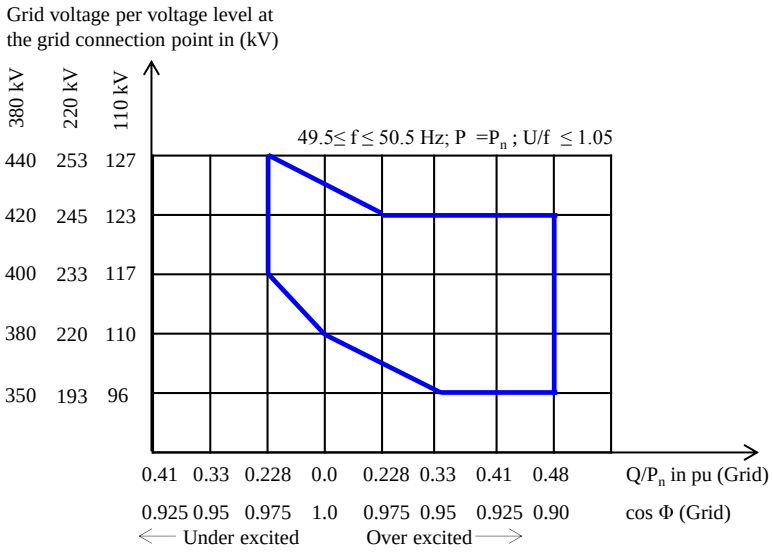

Figure 6.4 German TSO's reactive power demand for wind power plants as function of the voltage at nominal active power [115].

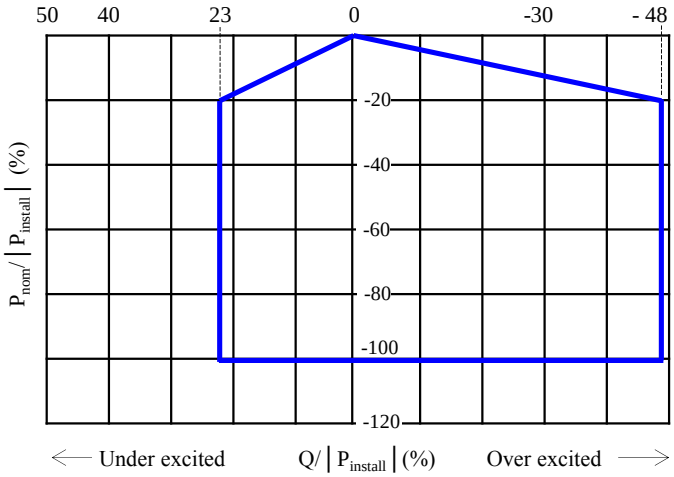

Figure 6.5. German TSO's reactive power requirement for wind power plants plant as function of the active power when the WPP is working at de-rated power [115].

6.4 Supercapacitor Energy Storage

Grid integration of variable wind power is confronted with several challenges. Energy storage such can play an important role to enhance the voltage stability and LVRT capability of the wind firm. There are several energy storage technologies available for wind turbine applications such as battery, supercapacitor (SC), flywheel, and their hybrid combinations [116]-[119]. A STATCOM with supercapacitor energy storage is the most promising solution to solve the problems associated with grid integration of wind firm.

6.4.1 Construction and Features of Supercapacitor

Supercapacitor formerly known as electric double layer capacitor or ultracapacitor is an electrochemical capacitor [120]. Supercapacitors do not have a conventional solid dielectric like dielectric capacitors. Each supercapacitor cell has multiple electric double layers which consist of a porous electric insulator and electrodes on either side [121]. The cells are tightly packed together and immersed in an electrolyte as shown in Fig.6.6 [120]. The capacitance value of an electrochemical capacitor is determined by two storage principles, which both contribute indivisibly to the total capacitance [120];

- Double-layer capacitance – Electrostatic storage achieved by separation of charge in a Helmholtz double layer at the interface between the surface of a conductive electrode and an electrolyte [120]. The separation of charge is of the order of a few angstroms (0.3–0.8 nm), much smaller than in a conventional capacitor [120]
- Pseudocapacitance – Faradaic electrochemical storage with electron charge-transfer, achieved by redox reactions, intercalation or electrosorption [120].

Supercapacitor consists of two electrodes separated by an ion permeable membrane (separator), and an electrolyte connecting electrically the both electrodes. As shown in Fig.6.6(b), an electric double layer at both electrodes is formed by applying a voltage to the capacitor, which has a positive or negative layer of ions deposited in a mirror image on the opposite electrode [120].

The capacitance of the supercapacitor is given by [120];

$$C = \frac{\varepsilon \times A}{d} \tag{6-1}$$

where, ε - permittivity, A-Surface area, d- distance between plates.

The capacitance is highest in capacitors made from materials with a high permittivity, large electrode plate surface areas and reciprocal to the distance between plates [120]. The two electrodes form a series circuit of two individual capacitors C_1 and C_2. The total capacitance is given by [120];

$$C_T = \frac{C_1 \times C_2}{C_1 + C_2} \tag{6-2}$$

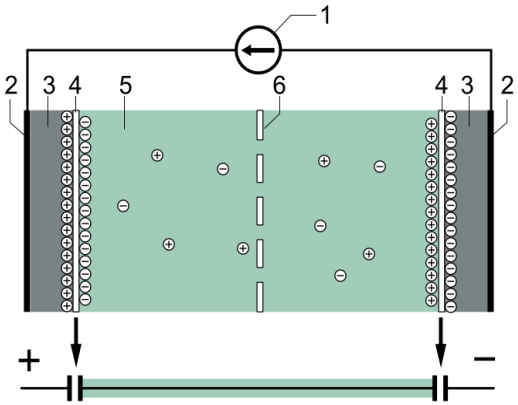

(1) - power source,
(2) - collector,
(3) - polarized electrode,
(4) - Helmholtz double layer,
(5) - electrolyte having positive and negative ions,
(6) - Separator.

(a) Structure of an ideal supercapacitor.

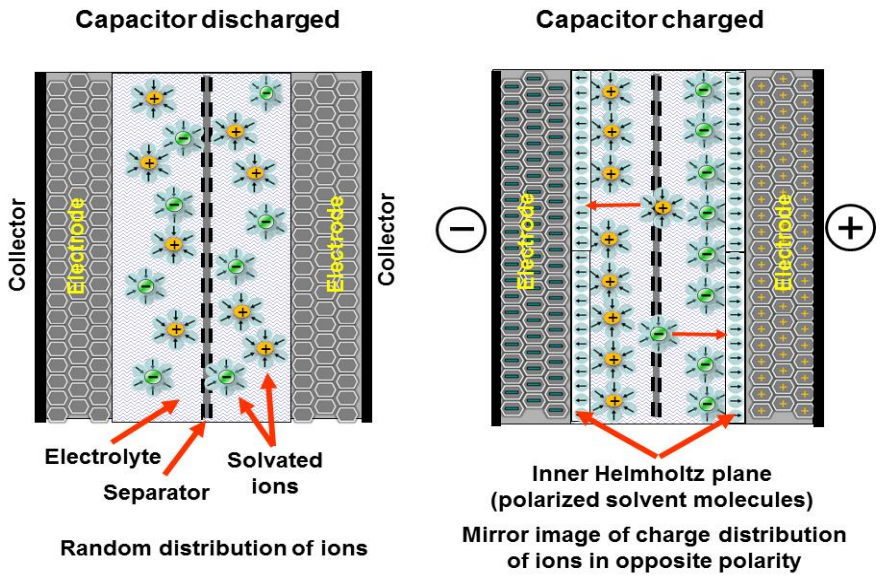

(b) Function of an ideal supercapacitor.

Figure 6.6. Construction and function of a supercapacitor [120].

The value of a supercapacitor can be in the order of thousands of times greater than an electrolytic capacitor. Larger super-capacitors have capacities up to 5000 farads [116]. The highest energy density in production is 30 Wh/kg, below rapid-charging Lithium-titanate batteries [117]. Due to the high permeability and close proximity of the electrodes, SCs have a low-voltage-withstand capability (typically 2–3 V) [118],[119]. Supercapacitors store energy by physically separating unlike charges. This has profound implications on cycle life, efficiency, energy, and power density. SCs have a long cycle life due to the fact that there are no chemical changes on the electrodes ideally in normal

operation [43]. SCs have superior efficiency. It is only a function of the ohmic resistance of the conducting path. SCs also provide exceptional power density, since the charges are physically stored on the electrodes [43]. Conversely, energy density is low since the electrons are not bound by chemical reactions. This lack of chemical bonding also implies that the SCs can be completely discharged, leading to larger voltage swings as a function of the state of charge [43], [118],[119].

Supercapacitors store energy by accumulating opposite charges on the electrodes [120] without involving chemical reaction. Therefore, they are faster and durable then the electrochemical energy storage such as batteries [122]. Supercapacitors have highest energy density among capacitors. They support up to 10,000 F/1.2 volt and up to 10,000 times that of electrolytic capacitors [120].

The supercapacitor contains a higher power density than the battery, which allows the supercapacitor to provide more power over a short period of time which is vital in wind energy applications [43]. For a corresponding high-efficiency discharge, batteries would have a much lower power capability. Conversely, the battery has a higher energy density to store more energy and release that over a longer period of time [43]. The supercapacitor has lower energy density than the battery and able to store far less amount of energy than a battery [118], [119].

Table 6.1 summarizes the characteristic parameters of different energy storage technologies [43], [119].

Table 6.1: Comparison of Energy Storage Systems

	Energy density (Wh/Kg)	Power (W/Kg)	Charge-Discharge efficiency	Self dis-Charge, (%/month)	Durability Cycle	Time Durability (Yrs)
Battery	30-200	150-3000	65-100%	3-30%	500-1K	2-10
Flywheel	100-130	1000	90%	-	>20K	>20
PHS	0.3	-	75%	Negligible	-	>75
SMES	30	Very High	95%	Negligible	-	-
CAES	10-30	-	50%	Negligible	-	>40
Super capacitor	Low	Very High	93%	Negligible	10K-100K	-

6.4.2 Supercapacitor Model

There are various models for supercapacitors. Depending on the type of application, more or less detail may be required. Fig.6.7 shows a supercapacitor model which contains inductance $L_{sc,}$ equivalent series resistance, R_{sc} and capacitance C_{sc}. This first-order supercapacitor model is a series *RLC* circuit, which is frequency, temperature, and voltage dependent in very accurate model as shown in Fig. 6.7 [123], [124]. This modelling is valid over the entire frequency spectrum, where the frequency-dependent part of the model is given by [124]:

$$Z_p(j\omega, V_{sc}) = \frac{\tau(V_{sc})\coth\left(\sqrt{j\omega\tau(V_{sc})}\right)}{C(V_{sc})\sqrt{j\omega\tau(V_{sc})}} \tag{6-3}$$

where, V_{sc} is the voltage across the capacitor which has a DC capacitance of C_{sc} and τ is the time constant.

Supercapacitors operate in a frequency range well below its self-resonant frequency in wind turbine applications. Therefore, the inductance is normally ignored. A constant capacitance and equivalent series resistance (ESR) model gives enough accuracy [124].

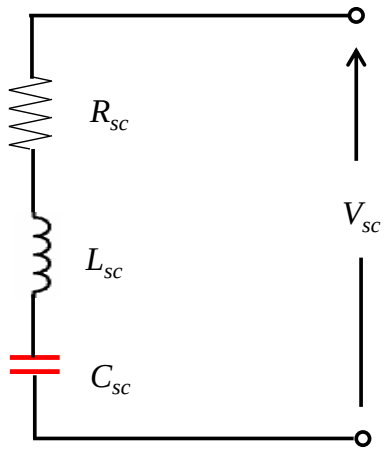

Figure 6.7. Supercapacitor model.

6.5 Reactive Power Compensation Techniques

The power system equipment and loads are rated for a specified voltage with acceptable band of voltage variations. Therefore, the grid voltage and reactive power are required to be controlled for efficient, stable and reliable operation of the power system. The problem of maintaining voltage within the required limits is complicated by the fact that the power system supplies power to a number of loads and is fed from many generating units [125]. Therefore, reactive power requirement varies with system disturbance, variations in load and generation and system faults. Since reactive power cannot be transmitted over long distance, voltage control has to be effected by using special devices dispersed throughout the system [125].

Dynamic stability is one of the main issues associated with the grid integration of wind farm. Limited reactive power support from the wind farms to meet LVRT requirements during grid disturbances is lower than that of the grid code requirements. Hence, additional reactive power compensating equipment such as Flexible AC Transmission System (FACTS) is needed to maintain system stability as fast as possible after the fault is cleared and thus the wind farms could remain connected to the power system without stability risks. The FACTS devices are widely used in power system as well as wind power application for stabilization of weak system voltage, to reduce transmission losses, to enhance transmission capacity, power oscillation damping, improving power factor, harmonics reduction and flicker mitigation. There are two categories of FACTS devices, one is thyristor based and another one voltage source converter (VSC) based. VSC based FACTS devices response time is much faster and bigger range of control than that of thyristor based [115], [126].

There are different types of reactive power compensation devices. The early generation of reactive power compensation devices uses thyristor switches and newer generation focuses on using voltage source converter (VSC). All the reactive power compensation devices provide similar services. However, the VSC technology is much faster and has a bigger range of control [127]. The Reactive power compensation devices can be divided in three groups as follows:

- Mechanical switch devices : fixed shunt reactor or capacitor, mechanical swiched shunt reactor or capacitor

- Thyristor based SVC devices : Thyristor switched reactor (TSR) or thyristor controlled reactor (TCR), Thyristor switched capacitor (TSC)
- Converter based devices : static synchronous compensator (STATCOM), static synchronous series compensator (SSSC), Unified power flow controller (UPFC)

There are various way to categorize the FACTS controllers is to group them in a way that they are connected to the power system such as shunt, series or shunt-series connection. In this thesis, FACTS device suitable for Wind turbine application are considered.

6.5.1 Static Var Compensator (SVC)

SVCs have the largest market share among the FACTS devices. They uses thyristor switches together with capacitor or inductor. They have fast voltage control capability and require more complex controller than the mechanical switch based devices. They are shun connected compensator and capable of supplying and absorbing reactive power. They can maintain the voltage stability of the power system by controlling the current of reactive element (capacitor or inductor) [115].

The configurations of SVCs are shown in Fig.6.8, which shows TCR/TSR, TSC and their combination. The TCR uses firing angle control to continuously increase/decrease the inductive current whereas in the TSR the inductors connected are switched in and out stepwise, thus with no continuous control of firing angle [115]. Usually SVC's are connected to the transmission lines, thus having high voltage ratings. Therefore the SVC systems have a modular design with more thyristor valves connected in series/ parallel for extended voltage level capability [115].

Fig.6.8 (a) shows the TCR which is controlled continuously to increase or decrease the inductive current. TSR is used to switch in or out the reactor without continuous control of firing angle. Fig.6.8 (b) shows TSC which is used to switch in or out the capacitor without continuous control of firing angle. To provide the needed reactive power generation/consumption in the network SVC's (TCR and TSC) adjust the conduction periods of each thyristor valve. When the thyristor switch is connected to the inductor,

reactive power is absorbed. Reactive power is generated when the thyristor switch is connected to the capacitor.

The voltage-current (V-I) characteristic of an SVC with the two operating zones is shown in Fig. 6.8(d) [115]. A slope around the nominal voltage is also indicated on the V-I characteristic [115]. During normal operation any voltage deviation is compensated by either the capacitive or inductive currents As the bus voltage drops, so does the current injection capability. This linear dependence is a significant drawback in case of grid faults, when large amount of capacitive current is needed to bring back the bus nominal voltage [115]. SVCs with thyristor switches are becoming obsolete due to their slow time responses and low dynamic performance. STATCOM is a better replacement option to overcome the drawbacks of SVCs.

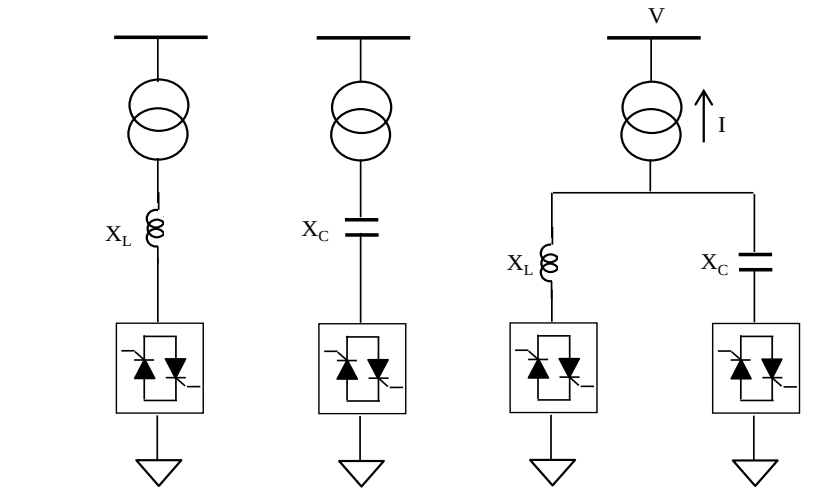

(a) TCR/TSR (b) TSC (c) TCR/TSR with TSC

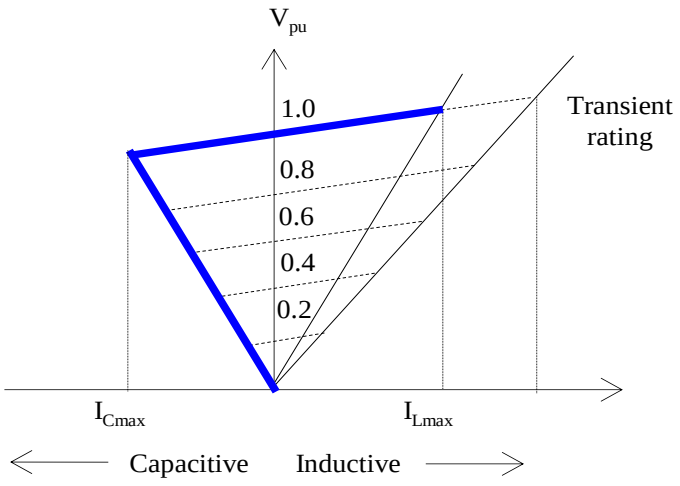

(d) *V-I* characteristic of SVC

Figure 6.8. Static Var Compensator (SVC) and its *V-I* characteristic [115].

6.5.2 Static Synchronous Compensator (STATCOM)

An alternative way to enhance the dynamic stability of wind firm is to use STATCOM to absorb or deliver reactive power to the grid during various disturbances. The characteristic of STATCOM is similar to that of a synchronous condenser. However, it has no inertia. STATCOM is one of the advanced FACTS devices which can be used to control voltage and reactive power for a stable power system operation. The main features of STACOM are [127]:

- lower investment cost,
- lower operating and maintenance costs and better dynamics are big advantages of this technology
- compact size
- wide range of operating conditions for voltage regulation and stabilization.
- high reliability, and
- flexibility

Fig.6.9 shows the schematic of the STATCOM and its V-I characteristics [115]. The STATCOM is consists of VSC with a capacitor in its DC side of the converter. AC side of the VSC is connected to the point of common coupling via transformer. Gate Turn-Off (GTO), Integrated Gate Commutated Thyristor (IGCT) or Insulated Gate Bipolar Transistor (IGBT) based VSCs are used in a STATCOM.

The reactive power output of the STATCOM Q_{sh} is controllable. Reactive power Q_{sh} is proportional to the magnitude of voltage difference V_s-V and is given by

$$Q_{sh} = \frac{V(V_s - V)}{X_s} \tag{6-4}$$

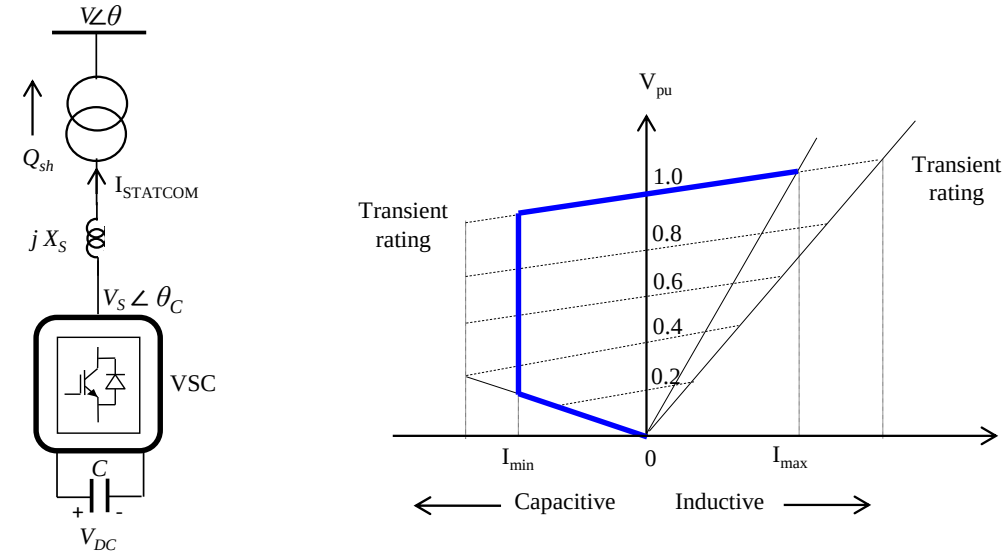

(a) STATCOM. (b) STATCOM *V-I* characteristic.

Figure 6.9. STATCOM and its *V-I* characteristic.

6.6 STATCOM Operation and Control Modes

When grid voltage is lower than the STATCOM terminal voltage, STATCOM inject reactive current to the grid to support the voltage and acts as a capacitor. When grid voltage is higher than the STATCOM terminal voltage, STATCOM absorb reactive current from the grid to decrease the voltage and acts as an inductor. Fig. 6.10 shows equivalent circuit of the STATCOM, where V_{pcc} and θ_{pcc} are the voltage and the angle of the bus to which STATCOM is connected. And V_{sh} and θ_{sh} are the voltage and the angle of the synchronous voltage source (STATCOM) and Z_{sh} is impedance through which statcom is connected to the point of common coupling (PCC). Real and reactive power exchange between PCC and statcom can be written as [115], [127];

$$P_{sh} = V_{pcc}^2\, G_{sh} - V_{pcc}V_{sh}\{G_{sh}\cos(\theta_{pcc} - \theta_{sh}) + B_{sh}\sin(\theta_{pcc} - \theta_{sh})\} \qquad (6\text{-}5)$$

$$Q_{sh} = -V_{pcc}^2 B_{sh} - V_{pcc}V_{sh}\{G_{sh}\sin(\theta_{pcc} - \theta_{sh}) - B_{sh}\cos(\theta_{pcc} - \theta_{sh})\} \qquad (6\text{-}6)$$

Where, G_{sh} is the conductance, B_{sh} is the sussceptance and $G_{sh} + B_{sh} = 1/ Z_{sh}$.

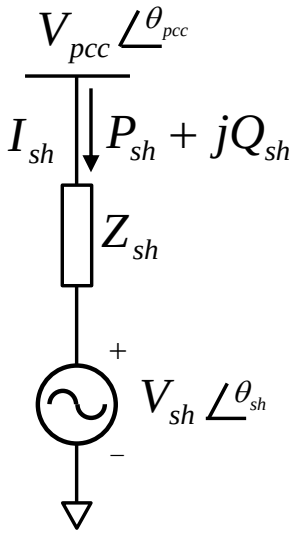

Figure 6.10. STATCOM equivalent circuit.

The control of reactive power flow provided by STATCOM can be realized in one of the following control modes [115], [127].

6.6.1 Reactive Power Control

In this control mode, STATCOM absorb or inject reactive power to the PCC according to a set reference reactive power Q_{sh}^{ref} by the wind farm controller. Thus reactive power control equation can be written as [127];

$$Q_{sh} - Q_{sh}^{ref} = 0 \tag{6-7}$$

6.6.2 Voltage Magnitude Control at PCC

In this control STATCOM absorb or inject reactive power to the PCC according to a set reference voltage magnitude V_{pcc}^{ref} by the wind farm controller. Thus voltage magnitude control equation can be written as [127];

$$V_{pcc} - V_{pcc}^{ref} = 0 \tag{6-8}$$

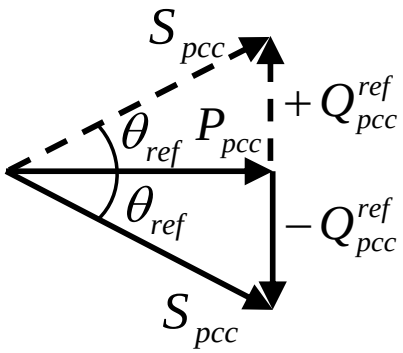

Figure 6.11. Reactive power of STATCOM for leading and lagging power factor.

6.6.3 Power Factor Control at PCC

In this power factor control method, STATCOM absorb or inject reactive power to the PCC according to a reference power factor, $cos\ \theta_{ref}$ by the wind farm controller. The reactive power control equation can be written as [127];

$$Q_{pcc} - Q_{pcc}^{ref} = 0 \tag{6-9}$$

In Fig.6.11 active and reactive power at PCC are P_{pcc} and Q_{pcc}^{ref} respectively. S_{pcc} and $cos\ \theta_{ref}$ are active power, reactive power, apparent power and desired power factor respectively. From Fig.6.11 it can be written as;

$$(P_{pcc})^2 + (Q_{pcc}^{ref})^2 = (S_{pcc})^2 \tag{6-10}$$

$$(Q_{pcc}^{ref})^2 = \frac{(P_{pcc})^2}{(cos\ \theta_{ref})^2} - (P_{pcc})^2 \tag{6-11}$$

$$Q_{pcc}^{ref} = \sqrt{\frac{(P_{pcc})^2}{(\cos\ \theta_{ref})^2} - (P_{pcc})^2} \tag{6-12}$$

From equation (6-12) for a required power factor, $cos\ \theta_{ref}$ by the wind farm controller can be achieved by absorbing or injecting reactive power Q_{pcc}^{ref} to the PCC.

6.7 STATCOM Modelling and Control

Fig. 6.12 shows a three-level NPC-based STATCOM configuration connected to the grid at PCC. The grid system is represented by a three-phase voltage source behind series RL elements in each phase. The STATCOM in Fig.6.12 either controls the power factor or regulates the voltage at the PCC by supplying/absorbing reactive power to the PCC. The STATCOM also regulates its dc bus voltage,, through real power exchange with the grid.

The ac side voltage equations of the STATCOM in Fig. 6.12 are given by

$$V_{abcs} = R_S i_{abcs} + L_S p(i_{abcs}) + V_{abc} \tag{6-13}$$

where,

Resistive loss in the system $R_S = diag\ \{R_S, R_S, R_S\}$

Leakage inductance of transformer windings $L_S = diag\ \{L_S, L_S, L_S\}$

p is the operator (d/dt)

STATCOM ac voltage $V_{abcs} = [\, V_{as}\ \ V_{bs}\, V_{cs}\,]^T$

STATCOM current, $i_{abcs} = [\, i_{as}\ \ i_{bs}\, i_{cs}\,]^T$

Voltage at point of common coupling $V_{abc} = [\, V_a\ \ V_b\, V_c\,]^T$

The equivalent circuit for phase 'a' is shown in Fig. 6.13 [127]. In this figure, V_a is the voltage at PCC, R_S is the resistance that represents loss in the system, L_S is the leakage inductance of transformer, ($V_{as1} - V_{as2}$) = V_{as} is the voltage across primary of transformer which is controlled by the STATCOM.

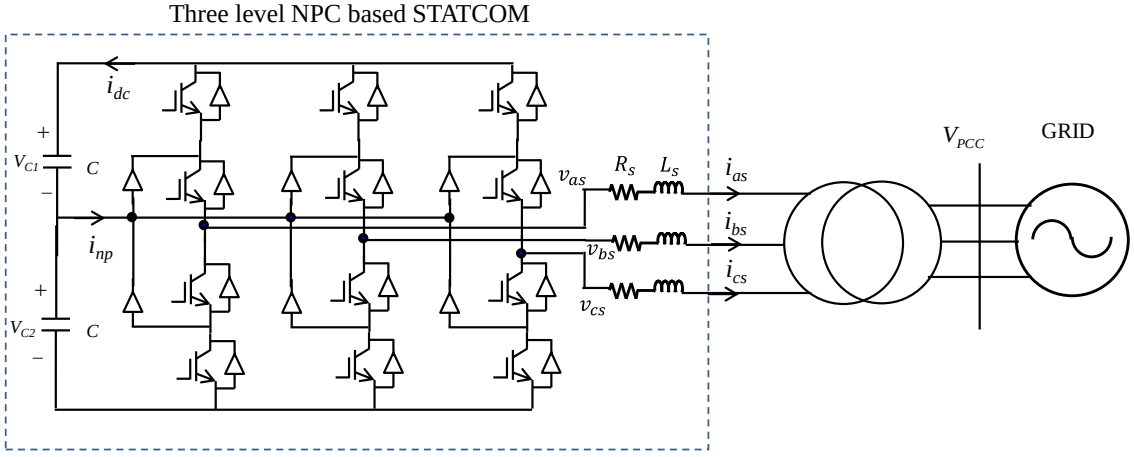

Figure 6.12 Three level NPC based STATCOM connected to the grid

The equivalent circuit for phase 'a' is shown in Fig. 6.13 [127]. In this figure, V_a is the voltage at PCC, R_S is the resistance that represents loss in the system, L_S is the leakage inductance of transformer, ($V_{as1} - V_{as2}$) = V_{as} is the voltage across primary of transformer which is controlled by the STATCOM.

The voltage equations for in abc variables are given by

$$V_a + R_S i_a + L_S \frac{di_a}{dt} - V_{as} = 0 \quad (6\text{-}14)$$

$$V_b + R_S i_b + L_S \frac{di_b}{dt} - V_{bs} = 0 \quad (6\text{-}15)$$

$$V_c + R_S i_c + L_S \frac{di_c}{dt} - V_{cs} = 0 \quad (6\text{-}16)$$

The above equations can be transformed to the d-q rotating reference frame. The q-axis component of the PCC voltage v_q is chosen to be zero and the d- axis voltage at PCC (v_d) is aligned with the reference frame. The d- and q-axis voltages of the STATCOM are [115]:

$$V_{ds} = V_d + R_S i_{ds} + L_S \frac{di_{ds}}{dt} - L_S \omega_s i_{qs} \quad (6\text{-}17)$$

$$V_{qs} = 0 + R_S i_{qs} + L_S \frac{di_{qs}}{dt} + L_S \omega_s i_{ds} \quad (6\text{-}18)$$

where

i_{ds} - d-axis current component

i_{qs} - q-axis current component

v_{ds} - d-axis voltage component

v_{qs} - q-axis voltage component, and

ω_s - system frequency

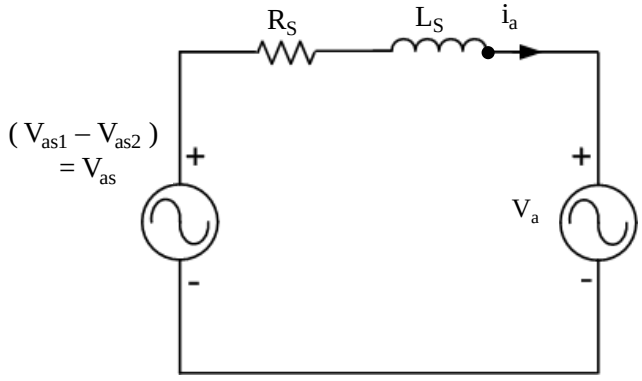

Figure 6.13 Single phase equivalent circuit of the STATCOM system.

Equations (6-17) and (6-18) indicate that the *d*- and *q*-axis current components i_{ds} and i_{qs} are cross-coupled. If there is any change in *q*-axis variables, that will affect the *d*-axis current. Similarly, a change in *d*-axis variable will also affect the *q*-axis current. A decoupled current controller is necessary to solve this problem, which is shown in Fig.6.14.

The vector control scheme of STATCOM with decoupled current controllers is shown in Fig.6.14. The dc link voltage controller is used to set *d*-axis current reference i_{ds}^* and maintain dc-bus voltage [128]. First PI controller in the second control path used to set *q*-axis current reference i_{qs}^* and maintain the voltage at point of common coupling (PCC) at desired level. Other two PI controllers keep track of reference currents (i_{ds}^*, i_{qs}^*) and the outputs are added to the cross coupling compensation terms to produce command voltages v_{ds}, v_{qs}. Finally, voltages v_{ds}, v_{qs} are converted to *abc*-reference frame to produce modulating signal [128].

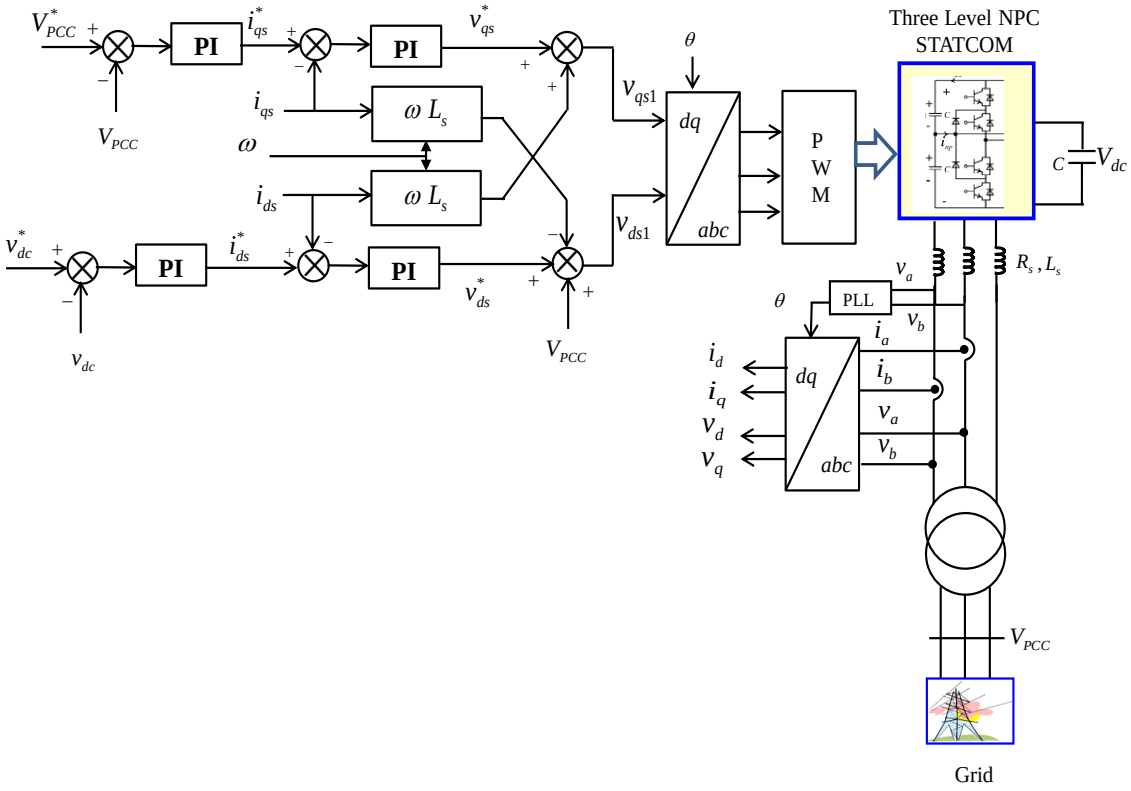

Figure 6.14. Control scheme of STATCOM with decoupled current controllers

6.8 Simulation Results and Discussions

6.8.1 System Structure

To evaluate the performance of the STATCOM with supercapacitor energy storage in enhancing dynamic voltage stability, a simulation model has been developed using *Matlab/SimpowerSystems*. Fig.6.15 shows the configuration of the studied system which include PMSG based wind turbines (9 MW), STATCOM (± 3.5 MVAR), lines, local loads, transformers and grid (100 MVA). The power system is studied to evaluate the system performance under different contingencies such as voltage swell, voltage sag, fault and sudden load change. The values and ratings of system components are presented in Fig.6.15. The short circuit capacity of the grid is 100 MVA and it is a weak grid. The system parameters are shown in Table 6.1

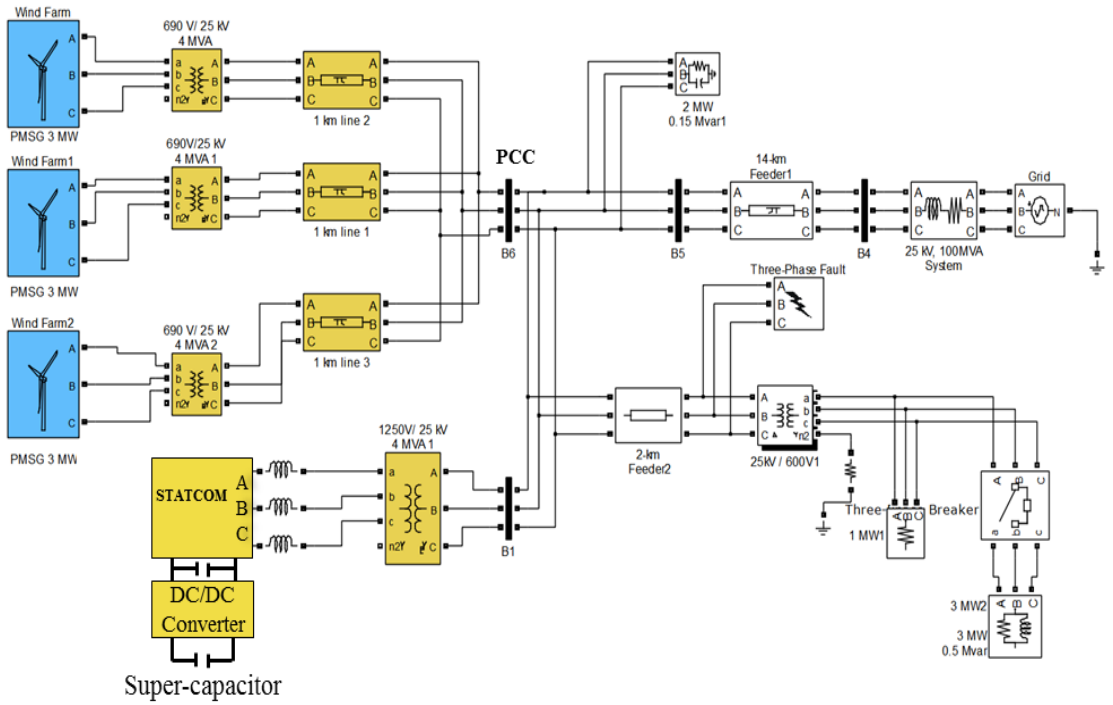

Figure 6.15. System configuration of the studied system.

Table 6.2: System parameters of studied system

Wind Turbine	3× 3 MW PMSG, 690 V
Transformers for the interface of wind turbines	3× 690V/25 kV, 4 MVA
Transformer for STATCOM	1250V/25kV, 4 MVA
Load side transformer	25kV/600V, 4 MVA
Load1	3 MW 0.5 MVAR
Load 2	3×1 MW

6.8.2 Performance Evaluation of STATCOM with Supercapacitor Energy Storage under Different Contingencies

6.8.2.1 Performance of the STATCOM during voltage swell and voltage sag

To evaluate the performance of the STATCOM with supercapacitor energy storage under voltage swell and voltage sag, the grid voltage is changed to ±12% of the rated voltage as shown. Initially the grid voltage is such that the STATCOM is inactive and it does not supply or absorb any reactive power. The grid voltage is increased by 12% at t=3.2 sec and the grid voltage becomes 1.12 pu as shown in Fig.6.16(a). The STATCOM absorbs reactive power (Q_s = + 3.2 MVAR) from the network (as shown in Fig.6.16 (b)) to compensate for the voltage rise at PCC. The grid voltage is reduced by 12% at t=3.5 sec. The STATCOM supply reactive power (Q_s = - 3.2 MVAR) to the network to maintain the PCC voltage close to 1 pu. The STATCOM controller performance and corresponding q-axis current (i_{qs}) are shown in Fig.6.19.

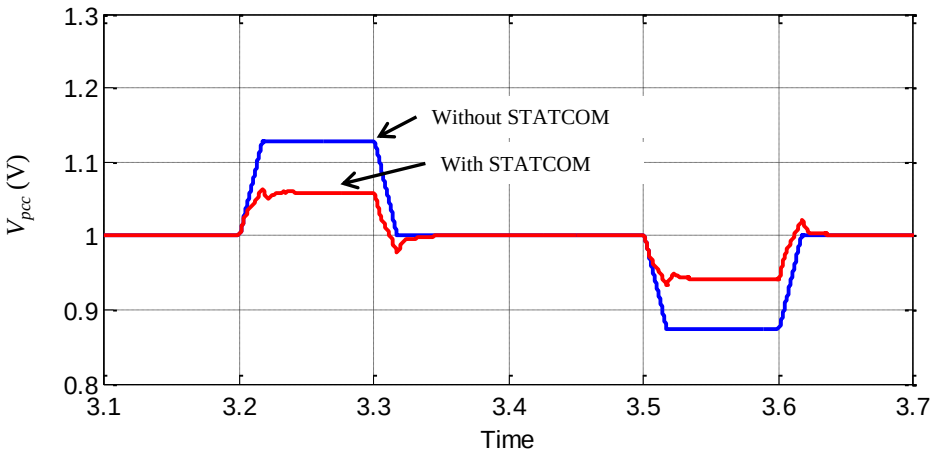

(a) Voltage at PCC with and without STATCOM during voltage swell and voltage sag.

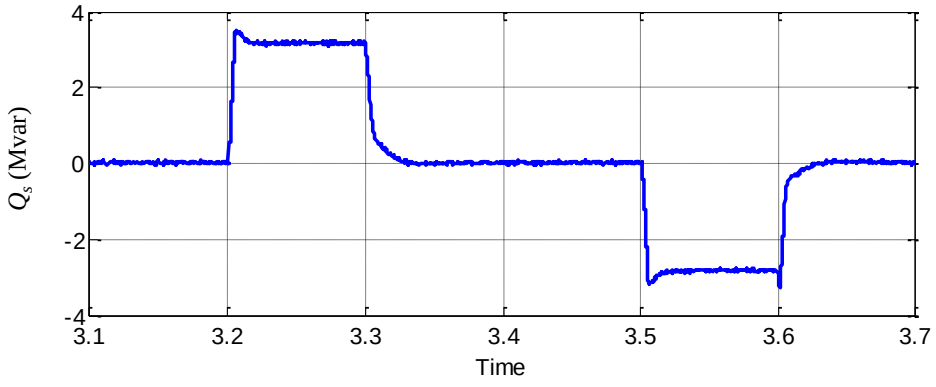

(b) Reactive power exchange from STATCOM during voltage swell and voltage sag.

Figure 6.16. Performance of STATCOM during voltage swell and voltage sag.

6.8.2.2 Performance of the STATCOM during three phase fault

The performance of the STATCOM is evaluated by introducing a three phase impedance short circuit fault as shown in Fig.6.15. Three phase short circuit fault is introduced at t=4.5 sec for 150 ms and cleared at t= 4.65 sec. Fig.6.17 (a) and (b) show the voltage and reactive power at PCC with and without STATCOM, respectively. It is seen that the voltage takes a longer time to recover after the fault has been cleared without any compensation. The voltage drops to 0.855 pu which may not fulfill the grid code requirement for certain transmission operator. With the STATCOM, the voltage recovery is faster with lesser voltage drop during fault. The STATCOM controller performance and corresponding q-axis current (i_{qs}) are shown in Fig.6.19.

Figure 6.17 (c) shows the performance of the STATCOM under unsymmetrical faults (single line to ground at t=1 sec and double line to ground at t=2 sec). It is observed that the STATCOM also performs well during unsymmetrical faults.

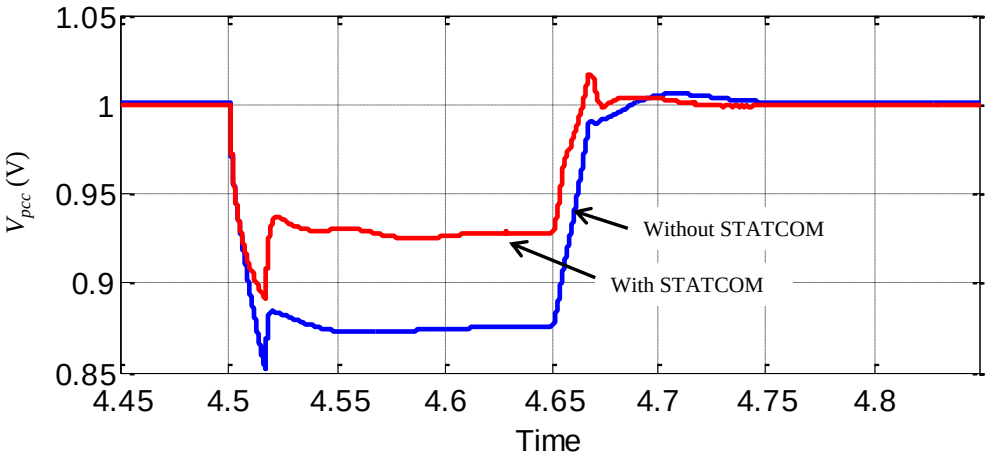

(a) Voltage at PCC with and without STATCOM during three phase faults.

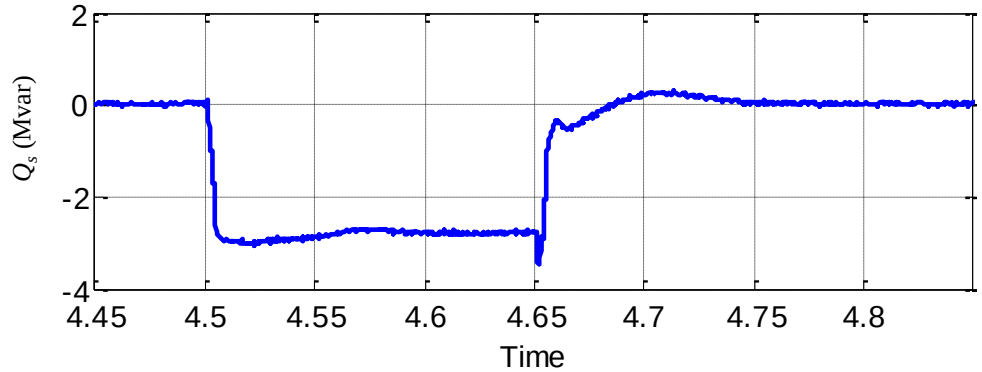

(b) Reactive power supplied by the STATCOM during three phase fault.

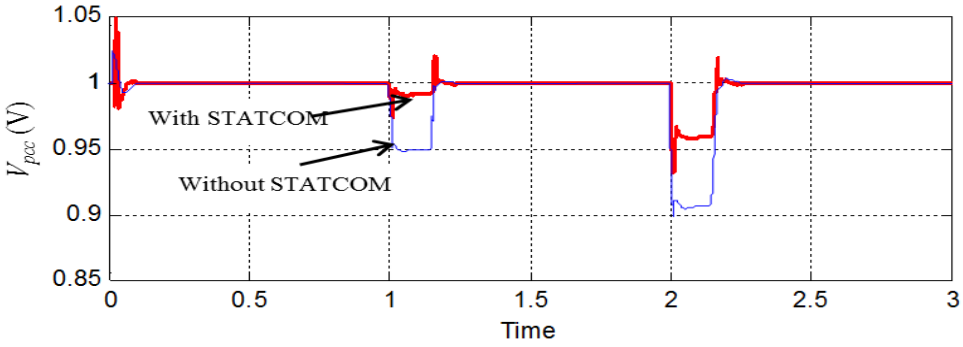

(c) Voltage at PCC with and without STATCOM during single phase to ground fault and double line to ground fault.

Figure 6.17. Performance of STATCOM during three, two and single phase short circuit.

6.8.2.3 Performance of the STATCOM during sudden load changes

The performance of the STACOM to provide support during sudden load change is investigated by adding a load of 3 MW, 0.5 MVAR at t=5 sec. The load is released from the network at t=5.5 sec. Fig.6.18 (a) shows the voltage at PCC with and without STATCOM. It is seen in Fig.6.18 (b) that the STATCOM is able to overcome the load disturbance by supplying reactive power (-1.9 MVAR) to the network and maintain the voltage at 1 pu.

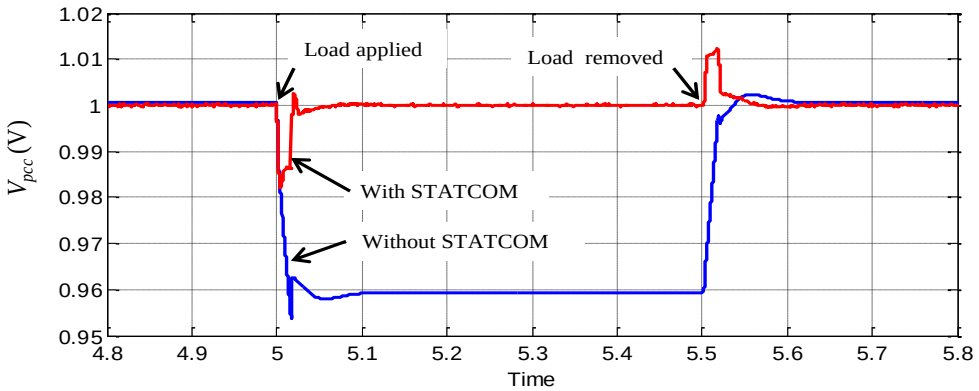

(a) Voltage at PCC with and without STATCOM during sudden load changes.

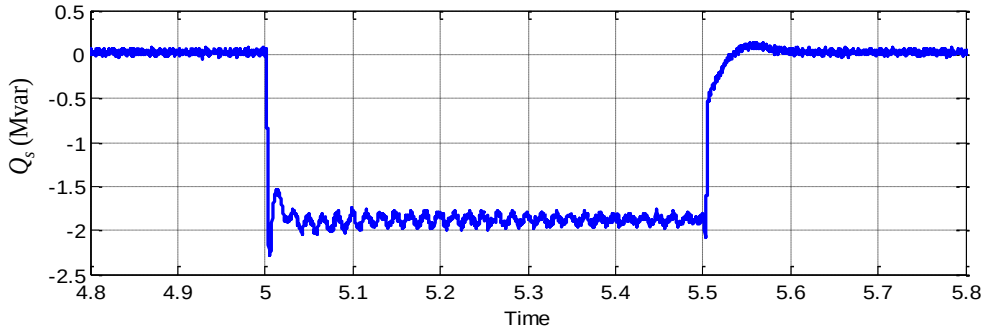

(b) Reactive power exchange by the STATCOM during sudden load changes.

Figure 6.18. Performance of STATCOM during sudden load changes.

6.8.2.4 Performance of the STATCOM Controllers under different contingencies

Fig.6.19 shows the performance of the STATCOM controllers under voltage swell, voltage sag, fault, and sudden load changes. Fig.6.19((a) to (d) show the voltage at PCC (V_{pcc}), *q*-axis current (i_{qs}), *d*-axis current (i_{ds}) and STATCOM dc link voltage (V_{dc}) together with their respective references, respectively. It is seen that voltage and current controllers follow their reference quite well during voltage swell/sag, grid fault and sudden load changes. The STATCOM controllers show very good dynamic and steady state performance and able to supply/absorb required reactive power based under different contingencies.

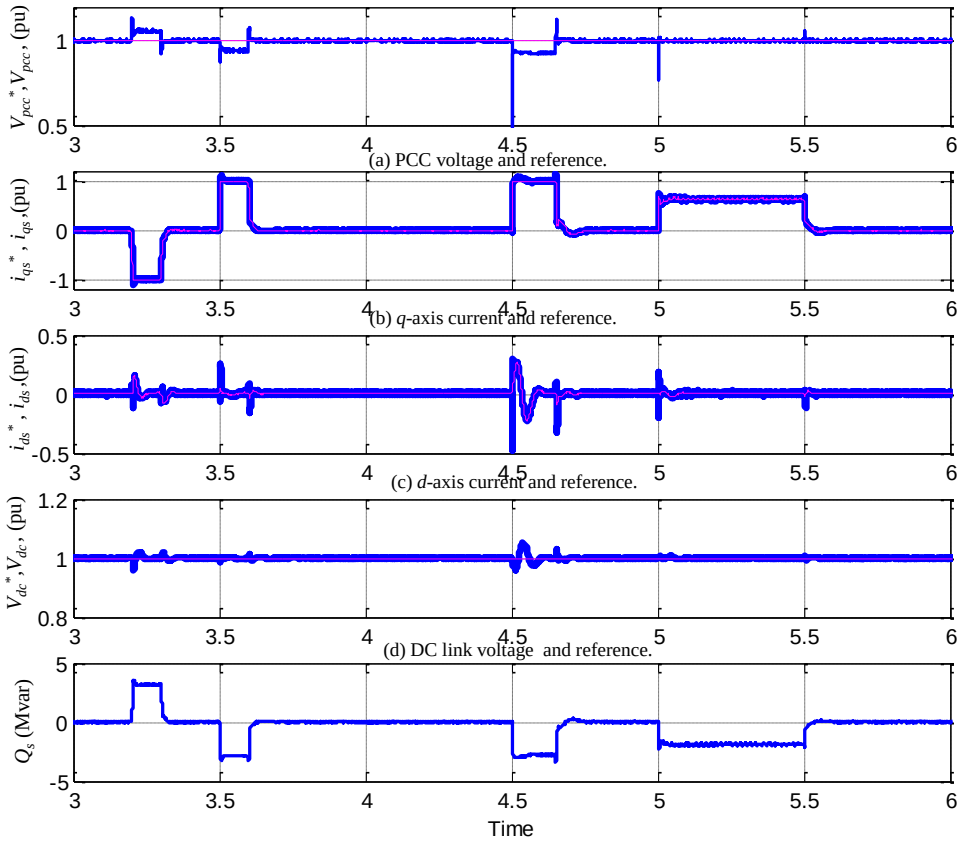

Figure 6.19. Performance of STATCOM controllers during voltage swell, voltage sag, fault and load changes.

6.8.2.5 *Performance Comparison of the STATCOM with Supercapacitor Energy Storage and SVC*

A performance comparison of STATCOM with super capacitor energy storage and SVC is shown in Fig.6.20. It is seen that STATCOM with supercapacitor energy storage perform better than traditional SVC under three phase fault and voltage swell.

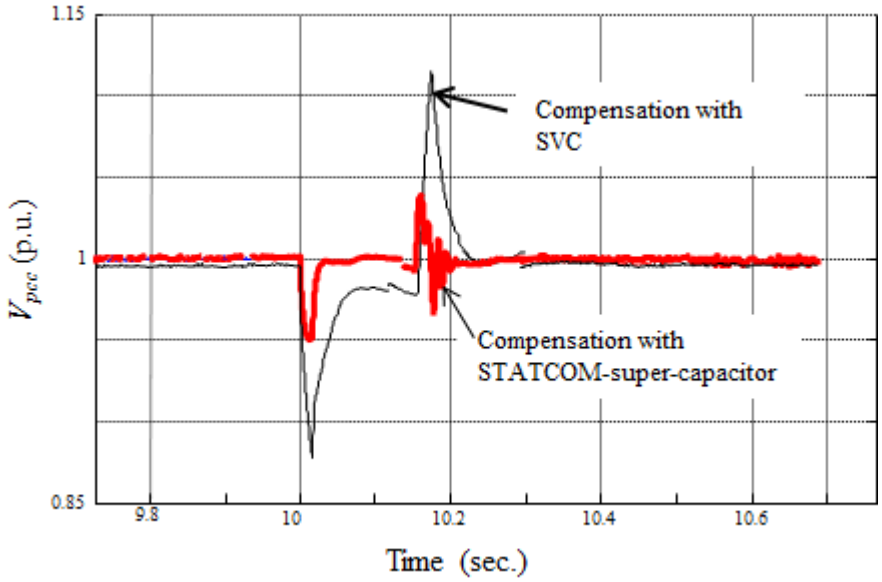

(a) Performance comparison during three phase fault

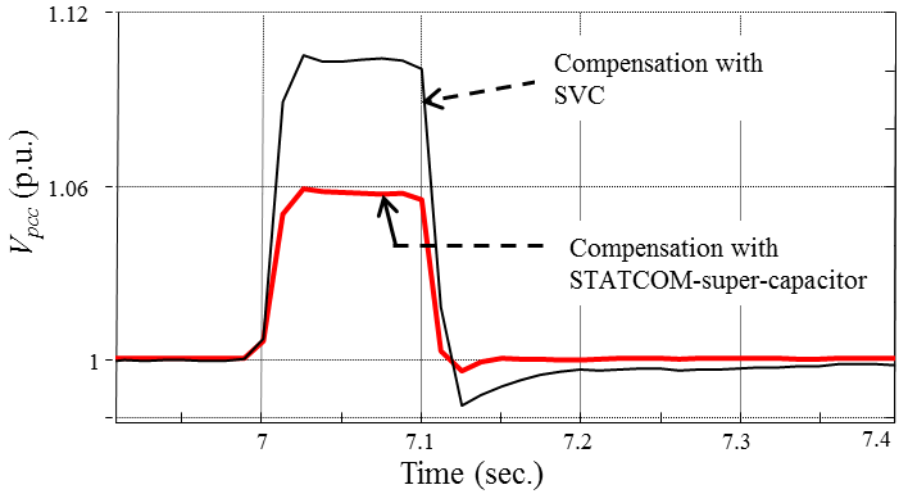

(b) Performance comparison during voltage swells.

Figure 6.20 Performance comparison of STATCOM with super capacitor energy storage and SVC.

6.9 Summary

The issues and impacts associated with the grid integration of wind energy system is reviewed in this chapter. It is necessary for the wind farm to provide necessary reactive power support to maintain the dynamic voltage stability of the power system. To enhance the voltage stability and fault ride through capability of wind farms, the application of STATCOM with supercapacitor energy storage is investigated in this chapter. To evaluate the performance of the STATCOM with supercapacitor energy storage in enhancing dynamic voltage stability, a simulation model has been developed using *Matlab/SimpowerSystems*. All the associated controllers are also implemented. The performance of the STATCOM with supercapacitor energy storage is evaluated under different contingencies such as Voltage swell/sag, fault, and sudden load changes. Results show that the STATCOM can improve the steady state and dynamic performance during various disturbances. The STATCOM controllers show very good dynamic and steady state performance and able to supply/absorb required reactive power under different contingencies to maintain the voltage stability.

Chapter 7

Conclusions and Suggestions for Future Research

7.1 Conclusions

In this thesis, several aspects of modelling and control of interior permanent magnet synchronous generator based grid connected variable speed wind turbine with maximum power extraction are considered. Both the indirect and direct control strategies are addressed for IPM synchronous generator based variable speed wind turbines are investigated. The impacts and issue associated with grid integration of wind farm are also studied.

The main outcomes and contribution of the thesis are summarised as follows.

(vi) **Analysis and Modelling**: Mathematical Analysis, modelling of wind turbine and IPM synchronous generator based variable speed wind turbine. The detail analyses of IPM synchronous generator are presented in Chapter 2 and 3, which are used to develop control strategies presented in this thesis.

(vii) **Parameter Measurement of IPM Synchronous Generator:** Simple parameter measurement methods are developed for accurate measurement of parameters of IPM synchronous generator. The accurate machine model and parameters are required to analyse the performance and to design high performance controllers. Analysis and experimental results are presented in Chapter 3. Results show that that these methods can be used for accurate parameter measurement of IPM synchronous generator.

(viii) **Indirect Control of IPM Synchronous Generator**: An enhanced indirect control scheme for IPM synchronous generator is developed by incorporating maximum torque per ampere trajectory (MTPA) and maximum power extraction (MPE) algorithm with the control scheme of generator side PWM rectifier to enhance

the system performance and efficiency. The main advantage of incorporating MTPA trajectory in the control scheme is that it can generate the required torque with a minimum stator current. Therefore, the stator loss of the IPM synchronous generator is minimized. The MTPA control scheme ensures maximum utilization of the stator current. The detail analysis of the converter and the control scheme is presented in chapter 4. The proposed control scheme is simulated in *Matlab/SimpowerSystems* environment and experimentally implemented using DSpace DS1104 digital signal processor (DSP) system. The simulations and experimental results confirm the effectiveness of the proposed control scheme and shows very good dynamic and steady state performance. The control scheme can perform well and able to extract maximum/optimum power under varying wind speeds.

(ix) **Direct Torque and Flux Control Scheme of IPM Synchronous Generator:** In an indirect vector control scheme, the IPM synchronous generator torque is controlled by controlling the *d*- and *q*-axes currents. Therefore, the generator torque is controlled indirectly by controlling *d*- and *q*-axes currents in the rotor reference frame. As the calculations are done in the rotor reference frame, a coordinate transformation is necessary in this scheme. This scheme is affected by generator parameter variations and introduces delay in the control system. Therefore, an advanced direct torque and flux control scheme for IPM synchronous generator based variable speed wind turbine with MPE is proposed in chapter 5 to overcome the drawbacks associated with indirect vector control scheme. The DTFC scheme possesses advantages such as lesser parameter dependence and reduced number of controllers compared with traditional indirect vector control scheme. The direct control scheme is simpler and can eliminate the drawbacks of traditional indirect vector control scheme. Results show that the DTFC scheme can operate under varying wind speeds to extract maximum power.

(x) **Dynamic Voltage Stability Enhancement Using Supercapacitor Energy Storage**: Dynamic voltage stability and fault ride through are the important issues among the challenges for grid connected wind firms with large penetration level. The challenges and issue associated with the wind energy integration can be eliminated or minimized by integrating supercapacitor.

This storage system can be used to enhance LVRT capability of wind firm and to improve dynamic voltage stability. In this thesis, issues and impacts associated with the wind integration into the grid are discussed. The application of static synchronous compensator (STATCOM) with supercapacitor energy storage with is investigated to enhance the dynamic performance of a grid connected wind firm. The control strategy for the STATCOM with supercapacitor energy storage is developed to enhance the dynamic voltage stability of the wind firm. The main motivation for using choosing STATCOM is its ability to provide voltage support either by supplying and/or absorbing reactive power into the power grid. Simulation model and associated controllers have been implemented in *Matlab/SimpowerSystem* and results are discussed.

7.2 Suggestions for Future Research

The research work presented in this thesis produced promising results. However, These works can be further improved. The future research may include the followings:

(i) Study the effect of parameter variation, dead time of converter in DTFC scheme.

(ii) Development of sensor less DTFC scheme with SVM (Space Vector Modulation) and multilevel converter.

(iii) Conducting a detail study on the impacts and interaction of wind energy system connected to the grid and find remedial measures

(iv) Study the effect of voltage surge and sub-synchronous resonance in wind farm

(v) Application of robust/predictive control techniques to the design of control systems for the enhancement of dynamic voltage stability.

(vi) All of the above mentioned points should be verified through experimental investigation.

(vii) The application of variable structure theory based control strategy can be investigated. The items of investigation may include theoretical analysis, design and control algorithm development.

(viii) In a wind farm, power converters operate in parallel. However, But it can cause the zero-sequence circulating-current (ZSCC), which brings current discrepancy, current waveform distortion, power losses, and electromagnetic interference (EMI). Research can be conducted to develop Improved topology can be developed to overcome these problems.

(ix) Sensorless control strategy using sliding mode obsever can be applied to estimate rotor position of PMSG by using the measured stator currents and the commanded stator voltages obtained from the control scheme of the machine-side converter of the PMSG based direct drive wind turbine. A back-propagation artificial neural network can then be designed to estimate the wind speed in real time by using the estimated turbine shaft speed and mechanical power. The estimated wind speed can be used to determine the

optimal shaft speed reference for the PMSG control system. The validity of the proposed estimation and control algorithms can be verified using simulation and experiment.

(x) Adaptive Maximum Power Point Tracking (MPPT) controller for PMSG wind turbine and direct power control for grid side inverter can be developed for transformer less integration of wind energy. The optimal control strategy can be introduced for integrated control of PMSG maximum power extraction, DC link voltage control and grid voltage support.

Chapter 8

References

[1] "Global status report-REN21", Accessed on June 12, 2014 from http://www.ren21.net/Portals/0/documents/Resources/GSR/2014/GSR2014_full%20report_low%20res.pdf

[2] "Global wind energy council" Accessed on June 12, 2014 from http://www.gwec.net/wp-content/uploads/2014/04/GWEC-Global-Wind-Report_9-April-2014.pdf

[3] C. E. Banceanu and I. Vranceanu, " Coordinated control of Wind turbines", Master's Thesis, Aalborg Univeristy, Denmark, 2011

[4] S. Müller, M. Deicke, and R. W.D e Doncker, 'Doubly Fed Induction Generator System for Wind Turbines', *IEEE Industry Application Magazine,* pp. 26-33, May 2002.

[5] J. Hu, H. Nian, H. Xu, Y. He, "Dynamic Modeling and Improved Control of DFIG Under Distorted Grid Voltage Conditions", *IEEE Transaction on Energy Conversion*, vol. 26, no. 1, pp. 163-175, March 2011.

[6] M. Mohseni, M. S. M. Islam, and M. A. Masoum, "Enhanced Hysteresis-based Current Regulators in Vector Control of DFIG Wind Turbine", *IEEE Transaction on Power Electronics*, vol. 26, no. 1, pp. 223-234, Jan. 2011.

[7] R. Cardenas, R. Pena, S. Alepuz and G. Asher, " Overview of control systems for the operation of DFIGs in wind energy applications," IEEE Transaction on Industrial Electronics, vol. 60, no. 7, pp. 2776-2798, July 2013.

[8] V. C. Ganti, B. Singh, S. K. T. C. Aggarwal, " DFIG Based Wind Power Conversion With Grid Power Leveling for Reduced Gusts," IEEE Transaction on Sustainable Energy, vol. 3, no.1, pp.12-20, Jan. 2012.

[9] H. Nian and Y. Song, "Direct Power Control of Doubly Fed Induction Generator Under Distorted Grid Voltage," IEEE Transactions on Power Electronics, vol. 29, no. 2, pp. 894-905, Feb. 2014.

[10] A. R. de Marchi, P. S. Dainez, F. J. Von Zuben, and E. Bim, "A Multilayer Perceptron Controller Applied to the Direct Power Control of a Doubly Fed Induction Generator," IEEE Transactions on Sustainable Energy, vol. 5, no.2, pp. 498-506, April 2014.

[11] H. Li and Z. Chen, "Overview of different wind generator systems and their comparisons," *Renewable Power Generation, IET*, vol. 2, pp. 123-138, 2008.

[12] H. Aoyang, *et al.*, "Study of the factors affected the rotor over-current of DFIG during the three-phase voltage dip," in *Electric Utility Deregulation and Restructuring and Power Technologies, 2008. DRPT 2008. Third International Conference on*, 2008, pp. 2647-2652.

[13] C. N. Bhende, S. Mishra and S. G. Malla, Permanent Magnet Synchronous Generator Based Standalone Wind Energy Supply System, IEEE Transaction on Sustainable Energy, vol.2, no.4, pp. 361-373, 2011.

[14] K. Tan and S. Islam, Optimum control strategies in energy conversion of PMSG wind turbine system without mechanical sensors, IEEE Transactions on Energy Conversion,vol. 19, pp. 392-399, 2004.

[15] S. Zhang, K. J. Tseng, D. M. Vilathgamuwa, T. D. Nguyen, and X. Y. Wang, "Design of a Robust Grid Interface System for PMSG-Based Wind Turbine Generators," IEEE Transaction on Industrial Electronics, vol. 58, no. 1, pp. 316-328, Jan. 2011.

[16] M Chinchilla, S. Arnaltes, and J. C. Burgos, "Control of Permanent-Magnet Generators Applied to Variable-Speed Wind-Energy Systems Connected to the Grid" *IEEE Transaction on Energy Conversion*, vol. 21, no 1, pp. 130-135, March 2006.

[17] S. M. Deghan, M. Mohamadian and A. Y. Varjani, "A New Variable-Speed Wind Energy Conversion System Using Permanent-Magnet Synchronous Generator and Z-Source Inverter", *IEEE Transactions On Energy Conversion*, vol. 24, no. 3, pp. 714-724, Sept. 2009.

[18] S. Morimoto, H. Nakayama, M. Sanada, and Y. Takeda, "Sensorless Output Maximization Control for Variable-Speed Wind Generation System Using IPMSG", *IEEE Transaction on Industry Applications*, vol. 41, no 1, pp. 60-67, Jan./Feb. 2005.

[19] W. Qiao, L. Qu, and R. G. Harley, "Control of IPM Synchronous Generator for Maximum Wind Power Generation Considering Magnetic Saturation" *IEEE Transaction on Industry Applications*, vol. 45, no. 3, pp. 1095-1105, May/June 2009.

[20] H. Chen and N. David, "Analysis of Permanent-Magnet Synchronous Generator With Vienna Rectifier for Wind Energy Conversion System," IEEE Transactions on Sustainable Energy, vol. 4, no. 1, pp. 154-163, Jan. 2013.

[21] E. Veilleux, and P. W. Lehn, "Interconnection of Direct-Drive Wind Turbines Using a Series-Connected DC Grid," IEEE Transactions on Sustainable Energy, vol. 5, no. 1, pp. 139-147, Jan. 2014.

[22] A. Causebrook, *et al.*, "Fault Ride-Through of Large Wind Farms Using Series Dynamic Braking Resistors (March 2007)," *Power Systems, IEEE Transactions on*, vol. 22, pp. 966-975, 2007.

[23] M. E. Haque, M. Negnevitsky and K. M. Muttaqi, "A Novel Control Strategy for a Variable Speed Wind Turbine with a Permanent Magnet Synchronous Generator" *IEEE Transaction on Industry Applications*, vol. 46, no. 1, pp. 331-339, Jan./Feb. 2010.

[24] S. M. R. Kazmi, H. Goto, H. J. Guo and O. Ichinokura, A Novel Algorithm for Fast and Efficient Speed-Sensorless Maximum Power Point Tracking in Wind Energy Conversion Systems, IEEE transaction on Industrial Electronics, 58 (1) (2011) 29-36.

[25] M. F. Rahman, L. Zhong and K. W. Lim, “A direct Torque controlled Interior Permanent magnet Synchronous Motor Drive incorporating Field Weakening,” *IEEE Transaction on Industry Applications*, vol. 34, no. 6, 1246-1253, Nov. 1998.

[26] I. Takahashi and T Noguchi, “A New Quick response and high efficiency control strategy of an induction motor,” *IEEE Transaction on Industry Applications*, IA-22, pp. 820-827, Sept. 1986.

[27] U. Baader, M. Depenbrock and G. gierse, “ Direct self control of inverter-fed induction machine: A basis for speed control without speed measurement”, *IEEE Trans. on Industry Applications*, vol. 28, pp. 581-588, May/June, 1992.

[28] X. Lie and P. Cartwright, "Direct active and reactive power control of DFIG for wind energy generation," *IEEE Transactions on Energy Conversion*, vol. 21, pp. 750-758, 2006.

[29] G. Abad, M. A. Rodriguez, G. Iwanski, and J. Poza, "Direct Power Control of Doubly-Fed-Induction-Generator-Based Wind Turbines Under Unbalanced Grid Voltage," *IEEE Transactions on Power Electronics*, vol. 25, pp. 442-452, 2010

[30] A. Balogun, O. Ojo, and F. Okafor, "Decoupled Direct Control of Natural and Power Variables of Doubly Fed Induction Generator for Extended Wind Speed Range Using Feedback Linearization," *IEEE Journal of Emerging and Selected Topics in Power Electronics*, vol. 1, pp. 226-237, 2013.

[31] D. Seyoum, “The dynamic analysis and control of a self-excited induction generator driven by a wind turbine” *Ph.D Thesis*, University of New South Wales, 2003.

[32] Accessed on October 24, 2013 from

http://www.ga.gov.au/image_cache/GA17056.pdf

[33] Accessed on October 24, 2013 from http://windeis.anl.gov/guide/basics/

[34] G. M. Masters, “Renewable and efficient electric power systems”, *John Wiley and Sons*, 2004.

[35] B. Wu, Y. Lang, N. Zargari and S. Kouro “Power Conversion and Control of Wind Energy Systems”, *John Wiley and Sons*, 2011.

[36] S. Santoso “Power Systems/Quality and Renewable Energy in Wind Power”, *Workshop manual*, 2011.

[37] R. Mittal, K. S. Sandhu and D. K. Jain, “ An Overview of Some Important Issues Related to Wind Energy Conversion System (WECS)”, *Intl. Journal of Environmental Science and Development*, Vol. 1, No. 4, pp. 351-363, Oct. 2010.

[38] S. Mathew “Wind Energy Fundamentals, Resource Analysis and Economics” Springer 2006.

[38a] http://www.eon.com/content/dam/eon-content-pool/eon/company-asset finder/companyprofiles/ecr/2012_09_11_EON_Offshore_Factbook_en_pdf_%20final.pdf . E.ON Offshore Wind Energy Factbook /E.ON Climate & Renewables – September 2012. Accessed on 10th September2014.

[39] L. L. Freris, "Wind Conversion Systems", *Prentice Hall International*, London, 1990.

[40] J. Aho, A. Buckspan, J. Laks "Tutorial of Wind Turbine Control for Supporting Grid Frequency through Active Power Control" Preprint.

[41] Accessed on October 31, 2013 from

http://www.alternative-energy-news.info/technology/wind-power/wind-turbines/

[42] S. Heier, "Grid Integration of Wind Energy Conversion Systems", John Wiley and Sons Ltd, Chichester, 1998,pp 23.

[43] M. M. Chowdhury, M. E. Haque, M. Aktarujjaman, M. Negnevitsky and A. Gargoom, "Grid integration impacts and energy storage systems for wind energy applications — A review," *IEEE Power and Energy Society General Meeting*, Detroit, MI, USA, pp. 1-8, July 24-29, 2011.

[44] J. M. Carrasco, , L.G. Franquelo, J.T. Bialasiewicz, E. Galvan, R.C.P. Guisado, Ma.A.M. Prats, J.I. Leon, N. Moreno-Alfonso, " power electronic systems for the grid integration of renewable energy sources: a survey," *IEEE Trans.* On Industry Applications, vol. 53, no. 4, August 2006.

[45] E. Hau, Wind Turbines: Fundamentals, Technologies, Application, Economics, springer-Verlag, 2005.

[46] M. R. Patel, "Wind and Solar Power Systems", CRC Press LLC, Bocca Raton, pp 37, 1999.

[47] L. Drouen, J.F. Charpentier, E. Semail and S. Clenet., "Study of an innovative electrical machine fitted to marine current turbine", *in Proceedings of the IEEE OCEAN'07,* Aberdeen (Scotland), 6 pp., June 2007.

[48] M. M. Chowdhury, M. E. Haque, D. Das, A. Gargoom, and M. Negnevitsky, "Modeling, Parameter Measurement and Sensorless Speed Estimation of IPM Synchronous Generator for Direct Drive Variable Speed Wind Turbine Application", *Intl Transaction on Electrical Energy System*, April, 2014.

[49] H.P. Nee, L. Lefevre, P. Thelin and J. Soulard, "Determination of *d* and *q* Reactances of Permanent-Magnet Synchronous Motors Without Measurements of the Rotor Position," *IEEE Trans. on Industry Applications,* vol. 36, pp. 1330-1335, March 2000.

[50] Y. S. Chen, Z. Q. Zhu, and D. Howe, " Calculation of *d*- and *q*-Axis Inductances of PM Brushless ac Machines Accounting for Skew," *IEEE Transaction on Magnetics*, vol. 41, no. 10, pp.3940-3042, Oct. 2005.

[51] R. Dutta and M.F. Rahman , "A Comparative Analysis of Two Test Methods of Measuring *d*- and *q*-axes Inductances of Interior Permanent-Magnet Machine," *IEEE Trans on Magnetics*, vol. 42, pp. 3712-3718, June 2006.

[52] J. F. Gieras, E. Santini, and M. Wing, "Calculation of synchronous reactance of small permanent-magnet alternating-current motors: Comparison of analytical approach and finite element method with measurements," *IEEE Transaction on Magnetics*, vol. 34, no. 5, pp. 3712–3720, Sep. 1998.

[53] D. Pavlik, V. K. Garg, J. R. Repp, and J. Weiss, "A finite element technique for calculating the magnet sizes and inductances of permanent magnet machines," *IEEE Transaction on Energy Conversion*, vol. 3, no. 1, pp. 116–122, Mar. 1988.

[54] G. Kang, J. Hong, G. Kim, and J. Park, "Improved parameter modelling of interior permanent magnet synchronous motor based on finite element analysis," *IEEE Transaction on Magnetics*, vol. 36, no. 4, pp. 1867–1870, Jul. 2000.

[55] N. A. Demerdash and T. W. Nehl, "Electric machinery parameters and torques by current and energy perturbations from field computations. II. Applications and results," *IEEE Transaction on Energy Conversion*, vol. 14, no. 4, pp. 1514–1522, Dec. 1999.

[56] T. J. E. Miller, M. Popescu, C. Cossar, and M. McGilp, "Performance estimation of interior permanent-magnet brushless motors using the voltage-driven flux-MMF diagram," *IEEE Transaction on Magnetics* ,vol. 42, no. 7, pp. 1867–1872, Jul. 2006.

[57] L. Ji-Young, L. Sang-Ho, L. Geun-Ho, H. Jung-Pyo, and H. Jin, "Determination of parameters considering magnetic nonlinearity in an interior permanent magnet synchronous motor," *IEEE Transaction on Magnetics*, vol. 42, no. 4, pp. 1303–1306, Apr. 2006.

[58] L. Chang, "An improved FE inductance calculation for electrical machines," *IEEE Trans. Magn.*, vol. 32, no. 4, pp. 3237–3245, Jul. 1996.

[59] T. W. Nehl, F. A. Fouad, and N. A. Demerdash, "Determination of saturated values of rotating machinery incremental and apparent inductances by an energy perturbation method," *IEEE Trans. Power App. Syst.*, vol. 101, no. 12, pp. 4441–4451, Dec. 1982.

[60] IEEE GUIDE: Test Procedures for Synchronous Machine, Part I—Acceptance and Performance Testing, Part II—Test Procedures and Parameter Determination for Dynamic Analysis, *IEEE Standard* 1995, 115.

[61] IEEE Standard Procedure for Obtaining Synchronous Machine Parameters by Standstill Frequency Response Testing, *IEEE Standard* 1987, 115A.

[62] J.F. Gieras and M. Wing, *Permanent Magnet Motor Technology, Design and Applications*, 2nd edition. New York: Marcel Dekker, 2002.

[63] T. F. Chan and L. L. Lai, "An Axial-Flux Permanent-Magnet Synchronous Generator for a Direct-Coupled Wind-Turbine System," *IEEE Transaction on energy conversion,* vol. 22, no. 1, pp. 86-92, March 2007.

[64] Li. Hui, K. L. Shi, and P.G. McLaren, "Neural-network-based sensorless maximum wind energy capture with compensated power coefficient", *IEEE Trans. on Industry Applications,* vol. 41, No. 6, pp. 1548 –1556, Nov./Dec. 2005.

[65] H. Polinder, B.C. Mecrow, A.G. Jack, P.G. Dickinson and M.A. Mueller "Conventional and TFPM linear generators for direct-drive wave energy conversion", *IEEE Transaction on energy conversion,* vol. 20 no. 2, pp. 260-267, June 2005.

[66] Z. Guo and L. Chang; "Converter Topologies for Two-Phase Wind Turbine PMSG Generation System", *IEEE Applied Power Electronics Conference,* pp. 536-539, Feb. 2007.

[67] E. Miliani, M. Y. Ayad, D. Depernet and J. M. Kauffmann, "Experimental Analysis of a Six Phase Permanent Magnet Synchronous Generator in a Variable Speed Constant Frequency Generating System," *IEEE Applied Power Electronics Conference,* pp. 1727-1732, Feb. 2007.

[68] Y. Chen, P. Pillay and A. Khan, "PM wind generator topologies", *IEEE Trans. on Industry Applications,* vol. 41, No. 6, pp. 1619-1626, Nov./Dec. 2005.

[69] S. A. Saleh, M.A.S.K. Khan and M.A. Rahman "Steady-state performance analysis and modelling of directly driven interior permanent magnet wind generators" *IET Renew. Power Gener,* vol. 5, Issue 2, pp.137–147, 2011.

[70] P.C Krause, O. Wasynczuk and S. D. Sudhoff, *Analysis of electrical machinery and drive system,* IEEE Press, 2002.

[71] D. A. Staton, W. L. Soong, C. Cossar and T. J. E. Miller, "Unified theory of torque production in switched and synchronous reluctance motors," *IEEE Trans. on Industry Applications,* vol. 31, No. 2, pp. 67-72, March/April 2005.

[72] A. Chiba, F. Nakamura and T. Fukao, "Inductances of cageless reluctance-synchronous machines having nonsinusoidal space distributions," *Proc. of IEEE Industry applications society Annual Meeting,* pp. 314-319, Oct., 1989.

[73] M. J. Hossain, H. R. Pota, V. A. Ugrinovskii, and R. A. Ramos, "Simultaneous STATCOM and Pitch Angle Control for Improved LVRT Capability of Fixed-Speed Wind Turbines," *IEEE Transactions on Sustainable Energy,* vol. 1, no.3, pp 142-151, Oct. 2010.

[74] S. A. Papathanassiou and M. P. Papadopoulos, "Mechanical stresses in fixed-speed wind turbines due to network disturbances, *IEEE Transactions on Energy Conversion*," vol. 16, no. 4, pp. 361-367, Dec. 2001.

[75] T. F. Chan and L. L. Lai, "Permanent-magnet machines for distributed generation: a review," *IEEE Power Engg. Annual Meeting,* 2007, pp.1-6.

[76] M. E. Haque, Y. C. Saw and M. M. Chowdhury, "Advanced Control Scheme for an IPM synchronous generator-Based Gearless Variable Speed Wind Turbine," *IEEE Transactions on Sustainable Energy,* vol. 5, no.2, pp. 354-362, April 2014.

[77] F. Blaabjerg, M. Liserre, and K. Ma, "Power electronics converters for wind turbine systems," *IEEE Trans. Ind. Appl.*, vol. 48, no. 2, pp. 708–719, Mar./Apr. 2012.

[78] J. Wang, D. Xu, B. Wu, and Z. Luo, "A low-cost rectifier topology for variable-speed high-power PMSG wind turbines," *IEEE Trans. Power Electron.*, vol. 26, no. 8, pp. 2192–2200, Jan. 2011.

[79] J. Kikuchi, M. D. Manjrekar, and T. A. Lipo, "Complementary half controlled three phase PWM boost rectifier for multi-DC-link applications," in *Proc. 15th Annu. IEEE APEC*, 2000, pp. 494–500.

[80] Y. Wang, D. Panda, T. A. Lipo, and D. Pan, "Performance improvement of dual-half-controlled-converter and its applications in utility rectifiers," in *Proc. 8th Int. Conf. Power Electron./ECCE Asia*, Jeju, Korea, May 30–Jun. 3, 2011, pp. 1711–1718.

[81] D. W. Hart, "Power Electronics', McGraw Hill, 2011.

[82] M. P Kazimierkowski, F. Blaabjerg and R. Krishnan, " Control in Power Electronics: Selected Problems", Academic Press, 2002.

[83] A. Keyhani, "Design of Smart Power Grid Renewable Energy Systems", IEEE-Wiley, 2011.

[84] F. Blaabjerg, R. Teodorescu, M. Liserre, and A. V. Timbus, "Overview of control and grid synchronization for distributed power generation systems," *IEEE Transactions on Industrial Electronics*, vol. 53, pp. 1398–1409, 2006.

[85] C. French and P. Acarnley, "Direct torque control of permanent magnet drives," IEEE IAS Annual Meeting, vol.1, pp. 199-206, 1995.

[86] I. Takahashi and T. Noguchi, "Quick torque response control of an induction motor using a new concept", *IEEE J. Tech. Meeting in Rotating machines*, paper RM84-76, pp. 61-70, 1984.

[87] I. Takahashi and T. Noguchi, "A new quick torque response and high efficiency control strategy of an induction motor", *IEEE IAS Annual Meeting*, pp. 496-502, 1985.

[88] I. Takahashi and Y. Ohmori, "High-performance direct torque control of an induction motor", *IEEE Trans. on Industry Applications*, vol. 25, pp. 257-264, 1989.

[89] M. Depenbrock, “direkte selbstregelung (DSR) fur hochdynamische drehfeldantriebe mit Stromrichterspeisung”, *etzArchiv,* vol. 7, pp. 211-218, July, 1985.

[90] C. French and P. Acarnley, “Direct torque control of permanent magnet drives,” IEEE IAS Annual Meeting, vol.1, pp. 199-206, 1995.

[91] L. Zhong, M. F. Rahman and K. W. Lim, “The direct torque control strategy for permanent magnet synchronous motors*”, Proc. of the Australasian Universities Power Electronics Conference,* vol. 3, pp. 513-518, 1996.

[92] L. Zhong, M. F. Rahman and K. W. Lim, “Analysis of direct torque control in permanent magnet synchronous motor drives”, *IEEE Trans. on Power Electronics,* vol. 12, pp. 528-536, 1997.

[93] M. F. Rahman, L. Zhong, W. Y. Hu, K. W. Lim and M. A. Rahman, “A direct torque controller for PM synchronous motor drives”, *IEEE Trans. on Energy Conversion*, pp. 637-642, Sept. 1997.

[94] N. Heng and S. Yipeng, "Direct Power Control of Doubly Fed Induction Generator Under Distorted Grid Voltage," *IEEE Transactions on Power Electronics,* vol. 29, pp. 894-905, 2014.

[95] M. E. Haque and M. F. Rahman, “Permanent magnet synchronous motor drives: Analysis, Modeling and Control,”*VDM Verlag,* Germany, 2009.

[96] S. Teleke, M. E. Baran, A. Q Huang, S. Bhattacharya and L. Anderson, “Control strategies for battery energy storage for wind farm dispatching,” *IEEE Trans. Energy Conv.,* vol. 3, pp. 725-732, Sept. 2009.

[97] A. Abedini and A. Nasiri , "Applications of super capacitors for PMSG wind turbine power smoothing,” *in Proc. 2008 IEEE Industrial Electronics Conf. (IECON),* pp. 3347-3351.

[98] P. Eriksen, T. Ackermann, H. Abildgaard, P. Smith, W. Winter, and J. R. Garcia,“System operation with high wind penetration,” *IEEE Power and Energy Magazine,* vol.3, no.6, pp. 65–74, Nov.-Dec.2005.

[99] E. DeMeo, G.Jordan, C. Kalich, J. King, M. Milligan, C. Murley, B. Oakleaf, and M. Schuerger, “Accommodating wind’s natural behavior,” *IEEE Power and Energy Magazine*, vol.5, no. 6, pp. 59–67, Nov.-Dec. 2007.

[100] D. Gautam, V. Vittal, and T. Harbour, “Impact of increased penetration of DFIG-based wind turbine generators on transient and small signal stability of power systems,” *IEEE Trans. on Power Systems,* vol. 24, no. 3, pp. 1426–1434, Aug. 2009.

[101] C. Han, A. Q. Huang, M. E. Baran, S. Bhattacharya, W. Litzenberger, L. Anderson, A. L. Johnson, and A. A. Edris, “STATCOM impact study on the

integration of a large wind farm in to a weak loop power system," *IEEE Trans. Energy Convers.*,vol.23, no.1, pp. 226–233, Mar. 2008.

[102] D. M. Logan, J. S. Baylor, D. Cotcher, and D. Krauss, "Communicating the value of dispatchability for non-utility generation projects*," IEEE Trans. on Power Systems*, vol. 10, no.3, pp. 1408–1413, Aug. 1995.

[103] EPRI, "Evaluation of the Effectiveness of Automatic Generation Control (AGC) Alterations for Improved Control with Significant Wind Generation," Electric Power Research Institute, 2009. \

[104] A. Miller, E. Muljadi, and D. Zinger, "A Variable Speed Wind Turbine Power Control", IEEE Trans. on Energy Conversion, Vol. 12, No. 2, June 1997, pp. 181-186.

[105] A. Mullane and M. J. O'Malley, "The inertial-response of induction-machine based wind-turbines," IEEE Trans. Power Syst., vol. 20, pp. 1496–1503, Aug. 2005.

[106] K. . Yoshimoto, T. Nanahara, and G. Koshimizu, "New control method for regulating state-of-charge of a battery in hybrid wind power/battery energy storages ystem," *in Proc. IEEE Power Syst .Conf. Expo*., Oct.29–Nov.1, 2006, pp.1244–1251.

[107] Warren Katzenstein and Jay Apt, "Air Emissions Due to Wind and Solar Power*," Environmental Science and Technology*, vol. 43, no. 2, pp. 253-258, 2009.

[108] S. Rose and J. Apt, "The Cost of Curtailing Wind Turbines for Frequency Regulation and Ramp-Rate Limitation" *in Proc. 29th USAEE/IAEE North American Conference on Energy and the Environment: Conventional and Unconventional Solutions*, Oct. 14-16, 2010, pp. 1-18.

[109] S. Guner and B. Bilir, "Analysis of Transmission Congestion Using Power-Flow Solutions, Accessed form http://www.wseas.us/e-library/conferences/2010/Cambridge/EE/EE-54.pdf.

[110] Kaymaz, P., Valenzuela, J., and Park, C. S., Transmission Congestion and Competition on Power Generation Expansion, IEEE Transactions on Power System, Vol.22, No.1, , pp. 156-163, 2007.

[111] J. Arai, K. Iba, T. Funabashi, Y. Nakanishi, K. Koyanagi, and R. Yokoyama, "Power Electronics and its applications in renewable energy in Japan," IEEE Circuit and System Magazine, pp. 52-66, 2008.

[112] C. Li, W. Xu, "On the Ambiguity of Defining and Measuring Inter-Harmonics, *IEEE Power Engineering Review*, pp. 56-57, July 2001.

[113] M. Östman, "Dynamics of the low voltage ride through capabilities of generators" *Wartsila Technical Journal*, pp. 13-16, Jan., 2010.

[114] Accessed on June, 2014 from http://www.aemo.com.au/Electricity/Planning/Related-Information/Wind-Integration-Investigation

[115] "Reactive power control for Wind Power Plant with STATCOM" , Institute of Energy Technology, Aalborg University, Denmark. WPS4-1051 Spring Semester, 2010.

[116] "Nesscap", Available at http://www.nesscap.com/products_lineup.htm

[117] "A 30 Wh/kg Supercapacitor for Solar Energy and a New Battery" Available at http://www.jeol.com/NEWSEVENTS/PressReleases.

[118] S. M. Lukic, C. Jian, R. C. Bansal, F. Rodriguez, and A. Emadi, "Energy storage systems for automotive applications," *IEEE Trans. Industrial Electronics*., vol. 55, no. 6, pp. 2258–2267, Jun. 2008.

[119] S. Vazquez, S. M. Lukic, Eduardo Galvan, L. G. Franquelo, and J. M. Carrasco, "Energy Storage Systems for Transport and Grid Applications," *IEEE Trans. Industrial Electronics*., vol. 57, no. 12, pp. 38813895, Dec. 2010.

[120] Accessed on June, 2014 from http://en.wikipedia.org/wiki/Supercapacitor.

[121] N. Ran and Y. Hai, "Modeling and identification of electric double-layer supercapacitors," in *Robotics and Automation (ICRA), 2011 IEEE International Conference on*, 2011, pp. 1-4.

[122] C. Zhan-li, C. Wei-rong, L. Qi, J. Zhi-ling, and Y. Zhi-han, "Modeling and Dynamic Simulation of an Efficient Energy Storage Component-Supercapacitor," in *Power and Energy Engineering Conference (APPEEC), 2010 Asia-Pacific*, 2010, pp. 1-4.

[123] S. Buller, E. Karden, D. Kok, and R. W. De Doncker, "Modeling the dynamic behavior of supercapacitors using impedance spectroscopy," *IEEE Trans. Ind. Appl.*, vol. 38, no. 6, pp. 1622–1626, Nov./Dec. 2002.

[124] L. Wei, J. Geza and B. Jean, "Real Time Simulation of a Wind Turbine Generator Coupled With a Battery Supercapacitor Energy Storage System" *IEEE Transaction on Industrial Electronics*, vol. 53, no 4, April. 2010.

[125] P. Kundur, " Power System Stability and Control", McGrawhill,1994.

[126] A. Prabhakar, "Application of Statcom For Improved Dynamic Performance of Wind Farms in a Power Grid," Masters Thesis, Missouri University 0f Science and Technology, 2008.

[127] X.P. Zhang, C. Rehtanz, B. Pal "Flexible AC Transmission Systems: Modeling and Control", ISBN-13 978-3-540-30606-1, Springer-Verlag Berlin Heidelberg 2006.

[128] M. M. Chowdhury, M. E. Haque, A. Gargoom and M. Negnevitsky, "Performance Improvement of a Grid Connected Direct Drive Wind Turbine

Using Super-capacitor Energy Storage*" IEEE PES Innovative Smart Grid Technologies Conference (ISGT),* Columbia, USA, pp. 1-6, Feb. 24-27, 2013.

[129] A. Gargoom, A. M. O. Haruni, M. E. Haque, and M. Negnevitsky, "Smooth Synchronisation and Power Sharing Schemes for High Penetration Wind Diesel Hybrid Remote Area Power Systems," *Australian Journal of Electrical & Electronics Engineering, AJEEE*, AJEEE, Vol. 8, No 1, , pp. 75-84, 2011.